

GOUTAM PAHARI

INDEX NO.: 13/16/Chem/24

2022

EXPLORATION OF FUNCTIONALITIES IN SOME DESIGNED COORDINATION POLYMERS

**Thesis Submitted for the Degree of
Doctor of Philosophy (Science)
of
Jadavpur University
2022**



By
GOUTAM PAHARI

**DEPARTMENT OF CHEMISTRY
JADAVPUR UNIVERSITY
JADAVPUR, KOLKATA 700032
INDIA**

EXPLORATION OF FUNCTIONALITIES IN SOME DESIGNED COORDINATION POLYMERS

**Thesis Submitted for the Degree of
Doctor of Philosophy (Science)
of
Jadavpur University
2022**



By
GOUTAM PAHARI

**DEPARTMENT OF CHEMISTRY
JADAVPUR UNIVERSITY
JADAVPUR, KOLKATA 700032
INDIA**



JADAVPUR UNIVERSITY

Department of Chemistry

Kolkata 700032, India


Prof. Debajyoti Ghoshal

Professor

Email: debajyoti.ghoshal@jadavpuruniversity.in

CERTIFICATE FROM THE SUPERVISOR

This is to certify that the thesis entitled "**EXPLORATION OF FUNCTIONALITIES IN SOME DESIGNED COORDINATION POLYMERS**" submitted by Sri. Goutam Pahari, who got his name registered on 1st February, 2016 for the award of Ph.D. (Science) degree of Jadavpur University, is absolutely based upon his own work under the supervision of Prof. Debajyoti Ghoshal and that neither this thesis nor any part of it has been submitted for either any degree/diploma or any other academic award anywhere before.


28/01/22
(Prof. Debajyoti Ghoshal)

(Signature of the supervisor with official seal)



Dr. Debajyoti Ghoshal
Professor
Department of Chemistry
Jadavpur University
Kolkata - 700032

Dedicated to
Baba, Ma and my supervisor

Acknowledgements

A challenging journey of my life has now completed by the contribution and support of many people. Therefore, it's the time to express my thanks to everyone for their continuous help to get an unforgettable experience for me. First of all, I would like to convey my sincerest gratitude and thanks to my supervisor Prof. Debajyoti Ghoshal, who provided me an opportunity to work with his esteemed research group and for his sincere guidance, valuable suggestions and encouragement. His guidance helped me in all the time of research and write of this thesis.

I would also like to extend my sincere regards to collaborator Professor Dr. C Malla Reddy, IISER-Kolkata. I would also like to convey my sincere regards to Prof. Samarendra Bhattacharya, Prof. Sujoy Baitalik, Prof. Kajal Krishna Rajak, Prof. Kaushiki Sankar Pramanik, Prof. Chittaranjan Sinha, Dr. Arup Gayen, Dr. Partha Mahata, Dr. Saurabh Das, and Dr. Partha Roy for their constant encouragement and valuable suggestions. All other faculty members of the Department of Chemistry are also acknowledged for their timely help.

The financial assistance received from the University Grant Commission, India, is also gratefully acknowledged. I would like to gratefully acknowledge the Jadavpur University for providing infrastructural facility for carrying out my thesis work.

I would like to thank the staff members of Chemistry Department especially Mr. Samar Bhowmick, Mr. Soumendu Bhattacharya, and Mrs. Ratna Roy Choudhury. I would like to express my heartfelt thanks to my lab-seniors Dr. Rajdip Dey, Dr. Biswajit Bhattacharya, Dr. Dilip kumar Maity, Dr. Arijit Halder, Dr. Anamika Das, Dr. Sourav Biswas, and lab-mates Dr. Fazle Haque, Saheli Ghosh, Susanta Dinda, Anupam Maity and Pintu Das for their incessant help, kind advices and also valuable suggestions related to the research. I would like to convey thanks to all my seniors and friends in Jadavpur University specially: Madhuda, Surajitda, Animeshda, Ramesh, Arka, Debopam, Sima, Suvam, Aradhita, Arpita, Tirtha, Sweta, Sayantanu. I also thank all my friends and juniors elsewhere, specially: Parthada, Sandipda, Debajyotida, Bhubanda, Susobhan, Gopal, Pintu, Sukhamoy, Animesh, Dipak, Dibyendu, Samarjit, Anupam, Jyoti, Sanjay, Shovanlal, Malay, Mousumi, Nargis, Chaitali, Bibhasda, Santanu, Chandrima, Karabi, Sriparna, Ganesh, Prakash, Sourav, Shankar and lots of names which I fail to remember now. I am also thankful to Ms. Puja Banerjee for her help.

At this moment of achievement, I would like to pay respect and love to my father Sri. Haripada Pahari whose dream is my PhD. Also I would like to pay respect to my father's elder

brothers, Late Sri. Satish Chandra Pahari and Sri. Manik Chandra Pahari for their blessings and encouragement. I express my deepest gratitude from my deep heart to my beloved mother, elder brother, and my elder sister for their indefatigable love, support, and constant encouragement both mentally and physically being a very essential part of my life and for their emotional and inspirational support throughout my life-how far and how long the distance may be. I would like to convey special thanks to my elder brother, Sri. Manoranjana Pahari who has taken up all the familial responsibilities so that I can do my research work smoothly. I am glad to remember my niece Arovi, Arshi, and my son Aroha in this pleasant moment. Also I remember my niece and nephews Mun, Bulti, Munti, Soumi, Santu, Bubun, Mantu, Nantu and sister in law Mrs. Binshati Pahari and all of my family members, relatives for their support and inspiration throughout my life. I would like to pay respect and love to my home lord Jethu and Jethima. I would like to express my special thank to my wife Dr. Madhushree Mukherjee for her constant support and encouragement. I would like to convey special respect to my father in law Sri. Deb Kumar Mukherjee, mother in law, elder sister in law Jayshreedi, Masimoni, Meson, Chorda, Barda, Ranga, Mama, Maima, Mejda and Boumoni. Vai and Liza also deserve special thanks on my part. I would like to express special regards to Moni for spiritual and energetic support. I am also glad to remember my in laws nephews Sohag, Putus, Pratik and Ranima in this moment.

I would like to pay respect to my sir, Prof. Gandhi Kumar Kar, Dr. Dhruba Prosad Chatterjee, Dr. Subhas Chandra Bhat, Sri. Swapan Pahari, Late Sri. Pranab Kumar Das and also all of my teachers for their constant support and encouragement throughout my life.

Now I would like to acknowledge Government of West Bengal for giving me opportunity to continue my PhD. I would like to convey respect to Ex-Officer-In-Charge Dr. Dilip Kumar Thakur, Principal Dr. Sibaprasad De and all of my colleagues of Govt. College of Education, Burdwan for their constant support and encouragement.

Last, but not the least, or perhaps, above all, I thank all gods and goddesses for staying with me all the while in the toughest times and blessing me by providing me with strength against all odds.

Department of Chemistry
Jadavpur University
Kolkata 700032, India.

Goutam Pahari
(Goutam Pahari) 28.01.22

Contents

Chapter 1:	General introduction: a brief review on coordination polymers (CPs) and their various functionalities and summary of research works	Page No. 1-40
Chapter 1A:	General introduction: a brief review on coordination polymers (CPs) and their various functionalities	3-36
1. Preamble and terminology		3-12
1.1. Strategy for the synthesis of different functional coordination polymer		4-6
1.1.1. Single ligand approach for the synthesis of the CPs		4-5
1.1.2. Mixed ligand approach for the synthesis of the CPs		5-6
1.1.2.1. Acid–acid mixed-ligand CPs		5
1.1.2.2. Base–base mixed-ligand CPs		5
1.1.2.3. Acid–base mixed-ligand CPs		6
1.2. Role of variable factors for designing of CPs with various functionalities		6-10
1.2.1. Role of metal ions		6
1.2.2. Role of ligands		6-7
1.2.3. Role of solvent		7-8
1.2.4. Effect of non-covalent interaction		8-9
1.2.5. Effect of UV radiation as external stimuli		9
1.2.6. Role of pH of the medium		10
1.2.7. Role of temperature		10
1.2.8. Effect of counter anion		10
1.3. Different synthetic techniques for synthesis of functional CPs		10-11
1.3.1. Stirring		10-11
1.3.2. Solvothermal		11
1.3.3. Slow diffusion		11
1.4. Structural characterizations of CPs		11-12
2. Various potential applications of CPs/MOFs		12-22
2.1. Gas and solvent sorption		13
2.1.1. Nitrogen adsorption		13-14

2.1.2. Selective carbon dioxide adsorption	14-16
2.1.2.1. Selective carbon dioxide adsorption at high pressure	16
2.1.3. Hydrogen storage	16-17
2.1.4. Methane storage	17-18
2.1.5. Solvent adsorption	18
2.2. Proton conductivity	18-19
2.3. Electrical conductivity	19
2.4. Photo responsivity and mechanical properties	19-20
2.5. Anion exchange	20-22
3. Structural transformation and dynamicity in coordination polymers	22-25
3.1. Reason for structural dynamism	23
3.1.1. Structural transformation due to exchange of guest molecules or ions	23-24
3.1.2. Structural transformation due to change in temperature and solvent exchange	24
3.1.3. Structural transformation for change in pressure	24-25
3.1.4. Photoinduced structural transformation	25
4. Interpenetration in CPs	25-27
Chapter 1B: Summary of research works	37-40
Chapter 2 Mixed ligand coordination complexes using multicomponent ligand: syntheses, characterization and effect of non-covalent interactions on their framework structures	41-60
1. Introduction	43-44
2. Experimental section	44-47
2.1. Materials	44-45
2.2. Physical measurements	45
2.3. Syntheses	45-46
2.4. Crystallographic data collection and refinement	46-47
3. Results and discussion	47-57
3.1. Crystal structure descriptions	48-55
3.2. Infrared spectra	55-56
3.3. Powder X-ray diffraction (PXRD)	56
3.4. Solid-state absorption spectra	56-57
4. Conclusion	57

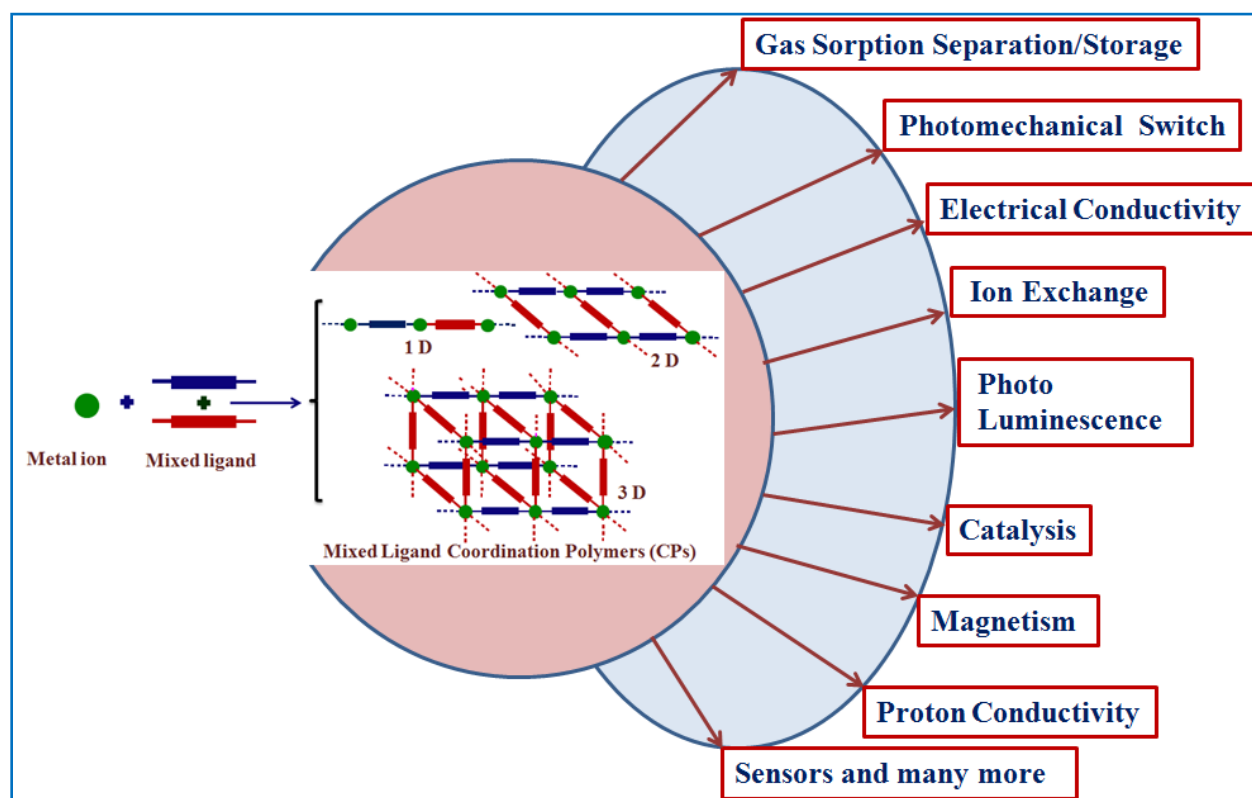
Chapter 3	Designing of three mixed ligand MOFs in searching of length induced flexibility in ligand for the creation of interpenetration	61-82
1. Introduction		63-65
2. Experimental section		65-69
2.1. Materials and methods		65
2.2. Physical measurements		65
2.3. Sorption measurements		65-66
2.4. Syntheses		66-68
2.5. Crystallographic data collection and refinement		68-69
3. Results and discussion		69-78
3.1. Structural description of the complexes		69-76
3.2. Powder X-ray diffraction (PXRD)		76
3.3. Thermogravimetric analysis (TGA)		76-77
3.4. Sorption study		77-78
4. Conclusion		78-79
 Chapter 4	 Synthesis of two cationic coordination polymers for the exploration of anion exchange properties	 83-106
1. Introduction		85-87
2. Experimental section		87-90
2.1. Materials and methods		87
2.2. Physical measurements		87
2.3. Syntheses		87-89
2.4. Crystallographic data collection and refinement		89-90
3. Result and discussion		90-103
3.1. Structural description of the complexes		90-97
3.2. Powder X-ray diffraction (PXRD) of the complexes		97
3.3. Thermogravimetric analysis		97-98
3.4. Anion exchange studies		98-102
3.5. Sorption Studies		102-103
4. Conclusion		103

Chapter 5	Structural transformations in metal organic frameworks for the exploration of their CO₂ sorption behavior at ambient and high pressure	107-140
1. Introduction		109-110
2. Experimental section		111-116
2.1. Materials		111
2.2. Physical measurements		111
2.3. Sorption measurements		111-112
2.4. Crystallographic data collection and refinement		112-113
2.5. Syntheses		113-115
2.6. Different binding modes of 3,3'-dmglut		115-116
3. Results and discussion		116-136
3.1. Structural descriptions		116-124
3.2. Thermogravimetric analysis (TGA)		124-125
3.3. Sorption study		126-131
3.4. Powder X-ray diffraction (PXRD) and structural transformations of the complexes		132
3.5. Indexing of PXRD data by TREOR 90 program and McMaille program		132-136
4. Conclusion		136
Chapter 6	A reversible photoinduced solid-state transformation in an interpenetrated 3D metal-organic framework with mechanical softness	141-166
1. Introduction		143-145
2. Experimental section		145-149
2.1. Materials and methods		145
2.2. Physical measurements		145
2.3. Sorption measurements		146
2.4. Syntheses		146-147
2.5. Crystallographic data collection and refinement		148-149
3. Results and discussion		149-163
3.1. Structural description of the compounds		149-154
3.2. Powder diffraction (PXRD) analysis		154-155
3.3. Gas sorption studies		155
3.4. Thermo gravimetric analysis (TGA)		156
3.5. Differential thermal analyses (DTA)		156-157

3.6. NMR study	157-158
3.7. Reversible photochemical solid-state transformation	159-160
3.8. Mechano-structural property correlation by nanoindentation experiments	160-163
4. Conclusion	163
List of publications	167-168

Chapter 1

General Introduction and Summary of Works



Section 1A: General introduction: a brief review on coordination polymers (CPs) and their various functionalities

Section 1B: Summary of research works

Chapter 1A

General introduction: a brief review on coordination polymers (CPs) and their various functionalities

1. Preamble and terminology

Coordination polymers (CPs) become the most active area of interest for the inorganic researcher over the past few decades. CPs are inorganic or organometallic polymeric structures consisting of repeating coordination units extending in one, two or three dimensions.¹⁻³ They've been recognised and researched since the mid twentieth century.⁴ However X-ray structure of coordination polymer of Prussian blue was first reported by Buser *et al* in 1977.⁵ Whereas the term metal–organic frameworks (MOFs) was generally used for the higher dimensional porous coordination polymers (PCPs) and having gas storage ability. Some other terms, like hybrid organic-inorganic materials, metal–organic hybrid etc. are also frequently used in different scientific research society. To solve the ambiguity about the different terminologies used in this field, IUPAC task group have defined the main three terminologies as follows.⁶

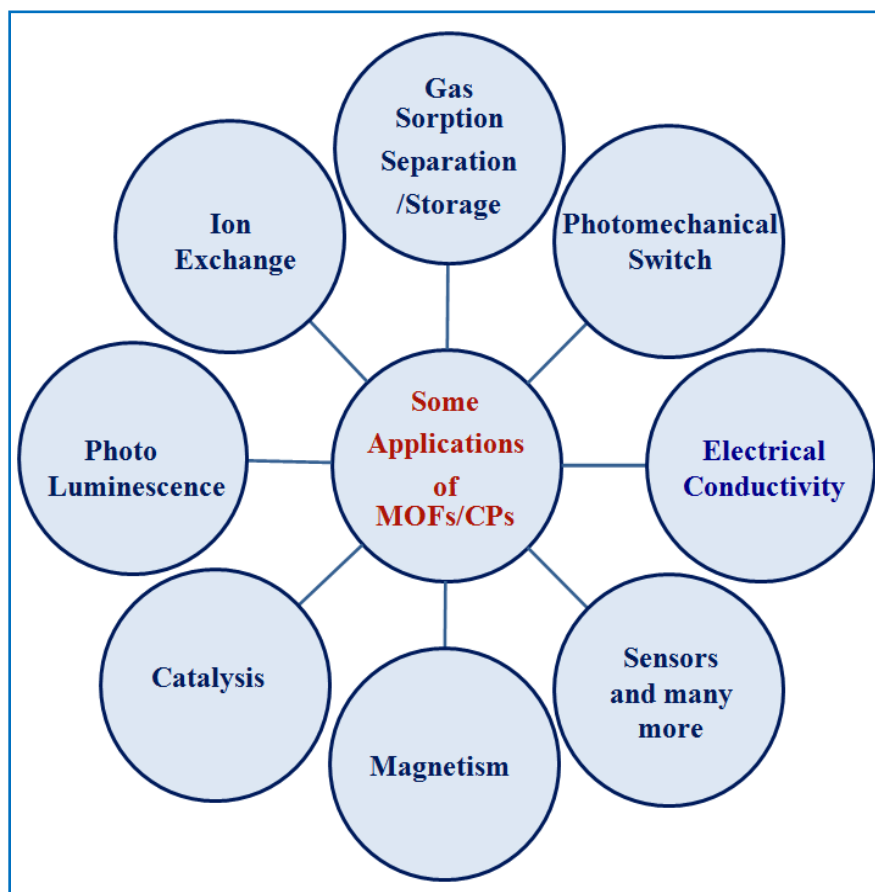
Coordination Polymer: A coordination compound continuously extending in 1, 2 or 3 dimensions through coordination bonds.

Coordination Network: A coordination compound extending, through coordination bonds, in 1 dimension, but with cross-links between two or more individual chains, loops or spiro-links, or a coordination compound extending through coordination bonds in 2 or 3 dimensions.

Metal-Organic Framework: Metal-Organic Framework, abbreviated to MOF, is a Coordination Polymer (or alternatively Coordination Network) with an open framework containing potential voids.

Higher dimensional coordination polymers or metal-organic frameworks (MOFs) are not only important for their diverse structural features but also very important for their potential applications (Scheme 1) in gas storage^{7,8} and separation,^{9,10} electrical/proton conductivity,^{11,12} photo luminescence,^{13,14} anion exchange,^{15,16} catalysis,^{17,18} magnetism,^{19,20} sensing,^{21,22} mechanical properties^{23,24} etc. For the inclusion of the functionality in coordination polymers, the foremost weightage will be given to the design and synthesis of CPs. Proper selection of metal ions and ligands during the synthesis of the coordination polymer is the key to create functional coordination polymers. In various cases structural flexibility as well as mechanical properties

plays a vital role for CPs to undergo particular reaction. To construct coordination polymers, account of several factors of influences like temperature,²⁵ pressure,²⁶ pH of the medium,²⁷ solvents²⁸ etc. and some other factors such as weak non-covalent interactions²⁹, exchangeable coordinated or lattice anions,³⁰ susceptibility towards UV radiation³¹ etc. are very essential. Due to the involvement of diverse factors of influence and various premeditated synthetic techniques this research field becomes very cultivated topic of researcher till now.



Scheme 1. Potential applications of CPs/MOFs in different fields.

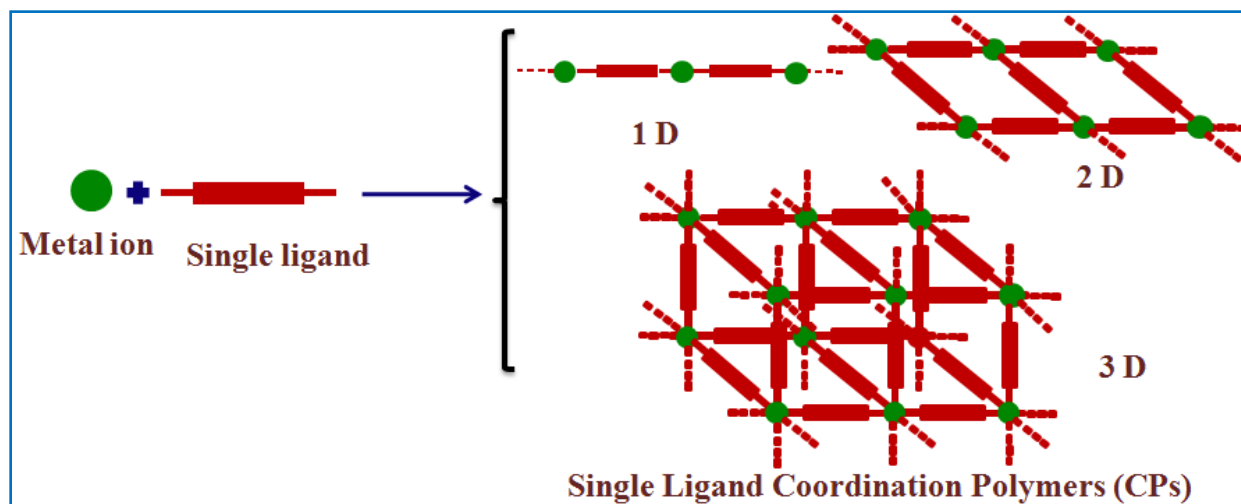
1.1. Strategy for the synthesis of different functional coordination polymer

Two major strategies are usually adapted for the synthesis of different functional coordination polymers.

1.1.1. Single ligand approach for the synthesis of the CPs

At the beginning, strategy of synthesis was based on single ligand approach in which metal ion or metal cluster is used along with one ligand to produce a coordination polymer (Scheme 2). Single ligand approach has been developed and widely used by Robson,³² Fujita,³³ Kitagawa,³⁴

Yaghi³⁵ and others³⁶. Large numbers of well known CPs like MIL series, MOF series, IRMOF series etc. have been synthesized based on this approach. In this time some anions have been used which can provide charge balance for the system as well as act as a ligand.^{37,38} Some N,N'-donor ligands^{39,40} also used for the syntheses of CPs and the charge balance is achieved by the counter anions of the metal salts.



Scheme 2. Schematic representation of synthesis of single ligand CPs.

1.1.2. Mixed ligand approach for the synthesis of the CPs

In searching of various functional CPs with diverse framework mixed ligand approach has been developed in recent two decades. In the mixed ligand approach for the synthesis of the CPs more than one type of ligand has been used (Scheme 3). This creates more variation in the structures which leads to better possibility to have functional material by this multi-ligand approach. There are mainly three types of mixed ligand approach.

1.1.2.1. Acid–acid mixed-ligand CPs

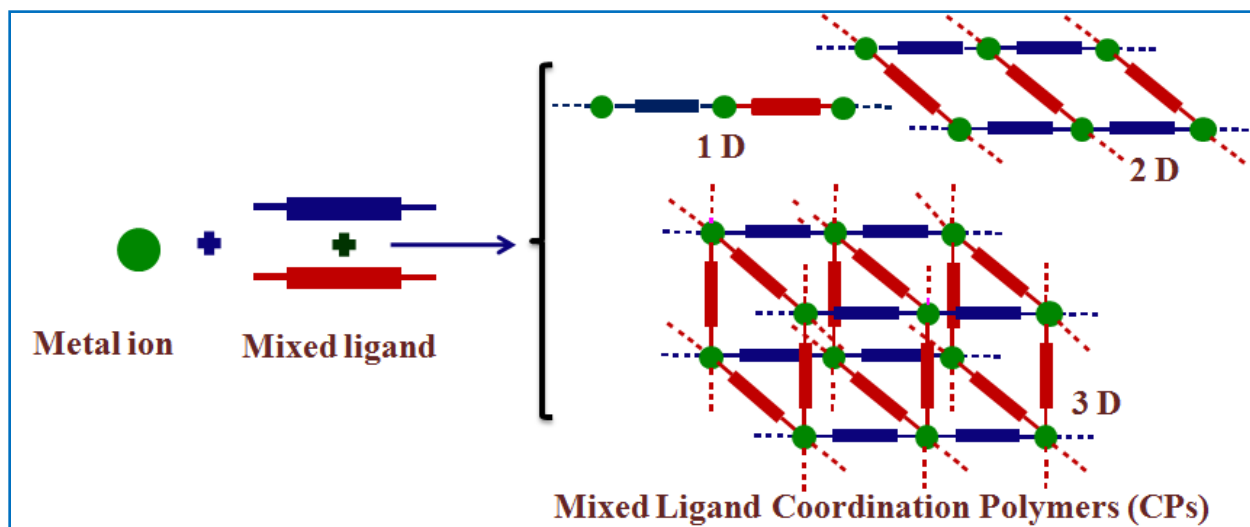
In this approach both the mixed- ligands are anionic in nature. Some examples of synthesized CPs in this strategy are 3D $[\text{Zn}_4\text{O}(\text{tp})(\text{tcb})_{4/3}]_n$ ⁴¹, interpenetrating 2D + 3D framework of $\{[(\text{CH}_3)_2\text{NH}_2][\text{Zn}_2(\text{tp})(\text{tcb})][\text{Zn}_3(\text{tcb})_2(\text{H}_2\text{O})_2](\text{DMA})_4(\text{EtOH})_2(\text{H}_2\text{O})_7\}_n$ ⁴², 3-fold interpenetrating framework of $\{[(\text{CH}_3)_2\text{NH}_2][\text{Zn}_2(\text{tp})(\text{tcb})](\text{DMF})_3(\text{H}_2\text{O})_2\}_n$ ⁴². Here both the ligands, H_2tp and H_3tcb , are acid $\{\text{H}_2\text{tp} = \text{terephthalic acid}; \text{H}_3\text{tcb} = 1,3,5\text{-tris(4-carboxyphenyl)benzene}\}$.

1.1.2.2. Base–base mixed-ligand CPs

Here both the ligands are neutral N,N- donor. One Example is 3D $[\text{Co}(\text{bpy})(\text{bimb})(\text{SCN})_2]_n$ is synthesized by hydrothermal reaction of mixed ligands bpy and bimb with $\text{Co}(\text{SCN})_2$.⁴³

1.1.2.3. Acid–base mixed-ligand CPs

The acid–base mixed-ligand approach is the most important and promising branch. Of course, acid and base ligands are ideal partners that can balance charge and coordination numbers, repulsive void and weakly interaction all at once. Therefore this strategy is widely used to produce various frameworks with diverse functionality.



Scheme 3. Mixed ligand approach to synthesize coordination polymer.

1.2. Role of variable factors for designing of CPs with various functionalities

1.2.1. Role of metal ions

As one of the most common factors metal ions can be viewed as a primary node of controllable building blocks for synthesis of functional CPs.⁴⁴ One particular metal ion with a given valence usually defines its fundamental coordination predilection and geometry.^{45,46} Again the various factors like size of the metal ion, coordination number, affinity to ligands, ligand field stabilization energy etc.^{47,48} can ultimately make a choice of metal towards a successful structure formation. Various types of metals such as alkali, alkaline earth, transition, lanthanides, and actinides may be used in synthesis of CPs. Among them transitional metal ions are considering to be most effective for the formation of versatile CP due to their dynamic coordination ability.

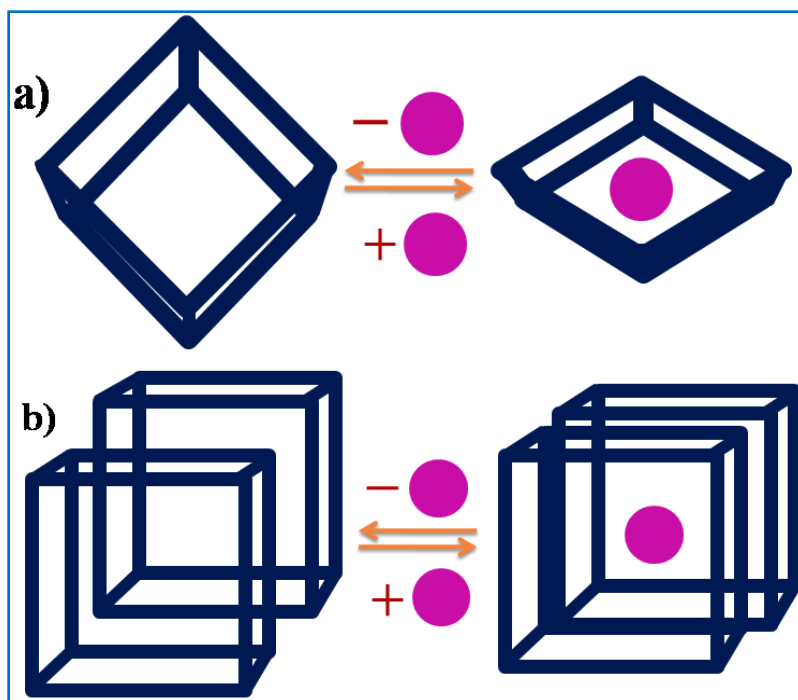
1.2.2. Role of ligands

Another most important factor for synthesizing functional CPs is the choosing of appropriate ligands. By calculatingly modulating the nature of ligands the resulting CP networks can be methodically and frequently attuned. In principle, rigid linkers have a propensity to construct 3D open networks with available cavities. With the increase of ligand length, interpenetration of

such nets generally occurs due to decrease in the empty volumes of the crystal lattices. Generally, two different types of ligands (charged and neutral) are mostly used for the meaningful synthesis of common mixed ligand CPs. The suitable variation of mixed ligands (dicarboxylates and N,N donor ligands) creates customized architecture in coordination polymers for which various functionality arises. It is conventional that N-donor and O-donor ligands are quite common in the field of coordination chemistry^{49,50} along with S-donor, P-donor or hetero donor ligands^{51,52} are parallelly helpful to construct interesting structure with potential applications. H₂tp (terephthalic acid) and bpy (4,4'-bipyridine) can be viewed as the most popular acid and base bridging ligands for preparing CPs, which have the paired functional groups (carboxyl and pyridine) in the two sides of their backbones. Different dicarboxylates and a family of conjugated aromatic ligands 4,4'-bpt {1H-3,5-bis(4-pyridine)-1,2,4-triazole}, bpb {1,4-bis(4-pyridine)benzene}, dfbpb {2,3-difluoro-1,4-bis(4-pyridine)benzene}, bpeb {1,4-bis(4-pyridineethynyl)benzene}, bpp {1,3-bis(4-pyridyl)propane}, bpds (4,4'-bipyridyl disulfide) and bpe {1,2-bis(4-pyridyl)ethylene} can be used to design the various functional CPs. Use of bis-imidazole and bis-triazole instead of bipyridine in N,N donor linkers is also very popular to form well-defined CPs.

1.2.3. Role of solvent

Generally, most CPs are synthesized from solvent media, but CPs are normally insoluble once formed, due to their polymeric nature. Solvent plays an essential role to build the crystal structure of the CPs and facilitates structural stability of the framework by the weak interaction (hydrogen bonding, C-H $\cdots\pi$) to the ligand systems. Moreover, variation of solvent from one to another and fixing of the metal and ligands produce completely different structures^{53,54} containing different potential applications. The solvent-induced breathing or swelling effect⁵⁵⁻⁵⁷ (Scheme 4) of the dynamic mixed-ligand CPs are also very important. That is, expanding and shrinking of the pores within the coordination networks is often concomitant with hydration and dehydration processes. Thus, the choice of solvent is significant to achieve the phase-pure preparation of such crystalline materials and construct diverse coordination networks.^{58,59}



Scheme 4. Schematic representation of the solvent-induced breathing and swelling effect of dynamic coordination frameworks.

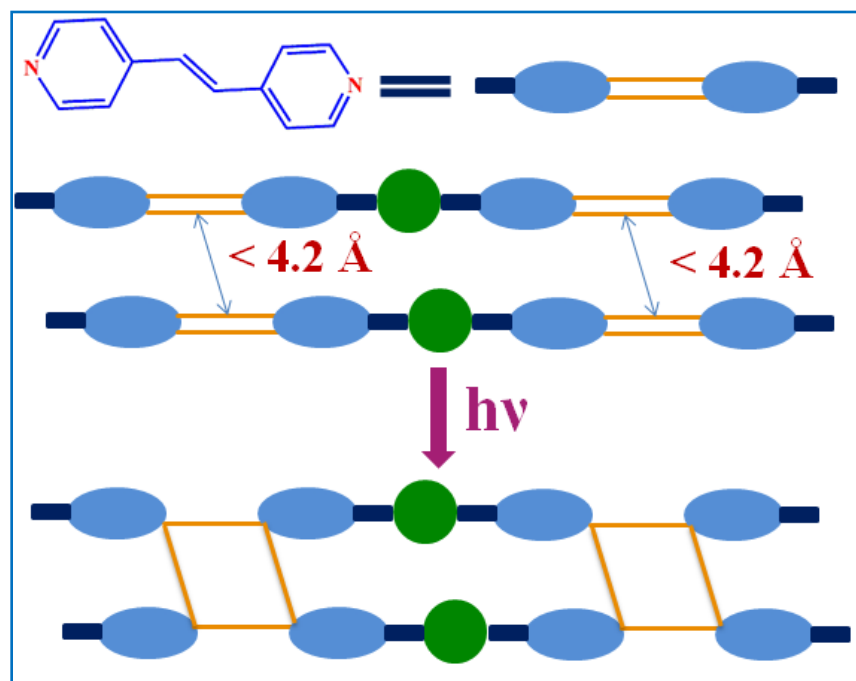
1.2.4. Effect of non-covalent interaction

Weak non-covalent interactions like H-bonding interactions (4–120 kJ/mol), π – π interactions (< 50 kJ/mol), CH... π , cation– π interactions (5–80 kJ/mol), anion... π , van der Waals interactions (5–80 kJ/mol), electrostatic interactions (e.g. ion-ion, dipole-dipole ~20 kJ/mol), hydrophobic interactions (<40 kJ/mol) etc. are very important factors in developing individual architecture. For the developing weak interaction within the structure the spatial orientation of the individual atoms or groups is very significant. The stability of the CPs or MOFs is largely influenced by various short and weak interactions existing between the building blocks. By controlling these weak forces, one can plot the final architecture of the crystal network. Although it is a difficult task to control these weak interactions, however the understanding of weak non-covalent interaction inside the architecture is very important to construct the different functional coordination polymer with diverse structure. Manimaran *et al.* reported a 2D rectangular framework $[\text{Mn}(\mu\text{-pz})(\mu\text{-Cl})_2]_n$ (pz = pyrazine) by the reaction of pyrazine and manganese chloride. Its solid-state structure showed a framework where the pz ligand face-to-face arrangement was protected via π – π interaction (3.64 Å).⁶⁰ Ghoshal *et al.* reported 1D complex $[\{\text{Mn}(\text{bpe})(\text{H}_2\text{O})_4\}(\text{C}_4\text{O}_4) \cdot 4.5\text{H}_2\text{O}]_n$ which finally form supramolecular 3D structure by π – π

interaction of two pyridine moiety of bpe ligand and extensive hydrogen-bonding.⁶¹ Ghosh *et al.* reported 2D complex $[\{Mn(bpds)_2(dca)_2(H_2O)_2\}(H_2O)_4(bpds)]_n$ in which 2D sheet structure is supported by H-bonding interactions.⁶² These 2D sheets involve in ‘sandwiched’ π -interaction involving both coordinated and solvated bpds to generate 3D supramolecular structure. Such short and weak interactions are recognised everywhere in nature especially in our human body.⁶³

1.2.5. Effect of UV radiation as external stimuli

External stimuli like UV radiation, may leads to single crystal to single crystal transformation for the CPs having photosensitive group. Transformed architecture may have better mechanical stability and applicability than the mother complex. Photoinduced [2+2] cycloaddition of olefins to form cyclobutane is a multipurpose organic reaction requiring only UV irradiation. Schmidt first studied the solid-state Photo-induced [2+2] cycloaddition reaction in cinnamic acids in 1964, establishing two essential geometric conditions.^{64,65} According to Schmidt’s criteria for a successful photoinduced cycloaddition reaction in solids, the reactive couple of C=C bond must be aligned parallel and separation should be less than 4.2 Å (Scheme 5). Photocyclization reactions generally increases the dimensionality of CPs. For example, Vittal and co-workers have reported higher dimensional polymers by linking 0D, 1D or 2D networks together^{66,67} through photo-induced structural transformation.



Scheme 5. Schematic presentation of photocyclization of ‘face-to-face’ olefin bond pairs.

1.2.6. Role of pH of the medium

In some cases, the pH of the medium of a coordination framework system can control the crystalline product. pH of the medium affects the crystals in different ways such as modifying the existing forms, binding fashions of carboxyl ligands, creating hydroxo bridges, and by activating the assembling reactions, etc.⁶⁸ For example, the pH of the reaction medium is decisive to yield diverse products for the mixed-ligand CP system.⁶⁹ In comparison, such pH effects inflict momentous influences on coordination systems of multicarboxylic acids as ligands.⁷⁰

1.2.7. Role of temperature

Temperature is another important external factor for any chemical reaction. Keeping other factors intact different CPs may be formed by varying temperature.^{71,72} Temperature sensitive CPs can exhibit several phases with different functionality.⁷³ Therefore in designing variety of functional CPs role of temperature should be in greater consideration for the researcher of this field.

1.2.8. Effect of counter anion

Diverse counter anions can affect the synthesis of the desired coordination polymers.^{74,75} Post synthetic modification of CPs sometimes monitored by incorporating various counter anions. These counter anions replace the weakly coordinated anions or lattice anions to form different crystals. The counter anions which usually occupy the framework void are sometimes weakly coordinated or uncoordinated to the metal centers. In most of the CPs, if lattice and coordinated anions are present, they determine the polarity of the void area of the CPs, thereby suggesting a post synthetic modification of the CPs by anion exchange can improve the various properties they possess. Moreover, these materials provide a unique opportunity for making anion receptors based on an anion-exchange approach.

1.3. Different synthetic techniques for synthesis of functional CPs

Various techniques are available for synthesis of coordination polymers. Among the several effective techniques for the preparation of coordination polymers some of them have been discussed follow.

1.3.1. Stirring

Traditional technique of preparing coordination polymers is stirring. In this process the concentrated solution of the reactants is stirred in reaction vessel for few hours to get a

homogeneous solution and then the resultant solution is kept to evaporate in a non-humid environment. After slow evaporation of solvent the desired crystal is formed. Solid crystals are collected by filtration and characterized by single crystal XRD.

1.3.2. Solvothermal

One of the popular techniques for synthesis of coordination polymers is solvothermal technique. This technique generally utilizes in the case of solvent insoluble ligands. In this technique the synthesis of CPs is carried out in a necessary solvent using high pressure and temperature. While the solvothermal reactions occur in teflon sealed reactor under autogenous pressure, the temperature of the reaction must be higher than the boiling point of the solvent. Considering all the external parameters like solvent, concentration of the reactants, stoichiometry, temperature, pH of the medium etc. the samples are taken in the thick walled teflon vessel. Then the reaction vessel is kept into an unperturbed autoclave and closed tightly and the temperature is applied considering the reactants and solvent inside the autoclave under autogenous pressure. After completion of reaction the autoclave is cooled gradually with fixing cooling rate. Crystals are usually formed *in-situ* (in teflon vessel) on cooling of the reaction mixture.

1.3.3. Slow diffusion

In this technique the reactants are added slowly to increase the chance of forming the required crystal. Here the metal ion and ligand solution are kept separated in a layer tube by a buffer solvent. Buffer solvent is prepared by mixing the two solvents used for metal ion solution and ligands solution at a particular ratio. Two different types of solutions, *i.e.* metal ion solution and ligand solution are mixed by slow diffusion technique and at the joint of the two solution crystals appear after a certain time.

There are also many more well-known available methods like reflux, ultrasonic, electrochemical synthesis, mechanochemical synthesis, microwave synthesis etc. to the synthetic chemist for easy and controlled synthesis of CPs.

1.4. Structural characterizations of CPs

Structural characterization of synthesized CPs is the most crucial steps of this field of research. Among all the methods and techniques, X ray crystallography is the main techniques for the specific structural determination of the CPs in both forms of the crystallography (single crystal and powder). First single crystal XRD data of the synthesized CPs are integrated and then solved by softwares, to obtain all the crystallographic parameters such as space group, crystal

symmetry, unit cell parameters, asymmetric unit, atoms orientation etc. These informations of asymmetric unit, crystal packing, different weak forces are determined that helps to understand the complete scenario of the structure. Powder X-ray diffraction (PXRD) is used for checking the bulk phase purity of the synthesized CPs by comparing peak position of the PXRD pattern of a complex with its simulated pattern obtained from SXRD study. In addition some other calculation can be performed to determine of the crystallographic parameters from the PXRD patterns with descendant software package like TREOR,⁷⁶ FullProf⁷⁷ etc.

Some other fundamental spectroscopic techniques are also used in support of the primary characterization of the synthesized ligands and CPs. These are Fourier transform infrared (FT-IR) spectroscopy, diffused reflectance UV-vis spectroscopy, solid state nuclear magnetic resonance (NMR) spectroscopy etc. By FT-IR spectroscopy the presence of different functional groups in any ligands or CPs is studied. Solid state UV-vis spectra is useful for the general characterization of the electronic transition from $\pi-\pi^*/n-\pi^*$ or $d-d$ transition through intra-ligand (ILCT) or metal to ligand (MLCT) charge transfer in the UV or in visible region for the CPs. NMR spectroscopy is based on the interactions between the nuclei and magnetic field. It marks the transition between nuclear spin states. There are several other techniques which have also been use to characterize the structure of the synthesized CPs. Among them thermogravimetric analysis (TGA) is very much useful to precisely understand the thermal stability at different temperature of the solid sample. Mechanical strength of synthesized CPs is important for potential functionality in real situation. The mechanical properties of materials are quantitatively ascertained by nanoindentation study.

2. Various potential applications of CPs/MOFs

Various structural features of CPs are not only important for the solid-state chemistry for the development of new compounds but also very important for the potential applications in gas storage^{7,8} and separation,^{9,10} electrical/proton conductivity,^{11,12} photo luminescence,^{13,14} anion exchange,^{15,16} catalysis,^{17,18} magnetism,^{19,20} sensing^{21,22} mechanical properties^{23,24} etc. On the other hand practical usability of CPs at real working condition of very high pressure or temperature is very much dependent on the mechanical stability of the CPs. In various cases structural flexibility as well as mechanical properties plays a vital role for CPs to show specific application. Particularly, structural design and delicate modification of the mixed-ligand building

components is most important to explore the potential structure–property correlation of CPs based on the mixed-ligand synthetic strategy.

Among the various potential applications CPs, some of them are selected and discussed with one or two important examples, that is relevant to the work discussed in this thesis.

2.1. Gas and solvent sorption

Gas and solvent sorption are the most popular applications of coordination polymers because of its versatile application in the field of industry as well as mankind.⁷⁸ Many CPs have also been employed for the removal of toxic gases.^{79,80} For gas and solvent sorption void containing framework or porous coordination polymers (PCPs) are very useful because individual adsorbate requires the scrupulous surroundings to get absorbed depending upon their intrinsic property (kinetic diameter, polarity, shape etc.). Moreover possibility of modification of pores with determined size and polarity makes these materials precious for specific gas like CO₂ adsorption. The subtle control and tuning of small cavities or window sizes for the CPs is vital to accomplish highly efficient storage and separation of guest molecules by the size-exclusion effect. In this regard, a simple strategy to construct the desired channels or pores of coordination networks by modifying the types of mixed-ligand components is of meticulous interest and significance. Other important phenomena in this context are the dynamicity of the framework and interpenetration in the structure.

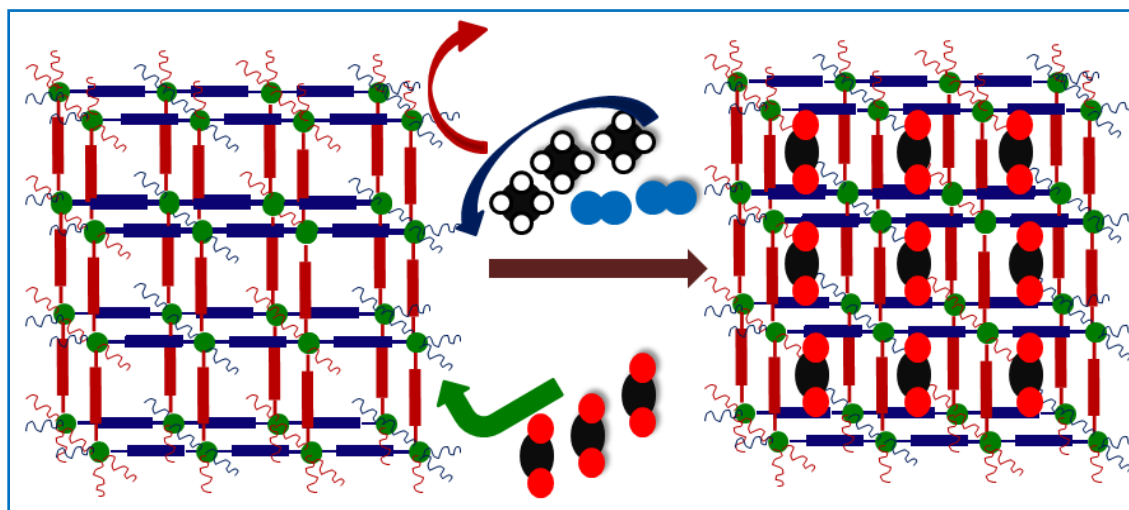
2.1.1. Nitrogen adsorption

Suitable assemble of metal ion with mixed ligands result complex structures of CPs with high surface areas and porosities. These resulting frameworks usually act as hosts for absorbing the small guest molecules. To obtain significant N₂ gas (kinetic diameter 3.6 Å) absorption value surface area of synthesized CPs is one of the most important factor. Generally, high surface area can be achieved by using extension of organic linker which results microporous coordination polymers (MCPs). Several factors can affect the framework in getting high surface areas such as framework collapse, incomplete guest removal, metal cluster geometry, presence of non-optimal linker or framework interpenetration etc.⁸¹ Such problems can be solved or minimized by the theoretical calculations which can predict either the synthesized material is capable of achieving its optimal surface area or not. Theoretical surface areas of a crystal structure can be measured most precisely by Grand Canonical Monte Carlo (GCMC) simulation.⁸² The nitrogen gas adsorption study is associated with the experimental study of isotherms of CPs. Among the

different calculations Brunauer-Emmett-Teller (BET) is found most reliable for calculating surface area.⁸³

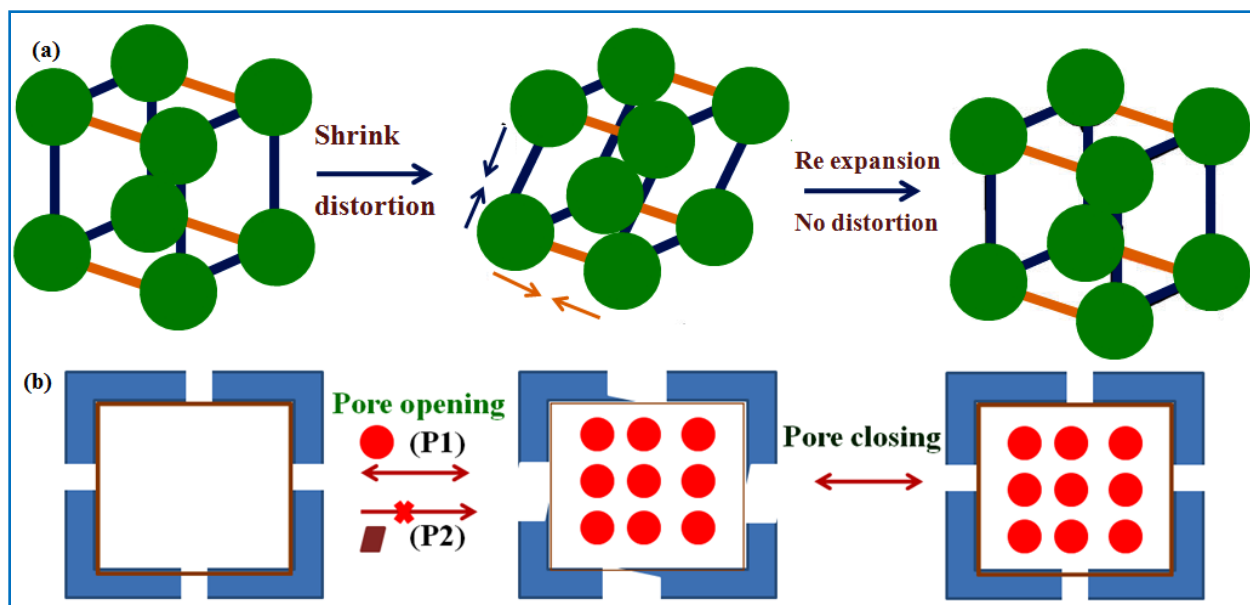
2.1.2. Selective carbon dioxide adsorption

Beyond 85% of the global energy requirement is being supported by fossil fuels burning. For this fossil fuels burning and also some other various phenomena related to global warming amounts of CO₂ into the atmosphere become high. Effective techniques to diminish CO₂ emission are thus immediately needed to keep up the global climate and to defend our environment. Again the captured CO₂ can be utilized for many other applications such as refrigerants, chemicals, cosmetics, precursor in the petroleum industry, and fertilizer etc. Among the various factors well decorated and optimized pore of the CPs is the main required parameter for selective adsorption of carbon dioxide. CP's pores have to be compatible with the kinetic diameter of the CO₂ molecules (3.3 Å). Another significant criterion is that the CPs with polar (–OH, –N = N–, –NH₂ and –N = C (R) –) pores have a higher CO₂ adsorption capacity due to the quadrupole moments of CO₂ molecules. Therefore, by designing the framework based on these criteria, it is possible to significantly improve the CO₂ adsorption capacity and selectivity (Scheme 6). Majority of the CPs have been used as a selective CO₂ adsorption are in the rigid categories, but currently the flexible CPs have taken more attention due to their outstanding abilities. Li *et al.* reported⁸⁴ the selective CO₂ sorption in the rigid CPs are dependent on three main factors: (i) size / shape exclusion, (ii) adsorbate–surface interactions, and (iii) simultaneous cooperation of both these factors.



Scheme 6. Schematic illustration of selective gas adsorption.

Many of the CPs have been used to adsorb different gases based on the molecular sieving effect. Therefore the molecules whose kinetic diameters are well-matched with the diameters of the pores are able to pass through the pores. Dybtsev *et al.* stated selectivity of CO₂ over CH₄, N₂, and Ar is achieved due to the presence of small windows in the channels.⁸⁵ For selective gas adsorption the nature of the guest molecules and their interaction with the surface of the adsorbent is also very important. Bae *et al.* synthesized a pillared-layer MOF Zn₂(ndc)₂(dpni) which show selective adsorption of CO₂ over CH₄ because of the kinetic effect and the quadrupole moment of CO₂.⁸⁶ The flexible (soft) MOFs have shown dynamic behaviours during the adsorption/desorption process. In case of sorption by flexible MOF during the gas adsorption/ desorption two factors should be considered. These are breathing phenomenon (Scheme 7a) and the gate-opening/closing (Scheme 7b). The distinction and importance of these two unique phenomena have been emphasized by Kitagawa (Seo *et al.*, 2009)⁸⁷ and Férey (Férey and Serre, 2009)⁸⁸. The size/shape exclusion can result in gas adsorption in some flexible MOFs. Chen *et al.* has been synthesized Zn(ADC)(4,4'-Bpe)_{0.5} containing paddlewheel dinuclear Zn₂ units with a 3D interpenetrated structure adsorbs CO₂ over CH₄ due to the molecular sieving effect (size and shape exclusion) arises from the compatibility of the pores size of the MOF.⁸⁹ The surface nature of the pores also acts a crucial role in selective adsorption of flexible MOFs. Bhattacharya *et al.* showed the enhanced CO₂ uptake by pore surface modification effected upon changing the pillar backbone from a -CH=N- to -CMe=N- group.⁹⁰ Maity *et al.* has nicely explained the effect of functional group and flexibility of the framework keeps a profound impact on the carbon dioxide adsorption of the synthesized structure.⁹¹ Park *et al.* reported controlled carbon dioxide uptake in which geometrical isomerism of the 2-(phenyldiazenyl)terephthalate ligand of synthesized zinc MOF take place under photoirradiation and thermal conditions respectively.⁹² Selective adsorption of CO₂ on flexible MOFs by gate-opening or closing or structural rearrangement can be happened by adsorbate-surface interactions. This process occurs in the small pores or even no pores containing MOFs to pass the guest molecules through the adsorbent. In this mechanism, when the framework is exposed to the guest molecules the pores start to expand, and such expansion is directly depends on the adsorbate-surface interactions with the framework (Scheme 7). Hayashi *et al.* in 2007 reported the best occasion of the flexible MOF in ZIF-20 where the gate opening occurs in the selective adsorption of CO₂ over CH₄.⁹³



Scheme 7. (a) The breathing phenomenon when an abrupt expansion/compression is applied to the unit cell of the MOF, (b) Schematic presentation of selective gas adsorption in the flexible framework based on gate opening/closing phenomena and guest specific pressures.

2.1.2.1. Selective carbon dioxide adsorption at high pressure

Moreover, most of the recent industrial process for CO_2/CH_4 separation via adsorption required substantially high operational pressure ranging up to 40–60 bar. Herm *et al.* experimentally reported the adsorption capacity of Mg-MOF-74 upto industrial operating process⁹⁴ and established Mg-MOF-74 can achieved faster breakthrough time and gave more than 50% higher sorption capacity of CO_2 and selectivity of CO_2/CH_4 in comparison to commercial zeolite 13X. Furukawa *et al.* reported⁹⁵ MOF-210 by using BTE and BPDC exhibited one of the best amount of CO_2 uptakes (~71 wt%) at 298 K and 50 bar. This high CO_2 uptake is related to the ultrahigh surface area of these MOFs. At high pressure, the CO_2 sorption ability depends on the pore volume and surface area of the framework. These could be attained by utilizing the large organic ligand like BTB and the BTC or extending the MOF structure in the synthesis part.^{95,96}

2.1.3. Hydrogen storage

Development of secure and effectual hydrogen storage systems is crucial for further execution of hydrogen in fuel cell technologies. Among the various approaches porous materials-based CPs or MOFs as hydrogen storage is regarded as a permanent solution due to the outstanding reversibility, excellent kinetics and the opportunity to stock up hydrogen at low pressures. Suitable modification of pores of the synthesized framework is one of the key factors for this

particular application. Previously most of the strategies intended to improve the performance of MOFs can be classified into two major categories: (i) presynthetic methods which includes catenation,⁹⁷ and ligand functionalization⁹⁸ etc. and (ii) postsynthetic noncovalent approaches.^{99,100} Wang *et al.* showed that by modifying the pore structure of MOFs, both hydrogen uptake and heat of adsorption can be significantly increased.¹⁰¹ Maity *et al.* reported flexibility induced inclined polycatenated 3D framework due to temperature variation which was responsible for excellent hydrogen uptake of this type of frameworks.¹⁰² Li *et al.* reported¹⁰³ two-fold interpenetrated MOF (UPC-501) based on a $\text{Zn}_4\text{O}(\text{COO})_6$ secondary building unit with the H_2 uptake of 14.8 mmol g^{-1} . Suksaengrat *et al.* reported different metal decorated M-MOF to study the effect of different metals such as titanium, vanadium, hafnium and zirconium on their capacity to store hydrogen.¹⁰⁴

2.1.4. Methane storage

Despite the fact that hydrogen has been considered as an ultimate renewable energy carrier for the future but there is lack of scope for storage and transportation of this gas. Natural gas, mainly composed of methane (CH_4), has been regarded as an alternative for conventional petroleum fuel for a long time because of its affluent reserves and low carbon emissions. Moreover in recent years, it has been established that methane has the greater ability to destroy the ozone layer than that of carbon dioxide (CO_2). Therefore the most common and acceptable solution is use of methane as clean fossil fuel because it gives a less carbon dioxide emission than other fuels. However, the raw gas of methane contains several additional substances such as moisture, acid gases, inert gases and heavier hydrocarbons, removing them are necessary to meet the specific requirements. Among these impurities N_2 is most problematic to get pure CH_4 because of similar properties of both like non-polar molecules without the dipole moments, similar kinetic diameter, polarizability and quadrupole moment. CPs or MOFs have shown the high adsorption capacity and selectivity for the separation of methane from N_2 containing mixtures, such as MIL-53(Al), $[\text{Cu}(\text{Me-4py-trz-ia})]$, MIL-101, MOF-5. Zhou *et al.* found that coordinately unsaturated large densities of metal sites could greatly improve the binding potency of methane [$\sim 200 \text{ cm}^3(\text{STP})/\text{cm}^3$ methane at 298 K and 35 bar] which was confirmed by neutron diffraction experiments in the $\text{Ni}_2(\text{DHTP})$ MOF (DHTP=2,5-dihydroxyterephthalate).¹⁰⁵ X. Y. Ren and T. J. Sun revealed that the $[\text{Ni}_3(\text{HCOO})_6]$ framework constructed by the smallest and shortest monodentate ligand HCOO^- , exhibited preferential adsorption of CH_4 over N_2 with methane

capacity of 0.75 mmol/g and CH₄/N₂ selectivity up to 6.5.¹⁰⁶ Niu *et al.* found the low polarity aliphatic hydrocarbon cavities and the unsaturated metal sites in Cu₂(ATC) (ATC=1,3,5,7-adamantane tetracarboxylic acid) could generate the preferential absorption site for methane.¹⁰⁷

2.1.5. Solvent adsorption

Diverse solvent sorption and separation by porous frameworks is also very fascinating. It exclusively depends on the criterion of the pore of synthesized structures. Kim *et al.* reported Zr-based MOF (MOF-801) that can attain water harvesting at a low RH environment¹⁰⁸ and allow water release of large amount with small temperature increase. Nguyen *et al.* reported highly porous two new series of metal–organic frameworks namely M-VNU-74-I and –II containing different metal (where M = Mg, Ni, Co) which exhibited remarkably high methanol uptake.¹⁰⁹ Wu *et al.* studied adsorptive separation of methanol-acetone on isostructural series of metal-organic frameworks M-BTC (where M = Ti, Fe, Cu, Co, Ru, Mo).¹¹⁰

2.2. Proton conductivity

In searching of alternative energy source, fuel cells (FCs) that can convert chemical energy into electrical energy through carbon-free emission processes, is very much relevant due to their high efficiency and environment friendly approach. For the production of the fuel cell suitable proton transfer membrane is the most important factor. Mainly porous CPs/ MOFs, is highly impressive to be treated as better proton conductive media. Four different approaches are considered to design proton conductive MOFs or CPs.¹¹¹⁻¹¹³

(i) For the first type, H₃O⁺, NH₄⁺, H₂PO₄[−], and Me₂NH₂⁺ are within the framework as proton sources. These groups are included into the pore of CPs during the preparation of the material and may act as a counter ion.

(ii) For the second type, some uncoordinated free group like -SO₃H, -PO₃H, -COOH are pre-installed on the organic linkers that can boost the proton conductivity by enhancing the pore acidity.

(iii) For the third type, active proton sources such as imidazole, triazole, tetrazole, ionic liquids, non volatile acids, organic carboxylic or hydroxyl groups are incorporated into the host framework by post-synthetic modification.

(iv) The fourth type includes metal center modifications, phase transformation, structural defects, and coordinative insertion of protonic molecules like H₂O, EtOH, and imidazole etc. into the metal center.

Lim *et al.* reported in their review work about the design strategies for proton-conductive MOFs, and degenerate water (hydronium or hydroxide)- or ammonia (ammonium)-mediated proton conduction system.¹¹¹ Bao *et al.* reported in another review about the various metal phosphonate frameworks work act as proton conductive materials.¹¹³

2.3. Electrical conductivity

MOFs or CPs are generally considered as insulators by means of conductivity less than 10^{-10} S cm^{-1} because of the unavailability of low-energy charge transfer pathways and free charge carriers. Several MOFs or CPs has been reported so far having outstanding electrical conductivity and high charge mobility. Conductive MOFs have potential applications as electrode materials, chemiresistive sensors, electrocatalysts, electrical energy storage, electronic devices, and spin-polarized transport materials. Usually, electrons rich metal ions (Cu^{2+} , Zn^{2+} , Cd^{2+} etc.) with redox active ligands are treated as best charge density carrier for MOFs. Ahmed *et al.* reported two CPs $[\text{Cd}(\text{adc})(4\text{-phpy})_2(\text{H}_2\text{O})_2]$ and $[\text{Zn}(\text{adc})(4\text{-phpy})_2(\text{H}_2\text{O})_2]$ (H_2adc = acetylenedicarboxylic acid and 4-phpy = 4-phenylpyridine) with enhanced conductivity for first CPs related with larger size of the cation Cd^{2+} than Zn^{2+} .¹¹⁴ Sun *et al.* reported the existence of an unpaired electron in the d orbital can also have vast impact on electrical conductivity.¹¹⁵ Yaghi *et al.* reported a 2D Cu(II) MOF contains conjugated tricatecholate, 2,3,6,7,10,11-hexahydroxytriphenylene, to display electrical conductivity of $1.8\text{--}2.1 \times 10^{-1}$ S cm^{-1} and charge storage capacity of 284 C g^{-1} (80 mA h g^{-1}).¹¹⁶ Various factors are there to influence the electrical conductivity of CPs such as ligand modification, non-covalent interaction, structural flexibility and effect of [2+2] cycloaddition etc. MacGillivray *et al.* reported a Ag-based metal–organic solid, $[\text{Ag}_2(4\text{-stilbz})_4][\text{CF}_3\text{SO}_3]_2$ which undergoes cycloaddition and photocyclized product that showed 40% increase in electrical conductivity than that of the parent.¹¹⁷

2.4. Photo responsivity and mechanical properties

Study of the mechanical properties of MOFs is also an interesting field in the context of their macroscopic performance under practical working conditions of very high pressure and temperature. In the recent past, anisotropic mechanical properties have been correlated well with internal arrangement of crystal packing and different molecular properties of MOF-type hybrid materials. Since applications of MOFs in different field often required repetitive temperature and pressure variations therefore sufficient mechanical stability of the framework have also the same importance.^{118,119} The mechanical stability for porous CPs or MOFs measures the rigidity of a

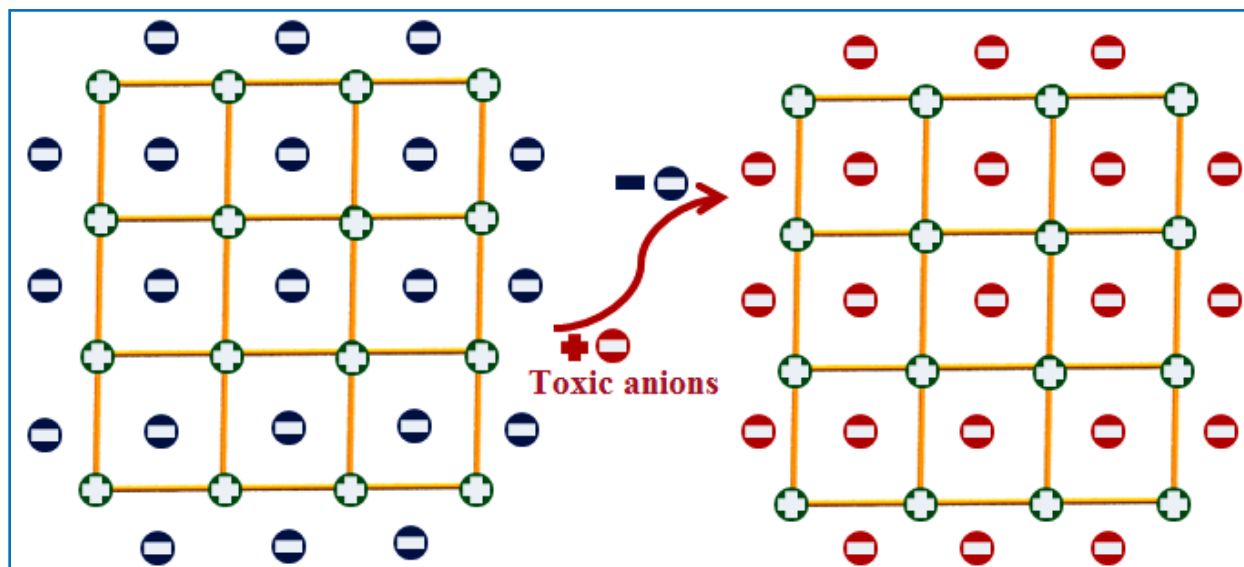
material to survive its framework under mechanical load. Obviously, external pressure deforms the pore size of the framework and results significant reduction in performance. The mechanical properties of materials fluctuate by several orders of magnitude with changing atomic composition and/or crystal structure.¹²⁰⁻¹²² Two strategies can be employed to improve the mechanical stability of a framework material: modifying the primary and/or secondary network. Recently it has been observed that the MOFs with high coordination number of metal nodes, have enhanced mechanical stability.^{123,124} Kapustin *et al.* developed a strategy to retrofit a particular MOF by addition of extra ligands to the framework.¹²⁵ Structural tuning to get better mechanical stability by photoinduced [2 +2] cycloaddition is one of the promising way and it also give a opportunity to produce photomechanical switch, sensor etc. Tuning mechanical properties by photocyclization reaction one should keep in mind the criterion of Schmidt's topochemical cycloaddition reaction (Scheme 5).^{64,65} There is a significant enhancement in the cell volume of the photoinduced products which is the major driving force for these change in mechanical properties.

Currently the measurement of mechanical properties by nanoindentation^{126,127} is a very consistent and widely used technique to quantitatively ascertain the mechanical properties of materials. Photochemical reversible structural transformation is very much useful in postsynthetic modification of framework and to exhibit smart functionality like photo-switches and photosensors. Lang and co-workers has extended [2+2] photocyclization further than structural applications for frameworks to control fluorescence switching in 3D frameworks.^{128,129} Again couple of C=C bonds of ligand covert to cyclobutane ring sometimes accompanied by achiral to chiral or chiral to achiral space group change which may useful to functionalize the CPs as chiroptical switches. Hu. *et al.* reported controlled formation of chiral networks and their reversible chiroptical switching behaviour by UV/microwave irradiation.¹³⁰

2.5. Anion exchange

Anion exchange is very much important in various chemical and biological processes. Post synthetic variation of the framework of CPs or MOFs can be done by anion exchange which can affect their functionalities. Anion exchange is very much useful in water purification and waste water management as removal of toxic and carcinogenic anions like ClO_4^- , AsO_4^{3-} and CrO_4^{2-} or control over anionic toxic pharmaceuticals (Scheme 8). To execute this function of anion exchange, positive frameworks like cationic CPs that has been utilized by so many researchers.

Cationic CPs can be used as potential anion exchange materials through the substitution of charge balancing anions in the framework along with other guest anions. In cationic CPs, the net positive charge in the frameworks requires charge-balancing extra counter anions. The counter anions which commonly occupy the framework void are sometimes weakly coordinated or uncoordinated to the metal centers. Therefore, these materials give an unique chance for making anion receptors based on an anion-exchange approach. In the production of cationic CPs, neutral nitrogen-containing ligands are the most fruitful choices which can make a bridge between transition-metal ions. In most of the cases, such N-donor ligands finally form 1D/2D frameworks where the charge balancing counter anions present either coordinated or lattice site. For the coordinated anions, the exchange of anions with the metal centers may depend on various factors like size, shape and coordinating abilities of the anions with that individual metal. But in case of lattice anion, it is comparatively easier because there is no involvement of any bond rupture or formation. Li *et al.* reported a cationic silver-triazolate MOF $\{[Ag_8(tz)_6](NO_3)_2 \cdot 6H_2O\}_n$ (tz^- = 3,5-diphenyl-1,2,4-triazolate) acts as an efficient function of Cr(VI) removal via anion exchange.¹³¹ Khanpour *et al.* synthesized four CPs among them two CPs $[Zn(\mu-bpdh)(H_2O)_4](NO_3)_2 \cdot 2bpdh$, $[Zn(\mu-bpdh)(H_2O)_4](ClO_4)_2 \cdot 2bpdh$ ($bpdh$ =2,5-bis(3-pyridyl)-3,4-diaza-2,4-hexadiene) capable of showing reversible solid-state anion exchange between ClO_4^- and NO_3^- .¹³² Coronado *et al.* reported a 3D CP $[Cu(btix)_2(BF_4)_2]_n$ [$btix$ = 1,4-bis(triazol-1-ylmethyl)benzene] which undergo anion exchange with N_3^- and form new CP of different

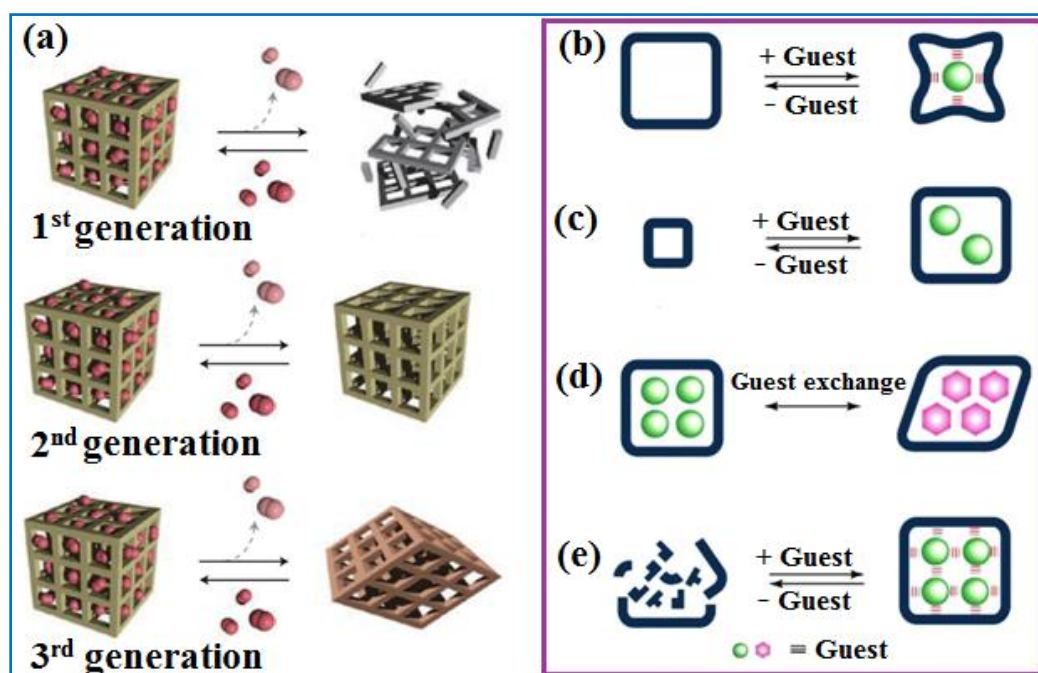


Scheme 8. Representative diagram to show the anion exchange process.

magnetic property.¹³³ Xu *et al.* synthesized five coordination polymers with flexible tripodal ligand 1,3,5-tris(imidazol-1-ylmethyl)benzene among them one CP $\{[\text{Zn}(\text{L})_2](\text{BF}_4)_2\}_n$ display exchange of nitrate and nitrite anion.¹³⁴

3. Structural transformation and dynamicity in coordination polymers

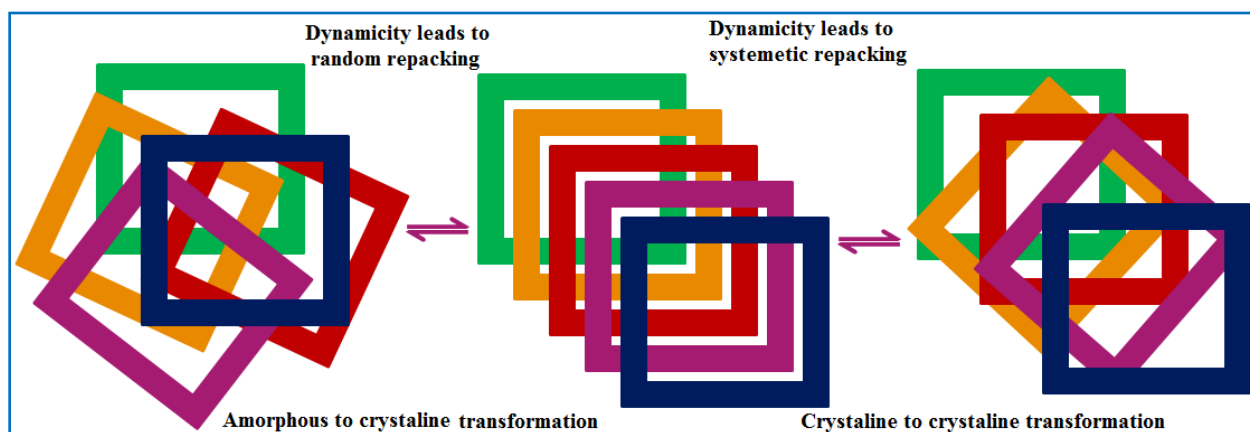
Generally coordination polymers are stable solid crystalline compound (called as rigid) upto certain temperature and pressure. Other than rigid coordination polymers there are another important category called flexible coordination polymer that undergoes structural transformation reversible or irreversible under certain condition. In 1998, Kitagawa *et al.* classified MOFs into three categories: 1st, 2nd, and 3rd generation MOFs.^{135,136} and according to them 3rd generation MOFs are flexible porous frameworks (Scheme 9a) that respond to external stimuli, and predicted their importance in the future. Kitagawa *et al.* also focused on the correlation between the guest molecules and pores of flexible MOFs in another review (Scheme 9b-e).¹³⁶ In designing different functional coordination polymer dynamicity and structural transformation plays a vital role. Fischer *et al.* in 2014 reported flexible MOFs in various criteria such as the external stimuli, composition like metal node/functionalised linker, and promising applications.¹³⁷



Scheme 9. (a) MOFs as 1st, 2nd, and 3rd generation ones (left side). Right side represent the behaviours of dynamic structures upon adsorption/desorption of guest molecules; (b) induced-fit-type pores, (c) breathing-type pores, (d) guest-exchange deformation-type pores, and (e) healing-type pores. Reproduced with permission from references (135) and (136).

3.1. Reason for structural dynamism

The Structural transformation process can happen in two principal ways, crystalline-to-crystalline transformation, and crystalline to amorphous conversion due to random repacking or systematic repacking in dynamic MOF (Scheme 10). Several physical stimuli such as temperature, pressure, light and electric potential etc. as well as some chemical stimuli like counter ions or guest molecules have been reported which are individually or mutually responsible to create structural dynamicity in MOFs. Structural dynamicity in the MOF finally occurs through the removal/exchange of coordinated/lattice ions, reorientation/modification of a functional group ligand, change in metal to ligand coordination, metal exchange, and so on. Additionally another important factor to drive the dynamism is the movement of the subnet in an interpenetrated network.¹³⁸ Some relevant factors corresponding to structural transformation are discussed here.



Scheme 10. Two types of phase transformations.

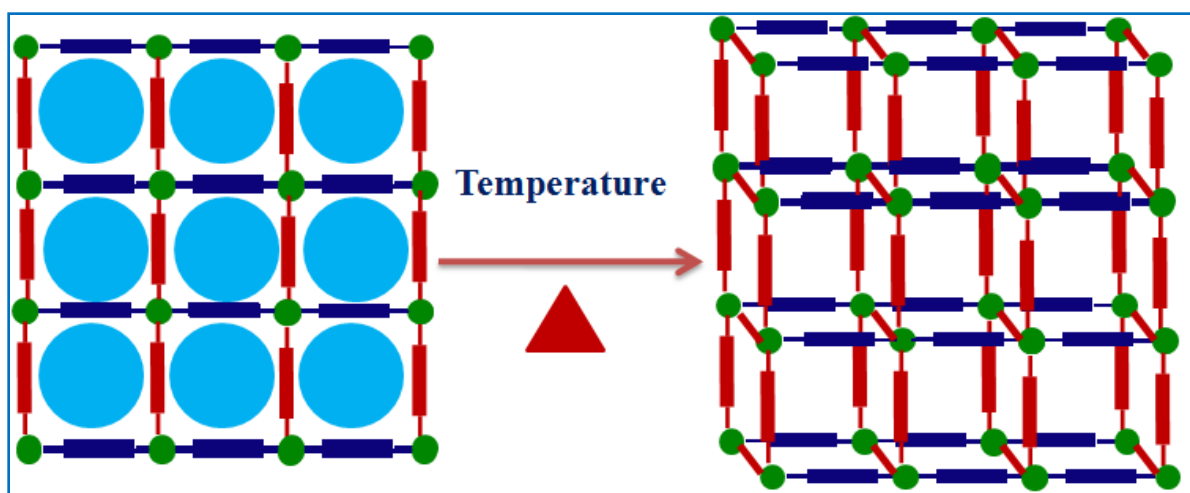
3.1.1. Structural transformation due to exchange of guest molecules or ions

The guest molecules or counter ions sitting in the porous aperture of the framework can control the structures in such a way so that the flexibility is introduced in the framework. So-called soft porous coordination polymers are renowned to exhibit such guest reliant structural dynamism. Gérard Férey published three reviews on flexible MOFs in 2009⁸⁸, 2012¹³⁹, and 2016¹⁴⁰ primarily focusing on MOFs with breathing behaviours. Dybtsev *et al.* reported 3D MOF $[\text{Zn}_2(1,4\text{-bdc})_2(\text{dabco})]_n$ (1,4-bdc = 1,4 benzenedicarboxylate and dabco = 1, 4-diazabicyclo[2.2.2]octane) exhibited guest benzene induced single crystal to single crystal transformation.¹⁴¹ Moreover the framework flexibility also depends on the nature of the guest molecules. In case of ionic CP the counter anions are solely accountable for the charge balance

of the overall framework. Hence the exchange of those anions may change the overall structure. Hou *et al.* reported a series of Cd^{2+} coordination polymer by exchanging NO_3^- anion of the solid $\text{CdL}_2(\text{NO}_3)_2 \cdot 2\text{THF}$ with different anions. In the aforesaid compound it has been observed that in case of Cl^- and Br^- exchanged product anion-induced structural transformation has been observed.¹⁴²

3.1.2. Structural transformation due to change in temperature and solvent exchange

Solvent removal or uptake can alter the structure of a CP and properties and yield a new one. Generally removal of the solvent from a structure is carried out by heating, evacuation or both. On the other hand addition of solvent can be done out by soaking in the suitable solvent. Here temperature acts as an important stimuli for expansion or contraction in MOFs. Mowat *et al.* reported change in temperature causes a reversible or irreversible phase transition.¹⁴³ The increase in temperature leads to the elimination of the solvent in the channels of the framework that cause the dynamic movement in the structure which may also causes structural transformation (Scheme 11). Kumar *et al.* synthesized a set of coordination polymers by varying solvent (polar/nonpolar) and fixing metal to ligand ratio.¹⁴⁴ Another example of such temperature effect is cyclobutane containing CP undergoes structural transformation under heating at suitable temperature.¹⁴⁵



Scheme 11. Effect of temperature change: solvent elimination and structural transformation.

3.1.3. Structural transformation for change in pressure

Pressure is another thermodynamic factor that is closely associated to the flexibility of materials. The effect of pressure on a CPs is straightforwardly interrelated with its mechanical stability, and

important factor in most of commercial applications. Soft CPs can rotate or relax more without difficulty in reply to external pressure. However the direct structural transformation connected with the pressure change is not achieved so far but the associative effect of pressure with the other essential stimuli can never be mistreated. Various changes occur in the framework because of the applied pressure such as change of coordination environment, movement between adjacent layers or rotation in an interpenetrated structure, change in unit cell volume etc. due to the compression or expansion of the framework. Graham *et al.* reported the first high-pressure study on the MOF-5 $[\text{Zn}_4\text{O}(\text{BDC})_3]$ (BDC=1,4-benzenedicarboxylate) and observed at 3.24 GPa sharper volume of unit cell drops and compression of the framework.¹⁴⁶ Moggach *et al.* in 2009 reported phase transformation ZIF-8 under high pressure of 1.47 GPa (14,700 bar).¹⁴⁷

3.1.4. Photoinduced structural transformation

Light can also be used as a stimulus for showing dynamic behaviour of MOFs that mainly occurs by change in conformation of photosensitive functional groups of the ligand upon irradiation. Azobenzene and related organic molecules can alter their conformation from trans- to cis- after exposing to UV-Vis light. Modrow *et al.* first reported such transformation on 3D $[\text{Zn}_2(2,6\text{ndc})_2(\text{azo-bipy})]$ (azo-bipy = 3-azo-phenyl-4,4'-bipyridine) where the layers of the $\text{Zn}_2(2,6\text{ndc})_2$ are pillared by the azo-bipy linkers.¹⁴⁸ Photochemical cycloaddition is another most effective method in solid-state structural transformation. Photochemical cycloaddition is a unique, green method to synthesize regioselective and stereospecific highly tensed cyclobutane derivatives. The systematic development of solid-state topochemical photodimerization, was started only after the revolutionary work of G. M. J. Schmidt.^{64,65} Photochemical [2+2] cycloaddition reactions (Scheme 5) are attractive way to create single crystal to single crystal structural transformations in the solid-state. Photoinduced cycloaddition reaction is also useful in many cases to prepare the higher dimensional framework. Vittal *et al.*⁶⁷ and Xie *et al.*¹⁴⁹ reported solid-state structural transformations from 2D interdigitated layers to 3D interpenetrated structures.

4. Interpenetration in CPs

Interpenetration in coordination polymers has been developed through two or more entangled periodic networks. Interpenetrated structure is characterized by the fact that the voids are occupied by one or more independent frameworks. It is almost inescapable to mention polycatenation when describing interpenetration because of their close relation. Among the

various difference between the two one important difference for polycatenation is all the constituent network have the lower dimensionality than that of final architectures.¹⁵⁰ Sometime interpenetration and polycatenation parallelly present in a framework.¹⁵¹ Interpenetrations are usually assisted by intermolecular non-covalent interactions like hydrogen bonding, π - π interactions, van der Waals interactions, ionic and dipolar forces. Increase in the degree of interpenetration is expected to decrease the pore size and void space. On the other hand it leads to improved structural stability, flexibility, selectivity and higher crystal density, all of these, assist the framework in preventing the possible collapse in the removal of the lattice solvent or guest molecules. Interpenetrated MOFs (IMOFs) can be classified into two types, homo-IMOFs and hetero-IMOFs. In homo-IMOFs identical networks are interpenetrated, and in hetero-IMOFs two or more different networks are interpenetrated. Within an interpenetrated network, flexibility can be attained sometime through the subnet movement (Scheme 12).

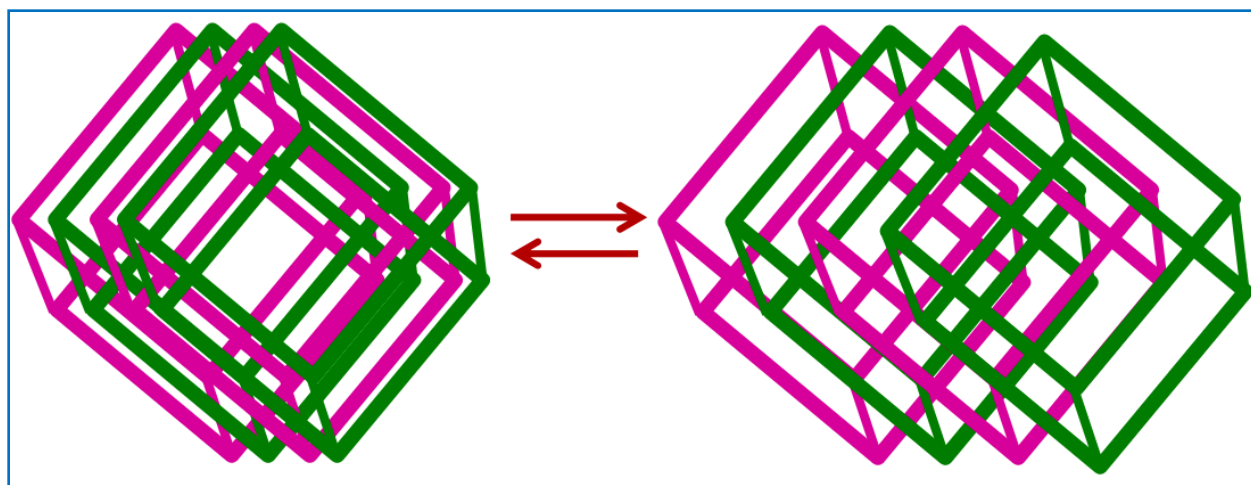


Figure 12. Dynamicity of interpenetrated MOFs through subnet movement.

In the synthesis of this type of framework the utilization of slim (long and thin) ligands has a better tendency to form interpenetrated MOFs compared to bulky ligands.¹⁵² As ligands become longer, the pore spaces and pore openings increase, and scope is made available for additional lattices. For example, in similar synthetic conditions, the short 1,4-benzenedicarboxylate ligand produces non-interpenetrated materials while the longer 4,4'-biphenyldicarboxylate ligand produces interpenetrated frameworks.¹⁵³ Presence of bulky groups on ligands tend to decrease the occurrence of interpenetration, simply through steric hindrance to the pores of the MOF. In one example, a bulky substituent¹⁵⁴ resulted in a non-interpenetrated framework, whereas the

bare backbone results in a two-fold interpenetrated framework. Solvent have an important role in determining interpenetration levels in some cases. Solvents with larger molecular sizes have a tendency to produce non-interpenetrated structures through the exclusion of additional ligand from the pores of a lattice. Temperature has also been used to successfully control the interpenetration. At low temperatures less interpenetrated products are more common. For example¹⁵⁵ IRMOF-8, which was originally an interpenetrated form via solvothermal synthesis, could be synthesized in non-interpenetrated form by performing the synthesis at room temperature after longer time period. Electrostatic interaction between ligands and solvent has also been acted¹⁵⁶ to prohibit interpenetration in a MOF family. In general these interpenetrated MOFs behave as less efficient in gas sorption case as they reduce the surface area and porosity, but many interpenetrated MOFs exhibit exceptional gas separation and selectivity because of their dynamicity (Scheme 12) which affects their pore sizes.⁸⁹ On the other hand, like paddle wheel containing framework, the interpenetrated framework also shows better hydrogen gas adsorption. Another important functionality of interpenetrated CPs is increase in thermal conductivity¹⁵⁷ by introducing vibrations of the framework.

5. References

- (1) R. M. -Ballesté, J. G. -Herrero and F. Zamora, *Chem. Soc. Rev.*, 2010, **39**, 4220–4233.
- (2) M. Tran, K. Kline, Y. Qin, Y. Shen, M. D. Greena and S. Tongaya, *Appl. Phys. Rev.*, 2019, **6**, 041311–041318.
- (3) H. Ōkawa, Y. Yoshida, K. Otsubo and H. Kitagawa, *Inorg. Chem.*, 2020, **59**, 623–628.
- (4) E. A. Tomic, *J. Appl. Polym. Sci.*, 1965, **9**, 3745–3752.
- (5) H. J. Buser, D. Schwarzenbach, W. Petter and A. Ludi, *Inorg. Chem.*, 1977, **16**, 2704–2710.
- (6) S. R. Batten, N. R. Champness, X. -M. Chen, J. G. -Martinez, S. Kitagawa, L. Öhrström, M. O’Keeffe, M. P. Suh and J. Reedijk, *CrystEngComm*, 2012, **14**, 3001–3004.
- (7) H. Li, L. Li, R. -B. Lin, W. Zhou, Z. Zhang, S. Xiang and B. Chen, *EnergyChem*, 2019, **1**, 100006.
- (8) K. J. Hartlieb, J. M. Holcroft, P. Z. Moghadam, N. A. Vermeulen, M. M. Algaradah, M. S. Nassar, Y. Y. Botros, R. Q. Snurr and J. F. Stoddart, *J. Am. Chem. Soc.*, 2016, **138**, 2292–2301.
- (9) R. -B. Lin, S. Xiang, H. Xing, W. Zhou and B. Chen, *Coord. Chem. Rev.*, 2019, **378**, 87–103.

- (10) V. Unnikrishnan, O. Zabihi, M. Ahmadi, Q. Li, P. Blanchard, A. Kiziltasb and M. Naebe, *J. Mater. Chem.A*, 2021, **9**, 4348–4378.
- (11) C. Li, L. Zhang, J. Chen , X. Li, J. Sun, J. Zhu, X. Wang and Y. Fu, *Nanoscale*, 2021, **13**, 485–509.
- (12) X. Chen and G. Li, *Inorg. Chem. Front.*, 2020, **7**, 3765–3784
- (13) T. -W. Wang, D. -S. Liu, C. -C. Huang, Y. Sui, X. -H. Huang, J. -Z. Chen and X. -Z. You, *Cryst. Growth Des.*, 2010, **10**, 3429–3435.
- (14) J. Dong, D. Zhao, Y. Lu and W. -Y. Sun, *J. Mater. Chem. A*, 2019, **7**, 22744–22767
- (15) Y. Wang, H. Cao, B. Zheng, R. Zhou and J. Duan, *Cryst. Growth Des.*, 2018, **18**, 7674–7682.
- (16) R. Custelcean and B. A. Moyer, *Eur. J. Inorg. Chem.*, 2007, 1321–1340.
- (17) V. R. Remya and M. Kurian, *Int. Nano Lett.*, 2019, **9**, 17–29.
- (18) Y. Tian, G. Liang, T. Fan, J. Shang, S. Shang, Y. Ma, R. Matsuda, M. Liu, M. Wang, L. Li and S. Kitagawa, *Chem. Mater.*, 2019, **31**, 8494–8503.
- (19) H. Zhao, F. Wang, L. Cui, X. Xu, X. Han and Y. Du, *Nano-Micro Letters*, 2021, **13**.
- (20) K. Liu, X. Zhang , X. Meng , W. Shi , P. Cheng and A. K. Powell, *Chem. Soc. Rev.*, 2016, **45**, 2423–2439.
- (21) Ü. Anik, S. Timur and Z. Dursun, *Microchimica Acta*, 2019, **186**.
- (22) L. Wang, *Sensors and Actuators A: Physical*, 2020, **307**, 111984.
- (23) J. C. Tan, C. A. Merrill, J. B. Orton and A. K. Cheetham, *Acta Materialia*, 2009, **57**, 3481–3496.
- (24) S. Khan, Akhtaruzzaman, R. Medishetty, A. Ekka, and M. H. Mir, *Chem Asian J.*, 2021, **16**, 2806–2816.
- (25) S. Sanda, S. Biswas, and S. Konar, *Inorg. Chem.*, 2015, **54**, 1218–1222
- (26) A. B. Gaspar, G. Levchenko, S. Terekhov, G. Bukin, J. V. -Muñoz, F. J. Muñoz-Lara, M. Seredyuk and J. A. Real, *Eur. J. Inorg. Chem.*, 2014, 429–433.
- (27) A. K. Ghoshal, A. Hazra, A. Mondal and P. Banerjee, *Inorganica Chim. Acta*, 2019, **488**, 86–119.
- (28) I. E. Claassens, V. I. Nikolayenko, D. A. Haynes and L. J. Barbour, *Angew. Chem.*, 2018, **130**, 15789–15792
- (29) S. K. Seth, *Crystals*, 2018, **8**, 455.

-
- (30) L. Huang, H. Cheng, L. Wang, X. Wu and B. Qin, *Cryst. Growth Des.*, 2021, **21**, 1905–1911.
- (31) J. –W. Cui, S. –X. Hou, Y. –H. Li and G. –H. Cui, *Dalton Trans.*, 2017, **46**, 16911–16924.
- (32) B. F. Hoskins and R. Robson, *J. Am. Chem. Soc.*, 1990, **112**, 1546–1554.
- (33) M. Fujita, J. Yazaki and K. Ogura, *J. Am. Chem. Soc.*, 1990, **112**, 5645–5647.
- (34) S. Kitagawa, M. Munakata and T. Tanimura, *Inorg. Chem.* 1992, **31**, 1717–1719.
- (35) O. M. Yaghi, Z. Sun, D. A. Richardson and T. L. Groy, *J. Am. Chem. Soc.*, 1994, **116**, 807–808.
- (36) S. S. Kaye, A. Dailly, O. M. Yaghi and J. R. Long, *J. Am. Chem. Soc.*, 2007, **129**, 14176–14177.
- (37) H. Li, M. Eddaoudi, M. O’Keeffe and O. Yaghi, *Nature*, 1999, **402**, 276–279.
- (38) D. J. Tranchemontagne, J. R. Hunt and O. M. Yaghi, *Tetrahedron*, 2008, **64**, 8553–8557.
- (39) D. M. Ciurtin, Y.-B. Dong, M. D. Smith, T. Barclay and H. -C. zur Loye, *Inorg. Chem.*, 2001, **40**, 2825–2834.
- (40) L. Song, S.-W. Du, J.-D. Lin, H. Zhou and T. Li, *Cryst. Growth Des.*, 2007, **7**, 2268–2271.
- (41) K. Koh, A. G. Wong-Foy and A. J. Matzger, *Angew.Chem.Int.Ed.*, 2008, **47**, 677–680.
- (42) L. Hou, J. P. Zhang and X. M. Chen, *Cryst. Growth Des.*, 2009, **9**, 2415–2419.
- (43) Y. Qi, Y. X. Che, S. R. Batten and J. M. Zheng, *CrystEngComm*, 2008, **10**, 1027–1030.
- (44) X. D. Chen, H. F. Wu, X. H. Zhao, X. J. Zhao and M. Du, *Cryst. Growth Des.*, 2007, **7**, 124–131.
- (45) X. J. Jiang, S. Z. Zhang, J. H. Guo, X. G. Wang, J. S. Li and M. Du, *CrystEngComm*, 2009, **11**, 855–864.
- (46) C. P. Li and M. Du, *Inorg. Chem. Commun.*, 2011, **14**, 502–513.
- (47) K. M. Blake, C. M. Gandolfo, J. W. Uebler and R. L. LaDuca, *Cryst. Growth Des.*, 2012, **12**, 5125–5137.
- (48) C. –S. Lim, J. K. Schnobrich, A. G. Wong-Foy and A. J. Matzger, *Inorg. Chem.*, 2010, **49**, 5271–5275.
- (49) Z. Zhang, J. –F. Ma, Y. –Y. Liu, W. –Q. Kan and J. Yang, *Cryst. Growth Des.*, 2013, **13**, 4338–4348.
- (50) I. F. H. –Ahuactzi, J. C. –Huerta, H. Tlahuext, V. Barba, J. G. –Alvarez and H. Höpfl, *Cryst. Growth Des.*, 2015, **15**, 829–847.
-

- (51) S. G. Thangavelu, R. J. Butcher and C. L. Cahill, *Cryst. Growth Des.*, 2015, **15**, 3481–3492.
- (52) Z. -X. Wang, L. -F. Wu, H. -P. Xiao, X. -H. Luo and M. -X. Li, *Cryst. Growth Des.*, 2016, **16**, 5184–5193.
- (53) A. Karmakar, G. M. D. M. Rúbio, M. F. C. G. da Silva, S. Hazra and A. J. L. Pombeiro, *Cryst. Growth Des.*, 2015, **15**, 4185–4197.
- (54) B. Bhattacharya, A. Halder, D. K. Maity and D. Ghoshal, *CrystEngComm*, 2016, **18**, 4074–4083.
- (55) M. Dua, C. -P. Li, C. -S. Liub and S. -M. Fang, *Coord. Chem. Rev.*, 2013, **257**, 1282–1305
- (56) T. Kundu, M. Wahiduzzaman, B. B. Shah, G. Maurin and D. Zhao, *Angew.Chem.Int.Ed.*, 2019, **58**, 8073–8077.
- (57) J. -J. Hou, X. -Q. Li, P. Gao, H. -Q. Sun and X. -M. Zhang, *Cryst. Growth Des.*, 2017, **17**, 3724–3730.
- (58) Y. Y. Yang, W. Guo and M. Du, *Inorg. Chem. Commun.*, 2010, **13**, 1195–1198.
- (59) S. C. Chen, Z. H. Zhang, K. L. Huang, Q. Chen, M. Y. He, A. J. Cui, C. Li, Q. Liu and M. Du, *Cryst. Growth Des.*, 2008, **8**, 3437–3445.
- (60) M. Karthikeyan, B. Bhagyaraju, C. R. Mariappan, S. M. Mobin and B. Manimaran, *Inorg. Chem. Commun.*, 2012, **20**, 269–272.
- (61) D. Ghoshal, T. K. Maji, G. Mostafa, T. -H. Lu and N. Ray Chaudhuri, *Cryst. Growth Des.*, 2003, **3**, 9–11.
- (62) A. K. Ghosh, D. Ghoshal, T. -H. Lu, G. Mostafa and N. Ray Chaudhuri, *Cryst. Growth Des.*, 2004, **4**, 851–857.
- (63) J. H. Jung, J. H. Lee, J. R. Silverman and G. John, *Chem. Soc. Rev.*, 2013, **42**, 924–936
- (64) J. Bregman, K. Osaki, G. M. J. Schmidt and F. I. Sonntag, *Topochemistry*, *J. Chem. Soc.*, 1946, **4**, 2021–2030.
- (65) G. M. J. Schmidt, *Pure Appl. Chem.*, 1971, **27**, 647–678.
- (66) B. B. Rath and J. J. Vittal, *CrystEngComm*, 2021, **23**, 5738–5752.
- (67) R. Medishetty, L. L. Koh, G. K. Kole and J. J. Vittal, *Angew. Chem.*, 2011, **50**, 10949–10952.
- (68) L. S. Long, *CrystEngComm*, 2010, **12**, 1354–1365.
- (69) C. P. Li, Q. Yu, J. Chen and M. Du, *Cryst. Growth Des.*, 2010, **10**, 2650–2660.

- (70) H. Wang, Y. Y. Wang, G. P. Yang, C. J. Wang, G. L. Wen, Q. Z. Shi and S. R. Batten, *CrystEngComm*, 2008, **10**, 1583–1594.
- (71) Y. -B. Dong, Y. -Y. Jiang, J. Li,; J. -P. Ma, F. -L. Liu,; B. Tang, R. -Q. Huang and S. R. Batten, *J. Am. Chem. Soc.*, 2007, **129**, 4520–4521.
- (72) J. Zhang, L. Wojtas, R. W. Larsen; M. Eddaoudi and M. J. Zaworotko, *J. Am. Chem. Soc.*, 2009, **131**, 17040–17041.
- (73) S. -S. Wang, R. -K. Huang, X. -X. Chen, W. -J. Xu, W. -X. Zhang and X. -M. Chen, *Cryst. Growth Des.*, 2019, **19**, 1111–1117.
- (74) D. K. Kumar, A. Das and P. Dastidar, *CrystEngComm*, 2006, **8**, 805–814.
- (75) S. Tripathi, R. Srirambalaji, S. Patra and G. Anantharaman, *CrystEngComm* 2015, **17**, 8876–8887.
- (76) P. E. Werner, L. Eriksson and M. Westdahl, *J. Appl. Crystallogr.*, 1985, **18**, 367–370.
- (77) J. R. -Carvajal, *Phys. B*, 1993, **192**, 55–69.
- (78) Y. Wang, M. He, X. Gao, S. Li, S. Xiong, R. Krishna and Y. He, *ACS Appl. Mater. Interfaces*, 2018, **10**, 20559–20568.
- (79) J. B. DeCoste and G. W. Peterson, *Chem Rev*, 2014, **114**, 5695–5727.
- (80) E. Barea, C. Montoro and J. A. R. Navarro, *Chem Soc Rev*, 2014, **43**, 5419–5430.
- (81) J. K. Schnobrich, K. Koh, K. N. Sura and A. J. Matzger, *Langmuir* 2010, **26**, 5808–5814.
- (82) K. S. Walton and R. Q. Snurr, *J. Am. Chem. Soc.* 2007, **129**, 8552–8556.
- (83) K. Koh, A. G. Wong-Foy and A. J. Matzger, *J. Am. Chem. Soc.* 2009, **131**, 4184–4185.
- (84) J. -R. Li, R. J. Kuppler and H. -C. Zhou, *Chem. Soc. Rev.*, 2009, **38**, 1477–1504.
- (85) D. N. Dybtsev, H. Chun, S. H. Yoon, D. Kim and K. Kim, *J. Am. Chem. Soc.*, 2004, **126**, 32–33.
- (86) Y. -S. Bae, K. L. Mulfort,, H. Frost, P. Ryan,, S. Punnathanam, L. J. Broadbelt and J. T. Hupp, *Langmuir*, 2008, **24**, 8592–8598.
- (87) J. Seo, R. Matsuda,, H. Sakamoto, C. Bonneau and S. Kitagawa, *J. Am. Chem. Soc.*, 2009, **131**, 12792–12800.
- (88) G. Férey and C. Serre, *Chem. Soc. Rev.*, 2009, **38**, 1380–1399.
- (89) B. Chen, S. Ma, F. Zapata, F. R. Fronczek, E. B. Lobkovsky and H. -C. Zhou, *Inorg. Chem.*, 2007, **46**, 1233–1236.

- (90) B. Bhattacharya, R. Halder, R. Dey, T. K. Maji and D. Ghoshal, *Dalton Trans.*, 2014, **43**, 2272–2282.
- (91) D. K. Maity, A. Halder, B. Bhattacharya, A. Das and D. Ghoshal, *Cryst. Growth Des*, 2016, **16**, 1162–1167.
- (92) J. Park, D. Yuan, K. T. Pham, J. -R. Li, A. Yakovenko and H. -C. Zhou, *J. Am. Chem. Soc.* 2012, **134**, 99–102.
- (93) H. Hayashi, A. P. Cote, H. Furukawa, M. O’Keeffe and O.M. Yaghi, *Nat. Mater.*, 2007, **6**, 501–506.
- (94) Z. R. Herm, R. Krishna and J. R. Long, *Microporous Mesoporous Mater*, 2012, **157**, 94–100.
- (95) H. Furukawa, N. Ko, Y. B. Go, N. Aratani, S. B. Choi,, E. Choi, A. Ö. Yazaydin, R. Q. Snurr, M. O’Keeffe and J. Kim, *Science*, 2010, **329**, 424–428.
- (96) L. Li, S. Tang,, C. Wang, X. Lv,, M. Jiang, H. Wu and X. Zhao, *Chem. Commun.*, 2014, **50**, 2304–2307.
- (97) S. Ma, D. F. Sun, M. Ambrogio, J. A. Fillinger, S. Parkin and H. -C. Zhou, *J. Am. Chem. Soc.*, 2007, **129**, 1858.
- (98) X. Lin, I. Telepeni, A. J. Blake, A. Dailly, C.M. Brown, J. M. Simmons, M. Zoppi, G. S. Walker, K. M. Thomas, T. J. Mays, P. Hubberstey, N. R. Champness and M. Schroder, *J. Am. Chem. Soc.*, 2009, **131**, 2159–2171.
- (99) M. Dincă and J. R. Long, *Angew. Chem.*, 2008, **120**, 6870–6884.
- (100) K. L. Mulfort, O. K. Farha, C. L. Stern, A. A. Sarjeant and J. T. Hupp, *J. Am. Chem. Soc.*, 2009, **131**, 3866–3868.
- (101) Z. Wang, K. K. Tanabe and S. M. Cohen, *Chem. Eur. J.*, 2010, **16**, 212 – 217.
- (102) D. K. Maity, A. Halder, G. Pahari, F. Haque and D. Ghoshal, *Inorg. Chem.*, 2017, **56**, 713–716.
- (103) F. -G. Li, C. Liu, D. Yuan, F. Dai, R. Wang, Z. Wang, X. Lu and Daofeng Sun, *CCS Chem.*, 2021, **3**, 1005–1011.
- (104) P. Suksaengrat, V. Amornkitbamrung, P. Srepusharawoot and R. Ahuja, *ChemPhysChem*, 2016, **17**, 879–884.
- (105) H. Wu, W. Zhou and T. Yildirim, *J. Am. Chem. Soc.*, 2009, **131**, 4995–5000.

- (106) X. Y. Ren, T. J. Sun, J. L. Hu and S. D. Wang, *Microporous Mesoporous Mater.*, 2014, **186**, 137–145.
- (107) Z. Niu, X. L. Cui, T. Pham, P. C. Lan, H. B. Xing, K. A. Forrest, L. Wojtas, B. Space and S. Q. Ma, *Angew. Chem. Int. Ed.*, 2019, **58**, 10138–10141.
- (108) H. Kim, S. Yang, S. R. Rao, S. Narayanan, E. A. Kapustin, H. Furukawa, A. S. Umans, O. M. Yaghi and E. N. Wang, *Science*, 2017, **356**, 430–434.
- (109) B. T. Nguyen, H. L. Nguyen, T. C. Nguyen, K. E. Cordova and H. Furukawa, *Chem. Mater.* 2016, **28**, 6243–6249.
- (110) Y. Wu, H. Chen, J. Xiao, D. Liu, Z. Liu, Y. Qian and H. Xi, *ACS Appl. Mater. Interfaces*, 2015, **7**, 26930–26940.
- (111) D. -W. Lim, M. Sadakiyo and H. Kitagawa, *Chem. Sci.*, 2019, **10**, 16–33.
- (112) S. Chand, S. M. Elahi, A. Pal and M. C. Das, *Chem. Eur. J.*, 2019, **25**, 6259–6269.
- (113) S. -S. Bao, L. -M. Zheng and G. K. H. Shimizu, *Coord. Chem. Rev.*, 2019, **378**, 577–594.
- (114) F. Ahmed, J. Datta, B. Dutta, K. Naskar, C. Sinha, S. M. Alam, S. Kundu, P. P. Ray and M. H. Mir, *RSC Adv.*, 2017, **7**, 10369–10375.
- (115) L. Sun, M. G. Campbell and M. Dincă, *Angew. Chem. Int. Ed.*, 2016, **55**, 3566–3579.
- (116) M. Hmadeh, Z. Lu, Z. Liu, F. Gándara, H. Furukawa, S. Wan, V. Augustyn, R. Chang, L. Liao and F. Zhou, *Chem. Mater.*, 2012, **24**, 3511–3513.
- (117) K. M. Hutchins, T. P. Rupasinghe, L. R. Ditzler, D. C. Swenson, J. R. G. Sander, J. Baltrusaitis, A. V. Tivanski and L. R. MacGillivray, *J. Am. Chem. Soc.*, 2014, **136**, 6778–6781.
- (118) J. C. Tan and A. K. Cheetham, *Chem. Soc. Rev.*, 2011, **40**, 1059–1080.
- (119) J. C. Tan, T. D. Bennett,; A. K. Cheetham, *Proc. Natl. Acad. Sci. U. S. A.*, 2010, **107**, 9938–9943.
- (120) R. Hill, *J. Mech. Phys. Solids* 1963, **11**, 357–372.
- (121) O. Sigmund, *Mech. Mater.*, 1995, **20**, 351–368.
- (122) M. D. Jong, W. Chen, T. Angsten, A. Jain, R. Notestine, A. Gamst, M. Sluiter, C. K. Ande, S. van der Zwaag, J. J. Plata, C. Toher, S. Curtarolo, G. Ceder, K. A. Persson and M. Asta, *Sci. Data*, 2015, **2**, 150009.
- (123) H. Wu, T. Yildirim, W. Zhou, *J. Phys. Chem. Lett.*, 2013, **4**, 925–930.
- (124) L. Sarkisov, R. L. Martin, M. Haranczyk and B. Smit, *J. Am. Chem. Soc.*, 2014, **136**, 2228–2231.

- (125) E. A. Kapustin, S. Lee, A. S. Alshammari and O. M. Yaghi, *ACS Cent. Sci.*, 2017, **3**, 662–667.
- (126) A. Demessence, P. Horcajada, C. Serre, C. Boissière, D. Grosso, C. Sanchez and G. Férey, *Chem. Commun.*, 2009, 7149–7151.
- (127) W. C. Oliver and M. Pharr, *J. Mater. Res.*, 1992, **7**, 1564–1583.
- (128) N. -Y. Li, D. Liu, B. F. Abrahams and J. -P. Lang, *Chem. Commun.*, 2018, **54**, 5831–5834.
- (129) N. -Y. Li, *Inorg. Chem.*, 2018, **57**, 849–856.
- (130) F. -L. Hu, H. -F. Wang, D. Guo, H. Zhang, J. -P. Lang and J. E. Beves, *Chem. Commun.*, 2016, **52**, 7990–7993.
- (131) L. -L. Li, X. -Q. Feng, R. -P. Han, S. -Q. Zang and G. Yang, *J. Hazard. Mater.*, 2017, **321**, 622–628.
- (132) M. Khanpour and A. Morsali, *Eur. J. Inorg. Chem.*, 2010, 1567–1571.
- (133) E. Coronado, M. G. -Marqués, C. J. G. -García and G. M. Espallargas, *Inorg. Chem.*, 2012, **51**, 12938–12947.
- (134) G. -C. Xu, Y. -J. Ding, Y. -Q. Huang, G. -X. Liu, W. -Y. Sun, *Microporous Mesoporous Mater.*, 2008, **113**, 511–522.
- (135) S. Horike, S. Shimomura and S. Kitagawa, *Nat. Chem.*, 2009, **1**, 695–704.
- (136) K. Uemura, R. Matsuda and S. Kitagawa, *J. Solid State Chem.*, 2005, **178**, 2420–2429.
- (137) A. Schneemann, V. Bon, I. Schwedler, I. Senkovska, S. Kaskel and R.A. Fischer, *Chem. Soc. Rev.*, 2014, **43**, 6062–6096.
- (138) S. Krause, V. Bon, U. Stoeck, I. Senkovska, D. M. Többs, D. Wallacher, S. Kaskel, *Angew. Chem. Int. Ed.* 2017, **56**, 10676–10680.
- (139) G. Férey, *Z. Anorg. Allg. Chem.*, 2012, **638**, 1897–1909.
- (140) G. Férey, *Dalton Trans.*, 2016, **45**, 4073–4089.
- (141) D. N. Dybtsev, H. Chun and K. Kim, *Angew. Chem. Int. Edn.*, 2004, **43**, 5033–5036.
- (142) S. Hou, Q. -K. Liu, J. -P. Ma and Y. -B. Dong, *Inorg. Chem.*, 2013, **52**, 3225–3235.
- (143) J. P. S. Mowat, V. R. Seymour, J. M. Griffin, S. P. Thompson, A. M. Z. Slawin, D. Fairen-Jimenez, T. Düren, S. E. Ashbrook and P. A. Wright, *Dalton Trans.*, 2012, **41**, 3937–3941.
- (144) D. K. Kumar, A. Das and P. Dastidar, *Cryst. Growth Des.* 2007, **7**, 2096–2105.
- (145) I. H. Park, R. Medishetty, H. H. Lee, C. E. Mulijanto, H. S. Quah, S. S. Lee and J. J. Vittal, *Angew. Chem., Int. Ed.*, 2015, **54**, 7313–7317.

- (146) A. J. Graham, D. R. Allan, A. Muszkiewicz, C. A. Morrison,;S. A. Moggach, *Angew. Chem. Int. Ed.*, 2011, **50**, 11138–11141.
- (147) S. A. Moggach, T. D. Bennett and A. K. Cheetham, *Angew. Chem. Int. Ed.*, 2009, **48**, 7087–7089.
- (148) A. Modrow, D. Zargarani, R. Herges and N. Stock, *Dalton Trans.*, 2011, **40**, 4217.
- (149) M. -H. Xie, X. -L. Yang, and C. -D. Wu, *Chem. Eur. J.*, 2011, **17**, 11424 –11427.
- (150) L. Carlucci, G. Ciani, D. M. Proserpio, Tatiana G. Mitina and V. A. Blatov, *Chem. Rev.*, 2014, **114**, 7557–7580.
- (151) H. Wu, J. Yang, Y. -Y. Liu, and J. -F. Ma, *Cryst. Growth Des.*, 2012, **12**, 2272–2276.
- (152) D. -m. Chen, X -p. Zhang, W. Shi and P. Cheng, *Cryst. Growth Des.*, 2014, **14**, 6261–6268.
- (153) M. Eddaoudi, J. Kim, N. Rosi, D. Vodak, J. Wachter, M. O'Keeffe and O. M. Yaghi, *Science*, 2002, **295**, 469–472.
- (154) D. J. Lun, G. I. Waterhouse and S. G. Telfer, *J. Am. Chem. Soc.*, 2011, **133**, 5806–5809.
- (155) J. I. Feldblyum, A. G. Wong-Foy and A. J. Matzger, *Chem. Commun.* 2012, **48** , 9828–9828.
- (156) M. S. Yazdanparast, V. W. Day and T. Gadzikwa, *Molecules*, 2020, **25**, 697.
- (157) K. B. Sezginel, P. A. Asinger, H. Babaei and C. E. Wilmer, *Chem. Mater.*, 2018, **30**, 2281–2286.

Chapter 1B

Summary of research works

Chapter 1: This chapter consists of two sections: chapter 1A and chapter 1B.

Chapter 1A: This chapter contains short introduction about coordination polymers which contains history of CPs, different terminologies, various strategy of synthesis and role of variable factors for designing functional coordination polymers. Characterization techniques of coordination polymers, discussion on various functionalities, structural transformation and interpenetration in CPs are also here.

Chapter 1B: It illustrates the brief summary which has been discussed in the thesis.

Chapter 2: This chapter contains the synthesis of three new coordination complexes $[\text{Mn}(\text{L1})(\mu\text{-azide})(\text{azide})]_2 \cdot 4\text{H}_2\text{O}$ (**1**), $[\text{Mn}(\text{L1})(\text{fum})]_n$ (**2**) [L1 = 2-methyl- N^1, N^2 -bis(pyridin-2yl)propane-1,2-diamine, fum= fumaric acid] and $[\text{Co}(\text{L2})(\text{azide})]$ (**3**) [L2 = 6-phenyl-1,3,5-triazine 2,4-diyl amino(pyridine-2yl)methanol]. All the complexes have been characterized by single crystal X-ray diffraction analysis. Complex **1**, a dinuclear Mn(II) complex is formed by bridging azide ligand and other coordination sites are satisfied by tetradentate ligand L1 and terminal azide ligand. The overall structure is an incomplete supramolecular 3D cage structure, formed by intermolecular π - π interaction of pyridyl ligand and hydrogen bonding. Complex **2** comprised of eight coordinated Mn(II) centre where ligand L1 and fumarate is bridged between the metal centers that leads to a one dimensional chain structure which further extended to a 3D structure by π - π and C-H... π interactions. The overall structure is further stabilized by hydrogen bonding with the guest water molecules. Complex **3**, a six coordinated mononuclear Co(II) discrete complex is consist of pentadentate ligand L2 and azide act as a terminal ligand. This Mononuclear complex is connected by π - π , C-H... π interactions and hydrogen bonding which ultimately leads to a supramolecular 2D architecture.

Chapter 3: This chapter is about the design and synthesis of interpenetrated metal organic frameworks (IMOFs). Interpenetrated metal organic frameworks (IMOFs) have occupied a top priority of interest in the last few decades due to their unexpected better potential applications in the various growing field. Like dynamic IMOFs, other IMOFs have also been important material due to their interesting structural phenomenon and inherent flexibility which is actually responsible for exhibition of different functionality even by a single framework. Interpenetrated

framework is generally formed by coordination of metals with rigid ligands but flexible ligand shows more interesting results in some cases. It is well established that the length of used ligands, irrespective of flexibility and rigidity plays a vital role in making of these type of structures. In searching of IMOFs, three MOFs, $\{\text{Cd}(\text{bix})_{0.5}(\text{adp})_{0.5}(\text{H}_2\text{O})\}_n$ (**1**), $\{[\text{Cd}(\text{bix})(2,2'\text{-dmglu})].(\text{H}_2\text{O})\}_n$ (**2**) and $\{\text{Cd}(\text{bpmp})(2,2'\text{-dmglu})(\text{H}_2\text{O})\}.(\text{H}_2\text{O})\}_n$ (**3**) have been synthesized by using two different N,N-donor linkers bix {bix = 1,4-bis(imidazol-1-ylmethyl)-benzene}, bpmp {bpmp = 1,4-bis(4-pyridinylmethyl)piperazine} and two different substituted dicarboxylate adp {adp = adipate}, 2,2'-dmglu {2,2'-dmglu = 2,2'-dimethylglutarate}. Among the three complexes, three fold interpenetrated framework has been shown by complex **3** where long length more flexible N,N-donor ligand, bpmp { bpmp = 1,4-bis(4-pyridinylmethyl)piperazine} has been used. Gas sorption studies are performed with the three synthesized MOFs which substantially correlate with their framework.

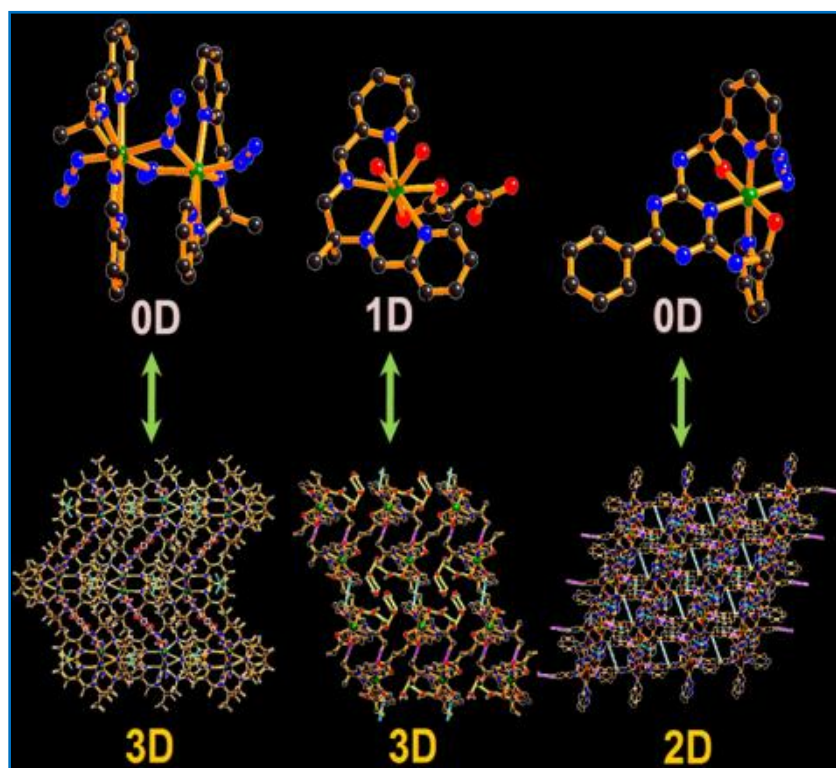
Chapter 4: In this chapter anion exchange properties of coordination polymers have been explored. Anion exchange materials are important for their application in toxic anion control process. Coordination Polymers (CPs) with weakly coordinated anions and lattice anions may be practically useful in anion exchange process. To explore this anion exchange properties by coordination polymers (CPs) two water insoluble cationic CPs $\{[\text{Mn}(\text{bix})_3(\text{H}_2\text{O})_2].\text{bix}.(\text{NO}_3)_2\}_n$ (**1**), $\{[\text{Cd}(\text{bix})_2(\text{NO}_3)_2].(\text{H}_2\text{O})_2\}_n$ (**2**) have been synthesized by using N,N-donors linkers bix {bix = 1,4-bis(imidazol-1-ylmethyl)-benzene}. Structure of complex **1** is 1D and contains lattice NO_3^- anion and the complex **2** is 2D and contains weakly coordinated NO_3^- anion. Both these complexes along with another previously published structurally similar CP $\{[\text{Cd}(\text{bix})_2(\text{NO}_3)_2]\}_n$ (**3**), response in anion exchange studies with foreign anions. All the anion exchange processes have monitored by FT-IR spectroscopy and PXRD measurements.

Chapter 5: This chapter contains the strategic design and synthesis of MOFs for CO_2 sorption at normal and high pressure. Metal organic frameworks with suitable void are promising materials for the execution of their exceptional functionalities. With the incorporation of proper void and modulating the structural flexibility, such frameworks have found very impressive for several applications. Accounting this phenomenon and to explore the structural diversity and sorption behavior of them, four metal organic frameworks namely $\{[\text{Cu}_3(3,3'\text{-dmglut})_3(\text{bte})].6(\text{H}_2\text{O})\}_n$ (**1**), $\{[\text{Cu}(3,3'\text{-dmglut})(\text{btp})_{0.5}].2(\text{H}_2\text{O})\}_n$ (**2**), $[\text{Zn}(3,3'\text{-dmglut})_{0.5}(\text{bpe})_{0.5}]_n$ (**3**) and $\{[\text{Mn}_2(3,3'\text{-dmglut})_2(\text{bpe})_2(\text{H}_2\text{O})_2].5(\text{H}_2\text{O})\}_n$ (**4**) have been synthesized. Here, three complexes exhibit 3D

structure and one is 2D. All the complexes except **3**, shows structural transformation upon activation. For the complexes **1** and **2**, ligand flexibility plays a vital role for their sorption behavior. In complex **3**, despite of low void space, it shows highest CO₂ sorption at high pressure, among all the complexes due to pore opening-closing phenomenon. In case of complex **4**; dynamicity and additional adsorbate-adsorbent interaction force to exhibit an interesting carbon dioxide sorption at 1 bar pressure though it possesses 2D structure. High pressure carbon dioxide sorption of these complexes has also been studied and correlated with the structural transformations observed in the individual complexes.

Chapter 6: This chapter contains the synthesis of a two-fold interpenetrated 3D MOF $\{[\text{Cd}_2(\text{bpe})_2(3,3\text{-dmglu})_2]\}_n$ (**1**) by using trans-1,2-bis(4-pyridyl)ethylene ligand (bpe) and 3,3-dimethylglutarate (3,3-dmglu) with crystallographically two distinct C=C bonds, which undergoes [2+2] photo-cycloaddition and thermal reversible reaction, in a single-crystal-to-single crystal (SCSC) manner. The newly synthesized two-fold interpenetrated 3D MOF (**1**) has been reversibly converted into a 3D interpenetrated MOF $\{[\text{Cd}_2(\text{rctt-tpcb})(3,3\text{-dmglu})_2]\}_n$ (**2**), {where, tpcb = tetrakis(4-pyridyl)cyclobutane), in rctt, the r = reference substituent group, c = cis and t = trans for indicating the relative orientation of the substituent on the cyclobutane ring with regard to the reference group} in SCSC manner by the cycloaddition of two distinct C=C bonds with shorter and longer separations, simultaneously. The soft mechanical behaviour in these two crystals indicates that the molecular movements and flexible coordination cite in solid state is responsible for the reversible photochemical reactions in the molecular crystals of the said MOF.

Chapter 2



Chapter 2: Mixed ligand coordination complexes using multicomponent ligand: syntheses, characterization and effect of non-covalent interactions on their framework structures

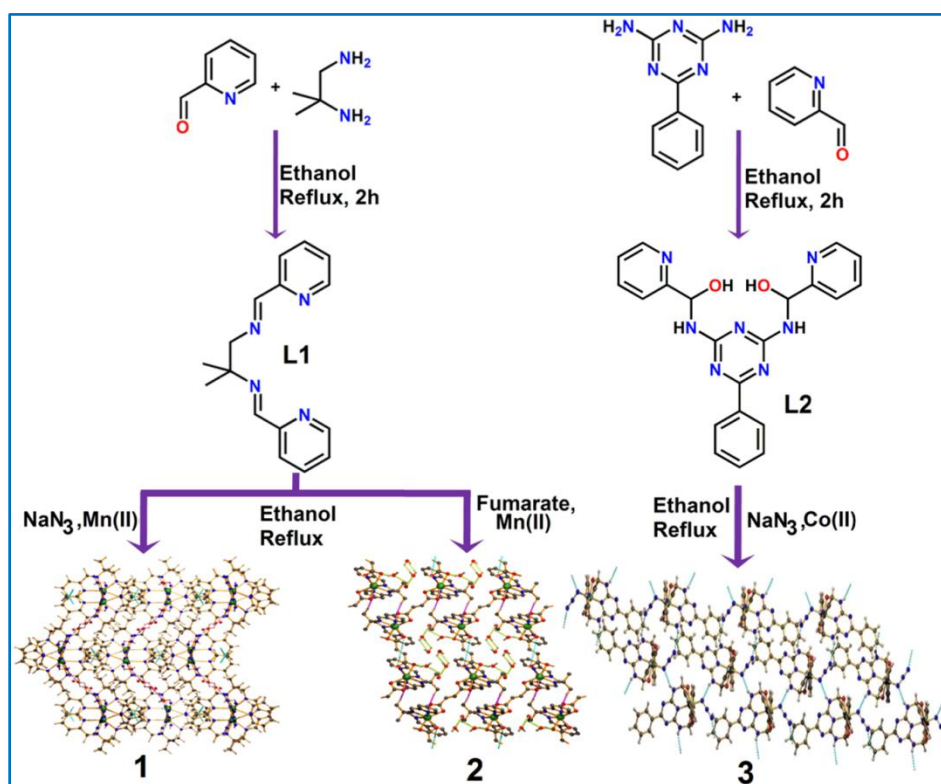
Chapter 2

Mixed ligand coordination complexes using multicomponent ligand: syntheses, characterization and effect of non-covalent interactions on their framework structures

1. Introduction

The structural prosperity of coordination compound would be unimaginable without multifunctional and polydentate ligands. The different types of transition metal nodes and N/ S/ O-donor ligands are combined to produce higher dimensional structure having potential property as a catalysis,¹⁻⁴ gas adsorption,⁵⁻⁹ magnetism,¹⁰⁻¹³ ion exchange,¹⁴⁻¹⁶ electric conductance,¹⁷⁻¹⁸ proton conductance¹⁹⁻²¹ photo luminescence²²⁻²⁴ etc. So the smart choice of organic linkers as well as the metal ions,²⁵⁻²⁶ counter anions,²⁷⁻²⁸ reaction temperatures,²⁹⁻³⁰ pH of the medium,³¹⁻³² solvents³³⁻³⁴ etc. can also play a vital role to create the overall structural and functional diversities in coordination complexes. Among the different type of ligands *Schiff* bases have long been used as end-capping ligands because of their ease of preparation, structural variety, varied denticities, and subtle steric and/or electronic effects. The pseudohalides such as azide, thiocyanate, dicyanamide etc., have been extensively used as co-ligands along with the N,N'-donor *Schiff* base multi-component ligands; for the extension of the polymeric structure having interesting property.³⁵⁻³⁶ Beside this, different dicarboxylates such as succinate, glutarate, fumarate, pyridine dicarboxylate, nicotinate have been widely used to create the diversity of the coordination complexes as well as their supramolecular architecture.³⁷⁻³⁹ In search of useful ligand, the domain of the N, N'-donor multi-component ligands with pyridyl rings, may be greatly useful. It is frequently observed that pyridyl groups are involved in the π - π interactions in the solid-state structure, which plays a considerable role for the stabilization of the extended structure of the complexes. However such supramolecular systems are somehow resembles bio-molecules, where weak forces dominate to create the overall structure. Therefore study of crystalline model structures with precise parameter could be an interesting venture to understand the behaviour of closely related bio-molecules. To explore such possibility, two different ligands have prepared using pyridine-2-carboxaldehyde and two different amines (Scheme 1). On reaction with different metal ions and the two ligands, three new complexes namely [Mn(L1)(μ -

azide)(azide)]₂·4H₂O (**1**), [Mn(L1)(fum)]_n (**2**), and [Co(L2)(azide)] (**3**) where L1= {2-methyl-N',N''-bis(pyridin-2-yl)propane-1,2-diamine}, L2= {6-phenyl-1,3,5-triazine-2,4-diyl-amino(pyridine-2-yl)methanol}, fum= fumaric acid have been synthesized (Scheme 1). Complex **1**, a distorted octahedral Mn(II) complex is obtained by double end-on azide bridged, tetradentate ligand L1 and pendent azide ligand, which leads to a supramolecular 2D structure by intermolecular π - π interaction constructed by pyridyl ring of ligand. Further hydrogen bonding stabilized the structure and forms an incomplete 3D structure. Complex **2**, instead of azide fumarate bridged⁴⁰⁻⁴¹ 1D Mn(II) complex is formed where crystal packing is responsible for supramolecular 3D structure by weak interactions. Complex **3**, a six coordinated mononuclear Co(II) complex is formed by a pentadentate ligand (L2) and terminal azide ligand which also leads to a supramolecular 2D structure by means of weak interactions.



Scheme 1. Synthetic outline for the ligands and the complexes.

2. Experimental section

2.1. Materials

High purity manganese(II) chloride tetrahydrate, cobalt(II) nitrate hexahydrate, pyridine-2-carboxaldehyde, 1,2-diamino-2-methylpropane, sodium azide, fumaric acid (fum) and 2,4-

diamino-6-phenyl-1,3,5-triazine have been obtained from Sigma-Aldrich Chemical Co. Inc. All other chemicals, including solvents, are of AR grade and have been used as received.

2.2. Physical measurements

The elemental analyses (carbon, hydrogen, and nitrogen) of compounds **1-3** have been carried out on a PerkinElmer 240C elemental analyzer. The Infrared spectra have been obtained at room temperature using KBr pellets on a PerkinElmer Spectrum BX-II IR spectrometer in the 4000-400 cm^{-1} region. To prepare samples embedded KBr pellets, respective powder samples and 20 mg dry KBr is mixed together and 50 kg/cm^2 pressure is applied for 60 seconds, which results formation of pellets from the powder materials. X-ray powder diffraction (PXRD) patterns of the bulk samples have been recorded in a Bruker D8 Discover instrument using $\text{Cu-K}\alpha$ radiation. UV-vis spectra have been recorded at room temperature on a PerkinElmer Lambda 35 UV-vis spectrophotometer attached with integrating sphere to measure UV-vis spectra in solid state of the compounds.

2.3. Syntheses

2.3.1. Synthesis of $[\text{Mn}(\text{L1})(\mu\text{-azide})(\text{azide})]_2 \cdot 4\text{H}_2\text{O}$ (**1**)

1,2-Diamino-2-methyl propane (1 mmol, 0.086g) and pyridine-2-carboxaldehyde (2 mmol, 0.214) have been dissolved in 25 ml of ethanol in a 100 ml flat-bottom flask and the reaction mixture has been refluxed. After two hours a greenish yellow colored solution containing L1 has been obtained [$\text{L1} = \{2\text{methyl-N}^1, \text{N}^2\text{-bis(pyridin-2yl)propane-1,2-diamine}\}$]. Then aqueous solution of $\text{MnCl}_2 \cdot 4\text{H}_2\text{O}$ (1 mmol, 0.197 gm) and sodium azide (2 mmol, 0.130g) have been added to that reaction mixture. The resulting solution is further refluxed for 30 mins at 70-80°C. Then solution has been filtered and filtrate has been kept in desk. After ten days block shaped yellow crystals suitable for X-ray diffraction analysis have been obtained. (Yield: 60%). Anal. Calc. for $\text{C}_{32}\text{H}_{46}\text{Mn}_2\text{N}_{20}\text{O}_5$ (**1**, %): C, 42.67; H, 5.15; N, 31.00. Found: C, 42.72; H, 5.49; N, 31.15.

2.3.2. Synthesis of $[\text{Mn}(\text{L1})(\text{fum})]_n$ (**2**)

This compound has been synthesized by following the same procedure as that of **1**. But instead of azide, disodium fumarate (2 mmol, 0.130g) has been added to the reaction mixture and further refluxed for four hours at 80°C. The obtained red color solution has been filtered and filtrate has been kept in desk. After ten days block shaped yellow crystals suitable for X-ray diffraction

analysis have been obtained from the filtrate. (Yield: 60%). Anal. Calc. for $C_{20}H_{36}MnN_4O_8$ (**2**, %): C, 46.60; H, 7.04; N, 10.87. Found: C, 46.84; H, 7.81; N, 10.92.

2.3.3. Synthesis of ligand L2 and complex [Co(L2)(azide)] (3**)**

2,4-Diamino-6-phenyl-1,3,5-triazine (1mmol, 0.1872g), and pyridine-2-carboxaldehyde (2 mmol, 0.214) have been taken in 25 ml of ethanol in a 100 ml flat-bottom flask and the reaction mixture has been refluxed for 2 hours. The resulting yellow colored solution containing L2 [L2= {6-phenyl-1,3,5-triazine-2,4-diyl-amino(pyridine-2yl)methanol}] has directly used without further separation, for synthesis of complex **3**. Then aqueous solution of $Co(NO_3)_2 \cdot 6H_2O$ (1 mmol, 0.182 gm) and sodium azide (1 mmol, 0.065g) has been added and solution has been refluxed for one and half hour. A deep green colored solution has been obtained which has been filtered and the filtrate has been kept in the desk. The block shaped green crystals suitable for X-ray diffraction analysis have been obtained after seven days. (Yield: 82%). Anal. Calc. for $C_{21}H_{17}CoN_{10}O_2$ (**3**, %): C, 50.41; H, 3.42; N, 27.99. Found: C, 50.84; H, 3.81; N, 27.95.

For the bulk synthesis of the product, upper mentioned procedures are repeated and crystals are manually separated from the respective container. The bulk phase PXRD analyses suggest that, identical peak positions of assynthesized pattern and simulated pattern confirms the phase purity of the compounds.

2.4. Crystallographic data collection and refinement

The single crystals of compounds **1**, **2**, and **3** have been mounted on the tips of glass fibers with commercially available glue. X-ray data collection of all three single crystals have been performed at room temperature using Bruker APEX II diffractometer, equipped with a normal focus, sealed tube X-ray source with graphite monochromated Mo-K α radiation ($\lambda = 0.71073 \text{ \AA}$). The data have been integrated by using SAINT⁴² program and the absorption corrections have been made with SADABS⁴³. All the structures have been solved by SHELXS-97⁴⁴ using Patterson method and have been followed by successive Fourier and difference Fourier synthesis. Full matrix least-squares refinements have been performed on F^2 using SHELXL-97⁴⁴ with anisotropic displacement parameters for all non-hydrogen atoms. During refinement of **1**, one lattice water molecule has been found disordered. The occupancies of these molecules have been fixed at 0.5 before the final refinement and isotropically refined. All the hydrogen atoms have been fixed geometrically by HFIX command and placed in ideal positions. Calculations have been carried out using SHELXS-97,⁴⁴ SHELXL-97,⁴⁴ PLATON v1.15,⁴⁵ ORTEP-3v2,⁴⁶

WinGX system Ver-1.80⁴⁷. Data collection and structure refinement parameters and crystallographic data for all the complexes are presented in Table 1. The selected bond lengths and bond angles are presented in Tables 2, 5, and 8.

Table 1. Crystallographic and structural refinement parameters for complexes **1**, **2**, and **3**

	1	2	3
formula	C ₃₂ H ₄₆ Mn ₂ N ₂₀ O ₅	C ₂₀ H ₃₆ MnN ₄ O ₈	C ₂₁ H ₁₇ CoN ₁₀ O ₂
formula weight	900.71	507.40	500.38
crystal system	orthorhombic	triclinic	monoclinic
space group	<i>Pbcn</i>	<i>P</i> $\bar{1}$	<i>C2/c</i>
<i>a</i> /Å	13.6652(3)	9.1864(5)	16.9468(4)
<i>b</i> /Å	16.6078(4)	9.7379(5)	21.1129(4)
<i>c</i> /Å	18.7190(4)	15.6341(11)	13.0074(3)
α /°	90	102.818(5)	90
β /°	90	95.542(5)	116.483(2)
γ /°	90	113.002(3)	90
<i>V</i> /Å ³	4248.26(17)	1228.84(13)	4165.64(17)
<i>Z</i>	4	2	8
<i>D</i> _c /g cm ⁻³	1.393	1.371	1.596
μ /mm ⁻¹	0.658	0.587	0.869
<i>F</i> (000)	1832	530	2048
θ range/°	1.9 - 27.6	1.4 - 26.4	1.6 - 27.6
reflections collected	20036	17191	35419
unique reflections	4865	4971	4824
reflections <i>I</i> > 2σ(<i>I</i>)	2821	3168	3437
<i>R</i> _{int}	0.080	0.060	0.064
goodness-of-fit (<i>F</i> ²)	1.00	1.03	1.02
<i>R</i> 1 (<i>I</i> > 2σ(<i>I</i>)) ^[a]	0.0599	0.0766	0.0388
<i>wR</i> 2(<i>I</i> > 2σ(<i>I</i>)) ^[a]	0.1973	0.2496	0.0993
$\Delta\rho$ min / max /e Å ³	-0.50, 1.10	-0.43, 1.45	-0.31, 0.36

$$^{[a]}R_1 = \sum ||F_o| - |F_c|| / \sum |F_o|, wR_2 = [\sum (w(F_o^2 - F_c^2))^2 / \sum w(F_o^2)^2]^{1/2}.$$

3. Results and discussion

Both the ligand, L1= {2methyl-N¹,N²-bis(pyridin-2yl)propane-1,2-diamine} and L2= {6-phenyl-1,3,5-triazine-2,4-diyl-amino(pyridine-2yl)methanol} have been synthesized by the reaction between pyridine-2-carboxaldehyde and amines, 1,2-diamino-2-methyl propane and 2,4-diamino-6-phenyl-1,3,5-triazine respectively in 1:2 molar ratio. All the complexes are prepared by adding aqueous solution of metal salt and azide or fumarate in the ethanolic solution followed

by stirring. The Structural analysis reveals that the different coordination modes of azide⁴⁰ and fumarate⁴¹ along with weak forces present in the molecular structure responsible for supramolecular architecture.

3.1. Crystal structure descriptions

3.1.1. [Mn(L1)(μ -azide)(azide)]₂·5H₂O (**1**)

Compound **1** crystallizes in the orthorhombic *Pbcn* space group with *Z* value 4 and the structure analysis reveals that dinuclear Mn(II) complex is formed with combination of tetra-dentate ligand L1 and azide ligand (Figure 1a). The asymmetric unit of **1** composed one crystallographically independent Mn(II) center, one L1 ligand, one pendant azide linker, one bridging azide⁴⁰ linker and also two and half guest water molecules. Central metal ions have distorted pentagonal bipyramidal coordination geometry with MnN₇ environment. Two pyridyl nitrogen atoms of the L1 ligand present at the axial position with nearly 180° angle (Table 2). The basal plane is formed by two imine nitrogen atoms of same L1 ligand, one nitrogen atom from the pendant azide linker and two nitrogen atoms of two different bridging azide linkers. These two nitrogens are also the part of basal plane for another equivalent Mn(II) moiety. Thus two metal atoms (Mn1, Mn1^a) are linked by two symmetry related nitrogen atoms of azide ligand (N6, N6^a) in EO mode. Separation between the metal centers is about 3.585 Å and bond angle is about 102.48° (11). In the basal plane the Mn–N bond lengths are in between 2.182(4) – 2.363(3) Å. The axial coordination sites bond distances are little elongated, 2.526(3) and 2.452(3) Å (Table 2) which is comparable to previous by reported structure.⁴⁸ In the solid state structure each of the dimeric unit are connected to four different other dimeric units by intermolecular π – π interactions (Figure 1b). In each side two symmetrically different pyridyl rings are connected to two pyridyl rings of adjacent dimeric complexes and extend the structure along crystallographic *a* axis (Figure 1b). At the other end of the dimeric system two remaining pyridyl rings are also involved in similar interactions. Thus the dimeric unit is acting as bridge for two sets of intermolecular π – π interactions and by that way, the structure is extending to a 2D supramolecular (Figure 1b and Table 3). The lattice water molecules reside in between supramolecular 2D structures (Figure 1c) are involved in hydrogen bonding (Figure 1d) between themselves and finally connected to the end of the pendant azide ligand (Table 4). This hydrogen bonding extends the structure to a 3D supramolecular arrangement (Figure 1e).

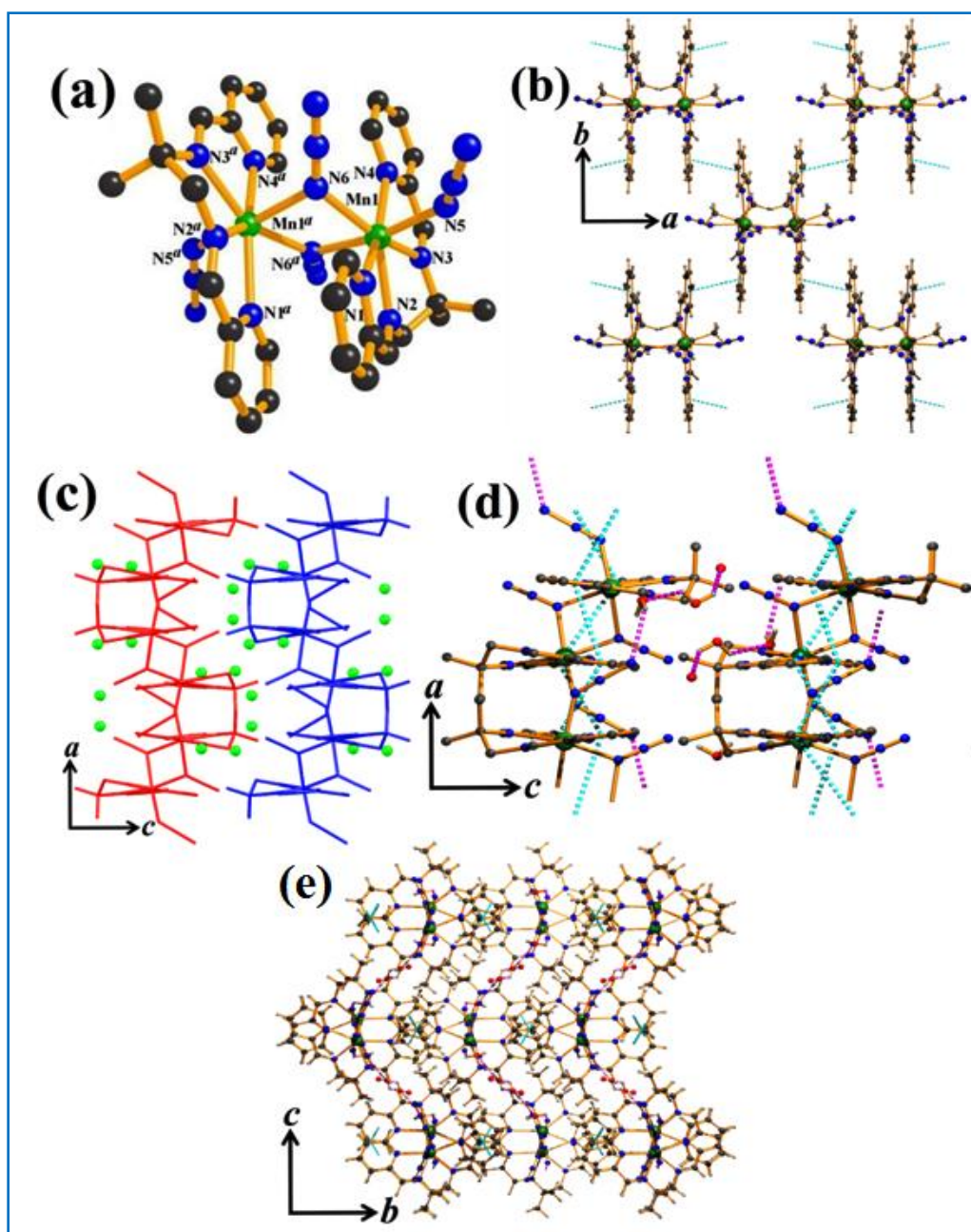


Figure 1. (a) Coordination environment around the Mn(II) ions in **1**; Mn (green), N (blue), O (red), C (black); (b) each dimeric unit is connected to four different dimeric moieties by π - π interaction (π - π interactions in cyan dotted lines) and forms a supramolecular 2D structure; (c) water present in between the 2D sheets created by the π - π interactions in **1**, Here different sheets are presented by different colors; (d) lattice water molecules are present in between the 2D structures and involved in hydrogen bonding; (e) possible supramolecular 3D structure of the complex.

Table 2. Selected bond lengths (Å) and bond angles (°) for complex **1**

Mn1–N1	2.526(3)	Mn–N2	2.313(3)	Mn1–N3	2.365(3)
Mn1–N4	2.452(3)	Mn1–N5	2.179(4)	Mn1–N6	2.301(3)
Mn1–N6 ^a	2.302(3)	N1–Mn1–N2	66.80(10)	N1–Mn1–N4	156.26(9)
N6–Mn1–N6 ^a	75.01(10)	N1–Mn1–N3	132.14(10)	N1–Mn1–N6 ^a	104.66(9)
N1–Mn1–N5	83.91(11)	N1–Mn1–N6	77.52(10)	N2–Mn1–N4	136.56(10)
N2–Mn1–N3	69.17(10)	Mn1–N6–N9	131.9(2)	N5–Mn1–N6 ^a	168.68(12)
Mn1–N6–Mn ^a	102.35(11)	N2–Mn1–N5	105.85(12)	N3–Mn1–N4	68.66(9)
N2–Mn1–N6	132.58(10)	N2–Mn1–N6 ^a	84.57(10)	N3–Mn1–N6 ^a	88.75(10)
N3–Mn1–N5	90.85(12)	N3–Mn1–N6	149.65(10)	N4–Mn1–N6 ^a	84.86(9)
N4–Mn1–N5	84.50(11)	N4–Mn1–N6	84.86(9)	N6–Mn1–N6 ^a	75.09(10)
N5–Mn1–N6	100.08(12)	N3–Mn1–N5	90.85(12)		

Symmetry code $a = 2-x, y, 1/2-z$.**Table 3.** π – π interactions in **1**

ring(i) \rightarrow ring(j)	distance of centroid(i) from ring(j), (Å)	dihedral angle (i,j) (deg)	distance between the (i,j) ring centroids, (Å)
R(1) \rightarrow R(2) ⁱ	3.791(2)	3.27(17)	-3.4769(13)
R(2) \rightarrow R(1) ⁱⁱ	3.791(2)	3.27(17)	-3.3857(15)

Symmetry code: i = $3/2-X, -1/2+Y, Z$; ii = $3/2-X, 1/2+Y, Z$.

R(i)/R(j) denotes the $i^{\text{th}}/j^{\text{th}}$ rings in the corresponding structures: R(1)= (N1)(C1)(C2)(C3)(C4)(C5); R(2)= (N4)(C12)(C13)(C14)(C15)(C16).

Table 4. Intermolecular H–bonding interactions in **1**

D–H \cdots A	D–H	H \cdots A	D \cdots A	\angle D–H \cdots A
O1W–H1WB \cdots N8 ⁱⁱⁱ	0.85	2.50	2.960(10)	115
O3W–H3WA \cdots O2W ^{iv}	0.85	1.84	2.476(8)	130
O3W–H3WB \cdots O1W ^{iv}	0.85	2.04	2.668(9)	130

Symmetry code: iii = $1/2+x, -1/2+y, 1/2-z$; iv = x, y, z .

3.1.2. [Mn(L1)(fum)]_n·4H₂O (**2**)

It crystallizes in the triclinic $P\bar{1}$ space group with Z value 2 and the structure determination reveals that Mn(II) atom is eight coordinated by tetradentate ligand L1 and bridged by four oxygen atoms of two different fumarate ligands (Figure 2a) to form MnN₄O₄ secondary building unit. The asymmetric unit contains one Mn(II) as central ion, one fumarate, one L1 ligand (Figure 2a) and four guest water molecules. Here, similar to **1**, four nitrogen atoms from ligand L1 (where N1, N4 are pyridyl nitrogen atoms and N2, N3 imine nitrogen atoms) are connected to the central metal ion with bond distances in the range of 2.303(6) – 2.408(6) Å (Table 5). The four oxygen atoms (O1, O2, O3, O4) of two different fumarate ligands (Figure 2b) are connected

to the Mn(II) centre with bond distances in between 2.390(5)–2.357(4) Å (Table 5). On changing from azide (in structure **1**) to fumarate, it connects two adjacent metal centre and forms 1D chain along crystallographic *b* axis (Figure 2b). The separation between the two symmetry related Mn(II) atom is 9.207 Å which is quite high to the other reported complexes.⁴¹ Each of these 1D chains is interconnected by intermolecular π – π interactions and forms a supramolecular 2D architecture (Figure 2c, Table 6). Such 2D arrays are linked to two others, by C–H... π interactions resulting 3D supramolecular structure (Figure 2d, Table 6). The guest water molecules reside in the supramolecular 1D pore along crystallographic *a* axis and stabilize overall structure by intermolecular hydrogen bonding (Figure 3, Table 7). By artificial removal of water molecules the void volume has been calculated as 273.1 Å³ which is about 22.2% of total crystal volume.

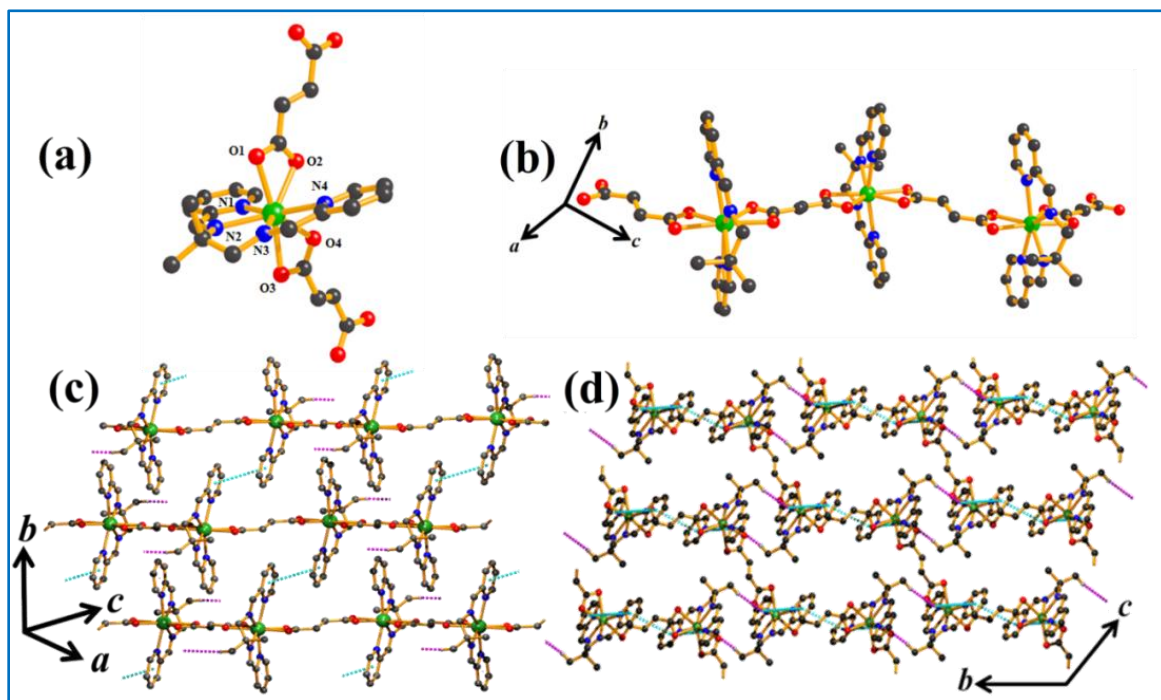


Figure 2. (a) Coordination environment around the Mn(II) ions in **2**; Mn (green), N (blue), O (red), C (black); (b) one dimensional chain structure of **2**; (c) supramolecular 2D structure by π – π interaction; (d) interconnected supramolecular 2D structure to form 3D structure by C–H... π interaction (π – π and C–H... π interactions: cyan and magenta dotted lines respectively).

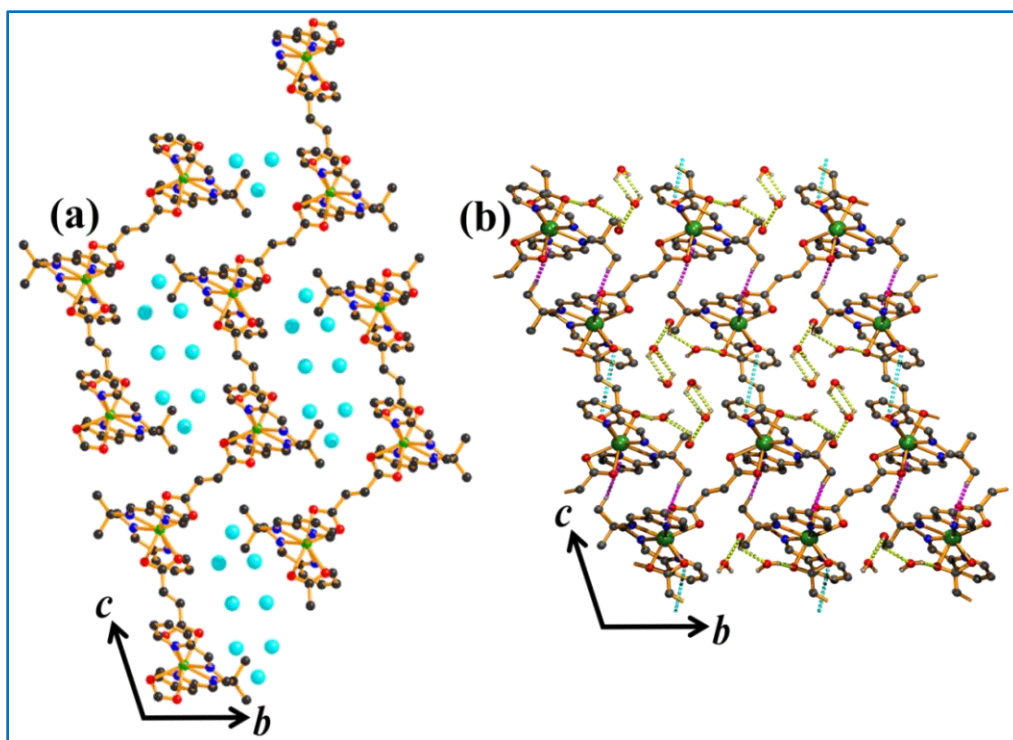


Figure 3. Water filled supramolecular pore in structure **2**, (a) without showing weak interaction and (b) showing weak interaction (π - π interactions, C-H... π interactions and H-bonding: cyan, magenta and greenish yellow dotted lines respectively) where Mn (green), N (blue), O (red), C (black) and H (grey).

Table 5. Selected bond lengths (Å) and bond angles (°) for complex **2**

Mn1-O1	2.390(5)	Mn1-O2	2.381(4)	Mn1-O3	2.374(5)
Mn1-O4	2.357(4)	Mn1-N1	2.389(5)	Mn1-N2	2.344(5)
Mn1-N3	2.303(6)	Mn1-N4	2.408(6)	N3-Mn1-N4	68.74(19)
O1-Mn1-O2	54.41(15)	O1-Mn1-O3	166.91(15)	O1-Mn1-O4	138.21(16)
O1-Mn1-N1	89.99(18)	O1-Mn1-N2	84.02(16)	O1-Mn1-N3	88.24(18)
O1-Mn1-N4	85.14(18)	O2-Mn1-O3	138.69(14)	O2-Mn1-O4	83.84(15)
O2-Mn1-N1	78.49(16)	O2-Mn1-N2	127.09(18)	O2-Mn1-N3	130.87(15)
O2-Mn1-N4	76.60(17)	O3-Mn1-O4	54.87(14)	O3-Mn1-N1	93.08(16)
O3-Mn1-N2	85.15(15)	O3-Mn1-N3	81.02(16)	O3-Mn1-N4	97.78(17)
O4-Mn1-N1	82.49(16)	O4-Mn1-N2	129.80(16)	O4-Mn1-N3	123.66(18)
O4-Mn1-N4	83.18(17)	N1-Mn1-N2	69.48(18)	N1-Mn1-N3	138.38(18)
N1-Mn1-N4	152.38(18)	N2-Mn1-N3	69.0(2)	N2-Mn1-N4	136.54(19)

Table 6. π - π interactions and C-H... π interaction in **2**

ring(i) \rightarrow ring(j)	distance of centroid(i) from ring(j), (Å)	dihedral angle (i,j) (deg)	distance between the (i,j) ring centroids, (Å)
R(2) \rightarrow R(2) ⁱ	4.072(4)	0.00(3)	-3.612(3)
C-H \rightarrow ring(j)	H...R distance (Å)	C-H...R angle (deg)	C...R distance (Å)
C(9)-H(9) \rightarrow R(1) ⁱⁱ	2.79	165	3.725(7)

Symmetry code: i = -1-X, 1-Y, 1-Z; ii = -X, 1-Y, 2-Z.

R(i)/R(j) denotes the ith/jth rings in the corresponding structures: R(1)= (N1)(C1)(C2)(C3)(C4)(C5); R(2) =(N4)(C12)(C13)(C14)(C15)(C16).

Table 7. Intermolecular H-bonding interactions in **2**

D-H...A	D-H	H...A	D...A	\angle D-H...A
O1-H1WA...O2W	0.85	2.16	2.796(7)	131
O1W-H1WB...O4W	0.85	2.11	2.697(8)	126
O2W-H2WA...O3W	0.85	2.35	2.812(6)	115
O3W-H3WB...O2W	0.85	2.27	2.812(6)	121
O4W-H4WA...O1 ⁱⁱⁱ	0.85	2.14	2.907(9)	149

Symmetry code: iii = x, 1+y, z.

3.1.3. [Co(L2)(azide)] (**3**)

Compound **3** crystallizes in the monoclinic $C2/c$ space group with Z value 8 and the structure analysis reveals that six coordinated mononuclear Co(II) complex is formed by a pentadentate ligand (L2) and one azide ligand which is terminally coordinated (Figure 4a). Here the ligand (L2) is connected to the central metal ions N_3O_2 donor set. From this donor set, two pyridyl nitrogen atoms (N1, N7) are connected to the metal centre at $\sim 180^\circ$ and also the two oxygen atoms (O1, O2) are almost connected with same angle (Table 8). Other two coordination sides are satisfied by one tetrazine nitrogen atoms (N2) from L2 ligand and another nitrogen atom (N8) from azide ligand. Angle of N2-Co1-N8 is 179.48° (Table 8), which suggest that slightly distorted octahedral coordination environment around the metal center. The monomeric Co(II) complex exhibits a supramolecular 2D structure by means of π - π and C-H... π interaction of pyridyl rings and triazine rings of L2 ligand (Figure 4b, Table 9). This supramolecular 2D structure is further stabilized by intermolecular hydrogen bonding interaction between N5, N6 triazine nitrogen and N8, N10 azide nitrogen (Figure 4c, Table 10).

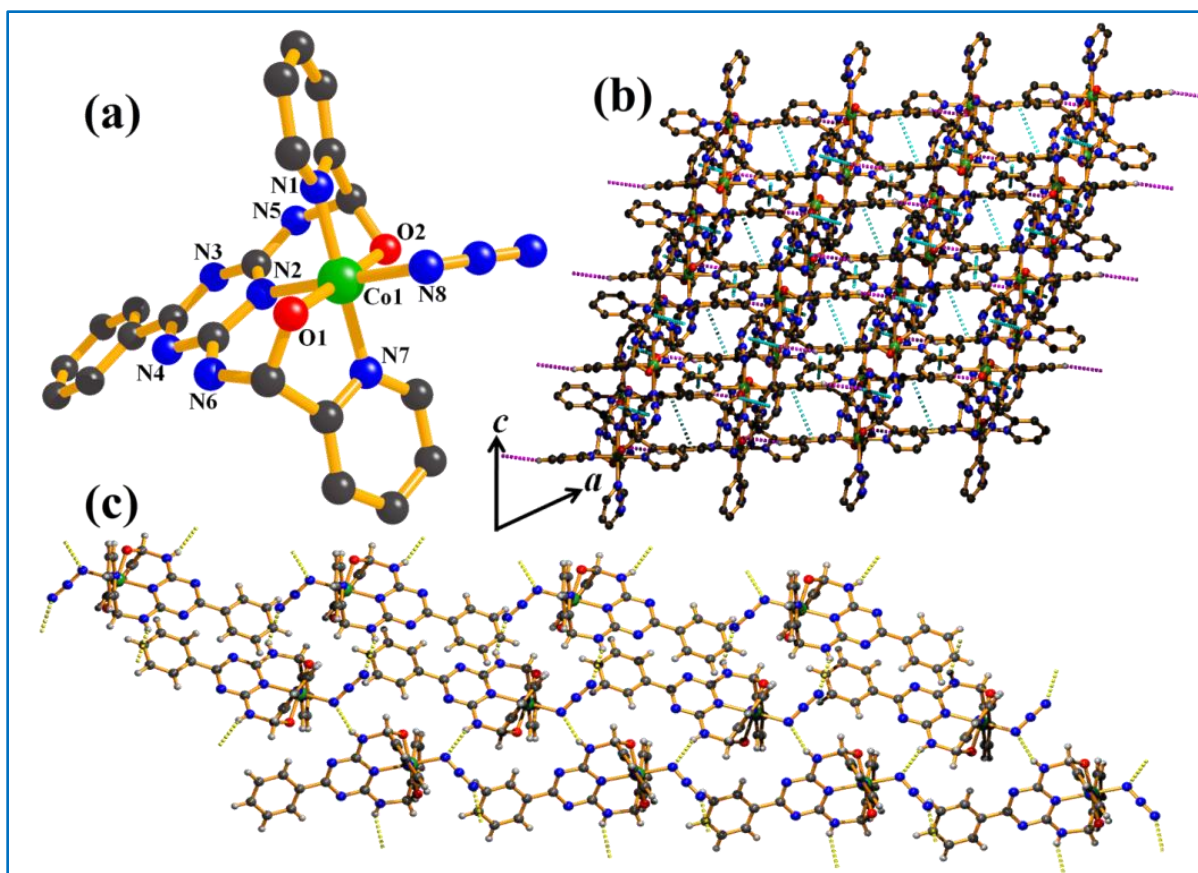


Figure 4. (a) Coordination environment around the Co(II) ions in **3**; Co (green), N (blue), O (red), C (black); (b) supramolecular 2D structure by π - π and C-H... π interaction in **3** (π - π and C-H... π interactions: magenta, cyan dotted lines respectively); (c) intermolecular hydrogen bonding interaction between hydrogen connected to triazine nitrogen and pyridyl nitrogen (H-bonding: yellow dotted lines).

Table 8. Selected bond lengths (Å) and bond angles (°) for complex **3**

Co1-O1	1.8819(17)	Co1-O2	1.8782(17)	Co1-N1	1.904(3)
Co1-N2	2.0113(19)	Co1-N7	1.910(2)	Co1-N8	1.957(2)
O1-Co1-O2	178.88(9)	O1-Co1-N1	93.89(9)	O1-Co1-N2	90.72(8)
O1-Co1-N7	84.81(9)	O1-Co1-N8	89.30(8)	O2-Co1-N1	84.99(9)
O2-Co1-N2	89.38(8)	O2-Co1-N7	96.30(9)	O2-Co1-N8	90.61(8)
N1-Co1-N2	91.05(9)	N1-Co1-N7	177.98(9)	N1-Co1-N8	89.47(10)
Co1-N8-N9	116.77(18)	N2-Co1-N7	90.52(9)	N2-Co1-N8	179.48(11)

Table 9. π - π interactions and C-H... π interaction in **3**

ring(i) \rightarrow ring(j)	distance of centroid(i) from ring(j), (Å)	dihedral angle (i,j) (deg)	distance between the (i,j) ring centroids, (Å)
R(1) \rightarrow R(1) ⁱ	3.8339(17)	5	-3.6114(12)
R(2) \rightarrow R(4) ⁱⁱ	4.0552(17)	7.28(15)	3.3919(10)
R(3) \rightarrow R(3) ⁱⁱⁱ	4.1767(16)	0	3.2718(11)
R(4) \rightarrow R(2) ⁱⁱ	4.0552(17)	7.28(15)	3.4959
C-H \rightarrow ring(j)	H...R distance (Å)	C-H...R angle (deg)	C...R distance (Å)
C(3)-H(3) \rightarrow R(2) ⁱ	2.75	161	3.644(4)

Symmetry code: i = -X,Y,3/2-Z; ii = 1/2-X,3/2-Y,1-Z; iii = X,Y,Z.

R(i)/R(j) denotes the $i^{\text{th}}/j^{\text{th}}$ rings in the corresponding structures: R(1)= N(1)C(1)C(2)C(3)C(4)C(5); R(2)= N(2)C(6)N(3)C(8)N(4)C(10); R(3)=N(7)C(17)C(18)C(19)C(20)C(21); R(4)=C(11)C(12)C(13)C(14)C(15)C(16).

Table 10. Intermolecular H-bonding interactions in **3**

D-H...A	D-H	H...A	D...A	\angle D-H...A
N5-H55...N10	0.72(3)	2.41(3)	3.040(4)	147(2)
N6-H66...N8	0.74(3)	2.26(3)	2.955(3)	157(2)

3.2. Infrared spectra

In case of complex **1** and **2** two distinct band due to azomethine (C=N) group within 1649–1573 cm^{-1} are observed (Figure 5). The lowering of the positions of the band is due to $\nu(\text{C}=\text{N})$ stretching vibration which indicates their coordination to the metal center. The presence of azide ligand is strongly determined⁴² by intense IR band at about 2000-2100 cm^{-1} . For Complex **2**, two intense bands are observed at 1545 cm^{-1} , 1405 cm^{-1} respectively which indicate $\nu_{\text{as}}(\text{COO}^-)$ and $\nu_{\text{s}}(\text{COO}^-)$ stretching frequency of fumarate ligand which is bridged between the metal centers. In case of complex **3**, a strong absorption band is observed at 2026 cm^{-1} which confirmed that the azide ligand is attached to the metal center (Figure 5). Besides these, bands at 1584, 1514, 1418 cm^{-1} are responsible for amino substituted triazine ring.

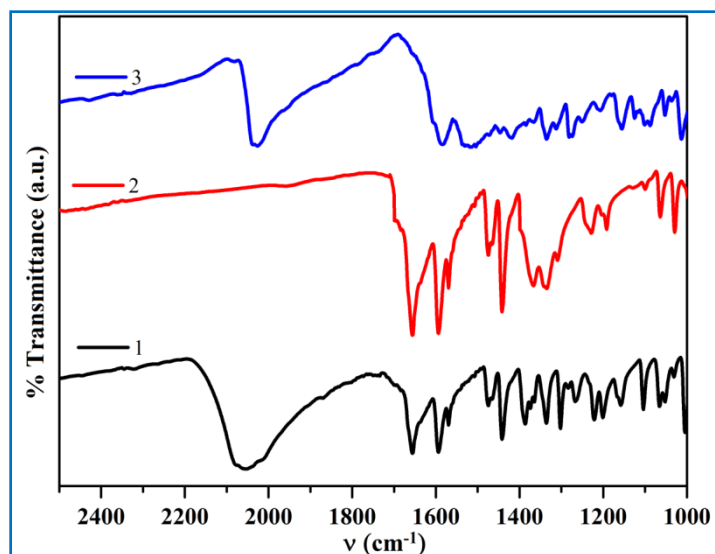


Figure 5. Selected region of IR spectra containing characteristics peaks.

3.3. Powder X-ray diffraction (PXRD)

To confirm the phase purity of the bulk materials, powder X-ray diffraction (PXRD) analysis have been carried out for **1-3** at room temperature. The experimental PXRD patterns of **1-3** are well matched with the simulated ones obtained from their corresponding single crystal structures (Figure 6), confirming the phase purity of the compounds **1-3**.

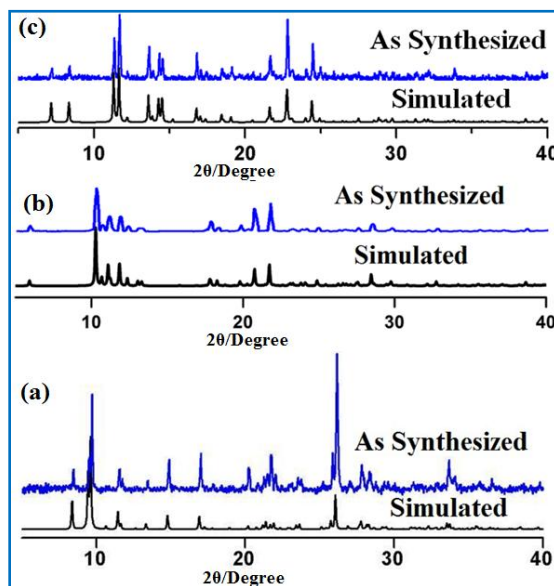


Figure 6. Powder X-ray diffraction patterns of (a) complex **1**, (b) complex **2**, and (c) complex **3**.

3.4. Solid-state absorption spectra

The UV-vis absorption spectra of complexes **1-3** have been measured in solid state at room temperature (Figure 7). The electronic transition spectra of manganese (II) complexes are very

low since the transitions from the ground state are doubly forbidden. As shown in Figures 7a, and 7b, for complexes **1** and **2**, a typical broad band at 378nm, 368nm is observed for *d-d* transitions. In case of complex **3**, a broad shoulder with bands at 710, 591, 372 nm are found respectively (Figure 7c) which is responsible for Co(II) metal complex.

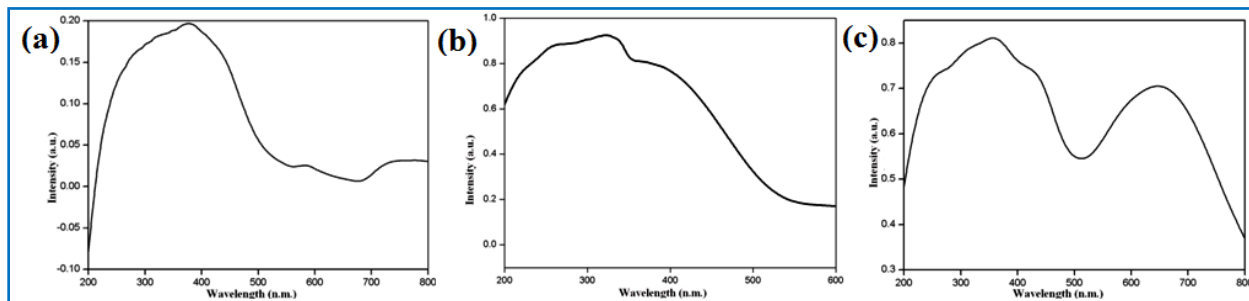


Figure 7. UV-vis absorption spectra of (a) complex **1**, (b) complex **2**, and (c) complex **3**.

4. Conclusion

In conclusion it can be ascertain that here three metal-organic complexes of Mn(II) and Co(II) has been synthesized by *in-situ* reaction with two multicomponent ligands along with azide or fumarate. The structural analysis by X-ray crystallography reveals some remarkable structural features. These compounds generate 0D or 1D structure by classical coordination bonds which extend to higher dimensions by various weak interactions. All of these major weak forces are identified and described step-wise formation of higher dimensional supramolecular structures. The complexes are also characterised with various physiochemical process like IR spectroscopy, UV-vis spectroscopy etc. Overall observation reveals that different supramolecular forces are the key factor for the formation of final architecture of the complexes. This kind of studies may helpful to synthesise weak force controlled materials which may helpful for the synthesis of biologically important materials.

Reference

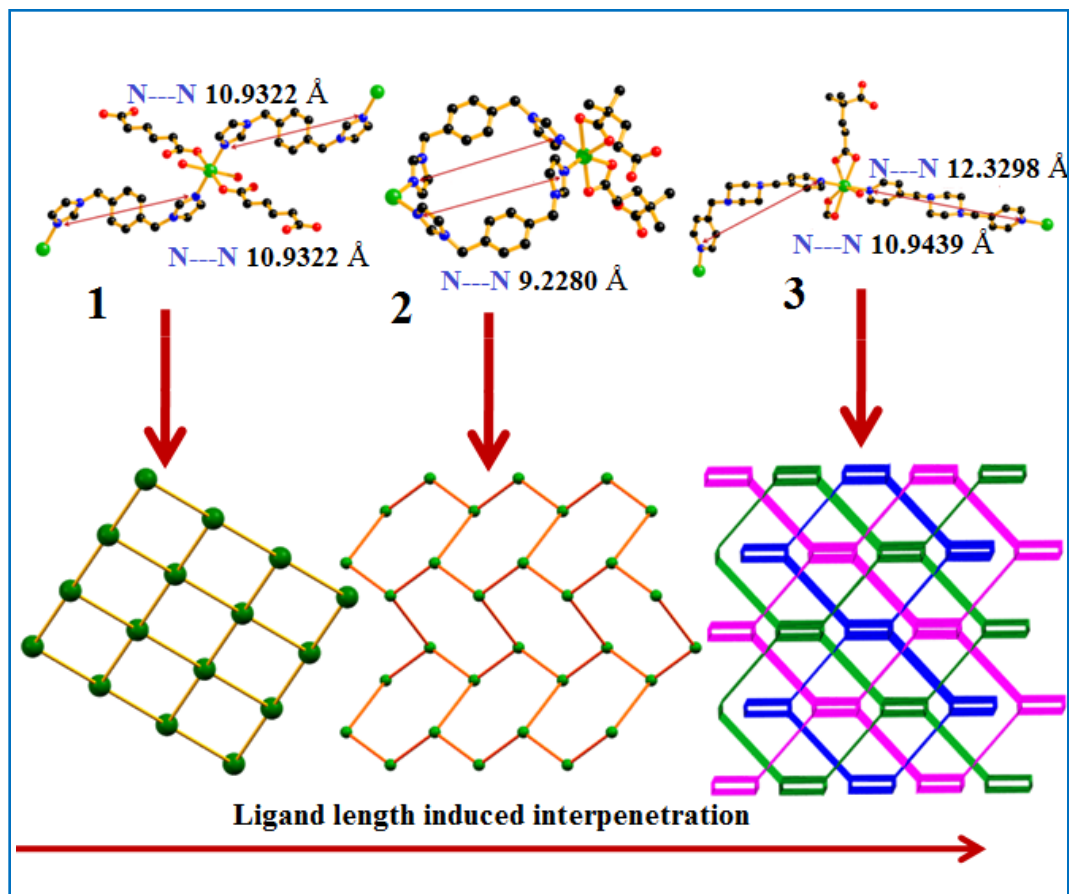
- (1) Y. Huang, T. Liu, J. Lin, J. Lü, Z. Lin and R. Cao, *Inorg. Chem.*, 2011, **50**, 2191–2198.
- (2) S. M. F. Vilela, A. D. G. Firmino, R. F. Mendes, J. A. Fernandes, D. Ananias, A. A. Valente, H. Ott, L. D. Carlos, J. Rocha, J. P. C. Tomé and F. A. A. Paz, *Chem. Commun.*, 2013, **49**, 6400–6402.
- (3) A. Bhunia, M. A. Gotthardt, M. Yadav, M. T. Gamer, A. Eichhöfer, W. Kleist and P. W. Roesky, *Chem. – Eur. J.*, 2013, **19**, 1986–1995.

- (4) B. Bhattacharya, D. K. Maity, P. Pachfule, E. Colacio and D. Ghoshal, *Inorg. Chem. Front.*, 2014, **1**, 414–425.
- (5) K. Jayaramulu, S. K. Reddy, A. Hazra, S. Balasubramanian and T. K. Maji, *Inorg. Chem.*, 2012, **51**, 7103–7111.
- (6) R. B. Getman, Y. -S. Bae, C. E. Wilmer and R. Q. Snurr, *Chem. Rev.*, 2012, **112**, 703–723.
- (7) T. A. Makal, J. R. Li, W. Lu and H. C. Zhou, *Chem. Soc. Rev.*, 2012, **41**, 7761–7779.
- (8) S. Mukherjee and P. S. Mukherjee, *Chem. Eur. J.*, 2013, **19**, 17064–17074.
- (9) J. A. Mason, M. Veenstra and J. R. Long, *Chem. Sci.*, 2014, **5**, 32–51.
- (10) L. -F. Ma, M. -L. Han, J. -H. Qin, L. -Y. Wang and M. Du, *Inorg. Chem.*, 2012, **51**, 9431–9442.
- (11) B. K. Tripuramallu, P. Manna, S. N. Reddy and S. K. Das, *Cryst. Growth Des.*, 2012, **12**, 777.
- (12) D. -S. Li, J. Zhao, Y. -P. Wu, B. Liu, L. Bai, K. Zou and M. Du, *Inorg. Chem.*, 2013, **52**, 8091–8098.
- (13) Y. -Z. Zheng, Z. Zheng and X. -M. Chen, *Coord. Chem. Rev.*, 2014, **258**, 1–15.
- (14) T. K. Maji, R. Matsuda and S. Kitagawa, *Nat. Mater.*, 2007, **6**, 142–148.
- (15) B. Manna, A. K. Chaudhari, B. Joarder, A. Karmakar, S. K. Ghosh, *Angew. Chem., Int. Ed.*, 2013, **52**, 998–1002.
- (16) D. K. Maity, B. Bhattacharya, A. Halder and D. Ghoshal, *Dalton Trans.*, 2015, **44**, 20999–21007.
- (17) B. Bhattacharya, A. Layek, M. M. Alam, D. K. Maity, S. Chakrabarti, P. P. Ray and D. Ghoshal, *Chem. Commun.*, 2014, **50**, 7858–7861.
- (18) G. Givaja, P. A. Ochoa, C. J. Gómez-García and F. Zamora, *Chem. Soc. Rev.*, 41, (2012) 115–147.
- (19) M. Yoon, K. Suh, S. Natarajan and K. Kim, *Angew. Chem. Int. Ed.*, 2013, **52**, 2688–2700.
- (20) S. S. Nagarkar, S. M. Unni, A. Sharma, S. Kurungot and S. K. Ghosh, *Angew. Chem. Int. Ed.*, 2014, **53**, 2638–2642.
- (21) D. K. Maity, K. Otake, S. Ghosh, H. Kitagawa and D. Ghoshal, *Inorg. Chem.*, 2017, **56**, 1581–1590.
- (22) G. B. Li, H. C. Fang, Y. P. Cai, Z. Y. Zhou, P. K. Thallapally and J. Tian, *Inorg. Chem.*, 2010, **49**, 7241–7243.

-
- (23) J. Heine and K. M. Buschbaum, *Chem. Soc. Rev.*, 2013, **42**, 9232–9242.
- (24) B. Bhattacharya, R. Dey and D. Ghoshal, *J. Chem. Sci.*, 2013, **125**, 661–666.
- (25) X. Zhang, Y. -Y. Huang, Q. -P. Lin, J. Zhang and Y. -G. Yao, *Dalton Trans.*, 2013, **42**, 2294–2301.
- (26) P. K. Yadav, N. Kumari, P. Pachfule, R. Banerjee and L. Mishra, *Cryst. Growth Des.*, 2012, **12**, 5311–5319.
- (27) J. -R. Li, X. -H. Bu and R. -H. Zhang, *Dalton Trans.*, 2004, 813–819.
- (28) S. Tripathi, R. Srirambalaji, S. Patra and G. Anantharaman, *CrystEngComm*, 2015, **17**, 8876–8887.
- (29) B. Zheng, H. Dong, J. F. Bai, Y. Z. Li, S. H. Li and M. Scheer, *J. Am. Chem. Soc.*, 2008, **130**, 7778–7779.
- (30) G. X. Liu, H. Xu, H. Zhou, S. Nishihara and X. M. Ren, *CrystEngComm*, 2012, **14**, 1856–1864.
- (31) N. D. Burrows, C. R. H. Hale and R. L. Penn, *Cryst. Growth Des.*, 2013, **13**, 3396–3403.
- (32) S. T. Wu, L. S. Long, R. B. Huang and L. S. Zheng, *Cryst. Growth Des.*, 2007, **7**, 1746–1752.
- (33) J. Yang, G. -D. Li, J. -J. Cao, Q. Yue, G. -H. Li and J. S. Chen, *Chem. Eur. J.*, 2007, **13**, 3248–3261.
- (34) X. -H. Bu, Y. -B. Xie, J. -R. Li and R. -H. Zhang, *Inorg. Chem.*, 2003, **42**, 7422–7430.
- (35) A. D. Garnovskii, A. L. Nivorozhkin and V. I. Minkin, *Coord. Chem. Rev.*, 1993, **126**, 1–69.
- (36) E. Q. Gao, S. Q. Bai, C. F. Wang, Y. F. Yue and C. H. Yan, *Inorg. Chem.*, 2003, **42**, 3642–3649.
- (37) B. Bhattacharya, D. Saha, D. K. Maity, R. Dey and D. Ghoshal, *CrystEngComm*, 2014, **16**, 4783–4795.
- (38) C. M. Nagaraja, R. Haldar, T. K. Maji and C. N. R. Rao, *Cryst. Growth Des.*, 2012, **12**, 975–981.
- (39) B. Bhattacharya, A. Halder, L. Paul, S. Chakrabarti and D. Ghoshal, *Chem. Eur. J.*, 2016, **22**, 14998–15005.
- (40) W. W. Sun, C. Y. Tian, X. H. Jing, Y. Q. Wang and E. Q. Gao, *Chem. Commun*, 2009, **31**, 4741–4743.
-

- (41) M. Devereux, M. McCann, V. Leon, M. Geraghty, V. McKee and J. Wikaira, *Polyhedron*, 2000, **19**, 1205–1211.
- (42) *SMART* (V 5.628), *SAINT* (V 6.45a), *XPREP*, *SHELXTL*, Bruker AXS Inc., Madison, WI, 2004.
- (43) G. M. Sheldrick, *SADABS* (Version 2.03), University of Göttingen, Germany, 2002.
- (44) G. M. Sheldrick, *SHELXS-97*, *Acta.Crystallogr.*, 2008, **A64**, 112.
- (45) A. L. Spek, *Acta.Crystallogr.*, 2009, **D65**, 148–155.
- (46) L. J. Farrugia, *J. Appl. Crystallogr.*, 1997, **30**, 565.
- (47) L. J. Farrugia, *J. Appl. Crystallogr.*, 1999, **32**, 837–838.
- (48) A. Das, G. M. Rosair, M. S. E. Fallah, J. Ribas and S. Mitra, *Inorg. Chem.*, 2006, **45**, 3295–3301.

Chapter 3



Chapter 3: Designing of three mixed ligand MOFs in searching of length induced flexibility in ligand for the creation of interpenetration

Chapter 3

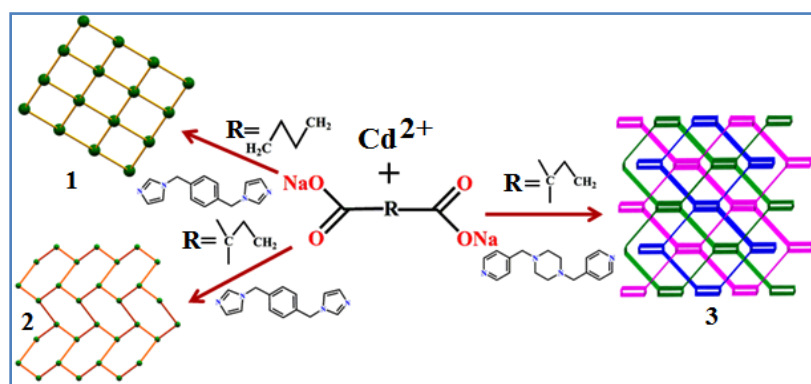
Designing of three mixed ligand MOFs in searching of length induced flexibility in ligand for the creation of interpenetration

1. Introduction

Fabrication of fascinating architecture, by interesting combination of suitable metal and ligands, is still under the limelight in the floor of modern material research principally due to the exhibition of their enthralling properties. Going towards the trend, it has been extremely relevant to design a proper pore inside a newly synthesized framework as the function of these well decorated pore/void, is important to show numerous modern and useful applications in the realm of metal organic frameworks (MOFs).¹⁻⁴ Synthesis of the resultant frameworks becomes more exciting if interpenetration⁵⁻⁸ or polycatenation⁹⁻¹¹ exist within the structure which can control the valuable application of the framework. Though interpenetrated metal organic frameworks (IMOFs) have been explored since a long time but the design and effective functionality of the interpenetrated two dimensional or three dimensional frameworks¹²⁻¹⁵ have held the same inquisitiveness to the researcher as it was in the very early days. Usually, interpenetration in MOFs are developed through two or more interlocked periodic networks where voids are occupied by one or more independent frameworks.^{16,17} To correlate the porosity and interpenetration in a MOF, it is observed that interpenetrated MOFs behave as less effective material in N₂ and CO₂ gas sorption as they possess less surface area and porosity. But recently many interpenetrated MOFs show exceptional gas separation and selectivity due to inherent dynamism in their structure, which actually affect their pore sizes¹⁸⁻²³ as well. As a result these transformable interpenetrated MOFs can display better functionalities compare to their non-interpenetrated analogue. Moreover, it has been observed that some of the interpenetrated framework also shows better hydrogen gas sorption like paddle wheel containing framework due to containing of optimum pore matched with the kinetic diameter of hydrogen molecules.^{24,25} For synthesizing interpenetrated frameworks, various factors like ligand length,²⁶⁻²⁹ ligand flexibility,³⁰⁻³³ different weak interactive forces,^{34,35} solvent,³⁶ concentration of precursors²⁹ and synthesis through sonication at various energies,³⁷ temperature,³⁸ etc. were found very important and hence considered. It has been noticed that in most of the cases, rigid ligand preferably forms

the interpenetrated structure but flexible ligand³⁰⁻³³ sometimes plays a vital role in creation of interpenetration. Additionally, ligand length is perhaps the most important factor to determine the interpenetration of a given framework among others; as having longer chain connectivity length²⁶⁻²⁹ of the ligands, the pore diameters within the structure generally increases. It actually assists the pore openings inside the framework by making available rooms for different gas adsorption. In common practice, polycarboxylates and N-donor ligands^{39,40} are used largely to produce the various functionality in the mixed ligand MOFs. Therefore introduction of long ligand with flexibility in these coligands, may increase the possibility of interpenetration or polycatenation and their void space within the structure will solely depend on the how the metal and ligands aggregate to result out a particular structure.

To understand the effect of ligand length and flexibility/rigidity on the creation of interpenetration on the structure, three MOFs, $\{\text{Cd}(\text{bix})_{0.5}(\text{adp})_{0.5}(\text{H}_2\text{O})\}_n$ (**1**), $\{[\text{Cd}(\text{bix})(2,2'\text{-dmglu})](\text{H}_2\text{O})\}_n$ (**2**) and $\{\text{Cd}(\text{bpmp})(2,2'\text{-dmglu})(\text{H}_2\text{O})\}_n$ (**3**) by using two different N,N-donor linkers bix {bix = 1,4-bis(imidazol-1-ylmethyl)-benzene}, bpmp { bpmp = 1,4-bis(4-pyridinylmethyl)piperazine} and two different substituted dicarboxylate adp {adp = adipate}, 2,2'-dmglu {2,2'-dmglu = 2,2'-dimethylglutarate} has been synthesized. All three MOFs have been characterized by single-crystal X-ray diffraction along with other physicochemical methods. Out of three complexes, only **3** shows interpenetration (Scheme 1). Along with the variation of the aliphatic moiety of dicarboxylate ligands, N,N-donor linkers have also been varied from rigid bix to long length, flexible bpmp ligand to study the effect of longer ligand and



Scheme 1. Schematic presentation for the synthesis of three MOFs.

flexibility on final structural outcome. This ligand variation effects on their sorption properties which has been described here by correlating their structural architecture. Average distance

between two donor atoms of N,N-donor linkers in the three complexes may be responsible for interpenetration in the said structure. Different gas adsorption experiments have been performed for all three MOFs.

2. Experimental section

2.1. Materials and methods

Highly pure metal salts cadmium (II) nitrate tetrahydrate, the required acids 2,2'-dimethylglutaric acid (2,2'-dmglu) and adipic acid (adp) have been obtained from Sigma-Aldrich Chemical Co. Inc. The other materials for the preparation of reported ligand synthesis bix^{41,42} and bpmp^{43,44} viz. imidazole, 1,4-bis(chloromethyl)benzene, piperazine, 4-(chloromethyl)pyridine hydrochloride have also been purchased from Sigma-Aldrich Chemical Co. Inc. Sodium salt for all the acids have been prepared by neutralizing it with Na₂CO₃ in 1:1 ratio and the neutralization process has been checked by measuring pH of the mixture. Other required materials and solvents are of AR grade and have been used without further purification.

2.2. Physical measurements

Using a Heraeus CHNS analyzer the elemental analyses (carbon, hydrogen, and nitrogen) have been carried out for all the complexes. The Infrared spectra have been measured in the 4000-400 cm⁻¹ region by a PerkinElmer Spectrum BX-II IR spectrometer, preparing KBr pellets for all the complexes. X-ray powder diffraction (PXRD) patterns of the as-synthesized complexes have been recorded in a Bruker D8 Discover instrument where Cu-K α radiation has been used. Thermal analysis (TGA) and stability of the complexes have been checked by a PerkinElmer Simultaneous Thermal Analyzer (STA 8000) under nitrogen atmosphere (flow rate: 50 cm³ min⁻¹), at a temperature range of 30–600 °C with a heating rate of 2 °C min⁻¹.

2.3. Sorption measurements

Using a Quantachrome Autosorb–iQ adsorption instrument, N₂ (77 K), CO₂ (195 K) and H₂ (77 K) adsorption isotherms have been measured for the dehydrated frameworks of **1–3**. Highly pure N₂ gas (99.999% purity), CO₂ gas (99.95%) and H₂ gas (99.999%) have been used for this measurement. The N₂ (at 77 K, liquid nitrogen bath), CO₂ (at 195 K, dry ice-acetone bath) and H₂ (at 77 K, liquid nitrogen bath) sorption measurements have been performed in the pressure range 0–1 bar using dehydrated samples of all the complexes. Before measurements, all the as-synthesized complexes (40 mg for each) have been dehydrated taking them in the sample tube at 413 K for 3 h under a 1 \times 10⁻¹ Pa vacuum. Controlled introducing ultra pure helium gas (99.999%

purity) into the sample tube and allowing it to diffuse into the sample has been done to measure the dead volume. The gas adsorption volume for each and every measurement has been calculated from the difference of pressure ($P_{\text{cal}} - P_e$), where P_{cal} signifies the calculated pressure without any gas adsorption and P_e indicates the observed pressure at equilibrium.

2.4. Syntheses

2.4.1. Synthesis of ligand {1,4-bis(imidazol-1-ylmethyl)-benzene} (bix)

The ligand bix has been synthesized according to modified procedure from literature.^{41,42} A mixture of imidazole (0.6808 g, 10 mmol) and KOH (~1.68 g, ~30 mmol) has been stirred in 30 mL of DMSO at 60 °C for 2 hrs. Then, 1,4-bis(chloromethyl)benzene (6.05 g, 5 mmol) has been added into the mixture drop wise and stirred at 50 °C for 4 hrs. After that, the reaction mixture has been allowed to cool to room temperature (30 °C). Then reaction mixture has been stirred with 300 mL of water and the crude product has been collected in DCM solvent by using separating funnel. The DCM part has been kept in room temperature (30 °C) for slow evaporation. Yellow crystalline product has been obtained after 1-2 days.

2.4.2. Synthesis of ligand {1,4-bis(4-pyridinylmethyl)piperazine} (bpmp)

This ligand has been synthesized using piperazine hexahydrate and 4-(chloromethyl)pyridine hydrochloride following a previously reported procedure.^{43,44} To a solution of NaOH (0.16g, 4mmol) and piperazine hexahydrate (0.194g, 1mmol) in 20 ml water, 4-chloromethylpyridine hydrochloride (0.328g, 2mmol) in 5 ml water has been added with constant stirring until the pH decreased to 8-9. The resultant deep red solution has been refluxed in an open beaker for two hours with the volume of the solution has been reduced. Finally, white product is formed, and it has been crystallized from a minimum amount of methanol after 1 day.

2.4.3. Synthesis of complex {Cd(bix)_{0.5}(adp)_{0.5}(H₂O)}_n (1)

Adipate (adp) salt (1mmol, 0.190 g) has been dissolved in 10 mL of water to prepare an aqueous solution of that salt which has been slowly added to the methanolic solution (10 mL) of the synthesized 1,4-bis(imidazol-1-ylmethyl)benzene (bix) (1mmol, 0.238 g). The resulting solution has been stirred for 20 mins to have homogeneous mixture. Then the metal salt of Cd(NO₃)₂·4H₂O (1 mmol, 0.308 g) has been dissolved in a separate beaker in 10 mL of water. After that, 2 ml of Cd(II) solution has been slowly and carefully layered followed by 4 ml of above mentioned mixed-ligand solution in a crystal tube. A buffer mixture, by mixing H₂O and MeOH in 1:1 ratio, has been used in junction to separate the mixed ligand solution and the

aqueous solution of metal. Finally, the tube has been kept sealed and undisturbed at room temperature. The white colored block shaped crystals has obtained after 5-6 weeks. The single crystals have been separated and washed for characterization (Yield 58%). Anal. Calc. for $C_{21}H_{26}N_4O_5Cd$ (**1**, %): C, 47.87; H, 4.97; N, 10.63. Found: C, 47.85; H, 4.96; N, 10.58. IR spectra (in cm^{-1}): $\nu(CH-Ar)$, 3085-3160; $\nu(H_2O)$, 3403; $\nu(C=C-Ar)$, 1530; $\nu(C-N-Ar)$, 1245; $\nu(C-N)$, 1071; $\nu(C-H, alkane)$, 2684 (stretch) 1311 (bending); $\nu(C=O)$, 1896 (stretch) and $\nu(C-O)$, 1228 (stretch) (Figure 1a).

2.4.4. Synthesis of complex $\{[Cd(bix)(2,2'-dmglu)](H_2O)\}_n$ (**2**)

Following the procedure of **1**, this complex has also been synthesized by varying 2,2'-dimethylglutarate ($2,2'-dmglu^{2-}$) (1 mmol, 0.204 g) in place of adipate (adp) salt (1mmol, 0.190 g). The off-white block shaped crystals have obtained after 3-4 weeks which has been suitable for characterization. The crystals have been separated from the solution and collected (Yield 62%). Anal. Calc. for $C_{20}H_{26}N_4O_6Cd$ (**2**, %): C, 45.25; H, 4.94; N, 10.55. Found: C, 45.23; H, 4.92; N, 10.54. IR spectra (in cm^{-1}): $\nu(CH-Ar)$, 3085-3160; $\nu(C=C-Ar)$, 1530; $\nu(H_2O)$, 3403; $\nu(C-N-Ar)$, 1245; $\nu(C-N)$, 1071; $\nu(C-H, alkane)$, 2684 (stretch) 1311 (bending); $\nu(C=O)$, 1896 (stretch) and $\nu(C-O)$, 1228 (stretch) (Figure 1b).

2.4.5. Synthesis of complex $\{Cd(bpmp)(2,2'-dmglu)(H_2O)](H_2O)\}_n$ (**3**)

Complex **3** has been synthesized following the same procedure as described in **1**. Here 1,4-bis(4-pyridinylmethyl)piperazine (bpmp) (1 mmol, 0.268 g) has been used in place of 1,4-bis(imidazol-1-ylmethyl)benzene (bix). The off-white colored needle shaped crystals suitable for X-ray diffraction analysis has obtained after 3-4 weeks. The crystals have been separated and washed with a methanol-water (1:1) mixture and dried under air (Yield 70%). Anal. Calc. for $C_{92}H_{136}N_{16}O_{24}Cd_4$ (**3**, %): C, 48.05; H, 5.96; N, 9.74. Found: C, 48.05; H, 5.95; N, 9.73. IR spectra (in cm^{-1}): $\nu(CH-Ar)$, 3085-3160; $\nu(H_2O)$, 3403; $\nu(C=C-Ar)$, 1530; $\nu(C-N-Ar)$, 1245; $\nu(C-N)$, 1071; $\nu(C-H, alkane)$, 2684 (stretch) 1311 (bending); $\nu(C=O)$, 1896 (stretch) and $\nu(C-O)$, 1228 (stretch) (Figure 1c).

Purity of all complexes has been checked by measuring solid state PXRD of the complexes at room temperature. Other techniques like elemental analysis and IR spectra of the complexes have further been performed to prove the purity of the bulk samples. The data obtained for all of these methods are in complete agreement with the single crystal data.

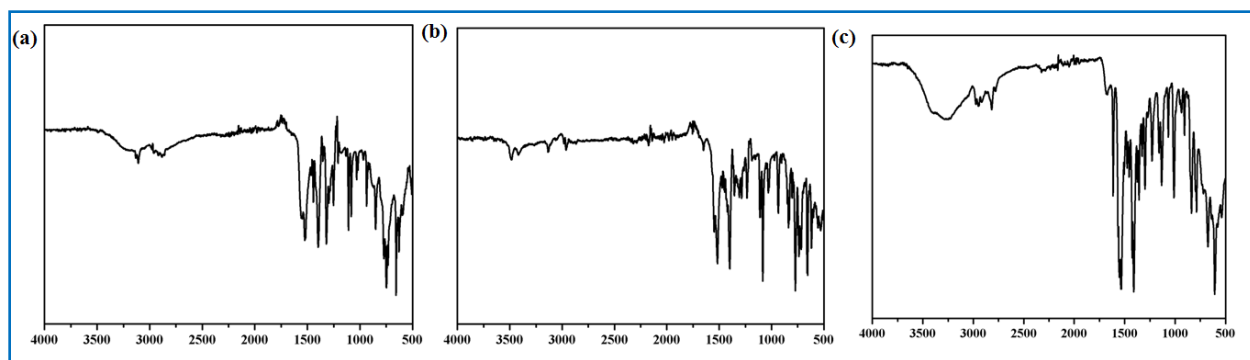


Figure 1. ATR spectra of (a) complex **1**, (b) complex **2**, and (c) complex **3**.

2.5. Crystallographic data collection and refinement

For data collection, the single crystals of all complexes have been mounted on the tips of glass fibers using commercial glue. Single crystal XRD for all the complexes have been performed using Bruker APEX II diffractometer which is equipped with a normal focus sealed tube X-ray source having graphite monochromated Mo-K α radiation ($\lambda = 0.71073 \text{ \AA}$). The collected data have been integrated using SAINT⁴⁵ program and the absorption corrections have been performed with SADABS.⁴⁶ The structures have been solved by SHELXS-2016.⁴⁷ The full-matrix least-squares refinements have been carried out on F^2 for all non-hydrogen atoms using with anisotropic displacement parameters also done by using SHELXL-2016.⁴⁷ All the hydrogen atoms were fixed geometrically by HFIX command and are placed in ideal positions. For complex **1**, carbon molecules C2 and C3 of the dicarboxylate moiety are found disordered. They have been refined isotropically without fixing H atoms on them and by fixing their occupancy at 0.5. For complex **2** the O atom of guest solvent water molecule is disordered and that has also been refined anisotropically without fixing H atoms on it. For complex **3** the guest solvent water molecule is disordered and that has been refined isotropically without fixing H atoms on it. All of these hydrogen atoms are considered and added to the molecular formula (Table 1). Calculations were carried out using SHELXS-2016,⁴⁷ SHELXL-2016,⁴⁷ PLATON v1.15,⁴⁸ WinGX system Ver-1.80,⁴⁹ DIAMOND,⁵⁰ TOPOS v3.2,^{51,52} and Mercury v3.0⁵³. Data collection and structure refinement parameters and crystallographic data for all the complexes are given in Table 1. The selected bond lengths and angles are given in Tables 2, 5, and 7.

Table 1. Crystallographic and structural refinement parameters for complexes **1-3**

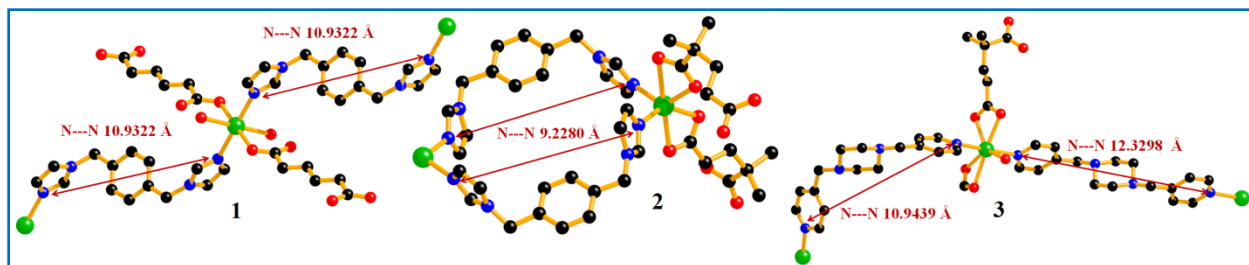
	1	2	3
formula	C ₂₀ H ₂₆ N ₄ O ₆ Cd	C ₂₁ H ₂₆ N ₄ O ₅ Cd	C ₉₂ H ₁₃₆ N ₁₆ O ₂₄ Cd ₄
formula weight	530.85	526.87	2299.81
crystal system	triclinic	monoclinic	monoclinic
space group	<i>P</i> $\bar{1}$	<i>P</i> 2 ₁ / <i>n</i>	<i>C</i> 2/ <i>c</i>
<i>a</i> /Å	5.5838(4)	9.4347(9)	13.4488(5)
<i>b</i> /Å	8.4023(7)	21.862(2)	26.3886(9)
<i>c</i> /Å	11.9976(9)	10.7267(10)	15.7329(6)
α /°	91.135(2)	90	90
β /°	95.422(2)	94.152(3)	109.240(2)
γ /°	106.082(2)	90	90
<i>V</i> /Å ³	537.82(7)	2206.7(4)	5271.7(3)
<i>Z</i>	1	4	2
<i>D</i> _c /g cm ⁻³	1.614	1.580	1.444
μ /mm ⁻¹	1.059	1.029	0.871
<i>F</i> (000)	262	1064	2352
θ range/°	1.7 - 27.6	1.9 - 27.6	1.8 - 27.6
reflections collected	17539	75977	42915
unique reflections	2485	5102	6066
reflections <i>I</i> > 2 σ (<i>I</i>)	2482	4565	5221
<i>R</i> _{int}	0.070	0.040	0.030
goodness-of-fit (<i>F</i> ²)	1.09	1.08	1.06
<i>R</i> 1 (<i>I</i> > 2 σ (<i>I</i>)) ^[a]	0.0311	0.0277	0.0275
<i>wR</i> 2(<i>I</i> > 2 σ (<i>I</i>)) ^[a]	0.0837	0.0806	0.0762
$\Delta\rho$ min / max /e Å ³	-0.58, 1.02	-0.31, 0.50	-0.40, 1.13

$$^{[a]}R_1 = \sum ||F_o| - |F_c|| / \sum |F_o|, wR_2 = [\sum (w(F_o^2 - F_c^2))^2 / \sum w(F_o^2)^2]^{1/2}.$$

3. Results and discussion

3.1. Structural description of the complexes

Before describing the structure of the complexes it is important to note the distance between two donor atoms of same N,N-donor linkers in all three complexes calculated from the single crystal X-ray structures of the respective complexes and are shown in Scheme 2. It has been observed that the average linear separation between two donor atoms of bpmp ligand in complex **3** is greater than that of other two complexes. In other words in complex **3** the lengths of N-N donor connectivity among the three complexes is largest.



Scheme 2. Different linear distances between two donor atoms in complex **1**, **2**, and **3**.

3.1.1. Crystal structure of $\{\text{Cd}(\text{bix})_{0.5}(\text{adp})_{0.5}(\text{H}_2\text{O})\}_n$ (**1**)

According to the single crystal structural analysis this complex crystallizes in triclinic $P\bar{1}$ space group. Complete structural analysis reveals that the complex forms 2D structure by the combination of Cd(II) metal ion with N,N'-donor ligand bix and the co-ligand adipate. The asymmetric unit contains one Cd(II) ion, half bix ligand, half adipate and one coordinated water molecule. Here the Cd(II) center possesses CdO_4N_2 environment which clearly implies that the metal center constructs distorted octahedral geometry. Four oxygen atoms (O1 , O1^a , O1W , O1W^a) from two different symmetry related adipate dicarboxylate and two symmetry related coordinated water molecules are associated to the metal center and two nitrogen atoms (N1 , N1^a) from two different bix ligands have been linked to the Cd(II) ion to build this hexa coordinated center (Figure 2a). Linear distance between two donor atoms (N) of same bix ligand linked to the Cd(II) metal center in the crystal is 10.9322(52) Å (Scheme 2). The Cd–O bond lengths are varying from 2.314(3) to 2.372(3) Å and the Cd–N bond lengths is 2.277(3) Å (Table 2). Each dicarboxylate attaches two metal centers through monodentate bridging mode and finally construct 1D metal adipate chain (Figure 2b). These 1D chains are further bridged by the N,N'-donor bix ligands along bc plane to form final 2D structure (Figure 2c). These 2D stairs are stacked by intermolecular H-bonding, π – π and $\text{C–H}\cdots\pi$ interactions to execute a supramolecular 3D structure (Figure 2d and Tables 3 and 4). The topological structural analysis of the complex indicates that it forms a 4-c uninodal net and the corresponding Schläfli symbol for the net is $\{4^4.6^2\}$ (Figure 2e).

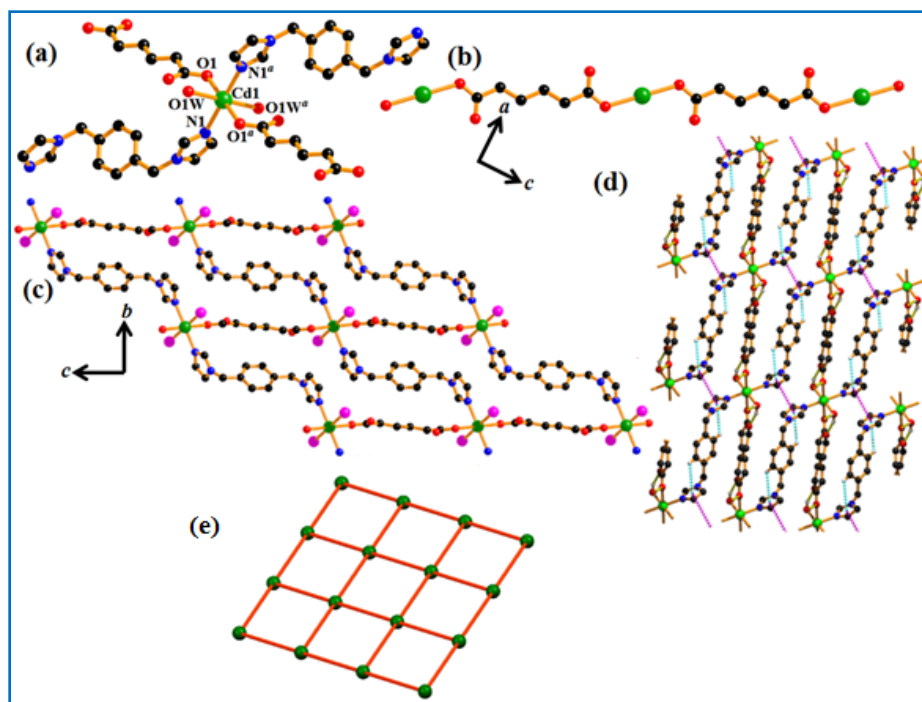


Figure 2. (a) Coordination environment of hexa coordinated Cd(II) center in complex **1**; where the color of Cd, O, N and C are green, red, blue and black respectively. (b) 1D metal–adp chain in **3** along the *a* axis. (c) 2D framework along the *bc* plane in **1**. (d) π – π (magenta), C–H $\cdots\pi$ (cyan) and hydrogen bonding (yellow) interactions form 3D supramolecular structure of complex **1**. (e) Simplified topological representation of 4-c uninodal net in **1**.

Table 2. Selected bond Lengths (Å) and bond angles (°) for **1**

Cd1–O1	2.313(2)	Cd1–O1W	2.367(2)
Cd1–N1	2.276(2)	Cd1–O1 ^a	2.313(2)
Cd1–O1W ^a	2.367(2)	Cd1–N1 ^a	2.276(2)
O1–Cd1–O1W	88.49(8)	O1–Cd1–N1	88.89(9)
O1–Cd1–O1 ^a	180.00	O1–Cd1–O1W ^a	91.51(8)
O1–Cd1–N1 ^a	91.11(9)	O1W–Cd1–N1	91.82(9)
O1 ^a –Cd1–O1W	91.51(8)	O1W–Cd1–O1W ^a	180.00
O1W–Cd1–N1 ^a	88.18(9)	O1 ^a –Cd1–N1	91.11(9)
O1W ^a –Cd1–N1	88.18(9)	N1–Cd1–N1 ^a	180.00
O1 ^a –Cd1–O1W ^a	88.49(8)	O1 ^a –Cd1–N1 ^a	88.89(9)
O1W ^a –Cd1–N1 ^a	91.82(9)		

Symmetry code: *a* = 2–*x*, –*y*, 2–*z*.

Table 3. Intermolecular π - π & C-H... π interactions in **1**

ring(i) \rightarrow ring(j)	distance of centroid(i) from ring(j), (Å)	dihedral angle (i,j) (deg)	distance between the (i,j) ring centroids, (Å)
R(1) \rightarrow R(1) ⁱ	3.7678(19)	0	3.4423(14)
C-H ring(j)	H...R distance (Å)	C-H...R angle (deg)	C...R distance (Å)
C(10)-H(10) \rightarrow R(1) ⁱⁱ	2.95	121	3.521(4)

Symmetry code: i = 2-X, 1-Y, 2-Z, ii = X, Y, Z.

R(i)/R(j) denotes the ith/jth rings in the corresponding structures: R(1) = N1/C4/C6/N2/C5.**Table 4.** Intermolecular H-bonding interactions in **1**

D-H...A	D-H	H...A	D...A	\angle D-H...A
O1W-H1WA...O1 ⁱ	0.80	1.96	2.755(3)	174
O1W-H1WB...O2	0.84	1.87	2.653(3)	155

Symmetry code: i = 1+x, y, z.

3.1.2. Structural description of $\{[\text{Cd}(\text{bix})(2,2'\text{-dmglu})](\text{H}_2\text{O})\}_n$ (2**)**

Structural analysis by single crystal X-Ray indicates that it crystallizes in monoclinic $P2_1/n$ space group and confirms the construction of two dimensional structure by the combination of the 2,2'-dimethylglutarate and the bix ligands with the Cd(II) metal center. The asymmetric unit in this case possess one Cd(II) metal, one 2,2'-dimethylglutarate, one bix ligand and one lattice water molecule. The hexa coordinated Cd(II) center forms CdO_4N_2 environment around the metal and achieves distorted octahedral geometry centering the Cd(II) ion. Four oxygen atoms (O1, O2, O3^b and O4^b) from two different 2,2'-dimethylglutarate has been ligated and two nitrogen atoms (N1 and N4^a) from two bix ligands has been attached to the metal center which makes the Cd(II) center hexa coordinated (Figure 3a). Here the linear separation between two donor atoms (N) of same bix ligand linked to the Cd(II) metal center is 9.2880 (28) Å (Scheme 2). The Metal-O bond lengths lie between the range of 2.2338(19) to 2.645(2) Å and the metal-N bond length varies from 2.229(2) to 2.263(2) Å for this complex (Table 5). The dicarboxylate 2,2'-dimethylglutarate bridges with two separate metal centers from the opposite ends through bidentate bridging mode from the both sides and this metal acid binding finally constructs a 1D angular chain along crystallographic *a* axis (Figure 3b). This 1D chains being attached by the

N,N'-donor ligand bix finally builds a 2D framework where the lattice water molecules are accommodated inside the pore of the structure (Figure 3c). This 2D framework undergoes π - π interactions to form supramolecular three dimensional structures (Figure 3d and Table 6). Without the water molecules the total solvent accessible void value estimated by PLATON is 83 \AA^3 which is 3.76% of the total crystal volume of 2206.7 \AA^3 . The topology of the structure indicates the formation of 3-c uninodal net with the corresponding Schläfli symbol $\{6^3\}$ (Figure 3e).

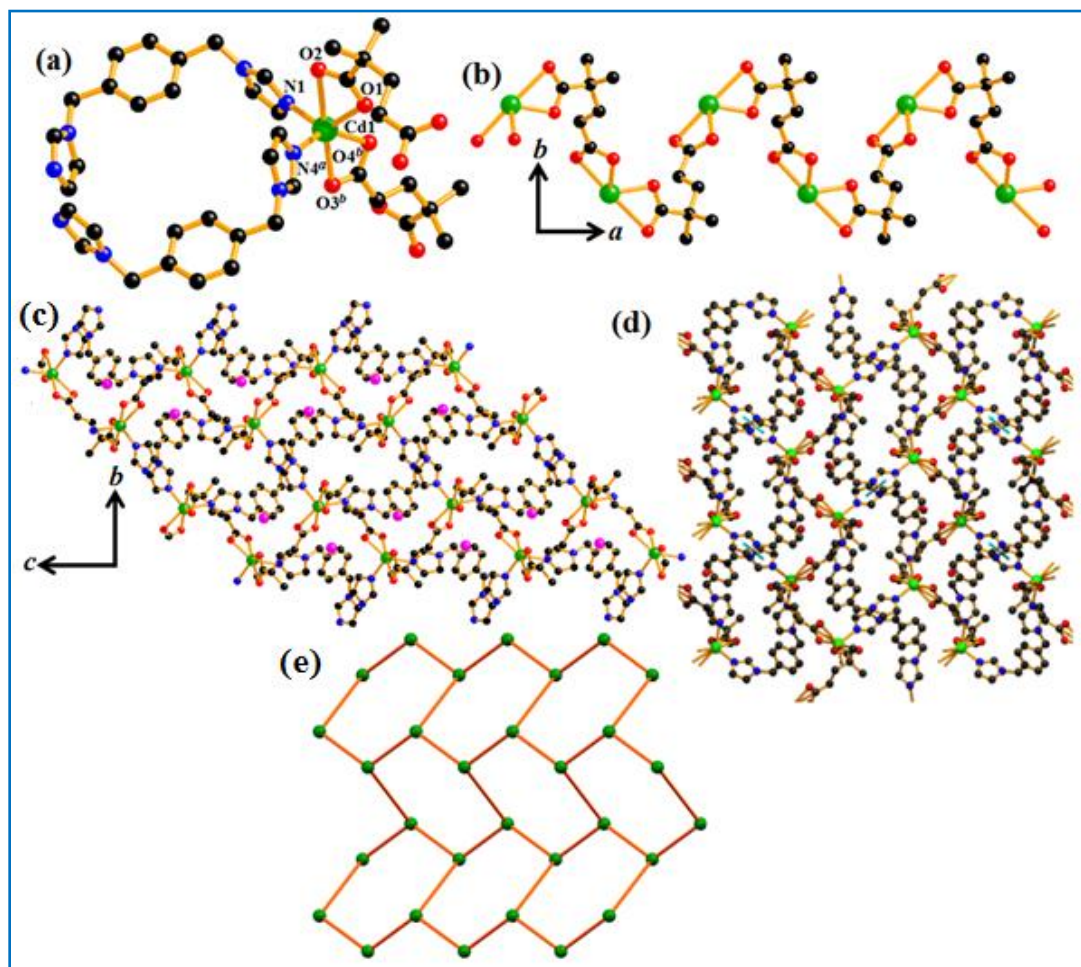


Figure 3. (a) Coordination environment of hexa coordinated Cd(II) center in complex **2**; where the color of Cd, O, N and C are green, red, blue and black respectively. (b) 1D zig-zag metal–2,2'-dmglut chain in **2** along the a axis. (c) 2D framework along the bc plane in **2**. (d) π - π (cyan) interactions form supramolecular structure of complex **2**. (e) Simplified topological representation of 3-c uninodal net in **2**.

Table 5. Selected bond lengths (Å) and bond angles (°) for **2**

Cd1–O1	2.2338(19)	Cd1–O2	2.645(2)
Cd1–N1	2.229(2)	Cd1–N4 ^a	2.263(2)
Cd1–O3 ^b	2.379(2)	Cd1–O4 ^b	2.3652(19)
O1–Cd1–O2	52.55(7)	O1–Cd1–N1	129.59(7)
O1–Cd1–N4 ^a	92.63(7)	O1–Cd1–O3 ^b	124.11(7)
O1–Cd1–O4 ^b	92.90(7)	O2–Cd1–N1	83.35(7)
O2–Cd1–N4 ^a	84.28(7)	O2–Cd1–O3 ^b	174.92(6)
O2–Cd1–O4 ^b	127.23(6)	N1–Cd1–N4 ^a	107.49(7)
O3 ^b –Cd1–N1	101.28(7)	O4 ^b –Cd1–N1	97.18(7)
O3 ^b –Cd1–N4 ^a	92.28(7)	O4 ^b –Cd1–N4 ^a	142.45(7)
O3 ^b –Cd1–O4 ^b	54.66(7)		

Symmetry code: $a = x, y, z$; $b = 0.5-x, 0.5+y, 1.5-z$.**Table 6.** Intermolecular π – π interactions in **2**

ring(i) \rightarrow ring(j)	distance of centroid(i) from ring(j), (Å)	dihedral angle (i,j) (deg)	distance between the (i,j) ring centroids, (Å)
R(1) \rightarrow R(1) ⁱ	4.1063(15)	0	3.3286(11)

Symmetry code: $i = -x, -y, -z$.

R(i)/R(j) denotes the $i^{\text{th}}/j^{\text{th}}$ rings in the corresponding structures: R(1) = N(1)/C(8)/N(2)/C(10)/C(9).

3.1.3. Structural description of $[\{\text{Cd}(\text{bpmp})(2,2'\text{-dmglu})(\text{H}_2\text{O})\}(\text{H}_2\text{O})]_n$ (**3**)

This complex crystallizes in monoclinic $C2/c$ space group which is proved from single-crystal structural analysis. Proper aggregation of Cd(II) metal ion with both the N,N'-donor bpmp linker and the dicarboxylate 2,2'-dimethylglutarate finally construct the complete structure. Asymmetric unit of the complex has one Cd(II) ion, one bpmp ligand and one 2,2'-dimethylglutarate as coligand, one coordinated and one lattice water molecules. Here, the metal centre possesses a distorted pentagonal bipyramidal geometry where five oxygen atoms (O1, O2, O3^a, O4^a, O1W) from two different 2,2'-dimethylglutarate centers and one coordinated water molecule forms the basal plane and two nitrogen atoms (N1 and N3) from two different bpmp ligands have also been ligated to the metal center to fill up the coordination sites (Figure 4a). This type of coordination helps Cd(II) centers to adopt CdO₅N₂ environment where the oxygen

atoms of the 2,2'-dimethylglutarate bridges the metal centers from the two opposite sides. Linear distances between two donor atoms (N) of same bpmp ligand linked to the Cd(II) metal center in the crystal are 10.9439(30) Å and 12.3298(29) Å (Scheme 2). The Cd–O bond lengths vary from 2.3529(18) to 2.4477(17); whereas the Cd–N bond lengths differ from 2.333(2) to 2.343(2) Å (Table 7). Each 2,2'-dimethylglutarate has been attached with two Cd(II) centers where the oxygen atoms of the dicarboxylate exhibits bridging binding mode for both the metal centers. This metal and 2,2'-dimethylglutarate binding finally forms a 1D zigzag chain (Figure 4b). and these 1D chains are further linked by the bpmp ligands in two different ways which finally produces 3D structure where the lattice water molecules lie along the *a*-axis constructing 1D channel of water molecules (Figure 4c). Without the water molecules the total solvent accessible void value estimated by PLATON is 204 Å³ which is 3.87% of the total crystal volume of 5271.7 Å³. The topological analysis of the complex depicts that the complex possesses a 3D framework with three fold interpenetrating net where Zt=3; Zn=1. The corresponding Schläfli symbol for the net is {4².6³.8} (Figure 4d). As mentioned before, the greater extent of flexibility of bpmp ligand may have facilitated the interpenetration in this structure in contrast to the previous two.

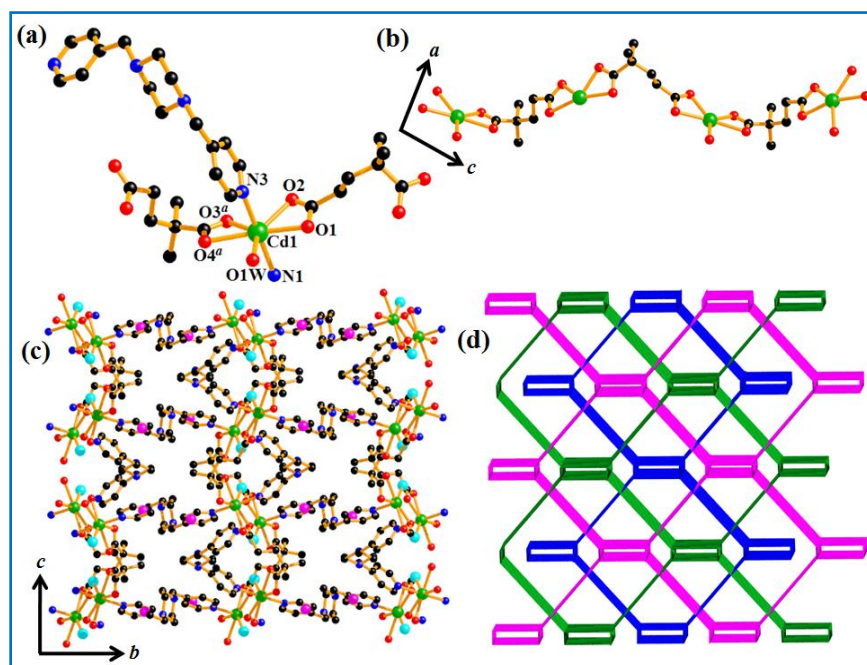


Figure 4. (a) Coordination environment of hexa coordinated Cd(II) center in complex **3**; where the color of Cd, O, N and C are green, red, blue and black respectively. (b) 1D metal–2,2'-dmglu chain in **3** along the *a* axis. (c) 3D framework in **3**. (d) Simplified topological representation of three fold interpenetrating net in **3**.

Table 7. Selected bond lengths (Å) and bond angles (°) for **3**

Cd1–O1	2.4477(17)	Cd1–O1W	2.340(2)
Cd1–O2	2.3578(17)	Cd1–N1	2.333(2)
Cd1–N3	2.343(2)	Cd1–O3 ^a	2.3529(18)
Cd1–O4 ^a	2.5055(17)	O1–Cd1–O1W	83.77(6)
O1–Cd1–O2	54.35(6)	O1–Cd1–N1	85.34(6)
O1–Cd1–N3	92.53(7)	O1–Cd1–O3 ^a	142.90(6)
O1–Cd1–O4 ^a	163.50(6)	O1W–Cd1–O2	136.81(7)
O1W–Cd1–N1	86.42(7)	O1W–Cd1–N3	87.73(7)
O1W–Cd1–O3 ^a	133.18(6)	O1W–Cd1–O4 ^a	80.68(6)
O2–Cd1–N1	98.81(7)	O2–Cd1–N3	84.45(7)
O2–Cd1–O3 ^a	89.62(6)	O2–Cd1–O4 ^a	139.20(6)
N1–Cd1–N3	173.96(8)	O3 ^a –Cd1–N1	92.78(7)
O4 ^a –Cd1–N1	99.11(7)	O3 ^a –Cd1–N3	92.33(7)
O4 ^a –Cd1–N3	81.41(6)	O3 ^a –Cd1–O4 ^a	53.19(5)

Symmetry code: $a = 0.5+x, 0.5-y, 0.5+z$.

3.2. Powder X-ray diffraction (PXRD)

The phase purity for bulk amount of all the synthesized complexes have been checked by performing powder X-ray diffraction (PXRD) analysis at ambient temperature. For all the complexes the as-synthesized pattern completely overlaps with the simulated pattern indicating almost exact matching for all the characteristics peaks. It clearly proves the phase purity for complexes **1–3** (Figure 5).

3.3. Thermogravimetric analysis (TGA)

TGA experiments of all the complexes **1–3** have been performed to study the thermal stability. All the TGA curves have been depicted in Figure 6. For the complex **1** one coordinated water has been removed at 120 °C by exhibiting 3.3% weight loss (calcd 3.4%). The framework is quite stable after that, up to 290 °C and finally dissociates into unknown products as a result of further heating (Figure 6a). For complex **2** one lattice water has been removed at 55 °C by exhibiting 3.31% weight loss (calcd 3.42%). The framework is quite stable up to 290 °C after the removal of water and finally dissociates into unknown products with further heating (6b). In case of the TGA of complex **3**, it is observed that the complex starts to lose weight from 67.5 °C and the

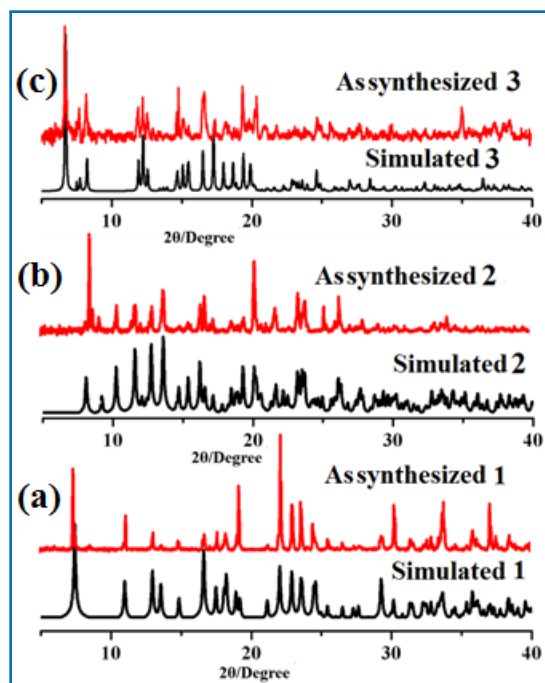


Figure 5. Powder X-ray diffraction patterns of (a) complex **1**, (b) complex **2**, and (c) complex **3**. process has been completed at 121.5 °C by exhibiting 6.32% loss (calcd 6.26%). This weight loss indicates the elimination of one lattice and one coordinated water from the structure and the resulting dehydrated framework is stable up to 280 °C. After this temperature it disintegrates into unidentified product with further heating (Figure 6c).

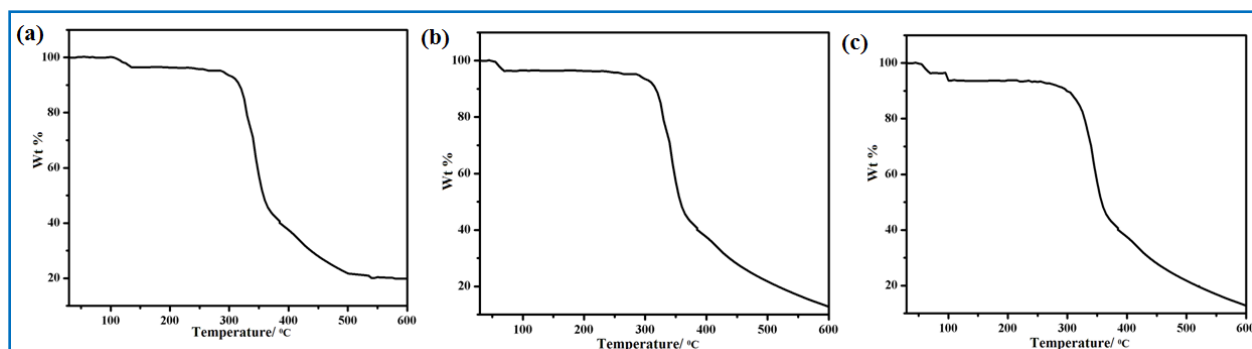


Figure 6. TGA analysis of (a) complex **1**, (b) complex **2** and (c) complex **3** from 30 °C – 600 °C.

3.4. Sorption study

CO₂, N₂ and H₂ gas adsorptions of the three complexes have been studied considering their different framework structures and thermal stability. All the complexes have been activated at 140 °C before starting the measurement. In case of nitrogen sorption study, all the complexes

exhibit surface phenomenon which is quite natural due to the non polar nature and larger kinetic diameter (3.64 Å) of nitrogen molecules. Moreover, complex **3** possess 3D interpenetrating net which results blocking of the pores. Hence the N₂ sorption is almost negligible for this complex and maximum uptake obtained up to 4.9 cc/g (Figure 7a). For the rest two 2D complexes (**1** and **2**) the maximum nitrogen uptake occurs up to 31.4 cc/g and 26.8 cc/g. Both the complexes show type-II uptake profile and there is a small hysteresis presents between the adsorption and desorption curves (Figure 7a). In case of carbon dioxide sorption all the complexes **1**, **2**, and **3** show negligible result for CO₂ that may be explained on the basis of blocking of the unidirectional pore channel by the comparatively larger size of CO₂ (3.3 Å) and non polar nature of the framework (Figure 7b). In case of H₂ sorption, the complex **3** containing interpenetrating structure shows maximum uptake of 43.6 cc/g among the three complexes (Figure 7c). The weak interactions^{11,25} between the H₂ molecules and nitrogen atom of bpmp ligand in such interpenetrated framework may also be responsible for such higher uptake. For the complexes **1** and **2**, H₂ uptake values are 28.98 cc/g and 16.2 cc/g indicating the surface sorption of H₂ in the framework.

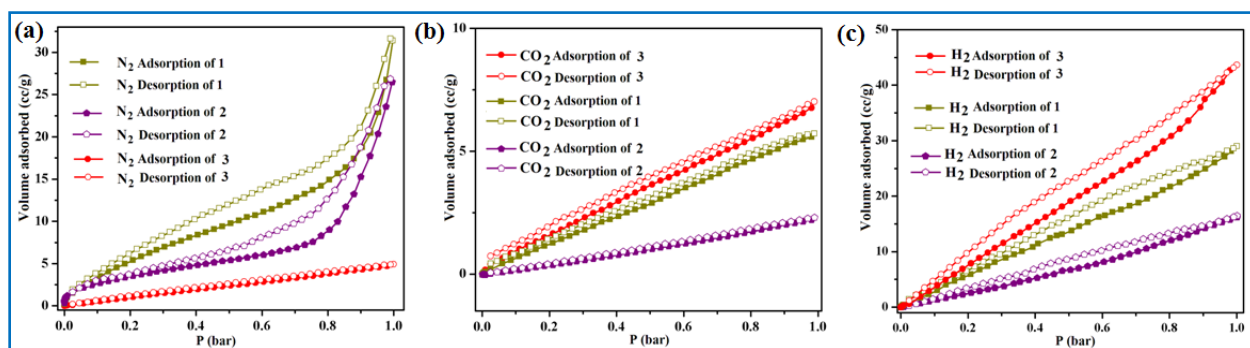


Figure 7. (a) N₂ sorption isotherms of **1**, **2** and **3**; at 77 K. (b) CO₂ sorption isotherms of **1**, **2** and **3**; at 195 K. (c) H₂ sorption isotherms of **1**, **2** and **3**; at 77 K. (dark yellow for complex **1**, Purple for **2** and red for **3**). Filled and open circles represent adsorption and desorption respectively.

4. Conclusion

For the investigation of interpenetrated metal organic frameworks (IMOFs) and to get a better structural insight of such framework, here it has been tried to control the lengths of N-N donor connectivity in synthesized complexes. Here, the main key factor is ligand flexibility that nicely controls the interpenetration of the frameworks. Therefore, this work nicely executes how longer flexible ligand (bpmp) can adjust the framework structure of MOFs from non-interpenetration

towards interpenetration. Different gas adsorption has been studied for all the three complexes and significantly the results obtained have been corroborated with their individual architecture. In case of interpenetrated MOF, the flexibility of bpmp provides optimum pore for hydrogen adsorption compared to the other two complexes whereas carbon dioxide and nitrogen adsorption shows similar result for all the three complexes. In a nutshell, this work is a nice example of designing and exploring IMOFs for their hydrogen storage application.

Reference

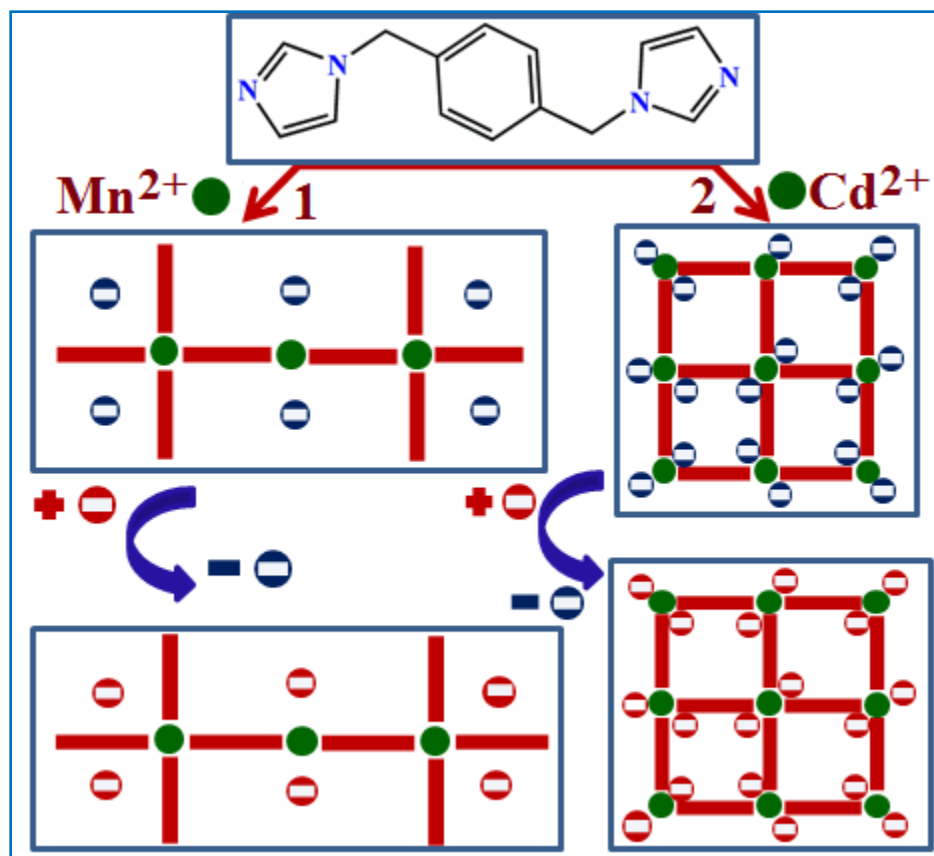
- (1) A. Dey, S. K. Konavapapu, H. S. Sasmal and K. Biradha, *Cryst. Growth Des.*, 2016, **16**, 5976–5984.
- (2) B. Bhattacharya, A. Layek, Md. M. Alam, D. K. Maity, S. Chakrabarti, P. P. Ray and D. Ghoshal, *Chem. Commun.*, 2014, **50**, 7858–7861.
- (3) S. Roy, V. M. Suresh, A. Hazra, A. Bandyopadhyay, S. Laha, S. K. Pati and T. K. Maji, *Inorg. Chem.*, 2018, **57**, 8693–8696.
- (4) D. K. Maity, K. Otake, S. Ghosh, H. Kitagawa and D. Ghoshal, *Inorg. Chem.*, 2017, **56**, 1581–1590.
- (5) L. Wei, Q. Wei, Z. E. Lin, Q. Meng, H. He, B. F. Yang and G. Y. Yang, *Angew. Chem. Int. Ed.*, 2014, **53**, 7188–7191.
- (6) M. Frank, M. D. Johnstone and G.H. Clever, *Chem. Eur. J.*, 2016, **22**, 1–23.
- (7) H. L. Jiang, T. A. Makal and H. C. Zhou, *Coord. Chem. Rev.*, 2013, **257**, 2232–2249.
- (8) F. ZareKarizi, M. Joharian and A. Morsal, *J. Mater. Chem. A*, 2018, **6**, 19288–19329.
- (9) T. -T. Wu, W. Hsu, X. -K. Yang, H. -Y. He and J. -D. Chen, *CrystEngComm.*, 2015, **17**, 916–924.
- (10) S. Wang, L. Mei, J. -P. Yu, K. -q. Hu, Z. -r. Liu, Z. -f. Chai and W. -q. Shi, *Cryst. Growth Des.*, 2018, **18**, 4347–4356.
- (11) D. K. Maity, A. Halder, G. Pahari, F. Haque and D. Ghoshal, *Inorg. Chem.*, 2017, **56**, 713–716.
- (12) X. -H. Bu, M. -L. Tong, H. C. Chang, S. Kitagawa and S. R. Batten, *Angew. Chem. Int. Ed.*, 2004, **43**, 192–195.
- (13) G. Pahari, B. Bhattacharya, C. M. Reddy and D. Ghoshal, *Chem. Commun.*, 2019, **55**, 12515–12518.

- (14) Y. -N. Gong, D. -C. Zhong and T. -B. Lu, *CrystEngComm*, 2016, **18**, 2596–2606.
- (15) L. Carlucci, G. Ciani, D. M. Proserpio, T. G. Mitina and V. A. Blatov, *Chem. Rev.*, 2014, **114**, 7557–7580.
- (16) K. Zhu, V. N. Vukotic, C. A. O’Keefe, R. W. Schurko and S. J. Loeb, *J. Am. Chem. Soc.*, 2014, **136**, 7403–7409.
- (17) F. A. Son, X. Wang, L. R. Redfern, M. C. Wasson, Z. H. Syed, Z. Chen, K. B. Idrees, T. Islamoglu, M. Delferro, W. R. Dichtel, F. X. Coudert, N. C. Gianneschi and O. K. Farha, *J. Am. Chem. Soc.*, 2021, **143**, 1503–1512.
- (18) P. Nugent, Y. Belmabkhout, S. D. Burd, A. J. Carins, R. Luebke, K. Forrest, T. Pham, S. Ma, B. Space, L. Wojtas, M. Eddaoudi and M. J. Zaworotko, *Nature*, 2013, **495**, 80–84.
- (19) L. Yang, X. Cui, Q. Ding, Q. Wang, A. Jin, L. Ge and H. Xing, *ACS Appl. Mater. Interfaces*, 2020, **12**, 2525–2530.
- (20) H. Kim, S. Das, M. G. Kim, D. N. Dybtsev, Y. Kim and K. Kim, *Inorg. Chem.*, 2011, **50**, 3691–3696.
- (21) D. Wu, J. Liu, J. Jin, J. Cheng, M. Wang, G. Yang and Y. -Y. Wang, *Cryst. Growth Des.*, 2019, **19**, 6774–6783.
- (22) J. Gu, X. Sun, L. Kan, J. Qiao, G. Li and Y. Liu, *ACS Appl. Mater. Interfaces*, 2021, **13**, 41680–41687.
- (23) X. -Y. Li, S. -Y. Zhang, S. -H. Zhang and K. -F. Yue, *J. Porous Mater.*, 2021, **28**, 773–777.
- (24) A. G. W. -Foy, A. J. Matzger, O. M. Yaghi, *J. Am. Chem. Soc.*, 2006, **128**, 3494–3495.
- (25) F. -G. Li, C. Liu, D. Yuan, F. Dai, R. Wang, Z. Wang, X. Lu and D. Sun, *CCS Chem.*, 2021, **3**, 1005–1011.
- (26) D. -m. Chen, X. -p. Zhang, W. Shi and P. Cheng, *Cryst. Growth Des.*, 2014, **14**, 6261–6268.
- (27) X. -L. Wang, C. Qin, E. -B. Wang and L. Xu, *Cryst. Growth Des.*, 2006, **6**, 2061–2065.
- (28) L. Zhang, Y. -L. Yao, Y. -X. Che and J. -M. Zheng, *Cryst. Growth Des.*, 2010, **10**, 528–533.
- (29) M. Eddaoudi, J. Kim, N. Rosi, D. Vodak, J. Wachter, M. O’Keeffe and O. M. Yaghi, *Science*, 2002, **295**, 469–472.
- (30) Y. -G. Huang, M. -Y. Wu, F. -Y. Lian, F. -L. Jiang and M. -C. Hong, *Inorg. Chem. Commun.*, 2008, **11**, 840–842.
- (31) L. Carlucci, G. Ciani, S. Maggini, D. M. Proserpio, *Cryst. Growth Des.*, 2008, **8**, 162–165.

-
- (32) L. -L. Qian, S. -S. Han, L. -Y. Zheng, Z. Yang, K. Li, B. -L. Li and B. Wu, *Polyhedron*, 2019, **162**, 303–310.
- (33) L. Tian, Z. -J. Zhang, A. Yu, W. Shi, Z. Chen and P. Cheng, *Cryst. Growth Des.*, 2010, **10**, 3847–3849.
- (34) S. Li, G. -L. Li, W. Wang, Y. Liu, Z. -M. Cao, X. -I. Cao and Y. -G. Huang, *Inorg. Chem. Commun.*, 2021, **130**, 108705–108709.
- (35) A. Bajpai, M. Lusi and M. J. Zaworotko, *Chem. Commun.*, 2017, **53**, 3978–3981.
- (36) J. H. Park, W. R. Lee, Y. Kim, H. J. Lee, D. W. Ryu, W. J. Phang and C. S. Hong, *Cryst. Growth Des.*, 2014, **14**, 699–704.
- (37) J. Kim, S. -T. Yang, S. B. Choi, J. Sim, J. Kim and W. S. Ahn, *J. Mater. Chem.*, 2011, **21**, 3070–3076.
- (38) M. Gupta and J. J. Vittal, *Coord. Chem. Rev.*, 2021, **435**, 213789.
- (39) M. Du, C. -P. Li, C. -S. Liu and S. -M. Fang, *Coord. Chem. Rev.*, 2013, **257**, 1282–1305.
- (40) J. Zhao, D. -S. Li, X. -J. Ke, B. Liu, K. Zou and H. -M. Hu, *Dalton Trans.*, 2012, **41**, 2560–2563.
- (41) B. F. Hoskins, R. Robson and D. A. Slizys, *J. Am. Chem. Soc.*, 1997, **119**, 2952–2953.
- (42) P. K. Dahl and F. H. Arnold, *Macromolecules*, 1992, **25**, 7051–7059.
- (43) B. Xu, H. Yang, J. Lin, X. Zhu, T. Liu and R. Cao, *J. Mol. Struct.*, 2009, **938**, 316–321.
- (44) Y. Niu, H. Hou, Y. Wei, Y. Fan, Y. Zhu, C. Du and X. Xin, *Inorg. Chem. Commun.*, 2001, **4**, 358–361.
- (45) SMART (V 5.628), SAINT (V 6.45a), XPREP, SHELXTL, Bruker AXS Inc., Madison, WI, (2004).
- (46) G. M. Sheldrick, *SADABS (Version 2.03)*, University of Göttingen, Germany, 2002.
- (47) G. M. Sheldrick, *Acta Cryst.*, 2015, **C71**, 3–8.
- (48) A. L. Spek, *Acta Crystallogr. Sect. D Biol. Crystallogr.*, 2009, **65**, 148–155.
- (49) L. J. Farrugia, *J. Appl. Crystallogr.*, 1999, **32**, 837–838.
- (50) K. Brandenburg, *DIAMOND, version 3.1 e, Crystal Impact*, Gbr, Bonn, Germany, 2007.
- (51) V. A. Blatov, A. P. Shevchenko and V. N. Serezhkin, *J. Appl. Crystallogr.*, 2000, **33**, 1193.
- (52) V. A. Blatov, L. Carlucci, G. Ciani and D. M. Proserpio, *CrystEngComm.*, 2004, **6**, 377–395.
-

(53) C. F. Macrae, P. R. Edgington, P. McCabe, E. Pidcock, G. P. Shields, R. Taylor, M. Towler and J. van de Streek, *J. Appl. Cryst.*, 2006, **39**, 453.

Chapter 4



Chapter 4: Synthesis of two cationic coordination polymers and the exploration of anion exchange properties

Chapter 4

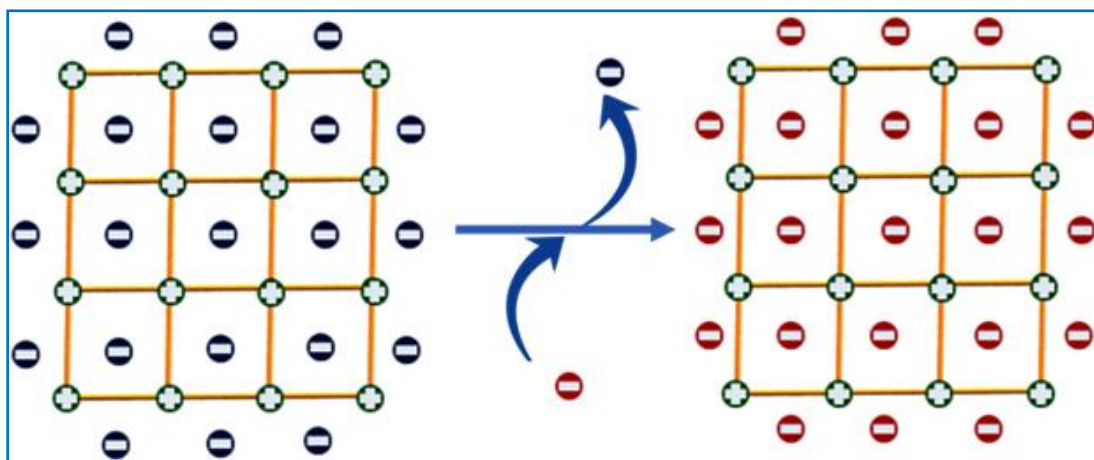
Synthesis of two cationic coordination polymers and the exploration of anion exchange properties

1. Introduction

Ion exchange materials^{1,2} are in receipt of a significant amount of interest in the field of various chemical processes like chemical synthesis,³ management of water and waste-water,⁴⁻⁶ mining,⁷ farming,⁸ food processing,⁹ medicinal research,^{10,11} purification of virus particles¹² and so on. In addition to that such materials have immense importance in different biological processes^{13,14} as various charged surfaces produced from polysaccharides, polynucleic acids, lipids and proteins. The accurate concentrations of anionic groups in the living system are essential while the concentration of free cations vary for different parts of the system.¹⁴ Till date, ion-exchange resins,¹⁵⁻¹⁷ a family of chelating organic molecules^{18,19} and various nanoparticles,²⁰ has been used as leading materials for the exchange and the separation of ions. However they have many limitations such as low thermal and radiation stability, organic and bacterial contaminations, toxic hazards, unstable in slight variation of pH from neutral medium etc. which affects their practical usability in various chemical, environmental and biological processes.^{21,22} In this context, chemically stable charged coordination polymers (CPs)^{23,24} can overlay the purpose of ion exchange in an environmentally sustainable way. Unique structural features of CPs^{25,26} may, therefore, lead to the development of a new model separation system, where charged CPs would take up the position of the conventional ion-exchange materials.

In this chapter it has been focused on the separation and exchange of anions, taking into account of their wide range of applications. It is needless to mention that requirement of stable anion exchanging materials are very important, especially for the removal of toxic and carcinogenic anions²⁷⁻²⁹ like ClO_4^- , AsO_4^{3-} and CrO_4^{2-} , separation of amino acids and nucleotides,^{30,31} or to control over anionic toxic pharmaceuticals ingredients^{32,33}. To fulfill such strategic anion exchange, cationic CPs³⁴⁻⁴⁰ are found very useful and due to the insoluble nature of these CPs, they are found useful in water purification and also in removal of different toxic anions⁴¹. Thus cationic CPs can be used as potential anion exchange materials through the replacement of charge balancing anions in the framework. The counter anions which usually occupy the

framework void are sometimes weakly coordinated or uncoordinated to the metal centers. Therefore, these materials provide a unique opportunity for making anion receptors based on an anion-exchange approach. In the construction of cationic CPs,³⁷⁻⁴¹ neutral nitrogen-containing ligand is one of the most common choices. These N-donor ligands connect the metal centers to finally form 1D/2D/3D networks where the charge balancing counter anions present either coordinated to the metal or in lattice site. For the coordinated anions, the exchange of anions with the metal centers may depend on factors like size, shape and coordinating abilities of the anions with that individual metal; but in case of lattice anion, it is comparatively easier to exchange as there is no involvement of any bond rupture or formation. Thus, it is the most logical choice to design a cationic CP, where the counter anion either present with a weak electrostatic interaction or creating a weak coordination bond, which can be broken during exchange process.



Scheme 1. Representative diagram to show the anion exchange process.

Considering these, two water insoluble cationic CPs $\{[\text{Mn}(\text{bix})_3(\text{H}_2\text{O})_2]\cdot\text{bix}\cdot(\text{NO}_3)_2\}_n$ (**1**), $\{[\text{Cd}(\text{bix})_2(\text{NO}_3)_2]\cdot(\text{H}_2\text{O})_2\}_n$ (**2**) with N,N-donors linkers bix {bix = 1,4-bis(imidazol-1-ylmethyl)-benzene} have been synthesized by varying the metal salt from manganese(II) nitrate tetrahydrate to cadmium(II) nitrate tetrahydrate, using slow diffusion technique. The structures of the complexes **1** and **2** are characterized by single crystal XRD, FT-IR, PXRD and other physicochemical techniques. For studying the anion exchange property, along with the aforesaid complexes, one previously reported⁴² similar type of cationic CP, $\{[\text{Cd}(\text{bix})_2(\text{NO}_3)_2]\}_n$ (**3**) with similar architectures has also been synthesized using the published procedure. For all three cationic CPs the counter anion NO_3^- , being a moderately weak coordinated anion,⁴³⁻⁴⁶ can easily be exchanged with several other anions. For complex **1**, lattice NO_3^- anion has been exchanged with other guest anions like SCN^- , N_3^- , NCO^- , CrO_4^{2-} , ClO_4^- . It is interesting to note that

complexes **2** and **3**, show relatively uncommon anion exchange property because of the exchange of coordinated NO_3^- anions with guest anions like SCN^- , N_3^- , NCO^- , CrO_4^{2-} , ClO_4^- . All the anion exchange studies have been studied and established by IR and PXRD experiments.

2. Experimental section

2.1. Materials and methods

Extremely pure metal salts of manganese (II) nitratetetrahydrate and cadmium (II) nitrate tetrahydrate have been procured from Merck, Sigma-Aldrich Chemical Co. Inc. and used the same as received. Ultrapure water derived from a Millipore water purification system ($\geq 18 \text{ M}\Omega$, Milli-Q, millipore) has been taken in all experiments. All other chemicals and solvents are of AR grade and have been used as received.

2.2. Physical measurements

Microanalyses (C, H, and N) have been carried out on a Heraeus CHNS analyzer. Infrared spectra ($4000\text{--}400 \text{ cm}^{-1}$) have been carried out on KBr pellets, using a PerkinElmer Spectrum BX-II IR spectrometer. Powder X-ray diffraction (PXRD) data of all samples have been collected on a Bruker D8 Discover instrument with $\text{Cu-K}\alpha$ radiation. Thermogravimetric analysis (TGA) has been carried out on a PerkinElmer Simultaneous Thermal Analyzer (STA 8000) in the temperature range of $30\text{--}600^\circ\text{C}$ under N_2 atmosphere at a heating rate of $10^\circ\text{C min}^{-1}$. The adsorption isotherms of N_2 (77 K), CO_2 (195 K) have been measured using a dehydrated sample of **2** and **3** in a Quantachrome Autosorb iQ instrument. In the sample tube a $\sim 40 \text{ mg}$ of **2** and **3** have been placed which is evacuated at 130°C under a $1 \times 10^{-1} \text{ Pa}$ vacuum for ~ 4 hours prior to measurement of the isotherms. Helium gas (99.999% purity) at a constant pressure has been introduced in the gas chamber and allowed to diffuse into the sample chamber by opening the valve to calculate the void volume of the sample tube. The amount of gas adsorbed has been calculated as of the pressure difference $P_{\text{cal}} - P_{\text{e}}$, where P_{cal} is the calculated pressure with no gas adsorption and P_{e} is the observed pressure at equilibrium. All operations have been computer-controlled and automatic.

2.3. Syntheses

2.3.1. Preparation of the ligand 1,4-bis(imidazol-1-ylmethyl)-benzene (bix)

The ligand bix has been synthesized according to modified procedure from literature.^{47,48} A mixture of imidazole (0.6808 g, 10 mmol) and KOH ($\sim 1.68 \text{ g}$, $\sim 30 \text{ mmol}$) have been stirred in 30 mL of DMSO at 60°C for 2 hrs. Then, 1,4-bis(chloromethyl)-benzene (6.05 g, 5 mmol) has

been added into solution drop wise and stirred at 50 °C for 4 hrs. After completion of reaction, the reaction mixture have been allowed to cool to room temperature (30 °C). Then reaction mixture has been stirred in 300 mL water and crude product has been collected in DCM part by using separatory funnel. The DCM part has been kept in room temperature (30 °C) for slow evaporation. Yellow crystalline product has been obtained after 1-2 days with yield 0.70g (58.8%).

2.3.2. Synthesis of the complexes $\{[\text{Mn}(\text{bix})_3(\text{H}_2\text{O})_2]\cdot\text{bix}(\text{NO}_3)_2\}_n$ (**1**) and $\{[\text{Cd}(\text{bix})_2(\text{NO}_3)_2]\cdot(\text{H}_2\text{O})_2\}_n$ (**2**)

Complexes **1** and **2** have been synthesized in the same reaction condition (Scheme 2). Each of $\text{Mn}(\text{NO}_3)_2\cdot 4\text{H}_2\text{O}$ (1 mmol, 0.251 g) and $\text{Cd}(\text{NO}_3)_2\cdot 4\text{H}_2\text{O}$ (1 mmol, 0.308 g) have been dissolved in 20 mL water and a 3 mL aliquot has been added to a 0.5 inch diameter layer tube. 5 mL of methanol/water buffer solution (1:1 v/v) have been layered on top. A methanolic solution (20 mL) of 1,4-bis(imidazol-1-ylmethyl)-benzene (bix) (1 mmol, 0.238 g) has been prepared and a 3 mL of bix ligand solution has been slowly and carefully layered on top of the methanol/water layer in the layer tube. After three weeks, yellowish white block shaped single crystals of **1** (yield 40%) and white colored needle shaped single crystals of **2** (yield 32%) have been formed at the inner wall of the layer tube; they have been collected by filtration and washed with a methanol-water (1:1) mixture followed by manual separation under a microscope.

Anal. calcd. for $\text{C}_{56}\text{H}_{56}\text{MnN}_{18}\text{O}_8$ (**1**, %): C, 57.58; H, 4.85; N, 21.58; O, 10.96. Found: C, 57.1; H, 4.80; N, 21.60; O, 11.00. IR for **1** (KBr pellet, cm^{-1}): $\nu(\text{CH-Ar})$, 3085-3160; $\nu(\text{H}_2\text{O})$, 3105; $\nu(\text{C=C-Ar})$, 1530; $\nu(\text{N-O, NO}_3)$ 1406; $\nu(\text{C-N-Ar})$, 1245 and $\nu(\text{C-N})$, 1071 (Figure 1a). Anal. calcd. for $\text{C}_{28}\text{H}_{32}\text{CdN}_{10}\text{O}_8$ (**2**, %): C, 44.90; H, 4.30; N, 18.70; O, 17.09. Found: C, 45.00; H, 4.2; N, 18.70; O, 17.10. IR for **2** (KBr pellet, cm^{-1}): $\nu(\text{CH-Ar})$, 3070-3140; $\nu(\text{H}_2\text{O})$, 3420; $\nu(\text{C=C-Ar})$, 1577; $\nu(\text{N-O, NO}_3)$ 1401; $\nu(\text{C-N-Ar})$, 1240 and $\nu(\text{C-N})$, 1090 (Figure 1b).

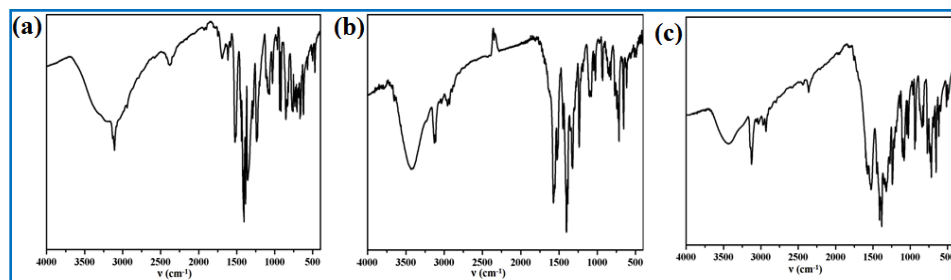
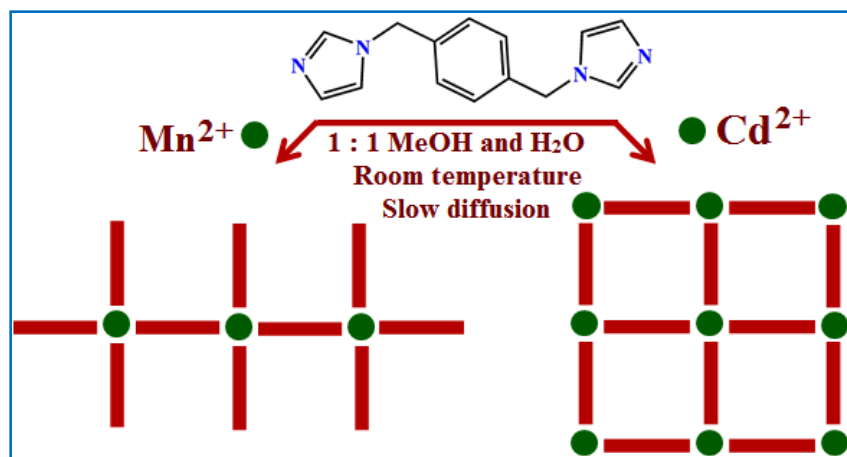


Figure 1. FT-IR spectra of (a) complex **1**, (b) complex **2**, and (c) complex **3**.



Scheme 2. Synthetic scheme of complexes **1** and **2**.

2.4. Crystallographic data collection and refinement

The suitable single crystal of complexes **1** and **2** have been mounted on the tip of thin glass fibers with commercially available super glue. X-ray single crystal structural data of all the complexes have been collected at room temperature (25 °C) on a Bruker APEX II diffractometer, equipped with a normal focus, sealed tube X-ray source by graphite monochromated Mo- K α radiation ($\lambda = 0.71073 \text{ \AA}$). After taking the data, it has been integrated using the SAINT⁴⁹ program in each case and the absorption corrections for the obtained data have been furnished with SADABS⁵⁰. The structure of complexes **1** and **2** have been solved by SHELXS 2016⁵¹ using the Patterson method and followed by successive Fourier and difference Fourier synthesis. SHELXL-2016⁵¹ has been used to perform full matrix least-squares refinements on F^2 . All nonhydrogen atoms have been refined anisotropically except few specific cases. For complex **1** all the atoms have been refined anisotropically without fixing H atoms only on water. In complex **2** all the oxygen atoms of the lattice water molecule and NO_3^- are disordered and oxygen atoms of lattice water molecules and O1 of NO_3^- refined isotropically without fixing hydrogen atom on water molecule. All the calculations have been carried out using SHELXS-2016,⁵¹ PLATON v1.15,⁵² WinGX system Ver-1.80,⁵³ DIAMOND,⁵⁴ TOPOS v3.2^{55,56} and Mercury v3.0⁵⁷. Data collection and structure refinement parameters and crystallographic data for complexes **1** and **2** are given in Table 1. The selected bond lengths and angles are given in Tables 2 and 5.

Table 1. Crystallographic and structural refinement parameters for complex **1** and **2**

	1	2
Formula	C ₅₆ H ₆₀ MnN ₁₈ O ₈	C ₂₈ H ₃₂ CdN ₁₀ O ₈
formula weight	1168.16	749.042
crystal system	triclinic	triclinic
space group	<i>P</i> $\bar{1}$	<i>P</i> $\bar{1}$
<i>a</i> /Å	10.0338(3)	8.2601(2)
<i>b</i> /Å	10.4550(3)	9.7780(2)
<i>c</i> /Å	13.5959(4)	10.0779(2)
α /°	92.477(2)	93.988(1)
β /°	95.220(2)	105.028(1)
γ /°	90.423(2)	97.689(1)
<i>V</i> /Å ³	1418.92(7)	774.42(3)
<i>Z</i>	1	1
<i>D_c</i> / g cm ⁻³	1.362	1.597
μ /mm ⁻¹	0.304	0.772
<i>F</i> ₀₀₀	607	378
θ range/°	1.5 - 27.7	2.1 - 27.5
reflections collected	25544	13077
unique reflections	6525	3549
reflections <i>I</i> > 2 σ (<i>I</i>)	4818	3067
<i>R</i> _{int}	0.033	0.033
goodness-of-fit (<i>F</i> ²)	1.04	1.16
<i>R</i> 1 (<i>I</i> > 2 σ (<i>I</i>)) ^[a]	0.0527	0.0605
<i>wR</i> ₂ (<i>I</i> > 2 σ (<i>I</i>)) ^[a]	0.1616	0.1737
$\Delta\rho$ min / max /e Å ³	-0.37, 0.74	-1.14, 1.06

$$^{[a]}R_1 = \sum ||F_o| - |F_c|| / \sum |F_o|, wR_2 = [\sum (w(F_o^2 - F_c^2)^2) / \sum w(F_o^2)^2]^{1/2}.$$

3. Results and discussion

The ligand 1,4-bis(imidazol-1-ylmethyl)-benzene (bix) has been synthesized according to modified procedure from literature^{47,48} by the reaction between imidazole and 1,4-bis(chloromethyl)benzene. Both the CPs has been synthesized from this bix ligands and metal salt combinations by using slow diffusion technique. The structures of CPs have been characterized by single crystal XRD and other characterization techniques. Bulk phase purity of all the complexes has been confirmed by PXRD measurements.

3.1. Structural description of the complexes

3.1.1. Crystal structure descriptions of {[Mn(bix)₃(H₂O)₂].bix.(NO₃)₂]_n (**1**)

Single crystal X-ray analysis confirms that the complex **1** forms a 1D chain structure made up by the Mn(II) ion and bix linkers. This complex crystallizes in the monoclinic *P* $\bar{1}$ space group. The asymmetric unit contains one Mn(II) metal center with one and half bix ligand, one coordinated

water, half bix ligand and one NO_3^- in the lattice. Here, metal center in MnO_2N_4 coordination environment is coordinated with two oxygen atoms (O1W, O1Wa) from two different coordinated water molecules whereas four nitrogen atoms (N1, N1^a, N5 and N5^a) are attached from four bix ligand to the Mn1 center (Figure 2a). This coordination environment is similar to the previously reported complex $[\text{Mn}(\text{bix})_4(\text{H}_2\text{O})_2]\text{Cl}_2$ ⁵⁸ and $[\text{Mn}(\text{bix})_3(\text{NO}_2)_2] \cdot 4\text{H}_2\text{O}$ ⁵⁹. The Mn–N bond length varies from 2.2381(19) – 2.2680(19) Å (Table 2), where Mn–O1W bond length is 2.2344(16) Å. Here two different binding modes of bix ligand have been observed. Two of four bix ligands present as pendant ligands whereas the other two connects adjacent Mn(II) centers to build a 1D chain (Figure 2b). These 1D chains are interconnected by intermolecular π – π and C–H... π interactions (Tables 3 and 4) between the benzene rings and imidazole rings of coordinated and lattice bix ligand resulting a supramolecular 3D structure (Figure 2c).

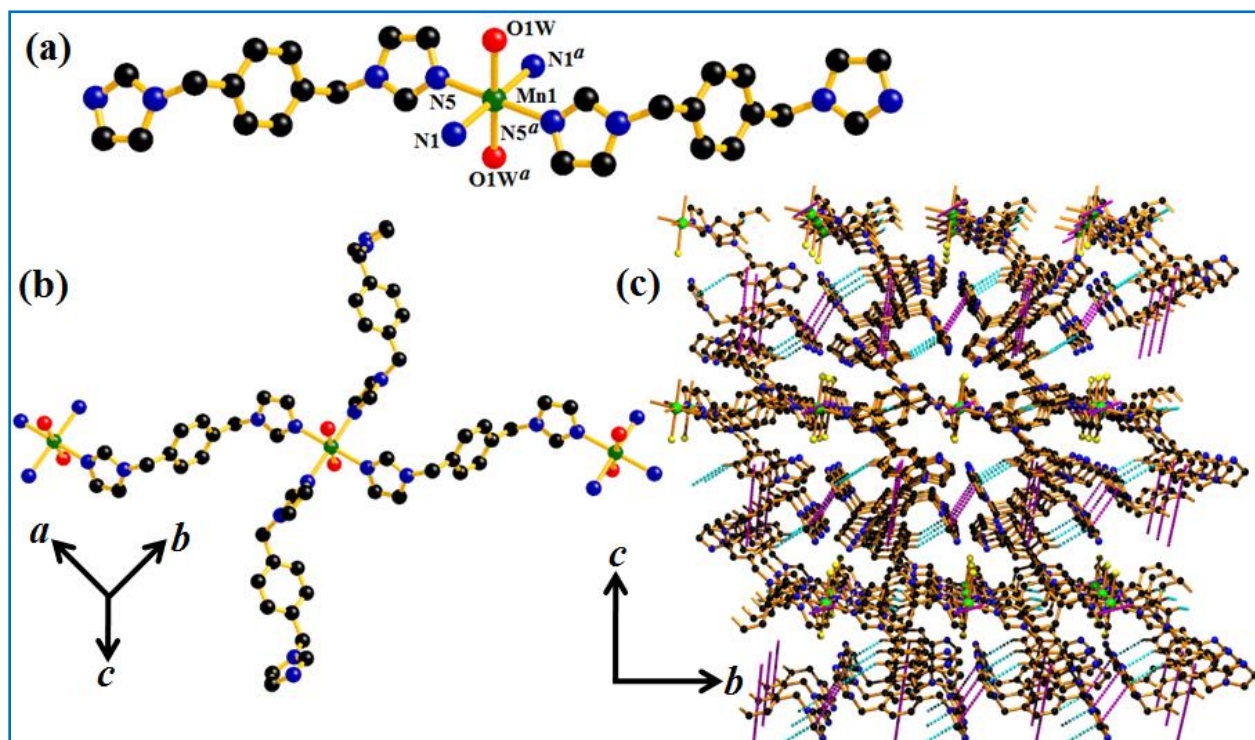


Figure 2. (a) Coordination environment around the Mn(II) ions in **1**; Mn (green), N (blue), O (red), and C (black). (b) 1D chain structure constructed through 4bix in **1**. (c) Possible supramolecular 3D structure of the complex **1** formed by π – π and C–H... π interactions (π – π and C–H... π interactions: magenta and cyan dotted lines respectively).

Table 2. Selected bond lengths (Å) and bond angles (°) for complex **1**

Mn1–O1W	2.2344(16)	N1–Mn1–N5	91.03(7)
Mn1–N1	2.2680(19)	O1W ^a –Mn1–N1	88.38(7)
Mn1–N5	2.2381(19)	N1–Mn1–N1 ^a	180.00
Mn1–O1W ^a	2.2344(16)	N1–Mn1–N5 ^a	88.97(7)
Mn1–N1 ^a	2.2680(19)	O1W ^a –Mn1–N5	90.06(7)
Mn1–N5 ^a	2.2381(19)	N1 ^a –Mn1–N5	88.97(7)
O1W–Mn1–N1	91.63(7)	N5–Mn1–N5 ^a	180.00
O1W–Mn1–N5	89.95(7)	O1W ^a –Mn1–N1 ^a	91.63(7)
O1W–Mn1–O1w ^a	180.00	O1W ^a –Mn1–N5 ^a	89.95(7)
O1W–Mn1–N1 ^a	88.38(7)	N1 ^a –Mn1–N5 ^a	91.03(7)
O1W–Mn1–N5 ^a	90.06(7)		

Symmetry code : $a = 2-x, -2-y, 2-z$.**Table 3.** Intermolecular π – π interactions in **1**

ring(i) → ring(j)	distance of centroid(i) from ring(j), (Å)	dihedral angle (i,j) (deg)	distance between the (i,j) ring centroids, (Å)
R(1) → R(1) ⁱ	4.1519(13)	0.00(13)	2.611
R(2) → R(4) ⁱⁱ	3.7043(15)	3.17(13)	1.077
R(2) → R(4) ⁱⁱⁱ	3.7043(15)	3.17(13)	1.077
R(3) → R(3) ^{iv}	3.9774(18)	0.00(17)	2.016
R(4) → R(2) ⁱⁱ	3.7044(15)	3.17(13)	1.189
R(4) → R(2) ⁱⁱⁱ	3.7043(15)	3.17(13)	1.189

 $i = 2-X, -1-Y, 2-Z$, $ii = X, Y, Z$, $iii = 1-X, -2-Y, 3-Z$, $iv = 1-X, -1-Y, 3-Z$.R(i)/R(j) denotes the $i^{\text{th}}/j^{\text{th}}$ rings in the corresponding structures: R(1) = N(5) / C(15) / C(17) / N(6) / C(16), R(2) = C(5) / C(6) / C(7) / C(10) / C(9) / C(8), R(3) = N(7) / C(22) / N(8) / C(24) / C(23), R(4) = C(26) / C(27) / C(28) / C(26)c / C(27)c / C(28)c.**Table 4.** Intermolecular C–H... π interactions in **1**

C–H ring(j)	H...R distance (Å)	C–H...R angle (deg)	C...R distance (Å)
C(3)–H(3) → R(5) ⁱ	2.96	131	3.635(3)
C(3)–H(3) → R(5) ⁱⁱ	2.96	131	3.635(3)
C(6)–H(6) → R(3) ⁱⁱⁱ	2.91	151	3.754(3)

Symmetry code: $i = -1+X, Y, Z$; $ii = 1-X, -2-Y, 2-Z$; $iii = X, Y, Z$.R(j) denotes the j^{th} rings in the corresponding structures: R(5) = C(19) / C(20) / C(21) / C(19)b / C(20)b / C(21)b, R(3) = N(7) / C(22) / N(8) / C(24) / C(23).

3.1.2. Crystal structure descriptions of $\{[\text{Cd}(\text{bix})_2(\text{NO}_3)_2] \cdot (\text{H}_2\text{O})_2\}_n$ (**2**)

Complex **2** crystallizes in the monoclinic $P2_1$ space group and the structure analysis reveals that the structure is a 2D lattice formed by Cd(II) centres bridged by bix ligands. The asymmetric unit of **2** contains one Cd(II) ion coordinated with one bix ligand and one NO_3^- ion, along with one water molecule in the lattice position. The hexa-coordinated Cd(II) with CdO_2N_4 coordination environments shows a distorted octahedral geometry (Figure 3a) created by four nitrogen atoms (N1, N1^a, N4 and N4^a) of four different bix linkers. The axial positions are occupied by two symmetry related oxygen atoms (O1 and O1a) of two coordinated NO_3^- ions. Coordination environment is similar to the previously reported⁴² complex $[\text{Cd}(\text{NO}_3)_2(\text{bix})_2]_n$ (**3**) which have no lattice water. These two polymorphs⁶⁰ crystallize in different space group with different Z values.

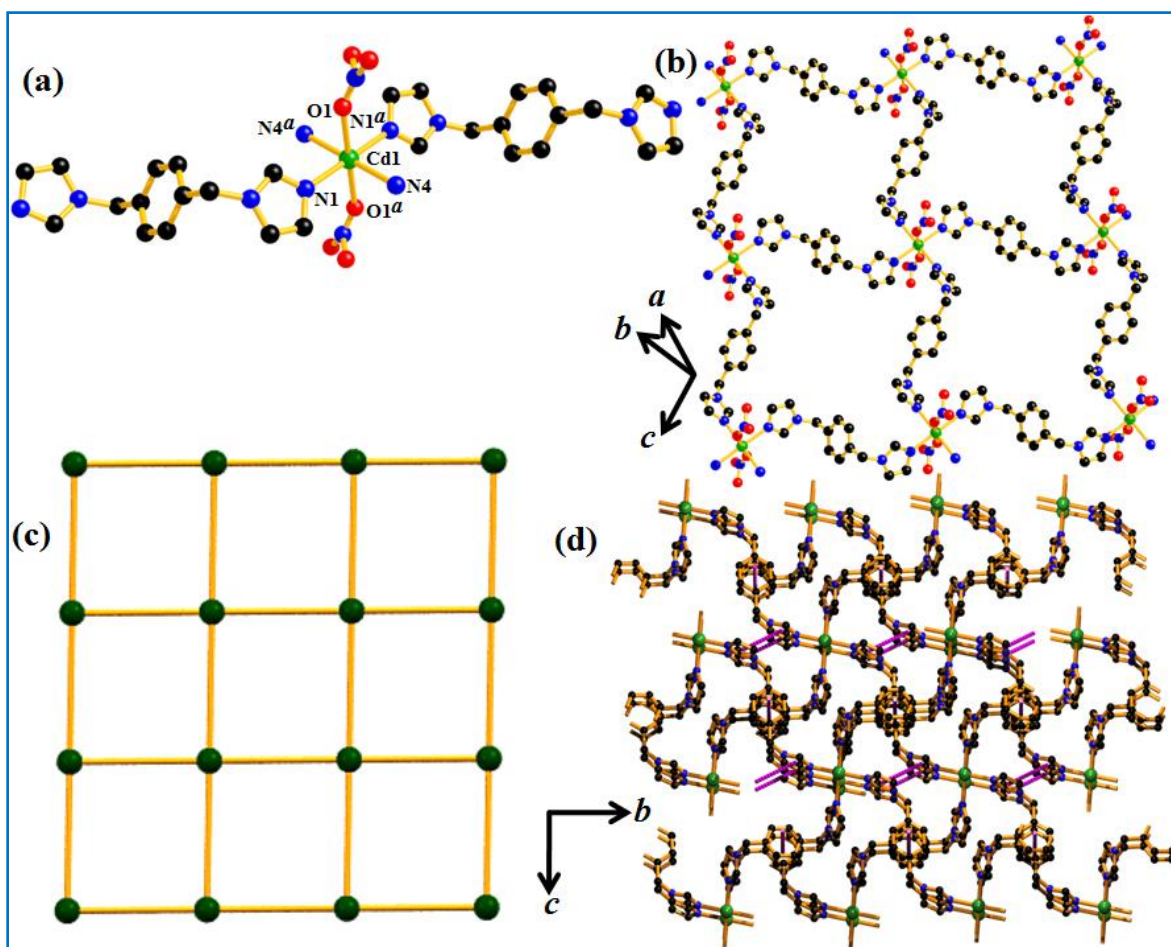


Figure 3. (a) Coordination environment around the Cd(II) ions in **2**; Cd (green), N (blue), O (red), and C (black). (b) 2D metal bix sheet in **2**. (c) Topological representation of the 4-connected uninodal net in **2**. (d) Supramolecular 3D structure by π - π interactions (π - π interactions: magenta dotted line).

A view of superimposed structures of these two polymorphs along with their discrete environment, are shown in Figure 4. In **2**, the Cd–N bond length varies from 2.290(4)–2.325(4) Å and the Cd–O bond length is 2.383(7) Å (Table 5). The other chosen bond lengths and bond angles are given in Table 3. Two nearby Cd(II) centers are linked by four bix linkers, resulting in the formation of a 2D structure containing water molecule at lattice position (Figure 3b). Total potential solvent accessible void space calculated by PLATON⁵² is ~2.7% (21 Å³) of the total crystal volume (774.42 Å³). Structural analysis with TOPOS^{55,56} suggests that the overall framework exhibits a 4-c uninodal net (Figure 3c) with corresponding Schläfli symbol for the net is {4⁴.6²}. This 2D structure finally form supramolecular 3D framework by means of π – π interactions (Table 6) of benzene rings and imidazole rings of bix ligand (Figure 3d).

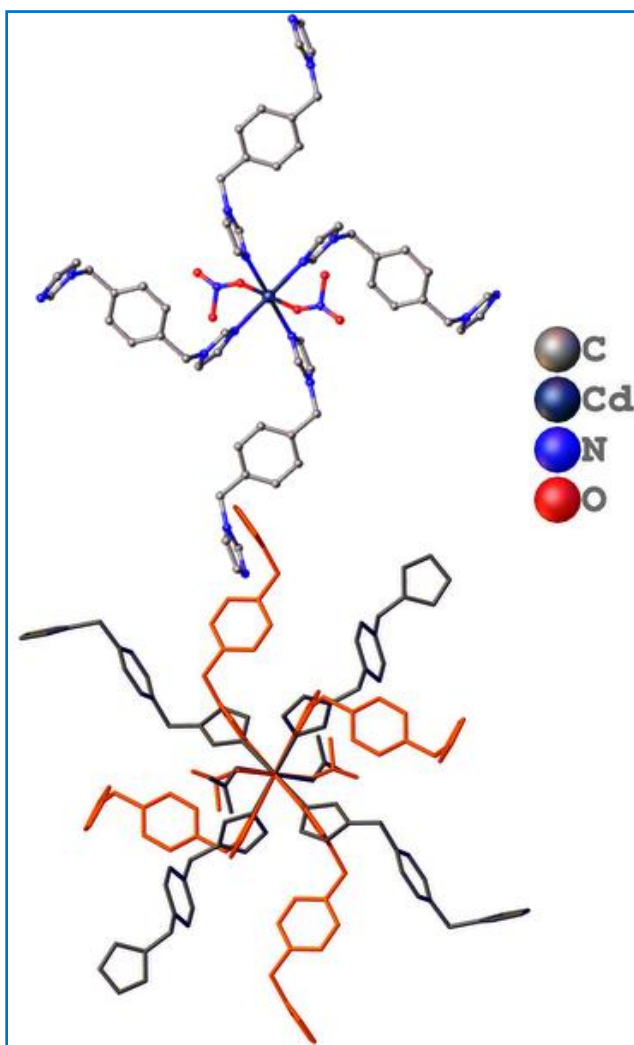


Figure 4. A view of a representative discrete complex **2** as a (top) and a plot of the complexes **2** in blue and **3** in red (bottom), where the CdN₄O₂ units are superimposed.

Table 5. Selected bond lengths (Å) and bond angles (°) for complex **2**

Cd1–O1	2.383(7)	N1–Cd1–N1 ^a	180.00
Cd1–N1	2.290(4)	N1–Cd1–N4 ^a	92.91(14)
Cd1–N4	2.325(4)	O1 ^a –Cd1–N4	90.86(19)
Cd1–O1 ^a	2.383(7)	N1 ^a –Cd1–N4	92.91(14)
Cd1–N1 ^a	2.290(4)	N4–Cd1–N4 ^a	180.00
Cd1–N4 ^a	2.325(4)	O1 ^a –Cd1–N1 ^a	84.15(19)
O1–N5	1.138(10)	O1 ^a –Cd1–N4 ^a	89.14(19)
O2–N5	1.138(9)	N1 ^a –Cd1–N4 ^a	87.06(14)
O3–N5	1.378(12)	N1–Cd1–N4	87.10(14)
O1–Cd1–N1	84.15(19)	O1 ^a –Cd1–N1	95.85(19)
O1–Cd1–N4	89.1(2)	Cd1–O1–N5	141.1(6)
O1–Cd1–O1 ^a	180.00	O1–N5–O2	138.1(9)
O1–Cd1–N1 ^a	95.85(19)	O1–N5–O3	109.3(8)
O1–Cd1–N4 ^a	90.86(19)	O2–N5–O3	112.3(8)

Symmetry code: $a = 2-x, -y, 2-z$.**Table 6.** Intermolecular π – π interactions in **2**

ring(i) → ring(j)	distance of centroid(i) from ring(j), (Å)	dihedral angle (i,j) (deg)	distance between the (i,j) ring centroids, (Å)
R(1) → R(1) ⁱ	4.411(3)	0.0(3)	2.870
R(2) → R(3) ⁱⁱ	4.130(3)	13.1(3)	2.252
R(2) → R(3) ⁱⁱⁱ	4.130(3)	13.1(3)	2.252
R(2) → R(3) ^{iv}	4.130(3)	13.1(3)	2.252
R(2) → R(4) ^v	4.130(3)	13.1(3)	2.252
R(3) → R(2) ^{vi}	4.131(3)	13.1(3)	1.430
R(3) → R(2) ^{vii}	4.130(3)	13.1(3)	1.430
R(3) → R(2) ^{iv}	4.131(3)	13.1(3)	1.430
R(3) → R(2) ^v	4.130(3)	13.1(3)	1.430

i = 2-X, -1-Y, 2-Z; ii = X, 1+Y, Z; iii = 1+X, 1+Y, Z; iv = 2-X, -Y, 3-Z; v = 3-X, -Y, 3-Z; vi = -1+X, -1+Y, Z; vii = X, -1+Y, Z.

R(i)/R(j) denotes the ith/jth rings in the corresponding structures: R(1) = N(3) / C(12) / C(13) / N(4) / C(14), R(2) = C(5) / C(6) / C(7) C(5)c / C(6)c / C(7)c, R(3) = C(8) / C(9) / C(10) / C(8)a / C(9)a / C(10)a.

3.1.3. Crystal structure descriptions of complex **3**

Complex **3** $\{[\text{Cd}(\text{bix})_2(\text{NO}_3)_2]\}_n$ is a polymorph with complex **2** (Figure 4) previously reported by F. –A. Li *et. al.*⁴² crystallizes in the monoclinic $P2_1/c$ space group having Z value of 2 and it exhibits a 2-dimensional (2D) structure of Cd(II) connected by bix ligands (Figures 5a and 5b). Asymmetric unit of **3** contains one Cd(II) ion coordinated with one bix ligand and one NO_3^- ion. Total potential solvent accessible void space calculated by PLATON⁵² is ~2.5% (37.1 Å^3) of the

total crystal volume (1509.1 \AA^3). Topological representation of the 4-connected uninodal net in **3** is shown in Figure 5c. This 2D structure finally form supramolecular 3D structure by π - π interaction (Table 7) of imidazole rings of bix ligands and C-H... π interactions (Table 8) between benzene rings and imidazole rings (Figure 5d).

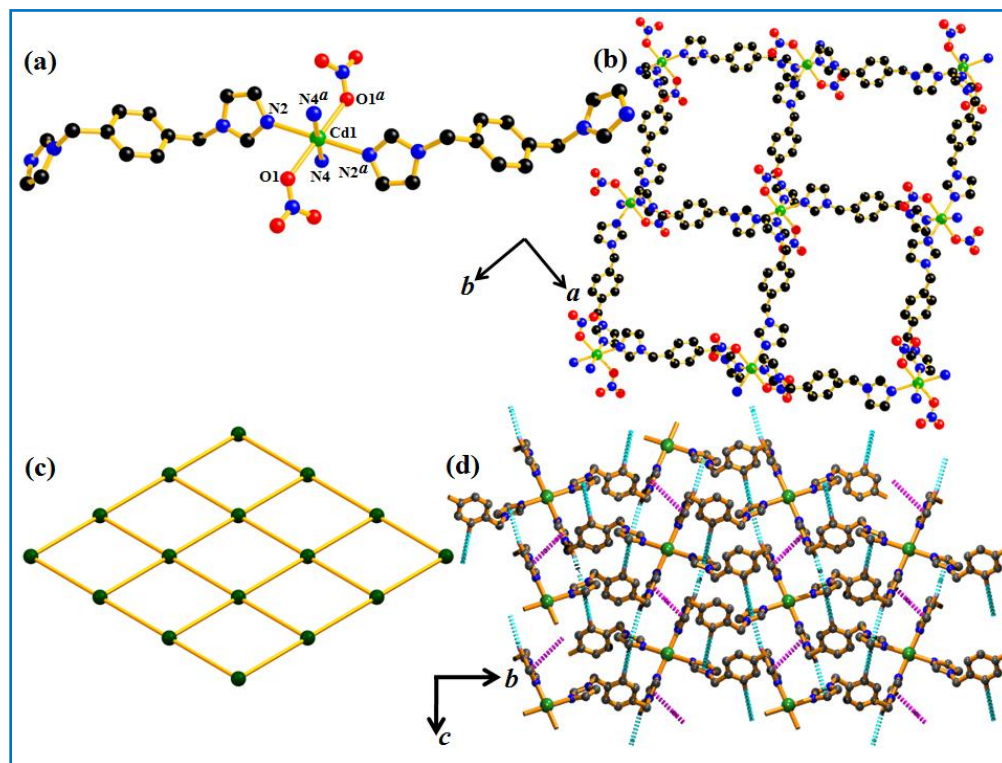


Figure 5. (a) Coordination environment around the Cd(II) ions in **3**; Cd (green), N (blue), O (red), and C (black). (b) 2D metal-bix sheet in **3**. (c) Topological representation of the 4-connected uninodal net in **3**. (d) Supramolecular 3D structure of the complex **3** formed by π - π and C-H... π interactions (π - π and C-H... π interactions: magenta and cyan dotted lines respectively).

Table 7. Intermolecular π - π interactions in **3**

ring(i) \rightarrow ring(j)	distance of centroid(i) from ring(j), (\AA)	dihedral angle (i,j) (deg)	distance between the (i,j) ring centroids, (\AA)
R(1) \rightarrow R(1) ⁱ	3.7988(16)	0.00(17)	1.084

i = -X, -Y, 3-Z

R(i)/R(j) denotes the $i^{\text{th}}/j^{\text{th}}$ rings in the corresponding structures: R(1) = N(4) /C(11) /C(13) / N(5)/ C(12).

Table 8. Intermolecular C–H... π interactions in **3**

C–H ring(j)	H...R distance (Å)	C–H...R angle (deg)	C...R distance (Å)
C(6)–H(6)→R(2) ⁱⁱ	2.77	106	3.162(3)
C(13)–H(13)→R(2) ⁱ	2.77	106	3.162(3)

Symmetry code: i = -X,-Y,3-Z; ii = X,-1/2-Y,1/2+Z.

R(j) denotes the jth rings in the corresponding structures: R(2) = N(2) / C(1) / C(2) / N(3) / C(3).

3.2. Powder X-ray diffraction (PXRD) of the complexes

Powder X-ray diffraction (PXRD) analysis has been carried out to confirm the phase purity of the bulk materials of both complexes at room temperature (30 °C). The experimental PXRD patterns of complexes **1** and **2** are in good agreement with the simulated ones from their corresponding single crystal structures (Figure 6), confirming the bulk phase purity of the complexes. Bulk phase purity of complex **3** also checked before the anion exchange studies.

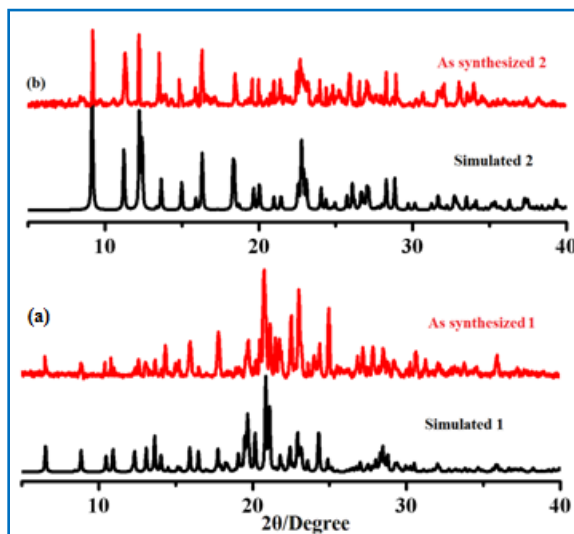


Figure 6. PXRD of (a) complex **1**, and (b) complex **2** indicating the bulk sample purity.

3.3. Thermogravimetric analysis

The TGA curve of complex **1** (Figure 7a) exhibits a weight loss of ~3.08% at ~104 °C, which reveals the presence of two coordinated water molecule (calc. wt% 3.08) and the dehydrated framework is stable up to 256 °C without any further weight loss, signifying the total elimination of all water molecules through the activation process. After 256 °C the dehydrated framework collapses and decomposes into unidentified products. The TGA curve of complex **2** (Figure 7b) exhibits the lattice water has been released at room temperature (30 °C) and dehydrated

framework is stable up to 296 °C without any further weight loss. After 296 °C the dehydrated framework collapses and decomposes into unidentified products.

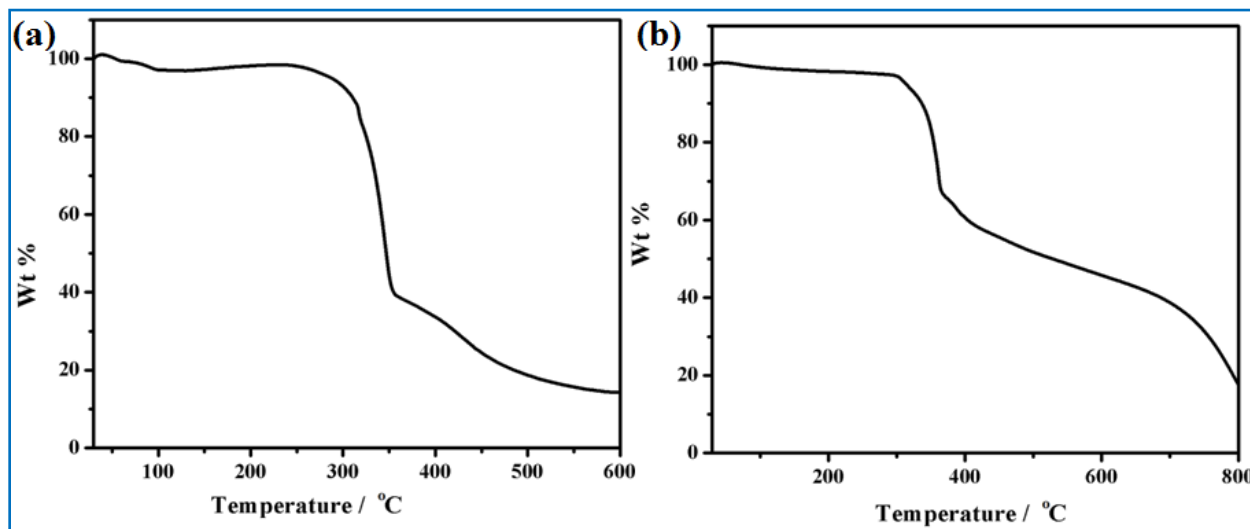


Figure 7. (a) TGA analysis of complex **1** from 30 °C – 600 °C. (b) TGA analysis of complex **2** from 30 °C – 800 °C. Complex **1** is stable up to 256°C and complex **2** is stable up to 296°C.

3.4. Anion exchange studies

The single crystal structure analysis of **1** shows the presence of the free NO_3^- anions in the lattice. Again the complex **1** is insoluble in water and common organic solvents. So here is a possibility of anion exchange properties due to the existence of the free lattice NO_3^- ion. For studying anion exchange properties, first 5 ml 0.01 M aqueous solution (taking deionized water) of different Sodium salt like NaN_3 , NaClO_4 , NaNCO , NaSCN and Na_2CrO_4 have been prepared individually. Then well-grounded fine particles of complex **1** (~58 mg) has been suspended in this 5 ml 0.01 M aqueous solution of Na(I) salt and stirred for 36 hours at room temperature (30 °C) to allow the anion exchange. After that each individual mixture has been filtered and precipitate has been washed with deionized water for 10 times. The phenomena of the anion exchange with the parent complex **1** have been monitored by FT-IR spectroscopy (Figure 8) and PXRD measurements of vigorously washed precipitate part. The IR spectra of **1** contain an intense band at ~1430 to 1368 cm^{-1} which indicates the presence of NO_3^- anions. After the anion exchange, the exchanged solids in the washed precipitate part (Figure 8), exhibit significant deteriorating of the NO_3^- bands in the IR spectra and an appearance of new characteristic peaks at ~2034 cm^{-1} for N_3^- (**1*** N_3^-), ~1122 and ~1051 cm^{-1} for ClO_4^- (**1*** ClO_4^-), ~2191 cm^{-1} for NCO^- (**1*** NCO^-), ~2040 cm^{-1} for SCN^- (**1*** SCN^-) and ~900 to 850 cm^{-1} for CrO_4^{2-} (**1*** CrO_4^{2-}).

correspondingly. The deteriorating of the NO_3^- bands and the creation of new distinctive bands of the respective anions used for the anion exchange affirmed the progression of the anion exchange process. Other peaks in the IR spectra remained almost unchanged, which indicates that the framework sustainability after the exchange process. Also in each case the filtrates are collected and dried to study the IR spectra. A significant signature of nitrate is present in all the IR spectra of the filtrates (Figure 9a) also supports the exchange of nitrate with the corresponding anions.

From the PXRD pattern of washed solid part of (exchanged solid) complex **1** (Figure 9b) it is noticed that $\mathbf{1} \cdot \text{ClO}_4^-$, $\mathbf{1} \cdot \text{NCO}^-$, $\mathbf{1} \cdot \text{SCN}^-$ and the mother **1** are almost similar which indicates the retention of skeletal structures of the frameworks. In the PXRD patterns (Figure 9b) of the washed precipitate part of other anion $\mathbf{1} \cdot \text{N}_3^-$ and $\mathbf{1} \cdot \text{CrO}_4^{2-}$ slight variation has been observed. For N_3^- ion, the strong coordinating ability may be responsible for such a change in the framework. In the case of CrO_4^{2-} the variation is probably due to the different charge and large size compared to the other anions. CrO_4^{2-} ; being a large binegative anion such a structural change in the framework may have taken place after the anion exchange process. As the complexes losses the single crystallinity during the anion exchange process so the study of anion exchange could not be possible by single crystal XRD.

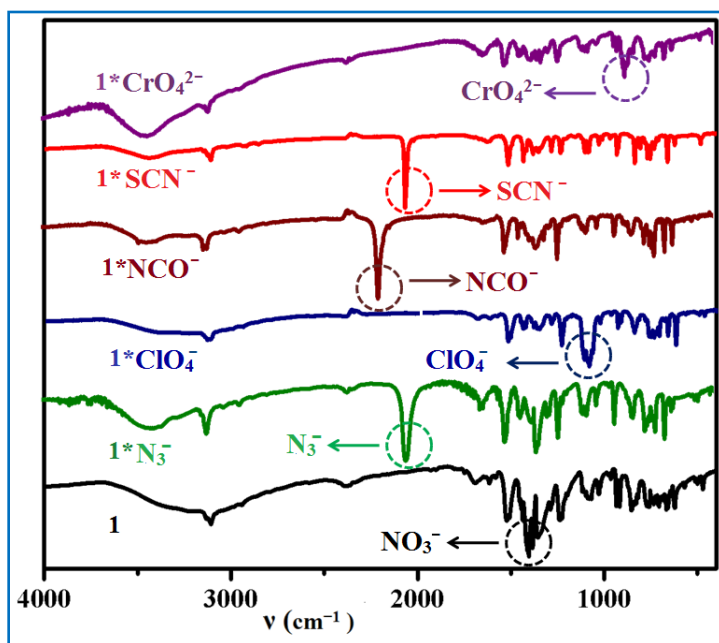


Figure 8. Combined FT-IR spectra of the parent complex **1** and its anion exchanged solids with highlighted bands of the corresponding anions.

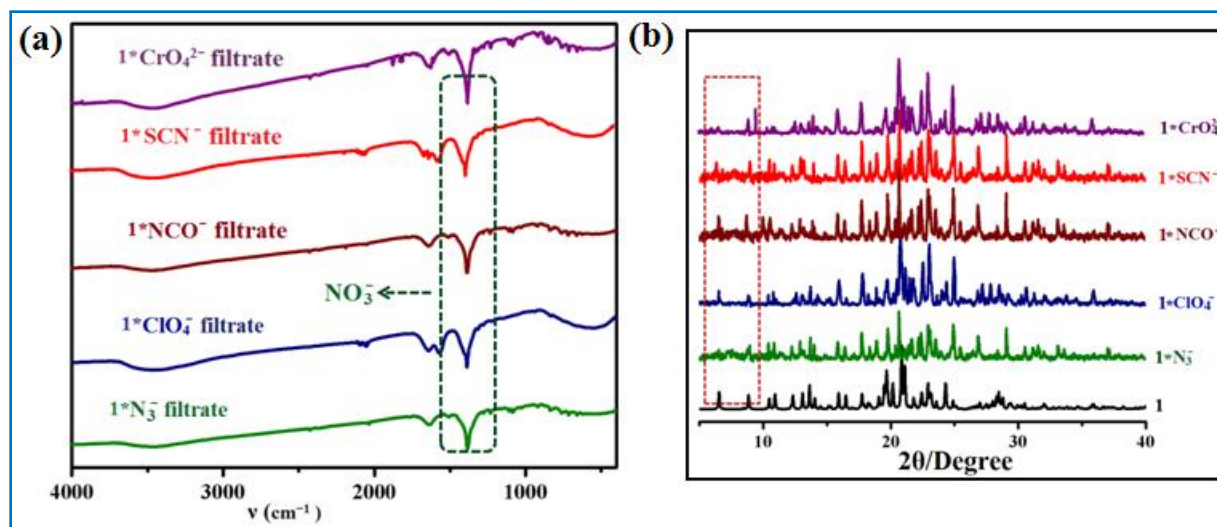


Figure 9. (a) IR of the filtrates of **1** with all guest anions. (b) PXRD of exchanged solid of **1** with all guest anions.

In case of **2** and **3** the relatively rare anion exchange process has been observed where coordinated NO_3^- anion has been exchanged with foreign anions. For **2** and **3** similar experimental procedure has been followed like in case of **1**. IR spectra of the washed precipitate of exchanged solid of complex **2** and **3** (Figures 10 and 12) clearly shows the weakening of NO_3^- peak which is present in the mother complexes and formation of new band corresponding to guest anions N_3^- , ClO_4^- , NCO^- , SCN^- and CrO_4^{2-} . Further, the IR spectra of the washed filtrates (Figures 11a and 13a) of **2** and **3** ($2 \cdot \text{N}_3^-$, $2 \cdot \text{ClO}_4^-$, $2 \cdot \text{NCO}^-$, $2 \cdot \text{SCN}^-$, $2 \cdot \text{CrO}_4^{2-}$ and $3 \cdot \text{N}_3^-$, $3 \cdot \text{ClO}_4^-$, $3 \cdot \text{NCO}^-$, $3 \cdot \text{SCN}^-$, $3 \cdot \text{CrO}_4^{2-}$) indicates the existence of significant amount of nitrate in all which supports the exchange of nitrate with the corresponding anions. The PXRD pattern of washed exchanged solid of complexes **2** and **3** (Figures 11b and 13b) indicates that except N_3^- and CrO_4^{2-} , the exchanged solid of NCO^- , SCN^- , ClO_4^- and the parent complex **2**, **3** are almost similar which indicates the retention of skeletal structures of the frameworks in **2** and **3** after anion exchange. Difference in size, coordination tendency⁶¹ and binegetive charge factor may play a vital role for which little exceptions in PXRD patterns of N_3^- and CrO_4^{2-} has been observed.

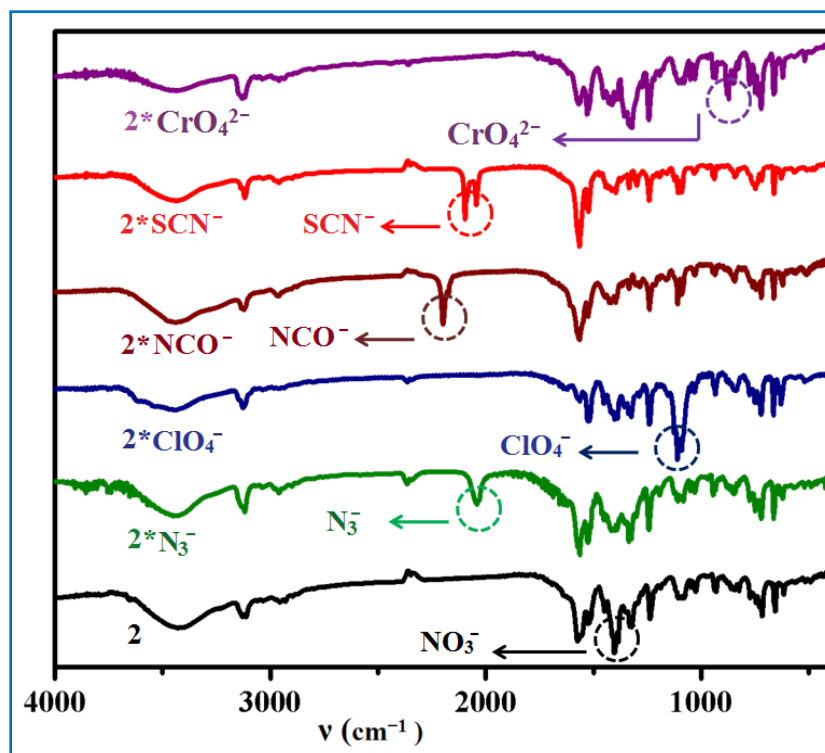


Figure 10. Combined FT-IR spectra of the parent complex **2** and its anion exchanged solids with highlighted bands of the corresponding anions.

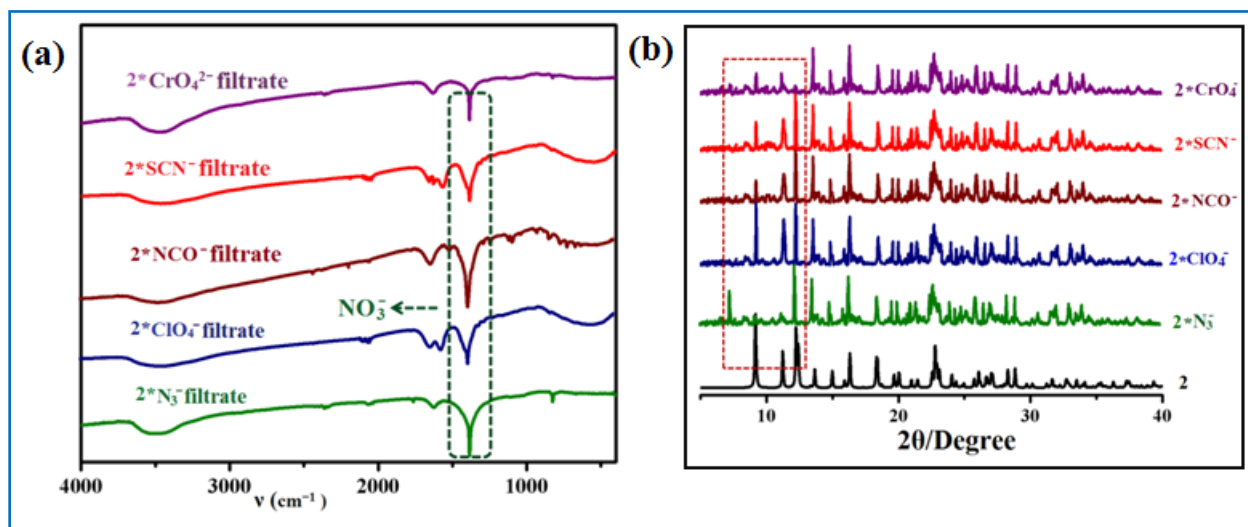


Figure 11. (a) IR of the filtrates of **2** with all guest anions. (b) PXRD of exchanged solid **2** with all guest anions.

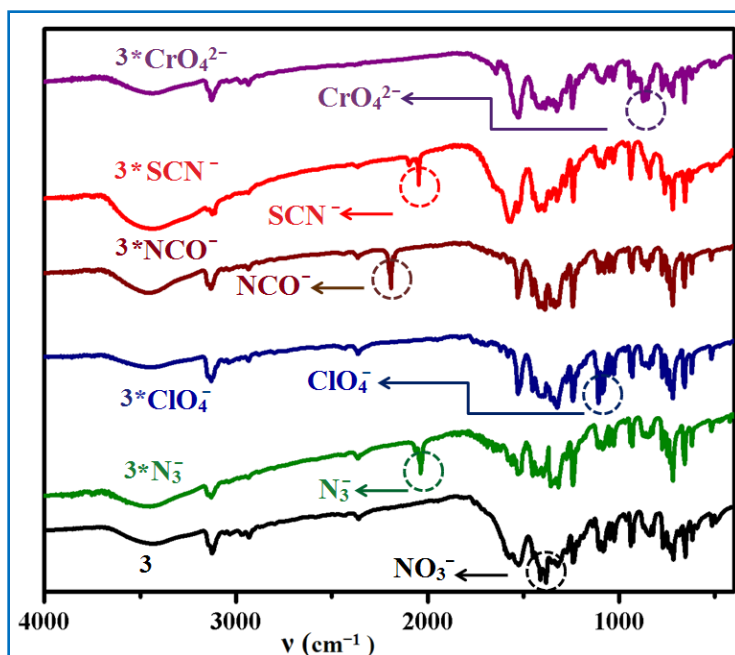


Figure 12. Combined FT-IR spectra of the parent complex **3** and its anion exchanged solids with highlighted bands of the corresponding anions.

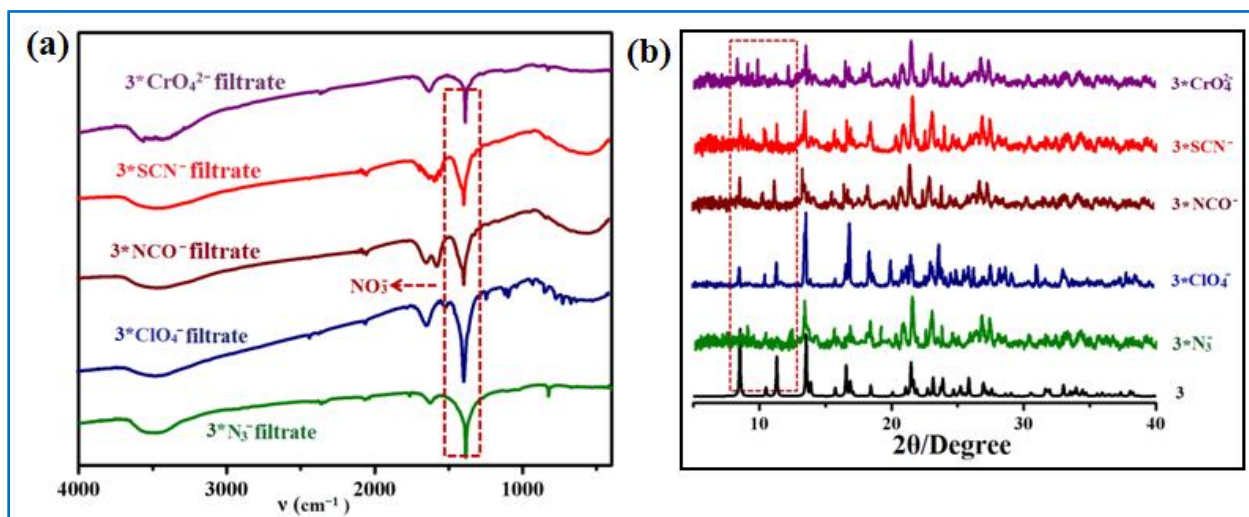


Figure 13. (a) IR of the filtrates of **3** with all guest anions. (b) PXRD of exchanged solid of **3** with all guest anions.

3.5. Sorption studies

Gas adsorption studies have been performed for the 2D compounds to understand their porous nature. The desolvated frameworks of **2** and **3** have been allowed to N₂ and CO₂ gas adsorption experiments. It shows mild absorbing behavior towards N₂ and CO₂ (Figures 14a and 14b). N₂

sorption exhibits the uptake upto 13.7 cc/g and 10.1 cc/g for the complex **2** and **3** respectively at 77K temperature and 1 bar pressure. The uptake value for CO₂ sorption is 18.4 cc/g and 14.3 cc/g at 1 bar pressure and 195 K temperature for the complex **2** and **3** respectively. Both the complexes have 2D architecture with smaller potential void (~2.7% for **2** and ~2.5% for **3**), so such low sorption values corroborate the surface adsorption.

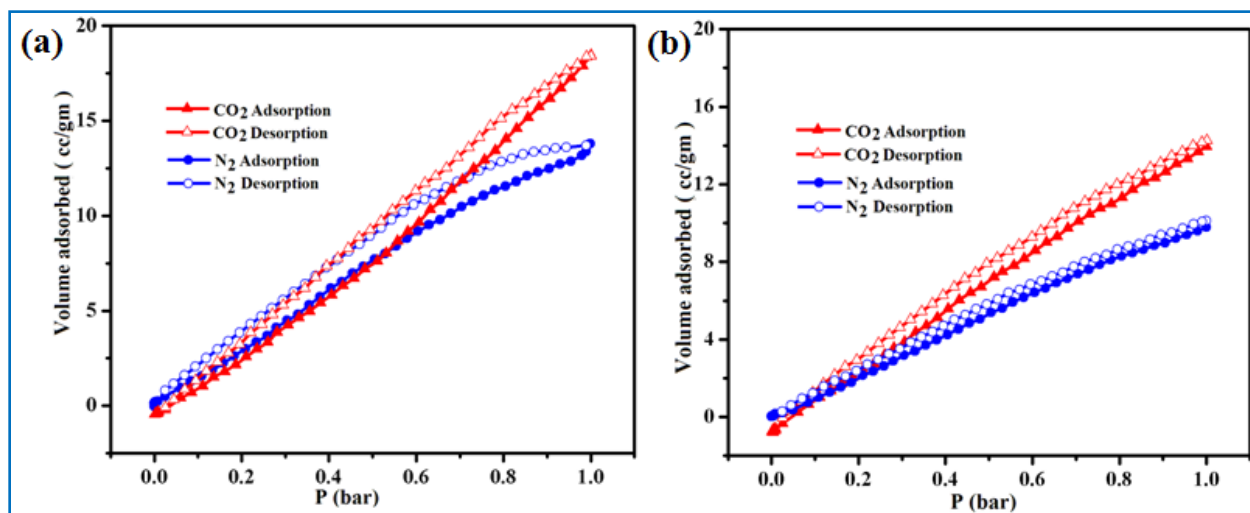


Figure 14. (a) Different sorption isotherms of **2**; N₂ at 77 K (blue circles), CO₂ at 195 K (red triangles). (b) Different sorption isotherms of **3**; N₂ at 77 K (blue circles), CO₂ at 195 K (red triangles). Filled and open circles represent adsorption and desorption respectively.

4. Conclusion

To investigate the anion exchange properties of CPs, we have synthesized here two cationic CPs with different anion exchange possibilities using bix ligand. Two cationic CPs **1** and **2** are not only interesting for their simple structures of formation but also for their excellent anion exchange property. The one-dimensional complex **1** contains lattice NO₃[−] ions with Mn(II) centers and performs well in anion exchange with the inclusion of foreign anions. On the other hand, complexes **2** and **3** shows relatively uncommon anion exchange of coordinated NO₃[−]. Both the complexes are water insoluble which makes them excellent candidates for the separation of pollutants and may be used as water purifier. Again post synthetic modification in the void area of CPs by using anion exchangeable CPs may amplify the capability of CPs in various sorption properties. In one word, it is a nice example of practical usability of coordination polymers as effective anion exchange materials.

References

- (1) A. A. Zagorodni, *Ion Exchange Materials: Properties and Applications*; Elsevier: Amsterdam, 2007.
- (2) R. Kunin and F. X. McGarvey, *Anal. Chem.*, 1964, **36**, 142–144.
- (3) H. Jaroszek and P. Dydo, *Open Chem.*, 2015, **14**, 1–19.
- (4) A. Alsbaiee, B. J. Smith, L. Xiao, Y. Ling, D. E. Helbling and W. R. Dichtel, *Nature*, 2016, **529**, 190–194.
- (5) T. Rana, A. K. Bera, D. Bhattacharya, S. Das and S. K. Das, *Comparative Clinical Pathology*, 2021, **30**, 277–284.
- (6) E. K. Paleologos, B. C. O’Kelly and C. S. Tang, *Environmental Geotechnics*, 2021, **8**, 193–207.
- (7) R. W. Gaikwad, V. S. Sapkala and R. S. Sapkal, *Acta Montan. Slovaca*, 2010, **15**, 298–304.
- (8) M. Mahesh, J. Thomas, K. A. Kumar, B. S. Bhople, N. V. Suresh, S. K. Vaid and S. K. Sahu, *Int. J. Curr. Microbiol. App. Sci.*, 2018, **7**, 2912–2924.
- (9) J. Kammerer, R. Carle and D. R. Kammerer, *J. Agric. Food Chem.*, 2011, **59**, 22–42.
- (10) S. Vijay and C. S. Chauhan, *J. Drug Deliv. Ther.*, 2014, **4**, 115–123.
- (11) J. G. Mahore, K. J. Wadher, M. J. Umekar and P. K. Bhoyar, *Int. J. Pharm. Sci. Rev. Res.*, 2010, **1**, 8–13.
- (12) H. J. Gye and T. Nishizawa, *J. Virol. Methods*, 2016, **238**, 21–28.
- (13) H. Sobotka and H. P. Gregor, *Ann. N. Y. Acad. Sci.*, 1953, **57**, 63–66.
- (14) R. J. P. Williams, *The importance of ion exchange processes in living systems*. In: P.A. Williams, M. J. Hudson (Eds), *Recent developments in ion exchange*, New York: Elsevier Applied Science., 1990, 3–15.
- (15) P. M. Cummins, K. D. Rochfort and B. F. O’Connor, *Ion-Exchange Chromatography: Basic Principles and Application*, Humana Press, New York, 2017, 1485.
- (16) R. Khayyam, N. Farshid, P. Mohammad, A. Samane and M. V. Sahajwalla, *J. Hazard. Mater.*, 2019, **371**, 389–396.
- (17) S. Wu, P. Yan, W. Yang, J. Zhou, H. Wang, L. Che and P. Zhu, *Chemosphere*, 2021, **264**, 128557.
- (18) O. Tavakoli, V. Goodarzi, M. R. Saeb, N. M. Mahmoodi and R. Borja, *J. Hazard. Mater.*, 2017, **334**, 256–266.

-
- (19) D. Kołodyńska, D. Fila and Z. Hubicki, *Environ. Res.*, 2020, **191**, 110171.
- (20) Y. S. Dzyazko, L. M. Rozhdestvenska, S. L. Vasilyuk, K. O. Kudelko and V. N. Belyakov, *Nanoscale Res. Lett.*, 2017, **12**, 438.
- (21) I. Khan, K. Saeed and I. Khan, *Arab. J. Chem.*, 2019, **12**, 908–931.
- (22) R. Mark and W. N. Findley, *Polym. Eng. Sci.*, 1978, **18**.
- (23) A. Chakraborty, S. Bhattacharyya, A. Hazra, A. C. Ghosh and T. K. Maji, *ChemComm*, 2016, **52**, 2831–2834.
- (24) J. Li, X. Wang, G. Zhao, C. Chen, Z. Chai, A. Alsaedi, T. Hayat and X. Wang, *Chem. Soc. Rev.*, 2018, **47**, 2322.
- (25) W. L. Leong and J. J. Vittal, *Chem. Rev.*, 2011, **111**, 688–764.
- (26) H. Kaur, S. Sinha, V. Krishnan and R. R. Koner, *Dalton Trans.*, 2021, **50**, 8273–8291.
- (27) K. Nath, K. Maity and K. Biradha, *Cryst. Growth Des.*, 2017, **17**, 4437–4444.
- (28) J. J. Testa, M. A. Grela and M. I. Litter, *Environ. Sci. Technol.*, 2004, **38**, 1589–1594.
- (29) E. T. Urbansky, *Environ. Sci. Pollut. Res. Int.*, 2002, **9**, 187–192.
- (30) P. B. Hamilton, *Anal. Chem.*, 1958, **30**, 914–919.
- (31) X. Zhao, C. Mao, K. T. Luong, Q. Lin, Q. -G. Zhai, P. Feng and X. Bu, *Angew. Chem. Int. Ed.*, 2016, **55**, 2768–2772.
- (32) J. S. Lee, H. Luo, G. A. Baker and S. Dai, *Chem. Mater.*, 2009, **21**, 4756–4758.
- (33) H. -R. Fu, Z. -X. Xu and J. Zhang, *Chem. Mater.*, 2015, **27**, 205–210.
- (34) E. Coronado, M. G. -Marque, C. J. G. -García and G. M. Espallargas, *Inorg. Chem.*, 2012, **51**, 12938–12947.
- (35) B. Li, Q. Lei, F. Wang, D. Zhao, Y. Deng, L. Yang, L. Fan and Z. Zhang, *J. Solid State Chem.*, 2021, **298**, 122117,
- (36) L. Zhu, C. Xiao, X. Dai, J. Li, D. Gui, D. Sheng, L. Chen, R. Zhou, Z. Chai, T. E. A. – Schmitt and S. Wang, *Environ. Sci. Technol. Lett.*, 2017, **4**, 316–322.
- (37) A. Aijaz, P. Lama and P. K. Bharadwaj, *Inorg. Chem.*, 2010, **49**, 5883–5889.
- (38) B. Manna, A. V. Desai and S. K. Ghosh, *Dalton Trans.*, 2016, **45**, 4060–4072.
- (39) B. Manna, A. V. Desai, N. Kumar, A. Karmakar and S. K. Ghosh, *CrystEngComm*, 2015, **17**, 8796.
- (40) D. K. Maity, B. Bhattacharya, A. Halder and D. Ghoshal, *Dalton Trans.*, 2015, **44**, 20999–21007.
-

- (41) A.V. Desai, B. Manna, A. Karmakar, A. Sahu and S. K. Ghosh, *Angew. Chem. Int. Ed.*, 2016, **128**, 7942–7946.
- (42) F. -A. Li, W. -C. Yang and X. -M. Hu, *Z. Kristallogr. NCS*, 2011, **226**, 587–588.
- (43) R. Custelcean and B. A. Moyer, *Eur. J. Inorg. Chem.*, 2007, 1321–1340.
- (44) F. Hofmeister, *Zur Lehre von der Wirkung der Salze*, Arch. Exp. Pathol. Pharmacol (Leipzig), 1888, **24**, 247–260.
- (45) P. Jungwirth (Eds), *J. Phys. Chem. Lett.*, 2013, **4**, 4258–4259.
- (46) R. Tian, G. Yang, Y. Tang, X. Liu, R. Li, H. Zhu and H. Li, *PLoS ONE*, 2015, **10** (2015) 0128602.
- (47) B. F. Hoskins, R. Robson and D. A. Slizys, *J. Am. Chem. Soc.*, 1997, **119**, 2952–2953
- (48) P. K. Dahl and F. H. Arnold, *Macromolecules*, 1992, **25**, 7051–7059.
- (49) SMART (V 5.628), SAINT (V 6.45a), XPREP, SHELXTL, Bruker AXS Inc., Madison, WI, 2004.
- (50) G. M. Sheldrick, *SADABS (Version 2.03)*, University of Göttingen, Germany, 2002.
- (51) G. M. Sheldrick, *Acta Cryst.*, 2015, **C71**, 3–8.
- (52) A. L. Spek, *Acta Crystallogr. Sect. D Biol. Crystallogr.* 2009, **65**, 148–155.
- (53) L. J. Farrugia, *J. Appl. Crystallogr.*, 1999, **32**, 837–838.
- (54) K. Brandenburg, *DIAMOND, version 3.1 e*, Crystal Impact Gbr, Bonn, Germany, 2007.
- (55) V. A. Blatov, A. P. Shevchenko and V. N. Serezhkin, *J. Appl. Crystallogr.*, 2000, **33**, 1193.
- (56) V. A. Blatov, L. Carlucci, G. Ciani and D. M. Proserpio, *CrystEngComm.*, 2004, **6**, 377–395.
- (57) C. F. Macrae, P. R. Edgington, P. McCabe, E. Pidcock, G. P. Shields, R. Taylor, M. Towler and J. van de Streek, *J. Appl. Cryst.*, 2006, **39**, 453.
- (58) T. P. J Garrett, J. M. Guss and H. C. Freeman, *Acta Crystallogr. Sect. C*, 1983, **39**, 1031.
- (59) H. -Y. Shen, D. -Z. Liao, Z. -H. Jiang, S. -P Yan, G. -L. Wang, X. -K. Yao and H. -G. Wang, *Acta Chem. Scand.*, 1999, **53**, 387–390.
- (60) T. Neumann, I. Jess, L. S. Germann, R. E. Dinnebier and C. Näther, *Cryst. Growth Des.*, 2019, **19**, 1134–1143.
- (61) R. D. –Torres and S. Alvarez, *Dalton Trans.*, 2011, **40**, 10742.

Chapter 5



Chapter 5 : Structural transformations in metal organic frameworks for the exploration of their CO_2 sorption behavior at ambient and high pressure

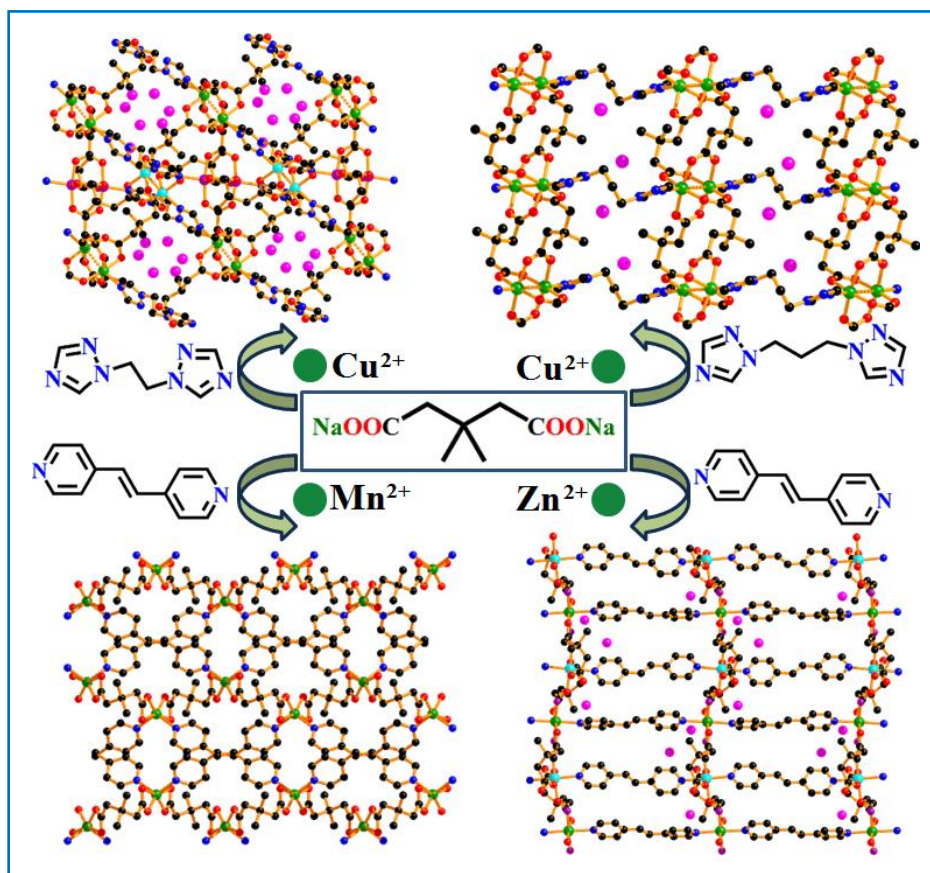
Chapter 5

Structural transformations in metal organic frameworks for the exploration of their CO₂ sorption behavior at ambient and high pressure

1. Introduction

Structural flexibility in metal-organic frameworks (MOFs)¹⁻³ has occupied the prior attention in recent days, to impose different functionalities, leading to their potential applications⁴⁻⁹. MOFs are well known for their highly tunable nature and directive structure property relationship.^{1,3} In addition to that, external stimuli responsive structural interchange for a flexible MOF, makes them even more impressive. Continuous study on such materials suggests that there are huge possibilities of retrofitting of different properties¹⁰⁻¹⁴ in such flexible MOFs, to use them according to the current demand for functionalities. Among many, selective sorption and separation of gases,¹⁵⁻¹⁸ by MOFs become very important topic of research at present. No doubt, CO₂ is one of such gases which needed to be captured selectively as the enhancement of CO₂ in atmosphere made carbon capture and sequestering as a foremost important step for the welfare of mankind. Different studies have shown that MOFs are certainly a good candidate for the CO₂ capture. In particular, mixed ligand MOFs^{19,20} have proven to be an extremely suitable material for this purpose due to their simple synthetic procedure²¹⁻²³ and tunable framework.^{24,25} Though a lot of mixed ligand MOFs, showing selective carbon dioxide sorption, has been reported earlier but the introduction of tuned and well decorated pore inside the structure eventually gives an enthusiastic outcome. Since pore dimension, pore environment and polarity of the pores inside the framework are the key parameters for better carbon dioxide adsorption,²⁶⁻²⁹ the appropriate choice of the mixed ligands to build up the networks with proper pores, is one of the key factors. Moreover, different binding modes of coligands^{30,31} create excellent topology and dimension in MOFs, which also has a great impact towards better gas sorption. In this regard, there are certain limitations in achieving appropriate structure with promising application.^{32,33} External stimuli responsive structural transformation is sometime found worthy to get rid of such limitations and to access appropriate architecture.³³⁻³⁶ Different studies are well documented till date, which show that this structural dynamicity is optimistically working in a structure to enhance material's application outcome.³³⁻³⁶

Inspired by these facts, a set of four new metal organic frameworks namely $\{[\text{Cu}_3(3,3'\text{-dmglut})_3(\text{bte})].6(\text{H}_2\text{O})\}_n$ (**1**), $\{[\text{Cu}(3,3'\text{-dmglut})(\text{btp})_{0.5}].2(\text{H}_2\text{O})\}_n$ (**2**), $[\text{Zn}(3,3'\text{-dmglut})_{0.5}(\text{bpe})_{0.5}]_n$ (**3**) and $\{[\text{Mn}_2(3,3'\text{-dmglut})_2(\text{bpe})_2(\text{H}_2\text{O})_2].5(\text{H}_2\text{O})\}_n$ (**4**) (Scheme 1) have been synthesized from the substituted glutarate, disodium 3,3'-dimethyl glutarate ($\text{Na}_2 3,3'\text{-dmglut}$) and three different N,N'-donor ligands, {1,2-bis(4-pyridyl)ethylene} (bpe), {1,2-bis(1,2,4-triazol-1-yl)ethane} (bte) and {1,3-bis(1,2,4-triazol-1-yl)propane} (btp). All the MOFs have been characterized by single-crystal X-ray diffraction along with other physicochemical methods. Here the aliphatic moiety in between two triazole moiety of N-donor ligand have been varried to study the effect of ligand flexibility on final structural outcome and it's consequences on their sorption properties. Out of four, three complexes shows structural transformation and that have a marked effect on their sorption properties. Different gas adsorption experiments have been performed for all these MOFs and CO_2 sorption experiments in all the cases are found interesting. Complex **3** shows quite a high CO_2 uptake amount at high presure due to pore opening-closing mechanism.³⁷



Scheme 1. Outline of synthesis for complexes **1–4**.

2. Experimental section

2.1. Materials

High purity copper(II) nitrate trihydrate, manganese (II) nitrate tetrahydrate, zinc(II) nitrate hexahydrate, 3,3'-dimethyl glutaric acid (H_2 -3,3'-dmglut), 1,2-bis(4-pyridyl)ethylene (bpe) have been purchased from the Sigma-Aldrich Chemical Co. and used without further purification. Other preparatory materials for the synthesis of 1,2-bis(1,2,4-triazol-1-yl)ethane (bte) and 1,3-bis(1,2,4-triazol-1-yl)propane (btp) have also been purchased from the Sigma-Aldrich Chemical Co. and the ligands have been synthesized following the previously reported procedure.^{38,39} Disodium salt of 3,3'-dimethyl glutaric acid has been prepared by the addition of $NaHCO_3$ to the aqueous suspension of the acid ligand in a 2 : 1 ratio and after complete neutralization (checking by pH paper) the resultant mixture has been allowed to evaporate at 100 °C to dryness. All other reagents and solvents have been purchased from commercial sources and have been used without further purification.

2.2. Physical measurements

Elemental analyses (carbon, hydrogen and nitrogen) of all the compounds have been accomplished by a Heraeus CHNS analyzer. Using a PerkinElmer Spectrum BX-II IR spectrometer, infrared spectra ($4000\text{--}400\text{ cm}^{-1}$) of all the four samples have been taken after preparing the KBr pellets of each compound. X-Ray powder diffraction (PXRD) patterns of the bulk samples have been proved by a Bruker D8 Discover instrument where Cu- $K\alpha$ radiation is used as the source. Lastly, the thermal analysis (TGA) has been carried out on a PerkinElmer Simultaneous Thermal Analyzer (STA 8000) using nitrogen atmosphere (flow rate: $50\text{ cm}^3\text{ min}^{-1}$), between the temperature range of 30–600 °C with a heating rate of $5\text{ }^\circ\text{C min}^{-1}$.

2.3. Sorption measurements

The N_2 (77 K) and CO_2 (195 K) adsorption isotherms have been measured for the dehydrated frameworks of **1–4** by using Quantachrome Autosorb-iQ adsorption instrument. In this instrument, highly pure N_2 gas (99.999% purity) and CO_2 gas (99.95%) have been used for the sorption measurements purpose. The ambient pressure volumetric adsorptions for N_2 maintaining liquid-nitrogen bath at 77 K and for CO_2 at 195 K using dry ice-acetone bath have been performed in the pressure range 0–1 bar taking the activated samples of all the compounds. Before studying the sorption, the as-synthesized compounds of **1–4** ($\sim 40\text{ mg}$ for each) have been activated at 413 K, for 4 h under a $1\times 10^{-1}\text{ Pa}$ vacuum by taking them in the sample tube to

prepare them for measurement of the isotherms. Then, the sorption measurements have been performed by using proper adsorbate. For different gas sorption experiments, helium is used for void volume calculations whereas ($P_{\text{cal}}-P_e$) is calculated from analyte gas pressure after diffusion in the cell. The ultra pure helium gas (99.999% purity) has been introduced to the gas chamber and let to diffuse into the sample tube by controlling the valve. Finally, from the difference of pressure ($P_{\text{cal}}-P_e$), where P_{cal} is the calculated pressure without any gas adsorption and P_e denotes the observed pressure at equilibrium, the gas adsorption volume has been calculated. The high pressure carbon dioxide sorption measurement has been performed using Quantachrome Isorb-iQ adsorption instrument and following almost the same previously mentioned stepwise procedure for Autosorb-iQ. In this case the carbon dioxide gas adsorption has been executed at 273K up to 20 bar pressure. All these procedures are computer controlled and automatic.

2.4. Crystallographic data collection and refinement

The suitable single crystal of compounds **1–4** have been mounted on a tip of thin glass fibers with commercially available super glue. X-ray single crystal structural data of all the compounds have been collected at room temperature on a Bruker APEX II diffractometer, equipped with a normal focus, sealed tube X-ray source with graphite monochromated Mo- $K\alpha$ radiation ($\lambda = 0.71073 \text{ \AA}$). After taking the data, it has been integrated using the SAINT⁴⁰ program in each case and the absorption corrections for the obtained data have been done with SADABS⁴¹. The structure of compounds **1–4** have been solved by SHELXS 2016⁴² using the Patterson method, followed by successive Fourier and difference Fourier synthesis. SHELXL-2016⁴² has been used to perform full matrix least-squares refinements on F^2 . All nonhydrogen atoms have been refined anisotropically except few specific cases. For compound **1** all the guest water molecules are highly disordered whereas for compound **2** only the lattice water molecule O2W is disordered. All these atoms have been refined isotropically without fixing H atoms on it. In the compound **4** all the oxygen atoms of the lattice water molecules are disordered and refined anisotropically without fixing hydrogen atom. All the calculations have been carried out using SHELXS-2016,⁴² SHELXL-2016,⁴² PLATON v1.15,⁴³ WinGX system Ver-1.80,⁴⁴ TOPOS v3.2^{45,46} and Mercury v3.0⁴⁷. Data collection and structure refinement parameters and crystallographic data for complexes **1–4** are given in Table 1. The selected bond lengths and angles are given in Tables 2, 4, 5 and 7.

2.5. Syntheses

2.5.1. $\{[\text{Cu}_3(3,3'\text{-dmglu})_3(\text{bte})]\cdot 6(\text{H}_2\text{O})\}_n$ (**1**)

An aqueous solution (3 mL) of disodium 3,3'-dimethyl glutarate ($\text{Na}_23,3'\text{-dmglut}$) (1 mmol, 0.204 g in 20 mL) has been prepared and mixed with a methanolic solution (3 mL) of 1,2-bis(1,2,4-triazol-1-yl)ethane (bte) (1 mmol, 0.164 g in 20 mL) homogeneously by stirring. This mixed ligand solution has been carefully layered over 3 mL aqueous solution of $\text{Cu}(\text{NO}_3)_2\cdot 3\text{H}_2\text{O}$ (1 mmol, 0.241 g in 20 mL). 1:1 (v/v) H_2O and MeOH solution has been used as buffer solution to separate the metal from the ligand mixture. The tube has been sealed and kept undisturbed at room temperature. Green-colored block shaped single crystals suitable for X-ray obtained at the

Table 1. Data collection and refinement parameters for single crystal analysis for complexes **1–4**

	1	2	3	4
formula	$\text{C}_{27}\text{H}_{50}\text{N}_6\text{O}_{18}\text{Cu}_3$	$\text{C}_{10.5}\text{H}_{19}\text{N}_3\text{O}_6\text{Cu}$	$\text{C}_{9.5}\text{H}_{10}\text{NO}_2\text{Zn}$	$\text{C}_{38}\text{H}_{54}\text{N}_4\text{O}_{15}\text{Mn}_2$
formula weight	937.37	346.82	202.88	916.73
crystal system	triclinic	monoclinic	orthorhombic	monoclinic
space group	$P\bar{1}$	$C2/c$	$Pnna$	$P2_1/c$
$a/\text{\AA}$	11.5584(4)	25.725(4)	9.6927(3)	16.2761(4)
$b/\text{\AA}$	12.6026(4)	10.4434(16)	10.8344(4)	13.9146(3)
$c/\text{\AA}$	14.4817(5)	13.605(2)	17.6382(6)	20.4241(4)
$\alpha/^\circ$	76.331(2)	90	90	90
$\beta/^\circ$	71.291(2)	120.199(9)	90	101.894(1)
$\gamma/^\circ$	88.362(2)	90	90	90
$V/\text{\AA}^3$	1938.88(12)	3159.0(9)	1852.27(11)	4526.25(17)
Z	2	4	4	4
$D_c/\text{g cm}^{-3}$	1.585	1.450	1.455	1.325
μ/mm^{-1}	1.710	1.409	1.352	0.625
$F(000)$	946	1424	840	1864
θ range/ $^\circ$	1.5 - 27.5	1.8 - 27.6	2.2- 27.5	1.8- 27.6
reflections collected	33318	21147	29205	75918
unique reflections	8831	3654	2142	10440
reflections $I > 2\sigma(I)$	6297	2546	1358	7520
R_{int}	0.052	0.093	0.082	0.041
goodness-of-fit (F^2)	1.07	1.11	1.01	1.03
$R1$ ($I > 2\sigma(I)$) ^a	0.051	0.0781	0.0421	0.0458
$wR2$ ($I > 2\sigma(I)$) ^a	0.1428	0.2886	0.1206	0.1492
$\Delta\rho$ min / max /e \AA^3	-0.93, 1.36	-0.78, 2.27	-0.36, 0.99	-0.37, 0.77

$$^a R_1 = \sum |F_o| - |F_c| / \sum |F_o|, wR_2 = [\sum (w(F_o^2 - F_c^2))^2 / \sum w(F_o^2)^2]^{1/2}.$$

wall of the tube after 3 weeks. After manually collection of the crystals it has been washed with a methanol-water (1:1) mixture and dried under air (yield 52% based on metal). Anal. calc. for $\text{C}_{27}\text{H}_{50}\text{N}_6\text{O}_{18}\text{Cu}_3$ (**1**, %): C, 34.59; H, 5.38; N, 8.96. Found: C, 34.54; H, 5.41, N, 8.91. IR spectra

(KBr pellet, 4000–400 cm^{-1}): $\nu(\text{H}_2\text{O})$, 3251; $\nu(\text{C}-\text{C})$, 1470; $\nu(\text{C}-\text{H})$ 1359; $\nu(\text{C}-\text{N})$, 1279 and $\nu(\text{C}-\text{O})$, 1171 (Figure 1a).

2.5.2. $\{[\text{Cu}(\mathbf{3},\mathbf{3}'\text{-dmglu})(\text{btp})_{0.5}]\cdot 2(\text{H}_2\text{O})\}_n$ (**2**)

This compound has been synthesized following the same procedure as in case of **1**, but here 1,3-bis(1,2,4-triazol-1-yl)propane (btp) (1 mmol, 0.178 g in 20 mL) has been used instead of 1,2-bis(1,2,4-triazol-1-yl)ethane (bte) (1 mmol, 0.164 g in 20 mL). After 4 weeks deep green block shaped crystal suitable for X-ray has been observed at the wall of the test tube with 47% yield. This compound has been separated manually and washed with (1:1) water–methanol. Anal. calc. for $\text{C}_{10.5}\text{H}_{19}\text{N}_3\text{O}_6\text{Cu}$ (**2**, %): C, 36.36; H, 5.52; N, 12.12. Found: C, 36.33; H, 5.47, N, 12.15. IR spectra (KBr pellet, 4000–400 cm^{-1}): $\nu(\text{H}_2\text{O})$, 3417; $\nu(\text{C}-\text{C})$, 1480; $\nu(\text{C}-\text{H})$, 1393; $\nu(\text{C}-\text{N})$, 1277 and $\nu(\text{C}-\text{O})$, 1195 (Figure 1b).

2.5.3. $[\text{Zn}(\mathbf{3},\mathbf{3}'\text{-dmglu})_{0.5}(\text{bpe})_{0.5}]_n$ (**3**)

This compound has also been synthesized by following the same technique as used in **1**. Here the metal has been changed from $\text{Cu}(\text{NO}_3)_2\cdot 3\text{H}_2\text{O}$ (1 mmol, 0.241 g in 20 mL) to $\text{Zn}(\text{NO}_3)_2\cdot 6\text{H}_2\text{O}$ (1 mmol, 0.297 g in 20 mL) and 1,2-bis(4-pyridyl)ethylene (bpe) (1 mmol, 0.184 g in 20 mL) has been used instead of 1,2-bis(1,2,4-triazol-1-yl)ethane (bte) (1 mmol, 0.164 g in 20 mL). White niddle shaped crystal suitable for X-ray at the wall of the test tube obtained with 61% yield after 4 weeks. The compound has been separated after washing with (1:1) water–methanol and dried under air. Anal. calc. for $\text{C}_{9.5}\text{H}_{10}\text{NO}_2\text{Zn}$ (**3**, %): C, 56.24; H, 4.97; N, 6.90. Found: C, 56.21; H, 4.95, N, 6.93. IR spectra (KBr pellet, 4000–400 cm^{-1}): $\nu(\text{CH}-\text{Ar})$, 3100–2900; $\nu(\text{C}=\text{C}, \text{Ar})$, 1530–1432; $\nu(\text{CH}-\text{alkane})$, 1431–1354; $\nu(\text{C}=\text{C})$, 1680–1560; $\nu(\text{C}-\text{C})$, 1480; $\nu(\text{C}-\text{H})$, 1393; $\nu(\text{C}-\text{O})$, 1250–1060 (Figure 1c).

2.5.4. $\{[\text{Mn}_2(\mathbf{3},\mathbf{3}'\text{-dmglu})_2(\text{bpe})_2(\text{H}_2\text{O})_2]\cdot 5(\text{H}_2\text{O})\}_n$ (**4**)

Using the same slow diffusion technique as **1**, this compound has been synthesized too, where $\text{Mn}(\text{NO}_3)_2\cdot 4\text{H}_2\text{O}$ (1 mmol, 0.251 g in 20 mL) is used instead of $\text{Cu}(\text{NO}_3)_2\cdot 3\text{H}_2\text{O}$ (1 mmol, 0.241 g in 20 mL) and 1,2-bis(4-pyridyl)ethylene (bpe) (1 mmol, 0.184 g in 20 mL) has also been used in place of bte (1 mmol, 0.164 g in 20 mL). Yellowish-orange colored block shaped crystal suitable for X-ray found in the wall of the test tube with 55% yield. These crystals have been collected by washing with (1:1) water–methanol. Anal. calc. for $\text{C}_{38}\text{H}_{54}\text{N}_4\text{O}_{15}\text{Mn}_2$ (**4**, %): C, 49.78; H, 5.94; N, 6.11. Found: C, 49.74; H, 5.91; N, 6.14. IR spectra (KBr pellet, 4000–400

cm^{-1}): IR spectra (in cm^{-1}): $\nu(\text{CH-Ar})$, 3100–2900; $\nu(\text{C=C, Ar})$, 1530–1432; $\nu(\text{CH-alkane})$, 1431–1354; $\nu(\text{C=C})$, 1680–1560; $\nu(\text{C-C})$, 1480; $\nu(\text{C-H})$, 1393; $\nu(\text{C-O})$, 1250–1060 (Figure 1d).

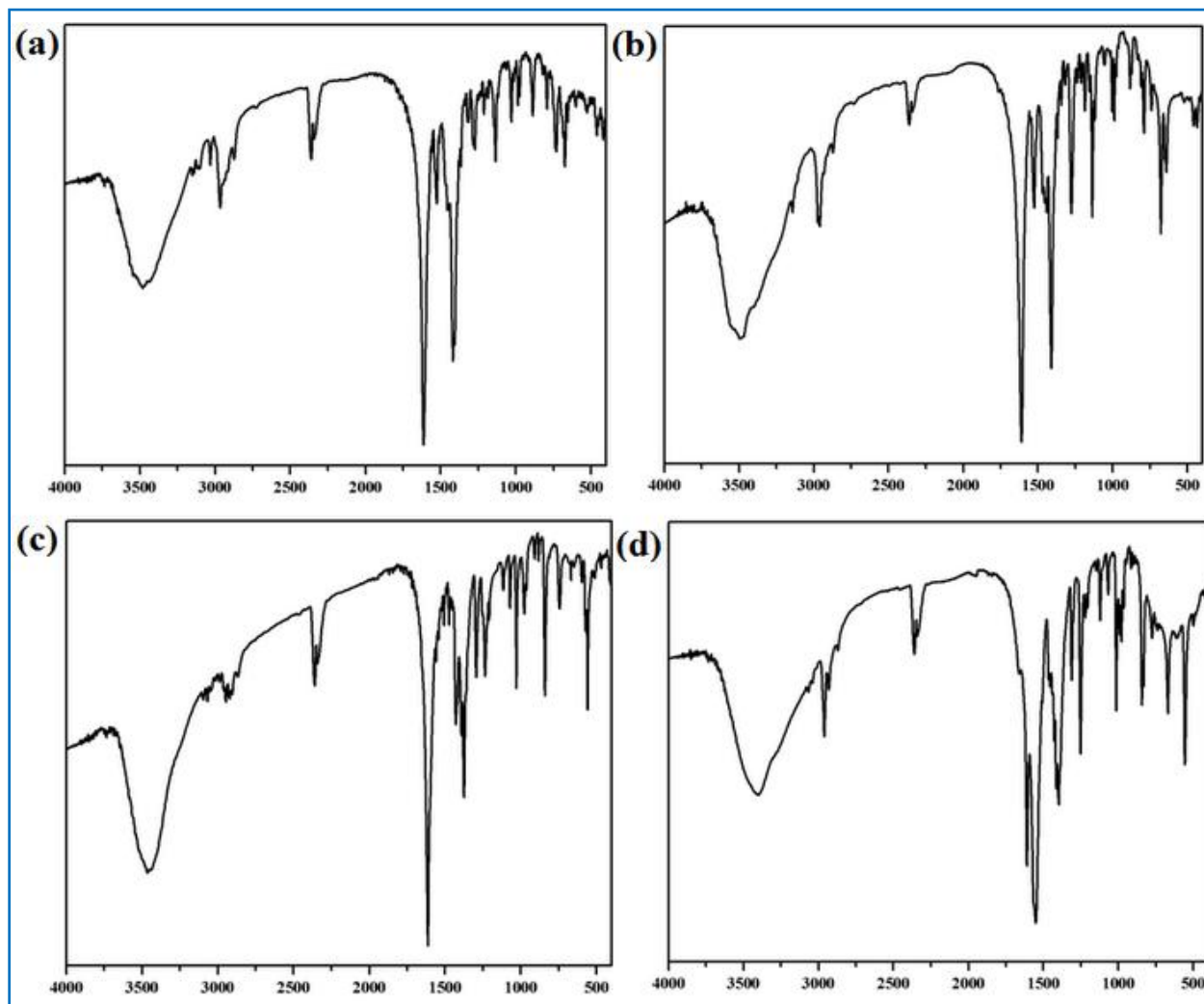
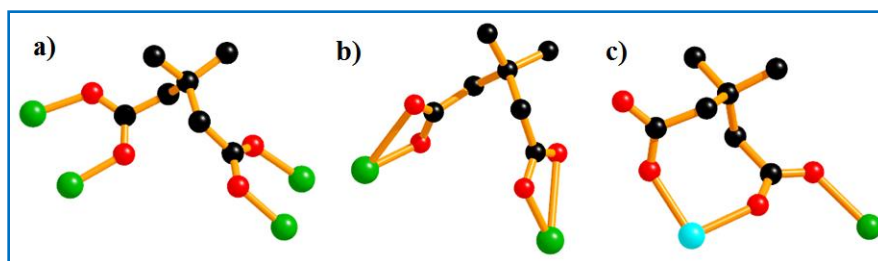


Figure 1. FT-IR spectra of (a) complex **1**, (b) complex **2**, (c) complex **3**, and (d) complex **4**.

2.6. Different binding modes of 3,3'-dmglut

Variable binding modes of the 3,3'-dmglut is very much relevant here which finally results structural diversity in synthesized MOFs. Moreover, this variation is completely responsible for different dimension of frameworks. Different binding modes of the 3,3'-dmglut obtained for these four reported structures has been depicted in Scheme 2.



Scheme 2. Different binding modes of the 3,3'-dmglut in **1–4**; (a) bis bidentate mode of the 3,3'-dmglut in **1** and **2**, (b) bis-chelating mode of the 3,3'-dmglut in **3**, (c) bidentate and monodentate modes from the two opposite carboxylate group of the 3,3'-dmglut in **4**.

3. Results and discussion

3.1. Structural descriptions

3.1.1. $\{[\text{Cu}_3(3,3'\text{-dmglut})_3(\text{bte})].6(\text{H}_2\text{O})\}_n$ (**1**)

It is confirmed from single crystal X-ray analysis that the complex **1** attains a porous 3D framework built by Cu(II) ions, 3,3'-dmglut and bte linkers. The complex crystallizes in the triclinic $P\bar{1}$ space group. The asymmetric unit of this complex contains three crystallographically independent Cu(II) centers (Cu1, Cu2 and Cu3 all are pentacoordinated), three 3,3'-dmglut ligands, one bte ligand and five guest water molecules. All these Cu(II) centers are with same distorted square pyramidal geometry and CuO_4N coordination environment. Each Cu(II) centers are connected to four oxygen atoms from four different 3,3'-dmglut ligands and one nitrogen atom from bte ligand^{48,49} (Figure 2a). The Cu–O bond length varies from 1.948(3) – 1.997(3) Å considering all the Cu (II) centers (Cu1, Cu2 and Cu3). The Cu–N bond lengths are in the range of 2.144(4) – 2.230(4) Å. Here, each 3,3'-dmglut connects two different metal centers by bidentate bridging mode from the both side. Hence, the three independent metal centers are attached by three different dicarboxylate to build a 3D arrangement (Figure 2b). Here each metal center (Cu1, Cu2, Cu3) forms the same paddle-wheel $\text{Cu}_2(\text{CO}_2)_4$ dinuclear secondary building units (SBUs)^{50,51} individually which finally construct the interesting 3D arrangement of metal-dicarboxylate. The metal centers Cu1–Cu1, Cu2–Cu2 and Cu3–Cu3 are separated by 2.6053 Å, 2.5974 Å and 2.6120 Å respectively. The bte linkers connect the 3D metal–carboxylate arrangement in a diagonal fashion to create a 3D framework (Figure 2c) with rectangular pores. Guest water molecules occupy these pores of the framework along the crystallographic *c* axis. The dimension of the solvent channel in the framework is about 3.7 Å × 2 Å which implies a

void space of $\sim 23.9\%$ (462.8 \AA^3) of the total crystal volume (1938.9 \AA^3). The 3D structure is also stabilized by intermolecular π - π interactions (Figure 3). Topological analysis of the network using TOPOS^{45,46} indicates the formation of (3,4,6)-connected trinodal net^{52,53} (Figure 2d).

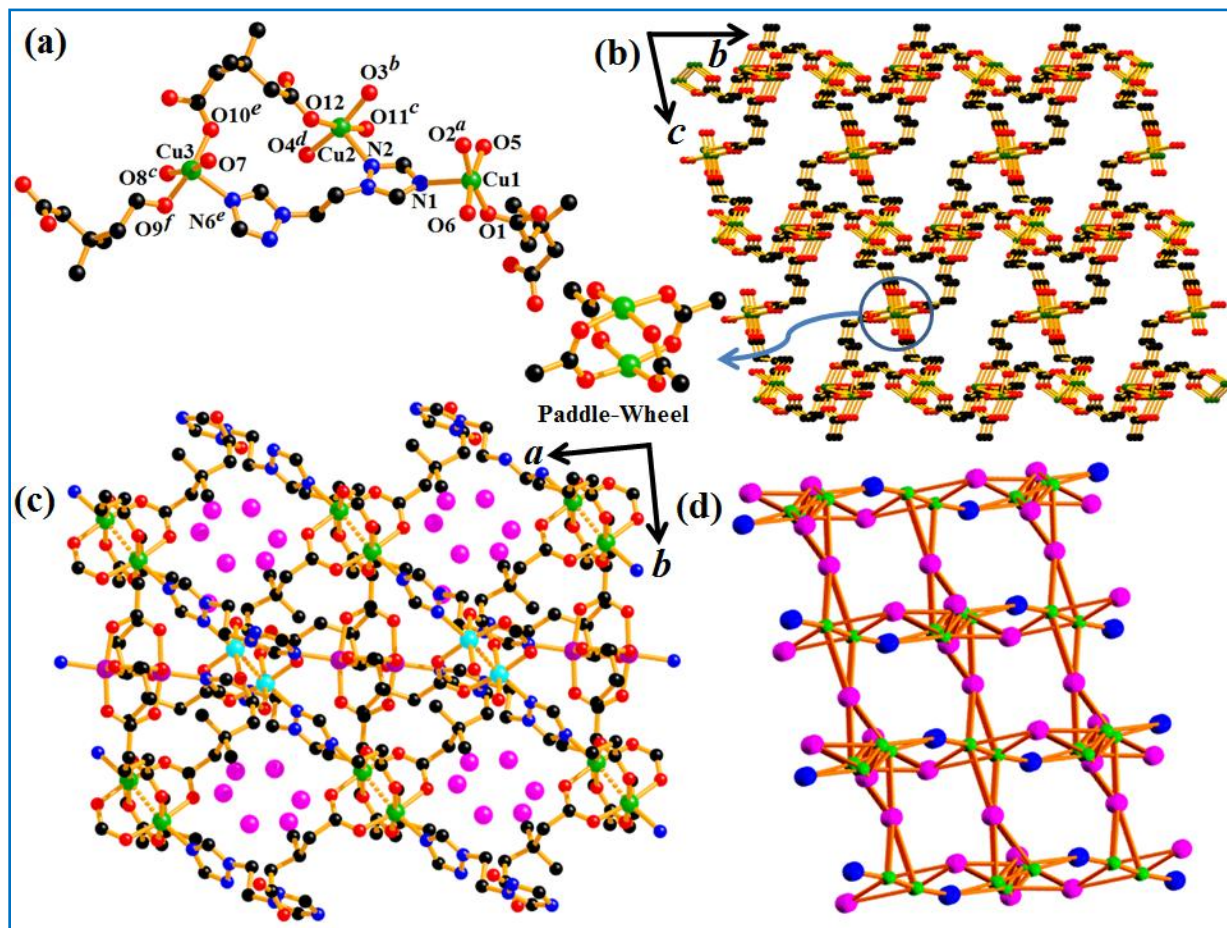


Figure 2. (a) Coordination environment of three penta coordinated Cu(II) center in complex **1**; where the color of Cu, O, N and C are green, red, blue and black respectively. (b) 3D metal carboxylate framework of **1** along crystallographic *a* axis (slightly tilted for clearly showing 3D framework), bte ligands and dimethyl groups are excluded for clear view. (c) Guest water filled channels in 3D framework of **1**, Cu1 (green), Cu2 (turquoise) and Cu3 (violet). (d) Simplified topological representation of 3,4,6-connected 3D net of complex **1**.

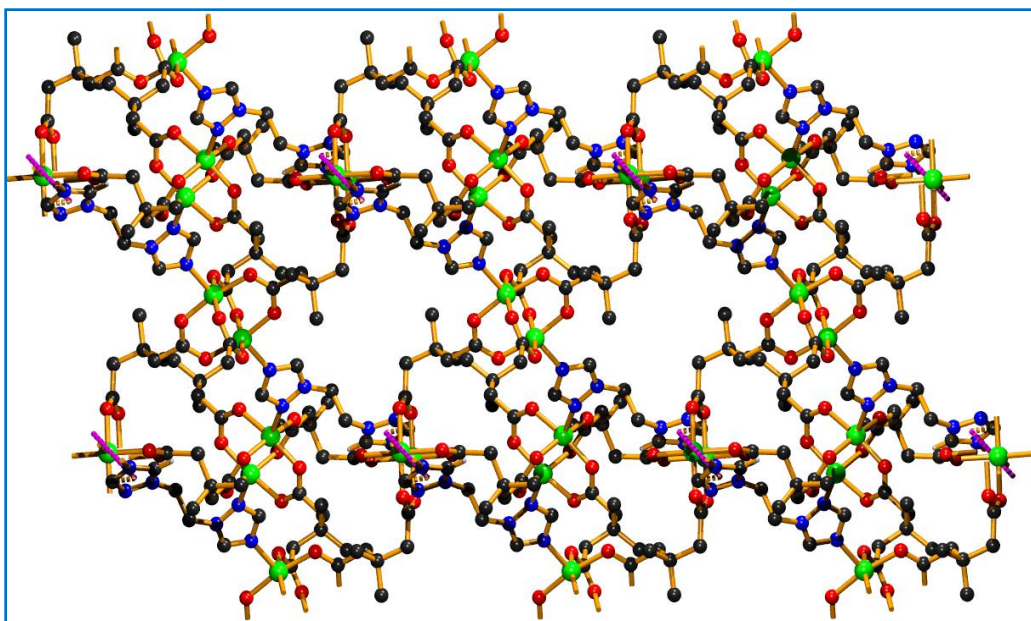


Figure 3. Intermolecular π - π interaction in complex **1**.

Table 2. Selected bond lengths (Å) and bond angles (°) for **1**

Cu1–O1	1.970(3)	Cu1–O5	1.961(3)
Cu1–N1	2.144(4)	Cu1–O2 ^a	1.997(3)
Cu1–O6	1.965(3)	Cu2–N2	2.230(4)
Cu2–O11 ^c	1.973(3)	Cu2–O3 ^b	1.970(3)
Cu2–O4 ^d	1.958(3)	Cu2–O12	1.948(3)
Cu3–O10 ^e	1.954(3)	Cu3–O8 ^c	1.978(3)
Cu3–O9 ^f	1.959(3)	Cu3–O7	1.989(3)
Cu3–N6 ^e	2.146(4)	O1–Cu1–O5	88.81(13)
O1–Cu1–N1	100.74(13)	O1–Cu1–O2 ^a	169.08(11)
O1–Cu1–O6	90.91(13)	O5–Cu1–N1	99.00(12)
O2 ^a –Cu1–O5	88.36(12)	O5–Cu1–O6	169.03(12)
O2 ^a –Cu1–N1	90.11(12)	O6–Cu1–N1	91.83(12)
O2 ^a –Cu1–O6	89.87(12)	O11 ^c –Cu2–N2	90.54(11)
O3 ^b –Cu2–N2	92.36(13)	O4 ^d –Cu2–N2	98.91(13)
O12–Cu2–N2	100.48(11)	O3 ^b –Cu2–O11 ^c	90.06(12)
O4 ^d –Cu2–O11 ^c	90.38(12)	O11 ^c –Cu2–O12	168.94(11)
O3 ^b –Cu2–O4 ^d	168.71(14)	O3 ^b –Cu2–O12	88.62(12)
O4 ^d –Cu2–O12	88.79(12)	O8 ^c –Cu3–O10 ^e	88.91(11)
O9 ^f –Cu3–O10 ^e	168.94(15)	O7–Cu3–O10 ^e	89.05(11)
O10 ^e –Cu3–N6 ^e	96.14(13)	O8 ^c –Cu3–O9 ^f	90.03(11)
O7–Cu3–O8 ^c	168.63(15)	O8 ^c –Cu3–N6 ^e	100.27(15)
O7–Cu3–O9 ^f	89.83(11)	O9 ^f –Cu3–N6 ^e	94.88(13)
O7–Cu3–N6 ^e	91.07(14)		

Symmetry code: *a* = -*x*, 1-*y*, 1-*z*; *b* = 1+*x*, *y*, *z*; *c* = 1-*x*, -*y*, 1-*z*; *d* = -*x*, -*y*, 1-*z*; *e* = *x*, *y*, *z*; *f* = 2-*x*, -*y*, -*z*.

Table 3. π – π interactions for **1**

ring(i) \rightarrow ring(j)	distance of centroid(i) from ring(j), (Å)	dihedral angle (i,j) (deg)	distance between the (i,j) ring centroids, (Å)
R(1) \rightarrow R(1) ⁱ	-3.358(2)	0	3.974(3)

Symmetry code: i = 1-x, -y, -z.

R(i)/R(j) denotes the $i^{\text{th}}/j^{\text{th}}$ rings in the corresponding structures: R(1) = N(4)/N(5)/C(5)/N(6)/C(6).

3.1.2. $\{[\text{Cu}(\text{3,3'-dmglut})(\text{btp})_{0.5}]\cdot 2(\text{H}_2\text{O})\}_n$ (**2**)

Single crystal X-ray analysis of complex **2** reveals that it crystallizes in the monoclinic $C2/c$ space group and creates a porous 3D structure with the help of Cu(II) ion, 3,3'-dmglut and btp linkers. One Cu(II) ion, one 3,3'-dmglut, half btp ligand and two lattice water molecules are present in the asymmetric unit of complex **2**. Same as **1**, each penta coordinated Cu(II) center with CuO_4N environment is neighboured by four oxygen atoms (O1, O2, O3, O4) from four different 3,3'-dmglut and one nitrogen atom (N1) from the btp ligand which finally makes a distorted trigonal bipyramidal geometry around the Cu(II) metal center (Figure 4a). The Cu–O bond length varies from 1.964(5) – 1.983(5) Å whereas the Cu–N bond length is 2.138(6) Å. Each 3,3'-dmglut ligand bridges with four different metal centers through bidentate mode from the both side and form a 2D sheet structure along the crystallographic bc plane (Figure 4b). Here four different glutarate units connect two Cu(II) centres to build a paddle-wheel^{50,51} $\text{Cu}_2(\text{CO}_2)_4$ dinuclear secondary building units (SBUs) like the previous case (complex **1**). The metal centers Cu1–Cu1 are separated by 2.6475 Å. This 2D sheets finally forms a 3D porous framework by zig-zag fashioned btp ligand. These 3D network contains rectangular pore along the crystallographic b axis which are filled by the guest solvent molecules (Figure 4c). The dimension of the water channel is about $7.6 \text{ Å} \times 3.5 \text{ Å}$ which provides a solvent accesible void of 743.6 Å^3 which is ~23.6% of the total crystal volume (3155.2 Å^3). Topological analysis of this structure using TOPOS^{45,46} clearly depicts the construction of (4,6)-connected binodal net, where the point symbol is $\{3^2.6^2.7^2\}\{3^4.4^6.6^4.7\}$ (Figure 4d).

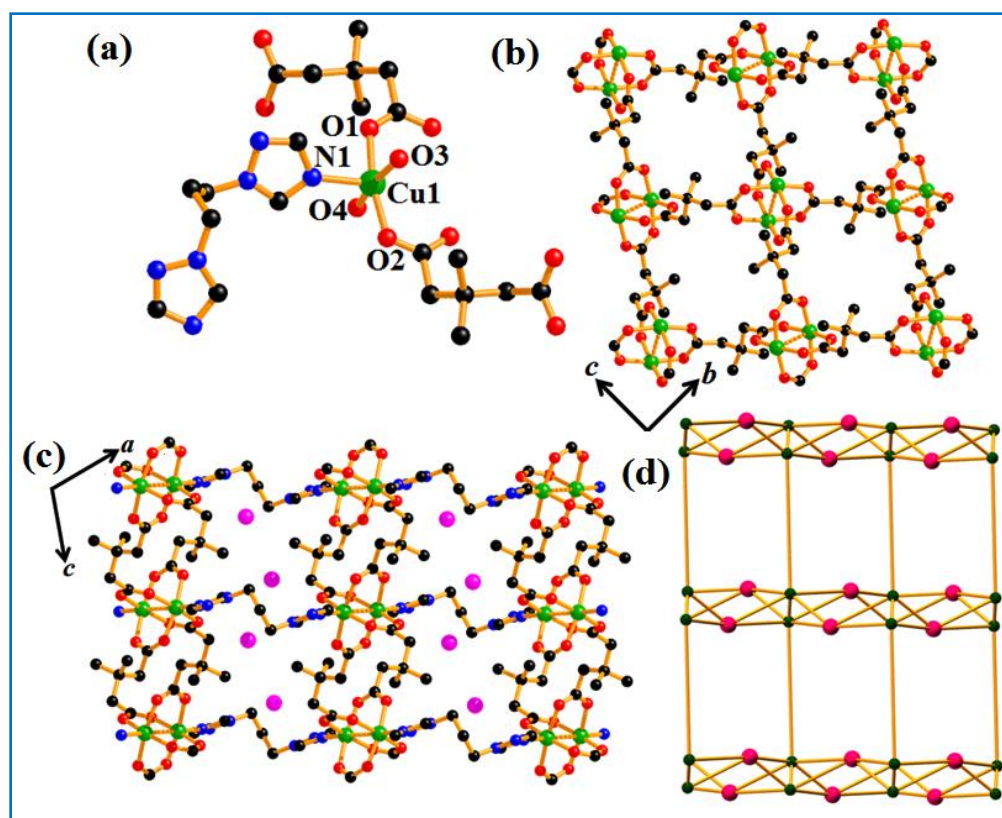


Figure 4. (a) Coordination environment of penta coordinated Cu(II) center in complex **2**; where the color of Cu, O, N and C are green, red, blue and black respectively. (b) 2D metal carboxylate sheet in **2** along the *bc* plane (btp ligands are excluded for clear view). (c) Guest water filled channel along the *b* axis in 3D framework of **2**. (d) Simplified topological representation of (4,6)-connected binodal net of **2**.

Table 4. Selected bond lengths (Å) and bond angles (°) for **2**

Cu1–O1	1.977(5)	Cu1–N1	2.138(6)
Cu1–O3	1.983(5)	Cu1–O4	1.977(5)
Cu1–O2	1.964(5)	O1–Cu1–N1	91.2(2)
O1–Cu1–O3	89.1(2)	O1–Cu1–O4	89.4(2)
O1–Cu1–O2	167.7(2)	O3–Cu1–N1	94.4(3)
O4–Cu1–N1	97.4(3)	O2–Cu1–N1	101.2(2)
O3–Cu1–O4	168.2(2)	O2–Cu1–O3	89.5(2)
O2–Cu1–O4	89.6(2)		

3.1.3. [Zn(3,3'-dmglut)_{0.5}(bpe)_{0.5}]_n (**3**)

Single crystal X-ray analysis reflects that the complex **3** forms a 3D framework built by Zn(II) ion, 3,3'-dmglut and bpe being crystallized in orthorhombic *Pnna* space group. The asymmetric unit for this complex has been constituted by the association of one Zn(II) ion, half 3,3'-dmglut

and half bpe linkers. The Zn (II) center is surrounded by four oxygen atoms (O1, O2, O1^a, O2^a) from two different symmetry related 3,3'-dmglut and by two nitrogen atoms (N1, N1^a) from two different symmetry related bpe ligands which finally builds a octahedral geometry (distorted) with ZnO₄N₂ environment (Figure 5a).

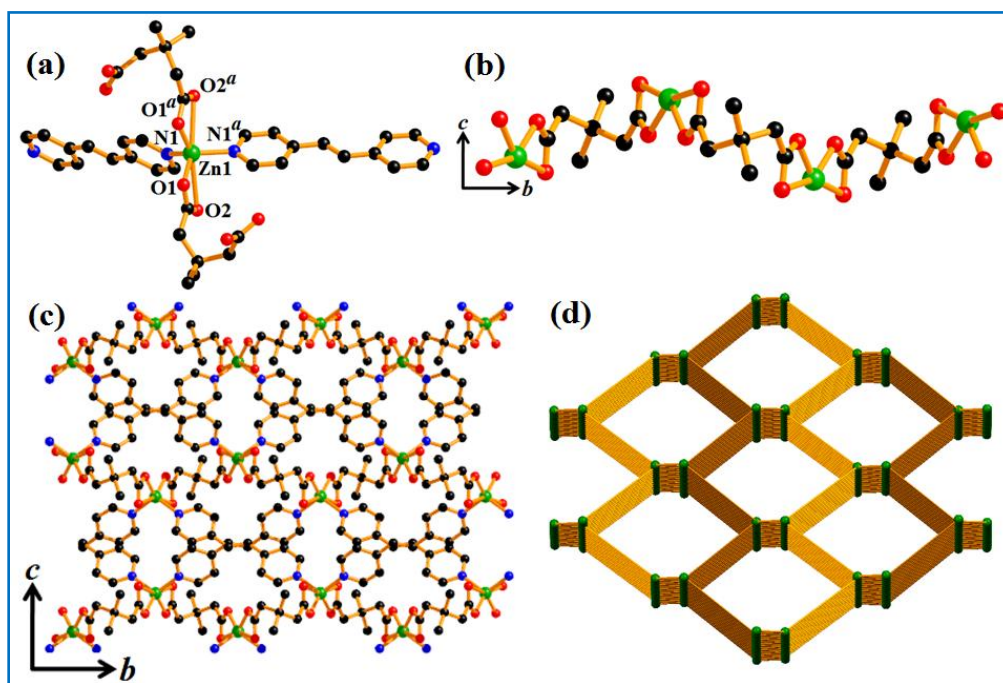


Figure 5. (a) Coordination environment of hexa coordinated Zn(II) center in complex **3**; where the color of Zn, O, N and C are green, red, blue and black respectively. (b) 1D zig-zag metal–3,3'-dmglut chain in **3** along the *b* axis (bpe ligands are excluded for clear view). (c) 3D framework along the *bc* plane in **3**. (d) Simplified topological representation of (4)-connected uninodal net in **3**.

Table 5. Selected bond lengths (Å) and bond angles (°) for **3**

Zn1–O1	1.958(2)	Zn1–O2	2.725(3)
Zn1–N1	2.042(2)	Zn1–O1 ^a	1.958(2)
Zn1–O2 ^a	2.725(3)	Zn1–N1 ^a	2.042(2)
O1–Zn1–O2	52.60(8)	O1–Zn1–N1	113.65(10)
O1–Zn1–O1 ^a	94.74(9)	O1–Zn1–O2 ^a	147.09(8)
O1–Zn1–N1 ^a	110.23(9)	O2–Zn1–N1	83.79(9)
O1 ^a –Zn1–O2	147.09(8)	O2–Zn1–O2 ^a	160.27(8)
O2–Zn1–N1 ^a	85.37(9)	O1 ^a –Zn1–N1	110.23(9)
O2 ^a –Zn1–N1	85.37(9)	N1–Zn1–N1 ^a	113.08(10)
O1 ^a –Zn1–O2 ^a	52.60(8)	O1 ^a –Zn1–N1 ^a	113.65(10)
O2 ^a –Zn1–N1 ^a	83.79(9)		

Symmetry code: *a* = - 0.5+x, 1+y, 1-z.

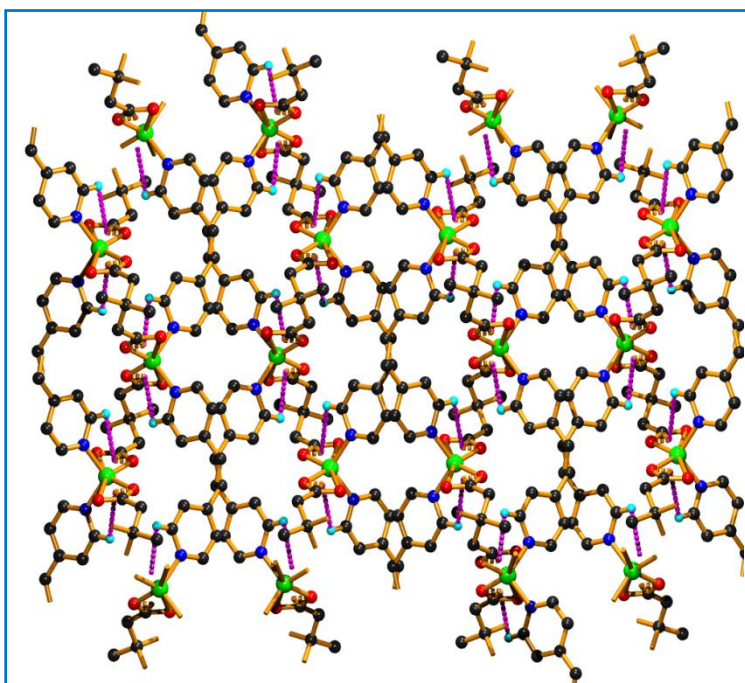
Table 6. Intermolecular π - π & C-H... π interactions in **3**

C-H ring(j)	H...R distance (Å)	C-H...R angle (deg)	C...R distance (Å)
C(10)-H(10)→R(1) ⁱ	2.77	106	3.162(3)
C(10)-H(10)→R(2) ⁱⁱ	2.77	106	3.162(3)

Symmetry code: i = 3/2-X, -Y, Z. ii = X, Y, Z.

R(j) denotes the jth rings in the corresponding structures: R(1) = Zn(1)/O(1)/C(1)/O(2); R(2) = Zn(1)/O(1)^a/C(1)^a/O(2)^a.

For this structure, the Zn-O bond lengths varies from 1.958(2) – 2.725(3) Å and the Zn-N bond lengths are 2.042(2) Å. Each 3,3'-dmglut connects with two metal centers through bidentate bridging mode from the both side and finally builds a 1D zig-zag chain along the crystallographic *b* axis (Figure 5b). These 1D metal carboxylate chains are again linked by the bpe linker in crisscross fashion to make an overall 3D framework along *bc* plane (Figure 5c). This 3D structure also participates in intermolecular C-H... π interactions in solid-state (Figure 6). Total potential solvent accessible void is 90.9 Å³ which is ~4.90% of the total crystal volume (1852.27 Å³). The use of unsubstituted dicarboxylate (glutarate in place of 3,3'-dmglut) gives 2D structure with larger void.⁵⁴ Network analysis by TOPOS^{45,46} confirmed the formation of (4)-connected uninodal net with the point symbol (Schläfli symbol) {6⁵·8} (Figure 5d).

**Figure 6.** Intermolecular C-H... π interactions in complex **3**.

3.1.4. $\{[\text{Mn}_2(3,3'\text{-dmglut})_2(\text{bpe})_2(\text{H}_2\text{O})_2]\cdot 5(\text{H}_2\text{O})\}_n$ (**4**)

Single crystal XRD confirms that the complex **4** being crystallized in the monoclinic $P2_1/c$ space group forms a 2D wavy sheet structure, made up by the Mn(II) ion, 3,3'-dmglut and bpe linkers. Asymmetric unit of this complex contains two crystallographically independent divalent metal centers (Mn1 and Mn2) associated with two 3,3'-dmglut, two bpe linkers and two coordinated water molecules along with five guest water molecules. Here, the Mn1 in octahedral MnO_4N_2 core is coordinated with four oxygen atoms (O2, O5, O1W, O2W) from two different 3,3'-dmglut and two coordinated water molecules along with two nitrogen atoms (N1, N2^c) from two different bpe ligands (Figure 7a).

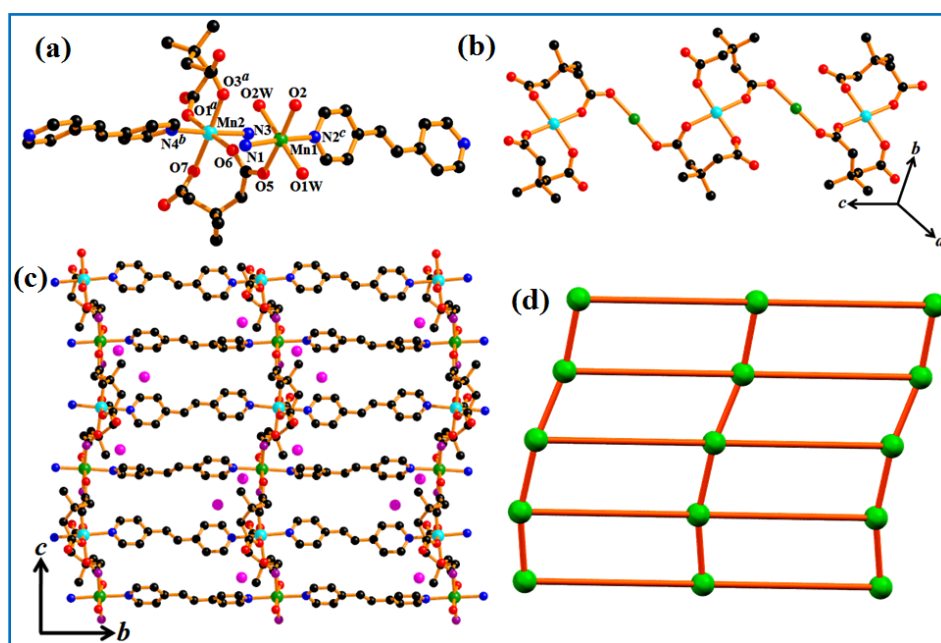


Figure 7. (a) Coordination environment of two hexa coordinated Mn(II) center in complex **4**; where the color of Mn, O, N and C are green, red, blue and black respectively. (b) 1D metal–3,3'-dmglut chain in **4** along the *c* axis (bpe ligands are excluded for clear view). (c) Water filled channel in 2D sheet of **4**. (d) Simplified topological representation of (4)-connected uninodal net in **4**.

On the other hand, Mn2 center creates MnO_4N_2 environment by four oxygen atoms (O1^a, O3^a, O6, O7) from two dicarboxylates and two nitrogen atoms (N3, N4^b) from two bpe ligands and forms the similar distorted octahedral moiety (Figure 7a). The Mn–O bond lengths are in the range of 2.1504(17)–2.2162(19) Å and the Mn–N bond length varies from 2.263(2) to 2.286(2) Å. Each 3,3'-dmglut bridges with two metal centers through bidentate mode from one side and

through monodentate mode from the other side to build a 1D chain along crystallographic *c* axis (Figure 7b). One oxygen atom from the 3,3'-dmglut, which is not attached to any metal centre is oriented towards the pore of the framework. These 1D chains are finally connected through the bpe linker resulting a 2D porous stair-like framework along *bc* plane (Figure 7c) which contain rectangular pores, filled up by the lattice water molecules. The dimension of the rectangular channel is about $2 \text{ \AA} \times 1.65 \text{ \AA}$ which generates a void space of $\sim 21.7\%$ (980.7 \AA^3) of the total crystal volume (4526.3 \AA^3). Network analysis by TOPOS^{45,46} exhibited that the framework forms (4)-connected uninodal net with the point symbol $\{4^4.6^2\}$ (Figure 7d).

Table 7. Selected bond lengths (Å) and bond angles (°) for **4**

Mn1–O1W	2.2162(19)	Mn1–O2	2.1757(19)
Mn1–O2W	2.2069(19)	Mn1–O5	2.1862(19)
Mn1–N1	2.286(2)	Mn1–N2 ^c	2.263(2)
Mn2–O6	2.1504(17)	Mn2–O7	2.1622(19)
Mn2–N3	2.283(2)	Mn2–N4 ^b	2.283(2)
Mn2–O1 ^a	2.1509(17)	Mn2–O3 ^a	2.1629(17)
O1W–Mn1–O2	99.52(7)	O1W–Mn1–O2W	179.17(7)
O1W–Mn1–O5	82.91(7)	O1W–Mn1–N1	88.16(7)
O1W–Mn1–N2 ^c	90.69(7)	O2–Mn1–O2W	79.68(7)
O2–Mn1–O5	176.66(7)	O2–Mn1–N1	89.33(8)
O2–Mn1–N2 ^c	94.78(7)	O2W–Mn1–O5	97.91(7)
O2W–Mn1–N1	92.02(8)	O2W–Mn1–N2 ^c	89.20(8)
O5–Mn1–N1	88.45(8)	O5–Mn1–N2 ^c	87.47(7)
N1–Mn1–N2 ^c	175.87(8)	O6–Mn2–O7	95.90(7)
O6–Mn2–N3	89.92(7)	O6–Mn2–N4 ^b	90.08(7)
O1 ^a –Mn2–O6	178.04(7)	O3 ^a –Mn2–O6	83.67(7)
O7–Mn2–N3	94.24(7)	O7–Mn2–N4 ^b	88.62(8)
O1 ^a –Mn2–O7	84.04(7)	O3 ^a –Mn2–O7	176.11(7)
N3–Mn2–N4 ^b	177.13(8)	O1 ^a –Mn2–N3	88.14(7)
O3 ^a –Mn2–N3	89.64(7)	O1 ^a –Mn2–N4 ^b	91.88(7)
O3 ^a –Mn2–N4 ^b	87.51(7)	O1 ^a –Mn2–O3 ^a	96.53(7)

Symmetry code: *a* = *x*, 0.5-*y*, 0.5+*z*; *b* = *x*, -1+*y*, *z*; *c* = *x*, 1+*y*, *z*.

3.2. Thermogravimetric analysis (TGA)

Thermogravimetric analysis (TGA) for all the complexes has been performed to check their thermal stabilities. Complex **1** shows a weight loss started at 62 °C and exhibits 11.49% (calcd, 11.53%) loss upto temperature 130 °C which validates the removal of six guest water molecules. After desolvation, complex **1** is stable up to ~ 255 °C without further weight loss; and it disintegrates into unspecified products with further heating above 260 °C (Figure 8). In case of complex **2**, the TGA curve reveals the weight loss of 10.43% (calcd, 10.39%) upto 134 °C which

has started from 58 °C. This weight loss corroborates the removal of two lattice water molecules from the framework and then the framework is stable upto 235 °C; and further heating above this temperature results some unidentified products of the complex (Figure 8). Complex **3** does not exhibit any significant weight loss up to 264 °C as no solvent molecule is present in the structure. If the framework is further heated above 264 °C, it collapses into unknown products (Figure 8). Being started at 47 °C, complex **4** shows a weight loss of 13.73% (calcd, 13.75%) which occurs up to 131 °C and confirms the presence of two coordinated and five lattice water molecules in the framework (Figure 8). After that, the framework is stable upto ~250 °C and finally decomposes into unspecified products by heating above ~250 °C. Thermogravimetric analysis (TGA) of all the complexes **1–4** after activation (denoted as **1'–4'**) has also been performed and given in Figure 9.

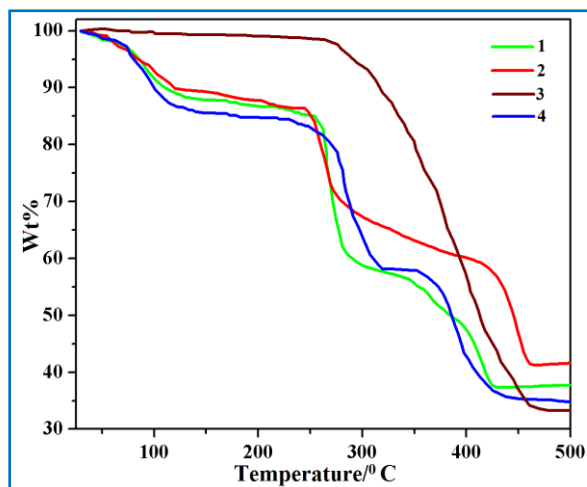


Figure 8. Thermogravimetric study (TGA) complexes **1–4**.

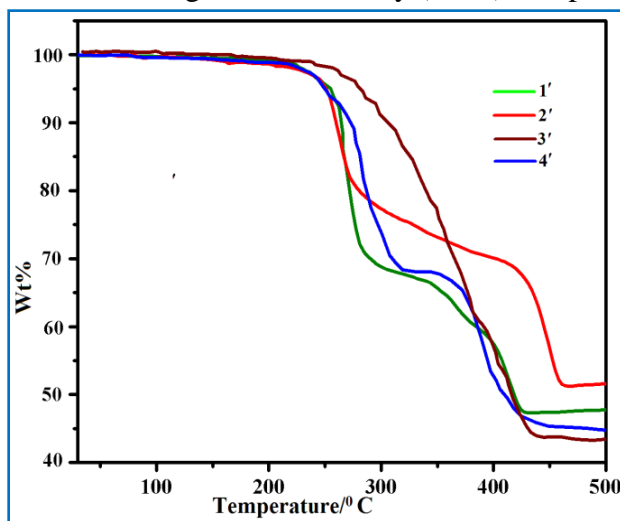


Figure 9. Thermogravimetric study (TGA) of complexes **1–4** after activation (denoted as **1'–4'**).

3.3. Sorption study

To investigate the porosity and keeping in mind about the solvent accessible void in the frameworks, the sorption behaviour has been studied using two different adsorbates (N_2 at 77K and CO_2 at 195K) for all the complexes after activation at certain temperature based on their stability after desolvation/activation. Though complex **1** contains channel along crystallographic c axis filled with lattice water molecules, it shows completely nonporous nature towards N_2 sorption (Figure 10a). It is due to the larger kinetic diameter of the N_2 molecules (kinetic diameter = 3.64 Å) and the transformation of structure after dehydration. The sorption affinity towards CO_2 also indicates the nonporous nature of the framework (Figure 10a) which can also be explained in terms of nonpolarity of the framework and blocking of the pore due to more rigid nature of the bte ligand. The uptake value for CO_2 sorption is 21 cc/g at 1 bar pressure and 195 K temperature. For N_2 , the uptake is up to 17 cc/g for complex **1** showing surface adsorption behaviour (Figure 10a). A high pressure sorption measurement^{55,56} of CO_2 at 273K (pressure varying from 0 to 20 bar) shows the maximum uptake is 123.82 cc/g (24.32 wt%) at 20 bar pressure in case of complex **1** (Figure 10b). This is due to the opening of blocked pore window at high pressure by pore opening/closing mechanism.³⁷ PXRD of desovated form of complex **1** substantially differs from its as-synthesized one, (Figure 11) indicating structural transformation. Again, a complete different PXRD pattern after high pressure sorption study is also found; which clearly indicates another structural transformation/reorganization from the

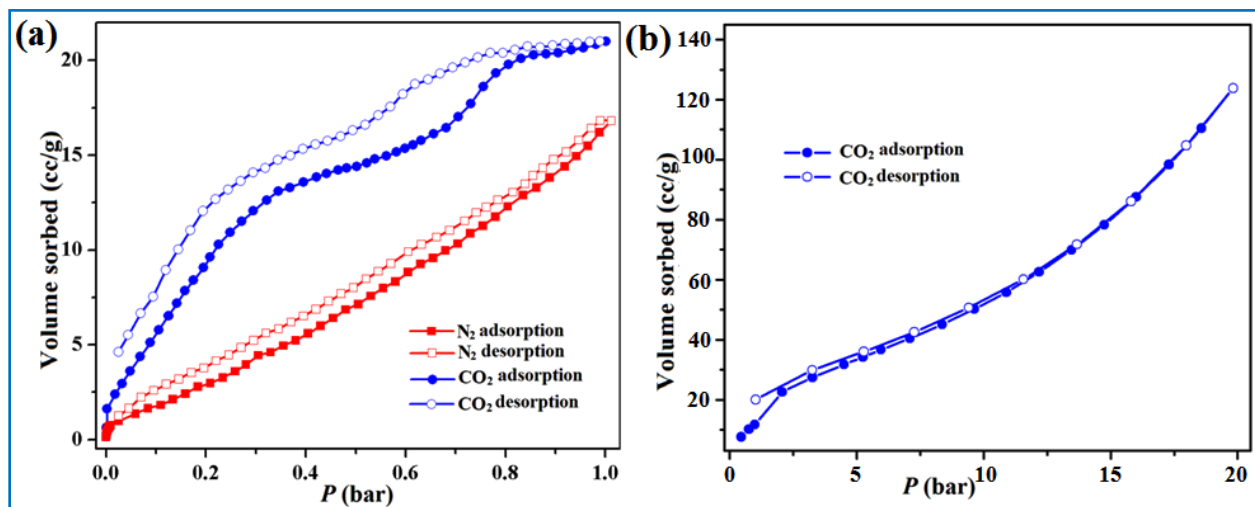


Figure 10. (a) N_2 adsorption (at 77 K) and CO_2 adsorption (at 195K) isotherms of **1**. (b) High pressure (upto 20 bar) CO_2 adsorption isotherms of **1** at 273K. Filled and open circles represent adsorption and desorption respectively.

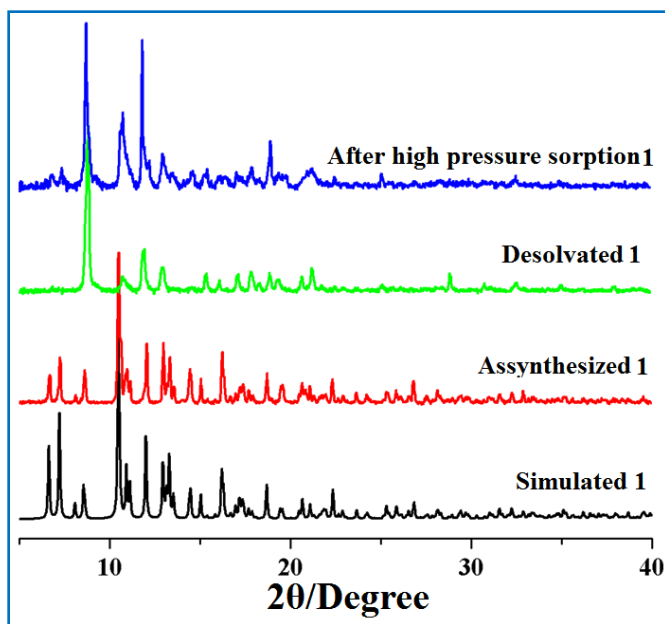


Figure 11. Powder X-ray diffraction (PXRD) of complex **1**.

desolvated phase, during high pressure sorption measurement (Figure 11). This structural transformation may also be responsible for higher uptake of CO₂ at 20 bar pressure for this complex.

In case of complex **2**, almost similar scenario has been observed. Here the used ligand (btp) is more flexible than the previous case (bte) but due to lack of polarity, here also no significant CO₂ sorption has been observed at ambient pressure (0 to 1 bar). Nitrogen sorption exhibits the uptake up to 15.6 cc/g whereas the CO₂ sorption isotherm shows the maximum uptake up to 26.2 cc/g (Figure 12a). Complex **2** shows slightly higher CO₂ uptake compared to **1**, at 1 atm pressure which occurs mainly due to the longer chain length of the ligands present in the framework of **2**. This enhancement of ligand size is directly responsible for pore size and creates the possibility of better CO₂ uptake for **2**. Alongside this enhancement in ligand size also can facilitated better pore appature during structural transformation which correlates the variation in CO₂ uptake for the complexes **1** and **2**. The structural transformation has also been supported by the PXRD study of the complex **2** after desolvation (Figure 13). This better flexibility of **2** become important in high pressure CO₂ sorption study as well.^{55,56} At 273K temperature and pressure range 0 to 20 bar the maximum uptake obtained upto 146.4 cc/g (28.75 wt%) for **2** (Figure 12b). The structural transformation after the high pressure measurement has also been supported by the PXRD study of the complex **2** (Figure 13).

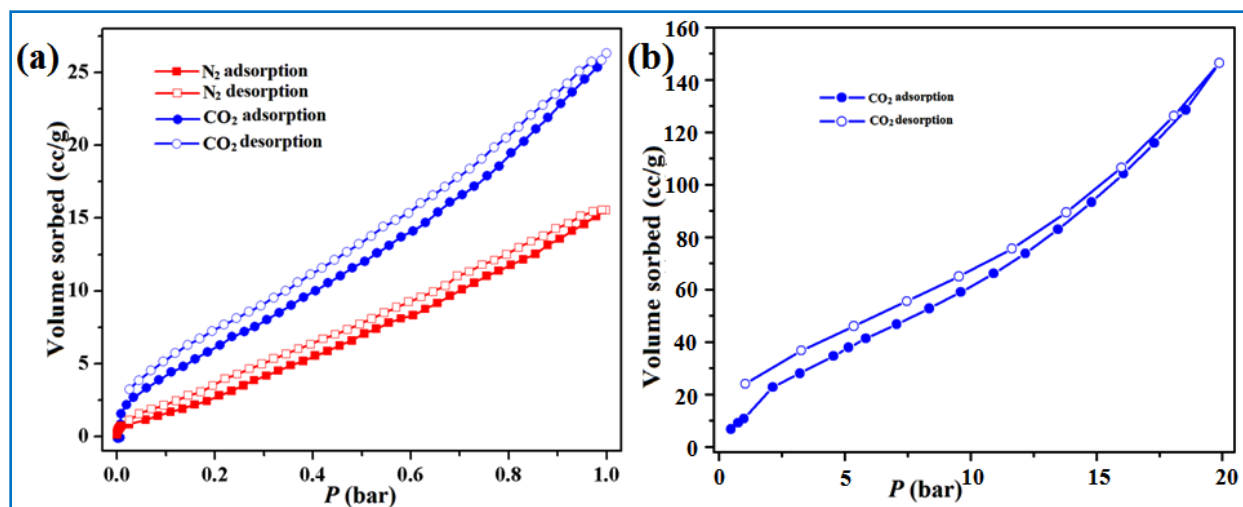


Figure 12. (a) N_2 adsorption (at 77 K) and CO_2 adsorption (at 195K) isotherms of **2**. (b) High pressure (upto 20 bar) CO_2 adsorption isotherms of **2** at 273K. Filled and open circles represent adsorption and desorption respectively.

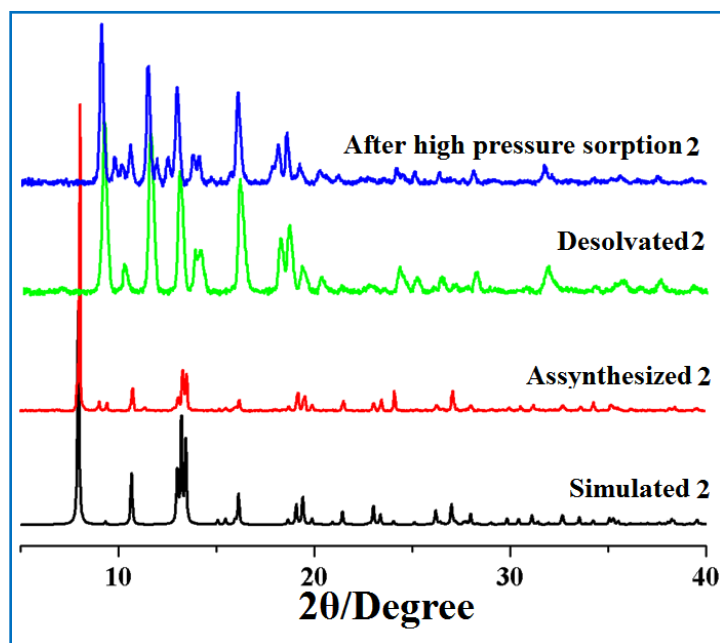


Figure 13. Powder X-ray diffraction (PXRD) of complex **2**.

Although, complex **3** is a 3D framework, it exhibits nonporous nature towards both N_2 and CO_2 with negligible uptake (Figure 14a). This is due to the complete blocking of the pore for presence of the bpe ligands in a criss-cross fashion in **3**. However at high pressure (0 to 20 bar) CO_2 sorption study^{55,56} at 273K; the maximum uptake obtained upto 157.8 cc/g (31 wt%) (Figure 14b). Structural integrity of the complex **3** after desolvation and after high pressure sorption

measurement has been supported by the PXRD study (Figure 15). The high CO₂ uptake value of complex **3**, at 273K, 20 bar pressure, which is maximum among these four complexes; is due to the opening of blocked pore window at high pressure (pore opening-closing mechanism)³⁷ which was not operative in ambient pressure. Additionally, the strong interaction between the polar CO₂ molecule with the properly organized C=C moiety of the bpe linker within the framework of complex is also responsible behind such kind of high uptake for **3**.^{29,57}

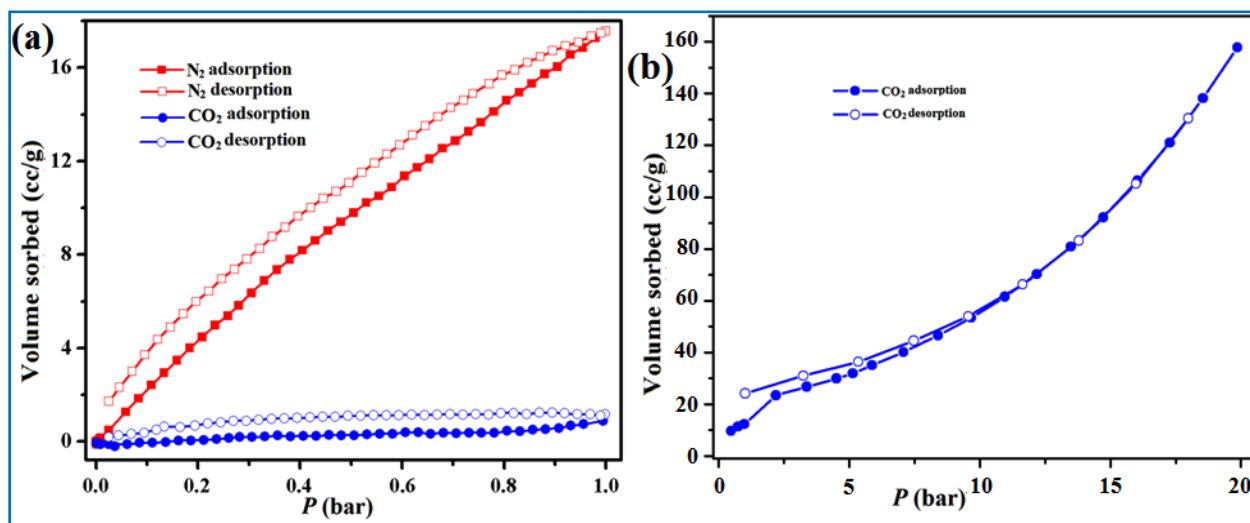


Figure 14. (a) N₂ adsorption (at 77 K) and CO₂ adsorption (at 195K) isotherms of complex **3**. (b) High pressure (upto 20 bar) CO₂ adsorption isotherms of **3** at 273K. Filled and open circles represent adsorption and desorption respectively.

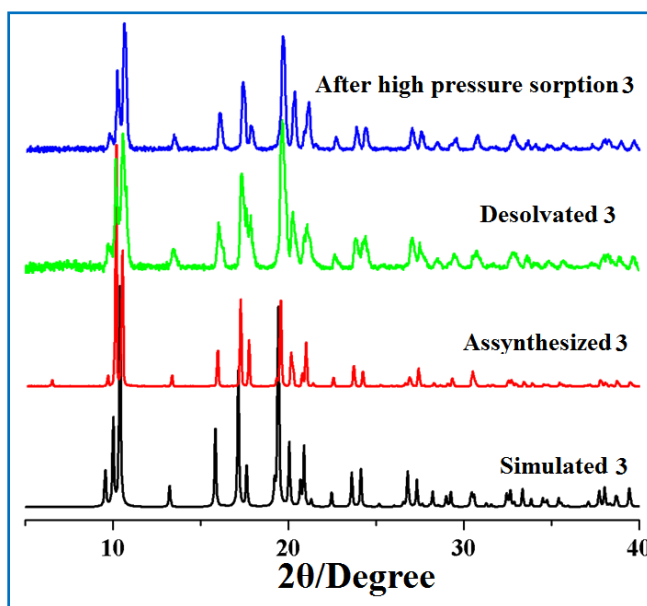


Figure 15. Powder X-ray diffraction (PXRD) of complex **3**.

Finally, the interesting result has been observed in case of complex **4** at ambient pressure region (0 to 1 bar) where the complex shows no significant uptake for N₂ sorption but it exhibits CO₂ sorption behavior with a maximum uptake of 61 cc/g (11.98 wt%) at 195K (Figure 16a). It is interesting to note that although **4** is a 2D system, it has highest CO₂ uptake ability at ambient pressure (0 to 1 bar) among the four, though it is not very uncommon for such dynamic system (Figure 17).⁵⁷ The dynamicity of the system in presence of CO₂ can be understandable by the sharp increase in uptake after 0.6 bar which is related to gate opening behaviour caused by the rotation of the perpendicular bpe moiety which enables more accessibility and kinetic retention of CO₂ in the framework. Here the presence of pendant oxygen atom from the dicarboxylate and C=C moiety of bpe linker has also contributed to create more interaction with the incoming CO₂ molecules.^{29,57} This additional adsorbate-adsorbent interaction⁵⁸⁻⁶¹ additively leads to better carbon dioxide sorption at ambient pressure (0 to 1 bar). The additional adsorbate-adsorbent interaction can be attributed by the hysteresis nature of sorption profile. The scenario is found

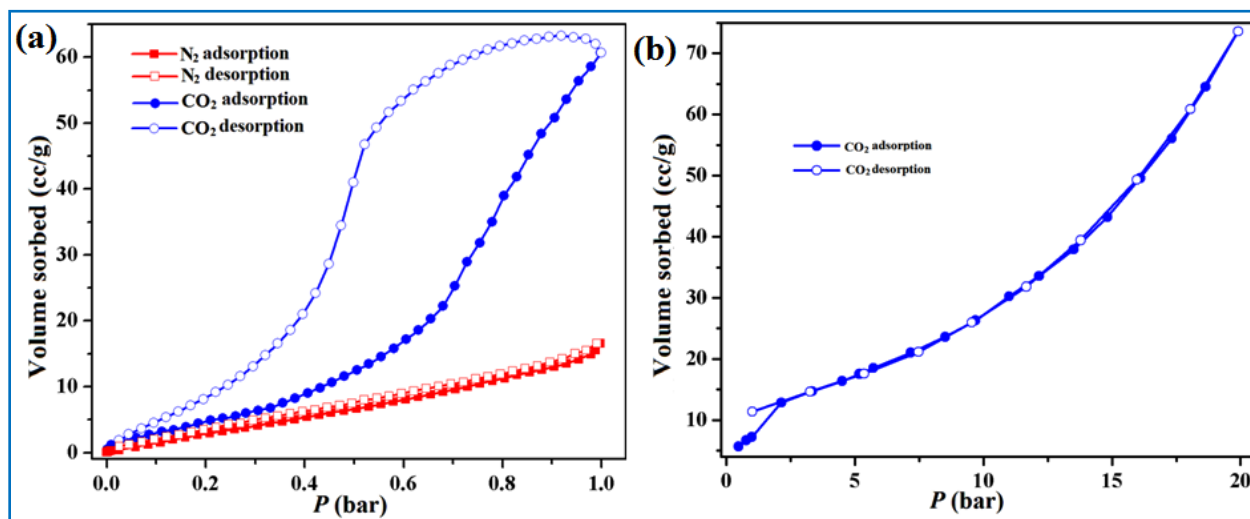


Figure 16. (a) N₂ adsorption (at 77 K) and CO₂ adsorption (at 195K) isotherms of **4**. (b) High pressure (upto 20 bar) CO₂ adsorption isotherms of **4** at 273K. Filled and open circles represent adsorption and desorption respectively.

completely changed if the measurement is done at 273K instead of 195K. In that case almost negligible uptake occurs and that is also kind of surface adsorption (Figure 18). This clearly indicates with the increase of kinetic energy of analyte CO₂, the framework loss the capacity to retain them. Although for this framework, high pressure CO₂ sorption measurement^{55,56} at 273K in the pressure range 0 to 20 bar, showing maximum uptake upto 73.5 cc/g (14.4 wt%) (Figure

16b). PXRD study after high pressure adsorption suggest that the process is associated with a structural transformation (Figure 17).

The CO₂ sorption study of all the MOFs in their retained/transformed phase are quite interesting and portray various interesting findings. The capacity of high pressure CO₂ sorption by these MOFs is also comparable with the previously reported high pressure CO₂ sorption values for related MOFs.⁶²

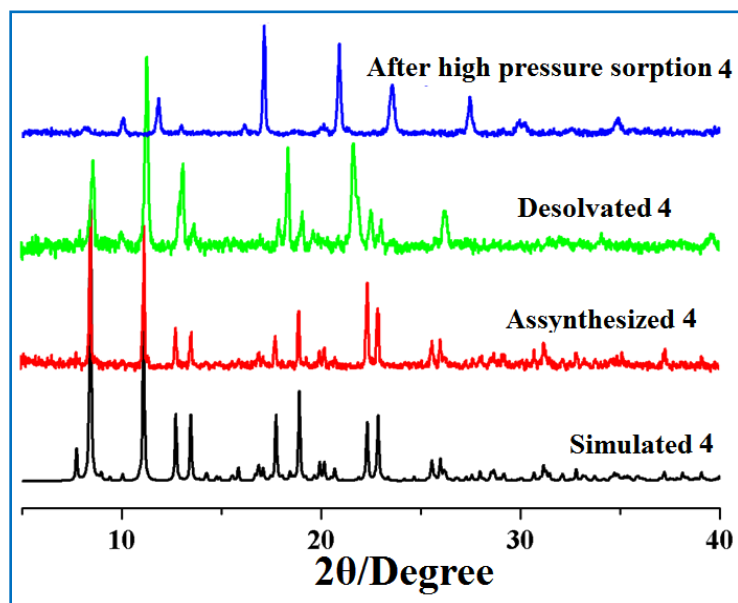


Figure 17. Powder X-ray diffraction (PXRD) of complex **4**.

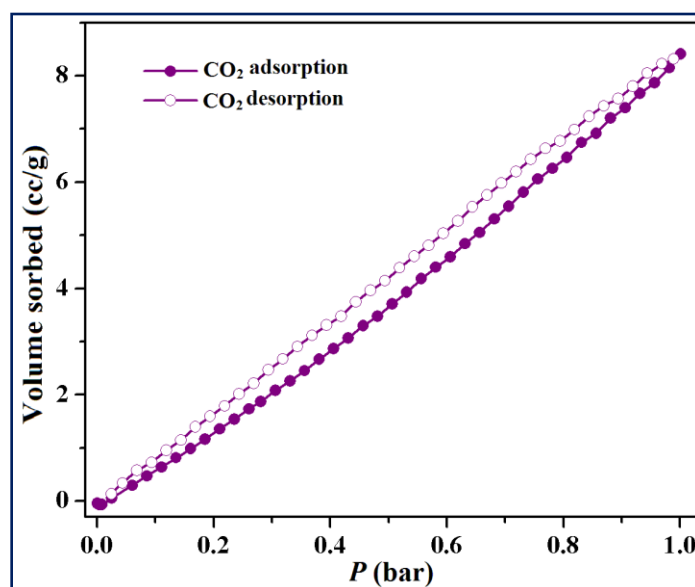


Figure 18. CO₂ adsorption (at 273K) isotherms of complex **4**. Filled and open circles represent adsorption and desorption respectively.

3.4. Powder X-ray diffraction (PXRD) and structural transformations of the complexes

The phase purity of bulk materials of all the complexes have been confirmed by the powder X-ray diffraction (PXRD) which has been carried out at room temperature. Exact matching of all characteristic peak positions obtained by the PXRD measurement of complexes **1-4** with the respective simulated ones, obtained from single crystal structures; indicate bulk phase purity of all (Figures 11, 13, 15, and 17). It has been mentioned previously that the high pressure carbon dioxide sorption has been studied for **1-4** in the pressure range of 0 to 20 bar. For **1**, mismatching of some characteristic peaks in PXRD for the desolvated complex in comparison to as-synthesized one, clearly indicates structural transformation of **1** after desolvation. After high pressure carbon dioxide sorption study of the desolvated complex of **1**, another dissimilar pattern in PXRD has been observed (Figure 11) which indicates another phase transformation. Similar trend is observed in case of **2**, first transformation occurred after desolvation and second transformation after high pressure carbon dioxide sorption study (Figure 13). In case of **3**, exact matching in PXRD pattern to its as-synthesized form has been observed for the desolvated complex and even after high pressure carbon dioxide sorption study. This indicates the structural rigidity (Figure 15) of complex **3** unlike the other complexes. Finally for the complex **4**, same trend as **1** and **2** has been observed where desolvation leads to a structural transformation and another structural transformation after high pressure sorption measurement (Figure 17). Thus in all the MOFs, except **3**, desolvation leads to formation of a new phase and at high pressure during the carbon dioxide sorption experiments, again converts them into another new phase. The structural transformation of **1**, **2** and **4** has been thoroughly investigated by indexing the PXRD data of the complexes after activation (at 130 °C), and also after high pressure sorption study; using TREOR program⁶³ (Figures 19-24). The results corroborates that in all three cases, there are two step structural transformations: one after the activation and the next is after the high pressure sorption study. The transformed cell of complexes **1**, **2** and **4** during transformation has been summarized in Tables 8-10 and the Le Bail fittings for the indexing are given in Figures 19-24.

3.5. Indexing of PXRD data by TREOR 90 program and McMaille program

To find a better insight of structural transformation of **1**, **2** and **4** after activation and after high pressure sorption slow scan PXRD experiment have performed. The powder patterns of isolated products of **1**, **2** and **4** after activation (130 °C) and after high pressure sorption measurement

have been indexed by TREOR 90⁶³ and McMaille program⁶⁴. A routine peak search generates a list of d values allied to the experimental diffraction peaks. These values are processed and finally provide the cell parameters. A statistical analysis is performed with the experimental diffraction intensities matched with the standard crystal system. This step is competent to offer a list of all the possible extinction symbols. For each extinction symbol, the consequent list of well-suited space groups (one or more than one) is obtained. Best results obtained for the propose of the structural transformation in each case are considered and the corresponding Le Bail fitting curve and indexing table have given in Figures 19 to 24 and Tables 8-10.

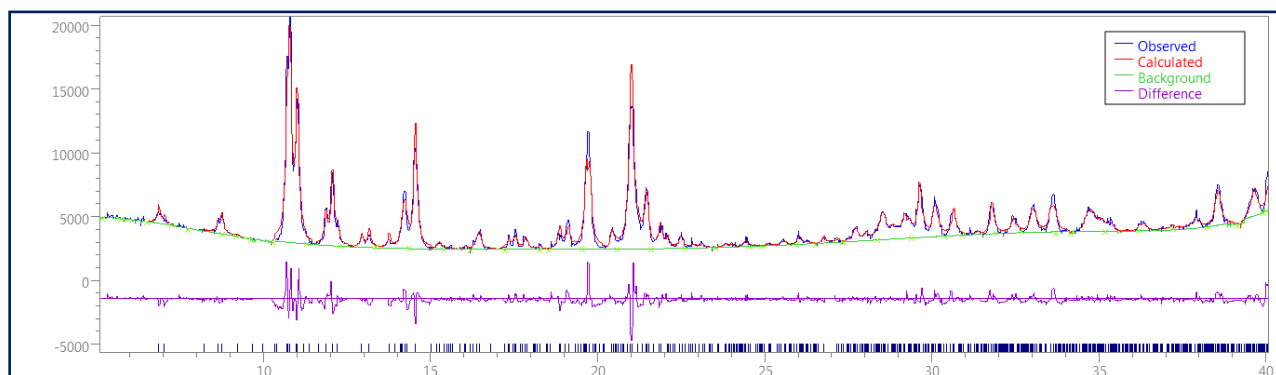


Figure 19. Le Bail fitting of powder pattern of complex **1** after activation using TREOR.

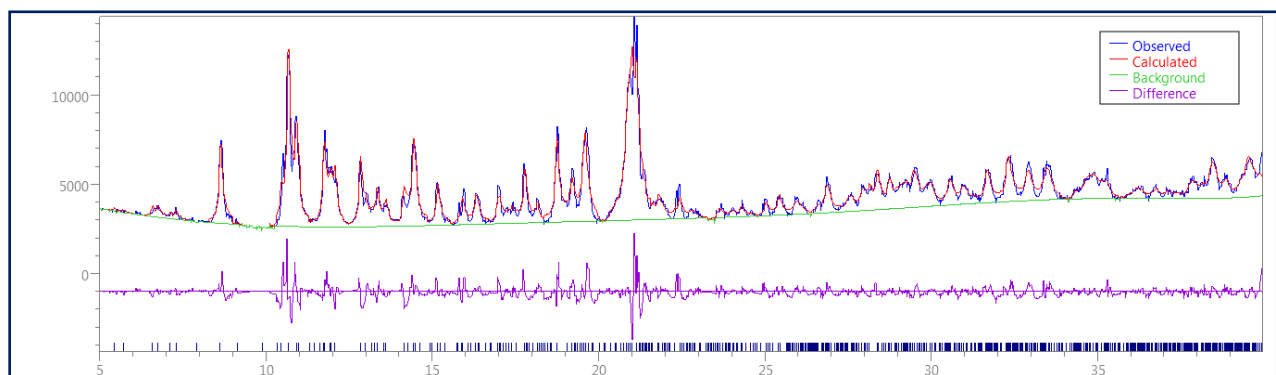


Figure 20. Le Bail fitting of powder pattern of complex **1** after high pressure sorption using TREOR.

Table 8. Summary of the transformed cell in **1**

	conventional cell of 1	transformed cell of 1 after activation	transformed cell of 1 after high pressure sorption
crystal system	triclinic	triclinic	triclinic
space group	$P\bar{1}$	$P\bar{1}$	$P\bar{1}$
$a/\text{\AA}$	11.5584	18.6637	17.3746
$b/\text{\AA}$	12.6026	18.0797	17.0048
$c/\text{\AA}$	14.4817	11.2075	15.1014
$\alpha/^\circ$	76.331	100.95	104.21
$\beta/^\circ$	71.291	101.68	115.22
$\gamma/^\circ$	88.362	89.28	93.61
$V/\text{\AA}^3$	1938.88	3634.73	3840.73

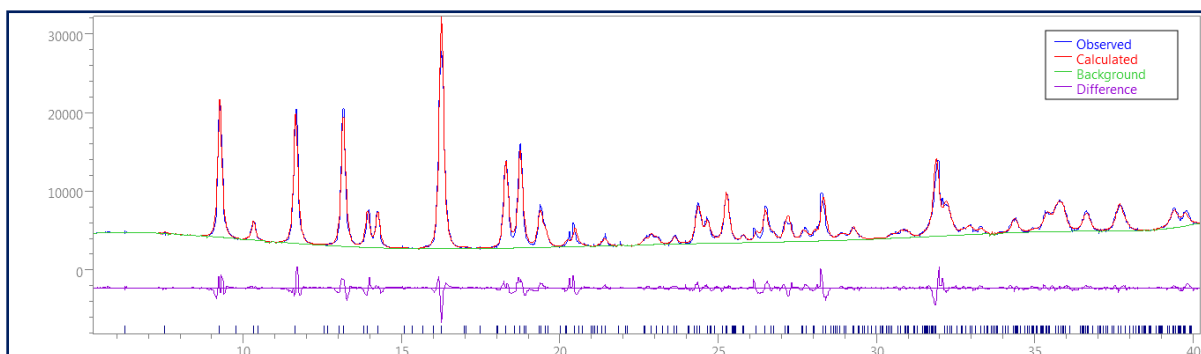
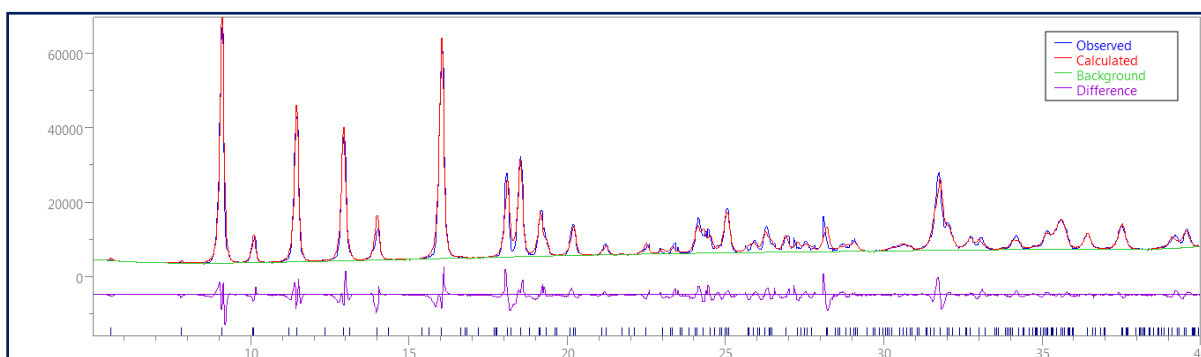
**Figure 21.** Le Bail fitting of powder pattern of complex **2** after activation using TREOR.**Figure 22.** Le Bail fitting of powder pattern of complex **2** after high pressure sorption using McMaille.

Table 9. Summary of the transformed cell in **2**

	conventional cell of 2	transformed cell of 2 after activation	transformed cell of 2 after high pressure sorption
crystal system	monoclinic	triclinic	monoclinic
space group	$C2/c$	$P\bar{1}$	$P2_1$
$a/\text{\AA}$	25.725	14.4728	11.396
$b/\text{\AA}$	10.4434	11.8790	10.573
$c/\text{\AA}$	13.605	9.2530	15.848
$\alpha/^\circ$	90	95.44	90.00
$\beta/^\circ$	120.199	101.42	96.529
$\gamma/^\circ$	90	95.14	90.00
$V/\text{\AA}^3$	3159.0	1542.67	1897.2

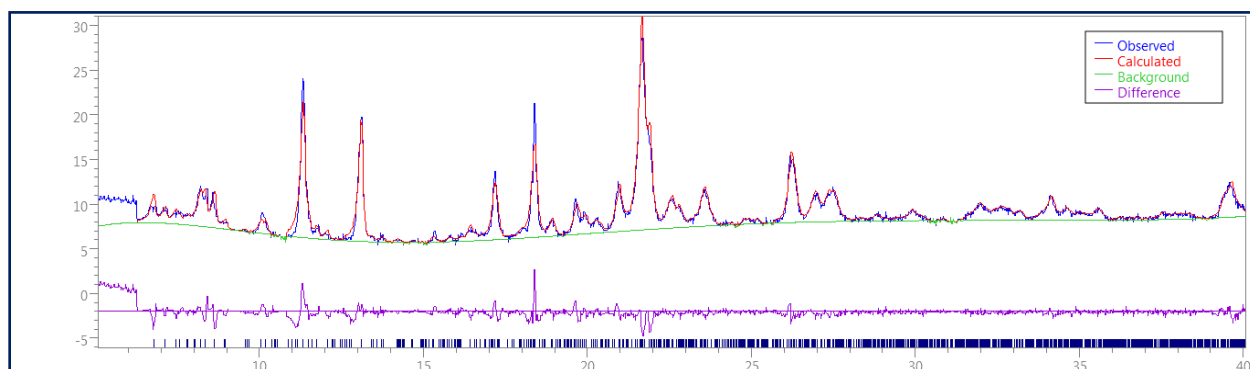
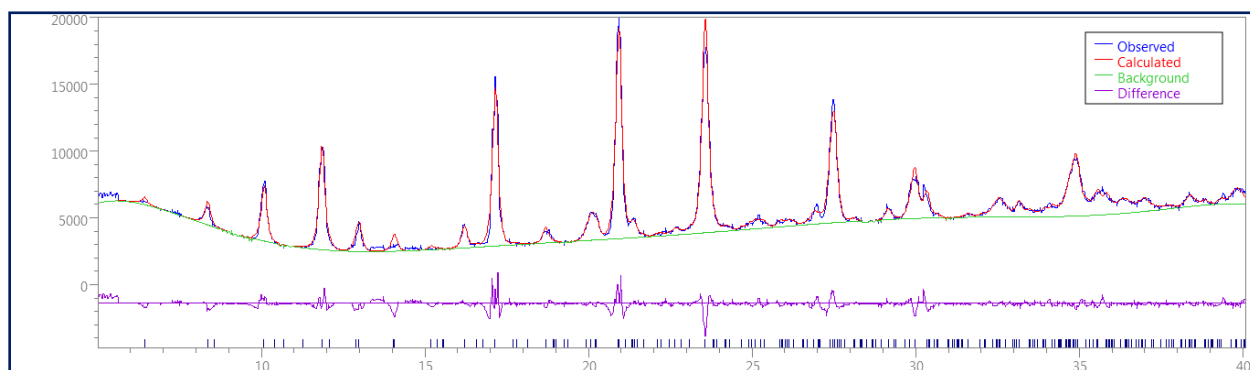
**Figure 23.** Le Bail fitting of powder pattern of complex **4** after activation using TREOR.**Figure 24.** Le Bail fitting of powder pattern of complex **4** after high pressure sorption using McMaille.

Table 10. Summary of the transformed cell in **4**

	conventional cell of 4	transformed cell of 4 after activation	transformed cell of 4 after high pressure adsorption
crystal system	monoclinic	triclinic	monoclinic
space group	$P2_1/c$	$P\bar{1}$	$P2_1$
$a/\text{\AA}$	16.2761	29.5717	13.7460
$b/\text{\AA}$	13.9146	14.1698	15.6887
$c/\text{\AA}$	20.4241	10.5840	10.5492
$\alpha/^\circ$	90	91.92	90
$\beta/^\circ$	101.894	95.80	91.55
$\gamma/^\circ$	90	91.05	90
$V/\text{\AA}^3$	4526.25	4408.70	2274.15

4. Conclusion

Following the variation of the metal ion and N-donor ligands here we have successfully synthesized four different metal organic frameworks (MOFs). All the complexes have been well characterized. Here, using the same dicarboxylate and varying N-donor ligands two 3D structures were obtained while the variation of both metal and ligand results 3D and 2D structures respectively. Interestingly, most of the complexes have shown CO₂ and N₂ adsorption commensurate with their respective pore dimension. The 2D structure interestingly exhibit better result for carbon dioxide sorption at ambient pressure due to strong adsorbate-adsorbent interaction in terms of surface adsorption compared to the rest three 3D structures. Excellent result in case of high pressure sorption have been obtained for all the 3D structures due to structural transformation in two cases and strong interaction of polar CO₂ group with properly oriented C=C moiety in one case. Pore window opening mechanism at higher pressure also plays a vital role for higher CO₂ uptake of all 3D structures. In one word, these versatile complexes and their transformed phase can be represented as a nice tool to exhibit carbon dioxide sorption to different extent related to their structural dimension and pore decoration as well.

References

- (1) P. K. Thallapally, J. Tian, M. R. Kishan, C. A. Fernandez, S. J. Dalgarno, P. B. McGrail, J. E. Warren and J. L. Atwood, *J. Am. Chem. Soc.*, 2008, **130**, 16842–16843.

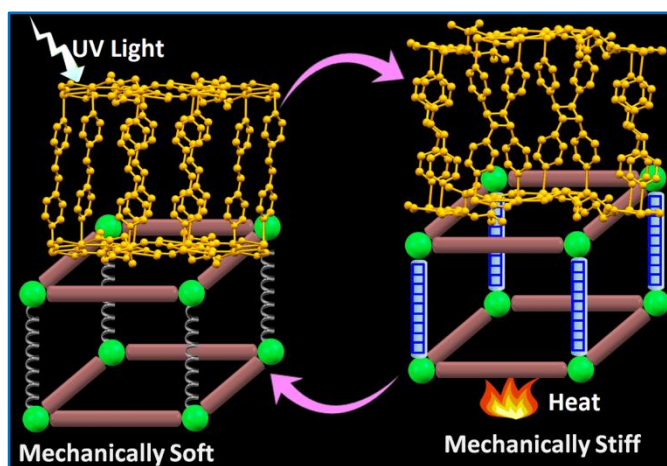
-
- (2) A. Halder, B. Bhattacharya, F. Haque and D. Ghoshal, *Cryst. Growth Des.*, 2017, **17**, 6613–6624.
- (3) A. Schneemann, P. Vervoorts, I. Hante, M. Tu, S. Wannapaiboon, C. Sternemann, M. Paulus, D. C. F. Wieland, S. Henke and R. A. Fischer, *Chem. Mater.*, 2018, **30**, 1667–1676.
- (4) B. Bhattacharya, A. Layek, Md. M. Alam, D. K. Maity, S. Chakrabarti, P. P. Ray and D. Ghoshal, *Chem. Commun.*, 2014, **50**, 7858–7861.
- (5) D. K. Maity, K. Otake, S. Ghosh, H. Kitagawa and D. Ghoshal, *Inorg. Chemistry*, 2017, **56**, 1581–1590.
- (6) A. Dey, S. K. Konavarapu, H. S. Sasmal and K. Biradha, *Cryst. Growth Des.*, 2016, **16**, 5976–5984.
- (7) B. Gole, A. K. Bar, A. Mallick, R. Banerjee and P. S. Mukherjee, *Chem. Commun.*, 2013, **49**, 7439–7441.
- (8) S. Roy, V. M. Suresh, A. Hazra, A. Bandyopadhyay, S. Laha, S. K. Pati and T. K. Maji, *Inorg. Chem.*, 2018, **57**, 8693–8696.
- (9) S. Sen, N. N. Nair, T. Yamada, H. Kitagawa and P. K. Bharadwaj, *J. Am. Chem. Soc.*, 2012, **134**, 19432–19437.
- (10) S. Goswami, S. Sanda and S. Konar, *CrystEngComm*, 2014, **16**, 369–374.
- (11) S. K. Dey, R. Chutia and G. Das, *Inorg. Chem.*, 2012, **51**, 1727–1738.
- (12) B. Zheng, J. Bai, J. Duan, L. Wojtas and M. J. Zaworotko, *J. Am. Chem. Soc.*, 2011, **133**, 748–751.
- (13) H. Wu, K. Yao, Y. Zhu, B. Li, Z. Shi, R. Krishna and J. Li, *J. Phys. Chem. C*, 2012, **116**, 16609–16618.
- (14) O. M. Yaghi, M. O’Keeffe, W. N. Ockwig, H. K. Chae, M. Eddaoudi and J. Kim, *Nature*, 2003, **423**, 705–14.
- (15) R. Krishna, *Chem. Soc. Rev.*, 2012, 41, 3099–118.
- (16) T. M. McDonald, W. R. Lee, J. A. Mason, B. M. Wiers, C. S. Hong and J. R. Long, *J. Am. Chem. Soc.*, 2012, **134**, 7056–7065.
- (17) N. A. -Janabi, H. Deng, J. Borges, X. Liu, A. Garforth, F. R. Siperstein and X. Fan, *Ind. Eng. Chem. Res.*, 2016, **55**, 7941–7949.
- (18) X. Su, L. Bromberg, V. Martis, F. Simeon, A. Huq and T. A. Hatton, *ACS Appl. Mater. Interfaces*, 2017, **9**, 11299–11306.
-

- (19) N. Chatterjee and C. L. Oliver, *Cryst. Growth Des.*, 2018, **18**, 7570–7578.
- (20) M. Du, X. -J. Jiang and X. -J. Zhao, *Inorg.Chem.*, 2007, **46**, 3984–3995.
- (21) S. Ghosh, G. Pahari, D. K. Maity, A. Halder and D. Ghoshal, *ChemistrySelect*, 2018, **3**, 8980–8991.
- (22) O. K. Farha and J. T. Hupp, *Acc. Chem. Res.*, 2010, **43**, 1166–1175.
- (23) A. W. Peters, K. Otake, A. E. Platero-Prats, Z. Li, M. R. DeStefano, K. W. Chapman, O. K. Farha and J. T. Hupp, *ACS Appl. Mater. Interfaces*, 2018, **10**, 15073–15078.
- (24) D. Zhao, D. J. Timmons, D. Yuan and H. C. Zhou, *Acc. Chem. Res.*, 2011, **44**, 123–133.
- (25) V. Colombo, C. Montoro, A. Maspero, G. Palmisano, N. Masciocchi, S. Galli, E. Barea and J. A. R. Navarro, *J. Am. Chem. Soc.*, 2012, **134**, 12830–12843.
- (26) W. Fan, X. Wang, X. Liu, B. Xu, X. Zhang, W. Wang, X. Wang, Y. Wang, F. Dai, D. Yuan and D. Sun, *ACS Sustainable Chem. Eng.*, 2019, **7**, 2134–2140.
- (27) S. Sen, S. Neogi, A. Aijaz, Q. Xu and P. K. Bharadwaj, *Inorg. Chem.*, 2014, **53**, 7591–7598.
- (28) J. An and N. L. Rosi, *J. Am. Chem. Soc.*, 2010, **132**, 5578–5579.
- (29) B. Bhattacharya and D. Ghoshal, *CrystEngComm*, 2015, **17**, 8388–8413.
- (30) G. B. Deacon and R. J. Phillips, *Coord. Chem. Rev.*, 1980, **33**, 227–250.
- (31) D. K. Maity, B. Bhattacharya, R. Mondal and D. Ghoshal, *CrystEngComm*, 2014, **16**, 8896–8909.
- (32) S. Mukherjee, B. Joarder, B. Manna, A. V. Desai, A. K. Chaudhari and S. K. Ghosh, *Sci Rep*, 2015, **4**, 5761.
- (33) A. Halder and D. Ghoshal, *CrystEngComm*, 2018, **20**, 1322–1345.
- (34) D. Tanaka, K. Nakagawa, M. Higuchi, S. Horike, Y. Kubota, T. C. Kobayashi, M. Takata and S. Kitagawa, *Angew. Chem. Int. Ed.*, 2008, **47**, 3914–3918.
- (35) A. Schneemann, V. Bon, I. Schwedler, I. Senkovska, S. Kaskel and R. A. Fischer, *Chem. Soc. Rev.*, 2014, **43**, 6062–6096.
- (36) F. Rouhani, B. Gharib and A. Morsali, *Inorg. Chem. Front.*, 2019, **6**, 2412–2422.
- (37) H. J. Choi, M. Dinca and J. R. Long, *J. Am. Chem. Soc.*, 2008, **130**, 7848–7850.
- (38) J. Torres, J. L. Lavandera, P. Cabildo, R. M. Claramunt and J. Elguero, *J. Heterocycl. Chem.*, 1988, **25**, 771–782.
- (39) L. -Y. Wang, Y. Yang, K. Liu, B. -L. Li and Y. Zhang, *Cryst. Growth Des.*, 2008, **8**, 3902–3904.

-
- (40) SMART (V 5.628), SAINT (V 6.45a), XPREP, SHELXTL, Bruker AXS Inc., Madison, WI, 2004.
- (41) G. M. Sheldrick, SADABS (Version 2.03), University of Göttingen, Germany, 2002.
- (42) G. M. Sheldrick, *Acta Cryst.*, 2015, **C71**, 3–8.
- (43) A. L. Spek, *Acta Crystallogr. Sect. D Biol. Crystallogr.*, 2009, **65**, 148–155.
- (44) L. J. Farrugia, *J. Appl. Crystallogr.*, 1999, **32**, 837–838.
- (45) V. A. Blatov, A. P. Shevchenko and V. N. Serezhkin, *J. Appl. Crystallogr.*, 2000, **33**, 1193.
- (46) V. A. Blatov, L. Carlucci, G. Ciani and D. M. Proserpio, *CrystEngComm*, 2004, **6**, 377–395.
- (47) C. F. Macrae, P. R. Edgington, P. McCabe, E. Pidcock, G. P. Shields, R. Taylor, M. Towler, and J. van de Streek, *J. Appl. Cryst.* 2006, **39**, 453.
- (48) B. Bhattacharya, R. Haldar, D. K. Maity, T. K. Maji and D. Ghoshal, *CrystEngComm*, 2015, **17**, 3478–3486.
- (49) A. W. Addison, T. N. Rao, J. Reedijk, J. van Rijn and G. C. Verschoor, *J. Chem. Soc. Dalton Trans.*, 1984, 1349–1356.
- (50) B. Bhattacharya, R. Haldar, R. Dey, T. K. Maji and D. Ghoshal, *Dalton Trans.*, 2014, **43**, 2272–2282.
- (51) M. Köberl, M. Cokoja, W. A. Herrman and F. E. Kühn, *Dalton Trans.*, 2011, **40**, 6834–6859.
- (52) Y. Kang, Q. Liu, W. Yin, W. Zhang and P. Liu, *Chin. J. Chem.*, 2013, **31**, 256–262.
- (53) J. -Y. Lee, C. -Y. Chen, H. M. Lee, E. Passaglia, F. Vizza and W. Oberhauser, *Cryst. Growth Des.*, 2011, **11**, 1230–1237.
- (54) I. H. Hwang, J. M. Bae, Y. -K. Hwang, H. -Y. Kim, C. Kim, S. Huh, S. -J. Kim and Y. Kim, *Dalton Trans.*, 2013, **42**, 15645–15649.
- (55) J. Y. Jung, F. Karadas, S. Zulfiqar, E. Deniz, S. Aparicio, M. Atilhan, C. T. Yavuz and S. M. Han, *Phys. Chem. Chem. Phys.*, 2013, **15**, 14319–14327.
- (56) J. H. Cavka, C. A. Grande, G. Mondino and R. Blom, *Ind. Eng. Chem. Res.*, 2014, **53**, 15500–15507.
- (57) N. Nijem, P. Thissen, Y. Yao, R. C. Longo, K. Roodenko, H. Wu, Y. Zhao, K. Cho, J. Li, D. C. Langreth and Y. J. Chabal, *J. Am. Chem. Soc.*, 2011, **133**, 12849–12857.
-

- (58) A. Halder, B. Bhattacharya, R. Dey, D. K. Maity and D. Ghoshal, *Cryst. Growth Des.*, 2016, **16**, 4783–4792.
- (59) P. Pachfule, T. Panda, C. Dey and R. Banerjee, *CrystEngComm*, 2010, **12**, 2381–2389.
- (60) J. -A. Hua, Y. Zhao, Q. Liu, D. Zhao, K. Chen and W. -Y. Sun, *CrystEngComm*, 2014, **16**, 7536–7546.
- (61) H. J. Park and M. P. Suh, *Chem. Commun.*, 2010, **46**, 610–612.
- (62) T. Ghanbari, F. Abnisa and W. M. A. Wan Daud, *Sci. Total Environ.*, 2020, **707**, 135090.
- (63) P. -E. Werner, L. Eriksson, M. Westdahl, *J. Appl. Crystallogr.*, 1985, **18**, 367–370.
- (64) A. L. Bail, *Powder Diffr.* 2004, **19**, 249.

Chapter 6



Chapter 6 : Mechanical softness and molecular movements aid a reversible photochemical solid-state transformation in an interpenetrated 3D metal–organic framework

Chapter 6

A reversible photoinduced solid-state transformation in an interpenetrated 3D metal–organic framework with mechanical softness

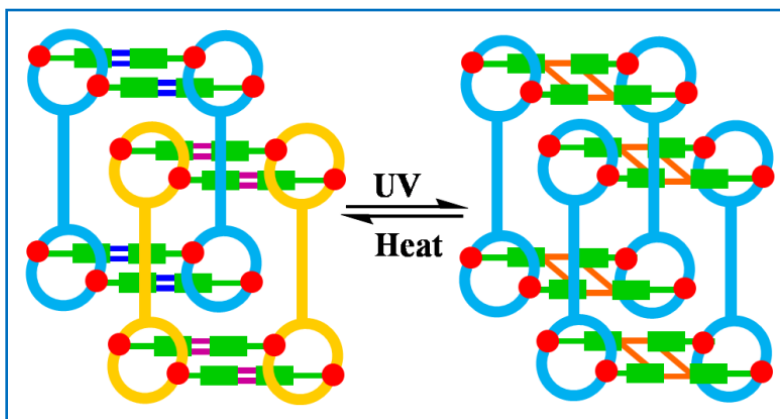
1. Introduction

Nowadays, topochemical reactions via [2+2] cycloaddition reaction in solid-state have taken the colossal interest of chemists and material scientists.¹⁻⁴ It provides an ideal way for synthesizing green, environmentally benign, regio-/stereospecific compounds under solvent-free conditions with high quantitative yields.⁵⁻⁶ In recent years, the mechanistic aspects and kinetics of photochemical reactions have been monitored during topochemical single-crystal-to-single-crystal (SCSC) transformations.⁷⁻¹⁵ Starting from *Schmidt* and co-workers^{16,17} several examples of SCSC transformations via [2+2] cycloaddition of C=C bonds in organic crystals and coordination polymers (CPs) or metal organic frameworks (MOFs) have been reported.⁷⁻¹¹ Such SCSC cycloaddition in three-dimensional coordination networks of MOF is very rare.^{18,19} According to Schmidt's criteria of topochemical addition, for a successful photoinduced cycloaddition reaction in solids, minimal atomic movement is required and the reactive species must be aligned within the distance of around 4.2 Å. Later research revealed that the cycloaddition can occur between the C=C bonds with a separation much higher than 4.2 Å. *Kaupp*²⁰⁻²² provided some insights into such exceptions of Schmidt's topochemical postulate. Using atomic force microscopic (AFM) data, they proposed that the molecular movement in the crystal packing plays a crucial role for solid-state [2+2] cycloaddition reactions. Therefore, to understand the photoinduced cycloaddition reactions of crystals having reactive C=C bonds, the mechanical properties²³⁻²⁵ should be considered as crystal packing and the weak interactions between the molecules in a crystal structure govern the mechanical properties and movement of molecules in crystals. Such studies provide insights into mechanistic understanding of photocycloaddition reactions and solid-state molecular movements in crystals. Study of mechanical properties of MOFs has also become an emerging field of interest in the context of their macroscopic performance under practical working conditions.^{26,27} In recent literature, anisotropic mechanical behaviour has been correlated well with internal arrangement of crystal packing and

different molecular properties of MOF-type hybrid materials.²⁸⁻³¹ Despite the immense significance, the effect of mechanical properties of the crystals due to cycloaddition reaction has not been explored yet in MOFs. In this regard, nanoindentation³² is a very reliable technique to quantitatively ascertain mechanical properties of materials. Recently, this technique has been widely utilized for determining the Young's modulus (E) and hardness (H) of molecular crystals of various organic and inorganic compounds as well as MOFs.^{18,19,33-36} In this regard, study of the effect of E and H of MOFs upon cycloaddition provides more insight into the mechanism.

In this chapter a newly synthesized two-fold interpenetrated Cd(II)-based 3D MOF $\{[\text{Cd}_2(\text{bpe})_2(3,3\text{-dmglu})_2]\}_n$ (**1**) with trans-1,2-bis(4-pyridyl)ethylene ligand (bpe) and 3,3-dimethylglutarate (3,3-dmglu) has been reported. In the crystal packing of the compound **1**, there are two crystallographically independent frameworks of Cd(II) where the C=C bonds in bpe ligands are distinct. In one unit the adjacent C=C bonds are at a distance of less than 4.2 Å, where as in other it is much higher (4.8 Å). Therefore, the present system is suitable to examine the *Kaupp's* proposition of molecular movements in a same single crystal system. Interestingly, here it is observed that both the C=C bonds undergo cycloaddition,³⁷⁻³⁹ upon UV radiation. The aforesaid MOF undergoes a unique photochemical SCSC transformation to $\{[\text{Cd}_2(\text{rctt-tpcb})(3,3\text{-dmglu})_2]\}_n$ (**2**), {where, tpcb = tetrakis(4-pyridyl)cyclobutane), in rctt, the r = reference substituent group, c = cis and t = trans for indicating the relative orientation of the substituent on the cyclobutane ring with regard to the reference group} by [2+2] photodimerization of C=C bonds of bpe to cyclobutane ring (Scheme 1) in both the crystallographic units accompanied by achiral to chiral space group change. Furthermore, it is important to note that cyclized compound comes back to the parent compound with achiral space group in SCSC manner upon heating at 250 °C for 3 hrs. Such rare reversible transformation⁴⁰⁻⁴² could be useful in various applications such as, making a achiral material to chiral, reshape the pore size and increasing the conductivity; so on and so forth.⁴³⁻⁴⁵ Here the mechanical properties of the parent and cyclized crystals have been determined quantitatively by nanoindentation technique to correlate molecular movements in these two systems. Here C=C bonds with shorter and longer separation are simultaneously cyclized in a SCSC manner accompanied with reversible space group change from achiral to chiral. The changes are

monitored with in the light of mechanical properties in a MOF involving a reversible photomechanical [2+2] cycloaddition reaction.



Scheme 1. Schematic representation of reversible [2+2] photocycloaddition and its thermal reversal in an inter-penetrated MOF.

2. Experimental section

2.1. Materials and methods

Cadmium(II) nitrate tetrahydrate, 3,3-dimethylglutaric acid (H_2 -3,3-dmglu) and 1,2-bis(4-pyridyl)ethylene (bpe) have been purchased from Sigma-Aldrich Chemical Co. Inc. and used as received. Disodium 3,3-dimethylglutarate (Na_2 -3,3-dmglu) has been synthesized by the slow addition of solid Na_2CO_3 to aqueous solution of H_2 -3,3-dmglu in a 1:1 ratio and allowed to evaporate until dryness. All other chemicals including solvents are of AR grade and has been used as received.

2.2. Physical measurements

C, H, and N analyses have been performed on a Heraeus CHNS analyzer. Infrared spectra ($4000\text{--}400\text{ cm}^{-1}$) have been taken on KBr pellet, using PerkinElmer Spectrum BX-II IR spectrometer. Powder X-ray diffraction (PXRD) data have been collected on a Bruker D8 Discover instrument with Cu-K α radiation. Thermo gravimetric analysis (TGA) has been carried out on a PerkinElmer STA 8000 thermal analyzer under nitrogen atmosphere with a flow rate of $10\text{ cm}^3\text{ min}^{-1}$ at a temperature range of $30\text{--}600\text{ }^\circ\text{C}$. UV–Vis spectra have been recorded on a Perkin Elmer Lambda 35 UV–Vis spectrophotometer. ^1H NMR spectra have been recorded at ambient temperature on Bruker Avance 300 instrument. The chemical shifts (δ) and coupling constants (J) have been expressed in ppm and Hz, respectively.

2.3. Sorption measurements

The adsorption isotherms of N₂ (at 77 K) and CO₂ (at 195 K) for **1** and **2** have been measured using Quantachrome Autosorb-iQ adsorption instrument. All operations have been computer-controlled and automatic. High purity gases have been used for the adsorption measurements (nitrogen, 99.999%; carbon dioxide, 99.95%). At the beginning the as synthesized compounds of **1** and **2** (~90 mg each) have been placed in the sample tube and dehydrated at 393 K, under a 1×10^{-1} Pa vacuum for about 4 hrs prior to measurement of the isotherms. Helium gas (99.999% purity) has been introduced in the gas chamber and allowed to diffuse into the sample chamber to measure the dead volume. Taking samples of **1** and **2** the N₂ adsorptions have been carried out at 77 K maintained by a liquid-nitrogen bath; whereas CO₂ adsorptions have been measured at 195 K (temperature maintained by dry ice-acetone cold bath) taking **1** and **2** in the pressure range from 0 to 1 bar. The amount of gas adsorbed have been calculated from the pressure difference ($P_{\text{cal}} - P_{\text{e}}$), where P_{cal} is the calculated pressure with no gas adsorption and P_{e} is the observed pressure at equilibrium. The solvent adsorption isotherms for H₂O have been measured at 298 K in the pressure region from 0 to 24 torr for H₂O, in their vapour state by taking the compounds of **1** and **2** using the same instrument. All the samples (~90 mg each) have been activated under similar conditions as mentioned earlier. The solvent molecule used to generate the vapour, has been degassed fully by repeated evacuation. The dead volume has been measured with helium gas.

2.4. Syntheses

2.4.1. Synthesis of {[Cd₂(bpe)₂(3,3-dmglu)₂]}_n (**1**)

Methanolic solution (20 mL) of 1,2-bis(4-pyridyl)ethylene (bpe) (1 mmol, 0.182 g) has been mixed with an aqueous solution (20 mL) of disodium 3,3-dimethyl glutarate (Na₂-3,3-dmglu) (1 mmol, 0.204 g) to mix up well and in another beaker 20 mL aqueous solution of Cd(NO₃)₂·4H₂O (1 mmol, 0.308 g) has been prepared. Then, 6 mL of this mixed ligand solution has been slowly and carefully layered above 3 mL of metal solution using 5 mL buffer (1:1 MeOH and H₂O) in a glass tube. After ten days, linear shaped white colored single crystal of **1** has been obtained at the wall of the tube with the yield of 60%; they have been washed with methanol-water (1:1) mixture and dried. Anal. Calc. for C₃₈H₄₀Cd₂N₄O₈ (**1**, %): C, 50.39; H, 4.45; N, 6.18. Found: C, 50.35; H, 4.40; N, 6.15. IR spectra (KBr, cm⁻¹): ν(CH-Ar), 3100–2900; ν(C=C, Ar), 1530–1432; ν(CH-alkane), 1431–1354; ν(C=C), 1680–1560; ν(C–C), 1480; ν(C–H), 1393; ν(C–O), 1250–

1060 (Figure 1a). The UV-vis absorption spectra of compounds **1** has been measured in solid state at room temperature (Figure 2a).

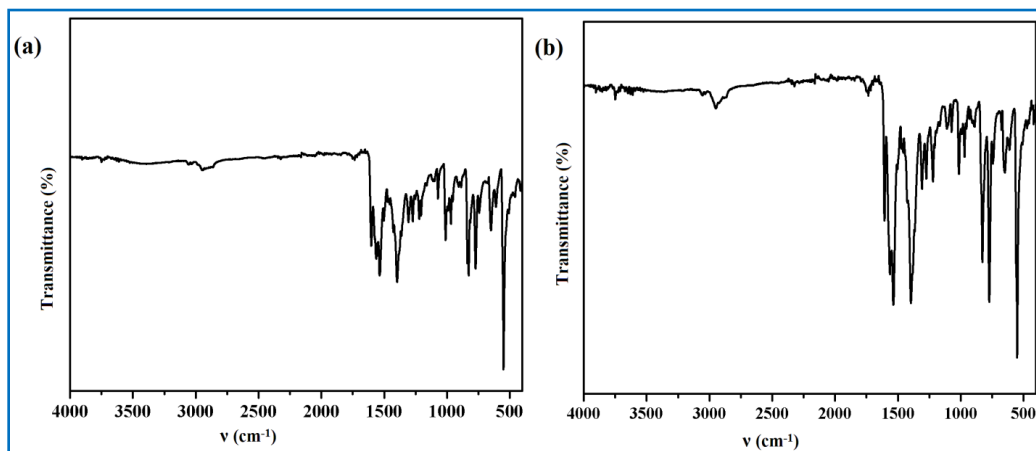


Figure 1. ATR spectra of (a) compound **1**, and (b) compound **2**.

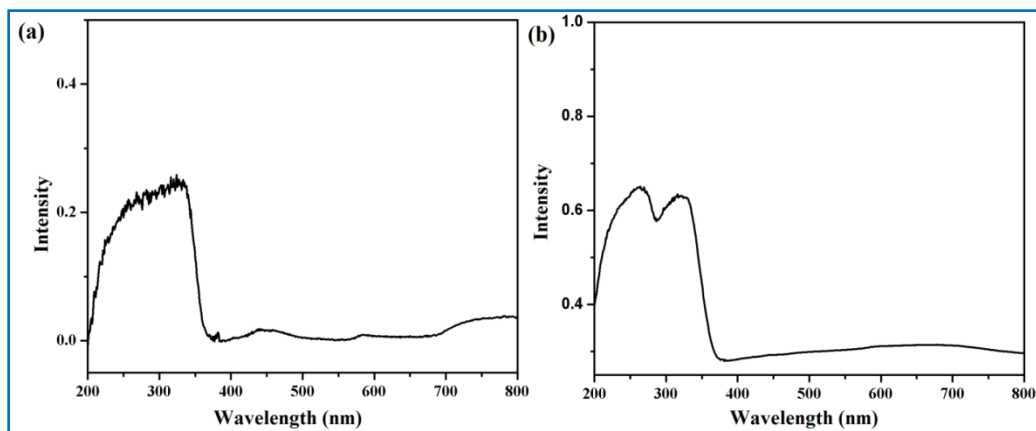


Figure 2. UV-Vis spectra of (a) compound **1**, and (b) compound **2**.

2.4.2. $[\text{Cd}_2(\text{rectt-tpcb})(3,3\text{-dmglu})_2]_n$ (**2**)

The single crystals of **2** have been obtained by UV irradiation of single crystals of **1** for 4 h. Anal. Calc. for $\text{C}_{38}\text{H}_{40}\text{Cd}_2\text{N}_4\text{O}_8$ (**2**, %): C, 50.39; H, 4.45; N, 6.18. Found: C, 50.38; H, 4.44; N, 6.18. IR spectra (KBr, cm^{-1}): $\nu(\text{CH-Ar})$, 3100–2900; $\nu(\text{C=C, Ar})$, 1530–1432; $\nu(\text{CH-alkane})$, 1431–1354; $\nu(\text{C=C})$, 1680–1560; $\nu(\text{C-C})$, 1480; $\nu(\text{C-H})$, 1393; $\nu(\text{C-O})$, 1250–1060 (Figure 1b). The UV-vis absorption spectra of compound **2** has been measured in solid state at room temperature (Figure 2b).

2.4.3. $[\text{Cd}_2(\text{bpe})_2(3,3\text{-dmglu})_2]_n$ (**1'**)

The single crystals of **2** have been heated to 250°C in a hot air oven. After 3 h, light white crystals of **1'** suitable for X-ray analysis have been obtained. Details of crystallographic parameters are provided in Table 1.

Table 1. Crystallographic and structural refinement parameters for compound **1**, **2**, and **1'**

	1	2	1'
formula	C ₃₈ H ₄₀ Cd ₂ N ₄ O ₈	C ₃₈ H ₄₀ Cd ₂ N ₄ O ₈	C ₃₈ H ₄₀ Cd ₂ N ₄ O ₈
formula weight	905.54	905.56	905.54
crystal system	monoclinic	monoclinic	monoclinic
space group	<i>P2₁/c</i>	<i>C2</i>	<i>P2₁/c</i>
<i>a</i> /Å	13.9823(5)	13.7767(8)	13.9867(5)
<i>b</i> /Å	15.7734(5)	14.4557(8)	15.7579(5)
<i>c</i> /Å	17.0202(6)	18.5563(11)	17.0260(5)
α /°	90	90	90
β /°	94.432(2)	91.428(4)	94.278(2)
γ /°	90	90	90
<i>V</i> /Å ³	3742.6(2)	3694.4(4)	3742.1(2)
<i>Z</i>	4	4	4
<i>D_c</i> / g cm ⁻³	1.602	1.628	1.602
μ /mm ⁻¹	1.193	1.208	1.193
<i>F</i> ₀₀₀	1812	1824	1812
θ range/°	1.5 - 27.6	2.0 - 27.6	1.5 - 27.7
reflections collected	70818	28749	57847
unique reflections	8699	8408	8717
reflections <i>I</i> > 2σ(<i>I</i>)	5848	5849	6574
<i>R</i> _{int}	0.093	0.067	0.038
goodness-of-fit (<i>F</i> ²)	1.04	1.03	1.04
<i>R</i> 1 (<i>I</i> > 2σ(<i>I</i>)) ^[a]	0.0461	0.0711	0.0423
<i>wR</i> ₂ (<i>I</i> > 2σ(<i>I</i>)) ^[a]	0.1140	0.1990	0.1059
$\Delta\rho$ min / max /e Å ³	-0.69, 0.82	-1.01, 2.79	-1.12, 1.59

$$^{[a]}R_1 = \Sigma ||F_o| - |F_c|| / \Sigma |F_o|, \quad wR_2 = [\Sigma (w(F_o^2 - F_c^2))^2 / \Sigma w(F_o^2)^2]^{1/2}.$$

2.5. Crystallographic data collection and refinement

The single crystal of compound **1**, **2**, and **1'** has been mounted on a thin glass fiber with commercially available super glue. X-ray single crystal data collection of all the crystals have been performed at room temperature using Bruker APEX II diffractometer, equipped with a normal focus, sealed tube X-ray source with graphite monochromated Mo-K α radiation (λ =

0.71073 Å). The data have been integrated using SAINT⁴⁶ program and the absorption corrections have been made with SADABS⁴⁷. The structure has been solved by SHELXS-2016⁴⁸ using Patterson method and followed by successive Fourier and difference Fourier synthesis. Full matrix least-squares refinement has been performed on F^2 using SHELXL-2016⁴⁸ with anisotropic displacement parameters for all non-hydrogen atoms except C23 in **1** and **1'**. During refinement one carbon atom (C23) of 3,3-dmglu moiety is found highly disordered and therefore splitted in two part (C23A and C23B) considering 0.5 occupancy of each thereafter refined isotropically imposing a DFIX restrains. The hydrogen atoms, bounded to this methyl carbon are not fixed however it has been added to the total molecular formula for both the compounds. All other hydrogen atoms of **1** have been fixed geometrically by HFIX command and placed in ideal positions. The potential solvent accessible area or void spaces have been calculated using the PLATON⁴⁹ multipurpose crystallographic software. All the calculations have been carried out using SHELXS-2016,⁴⁸ SHELXL-2016,⁴⁸ WinGX system Ver-1.80⁵¹, and TOPOS^{52,53}. Data collection and structure refinement parameters along with crystallographic data for **1**, **2** and **1'** are given in Table 1. The selected bond lengths and angles are given in Tables 2 and 3.

3. Results and discussion

3.1. Structural description of the compounds

3.1.1. Structure description of compound **1**

Compound **1** crystallizes in the monoclinic $P2_1/c$ space group ($Z = 4$) and the structural analysis reveals the formation of a two-fold interpenetrated 3D pillared-layer framework structure. The asymmetric unit of **1** contains two crystallographically independent Cd(II) centers (Cd1 and Cd2), two molecules of 3,3-dmglu ligand and two molecules of bpe linker (Figure 3a). The hepta-coordinated Cd1 with CdO_5N_2 coordination environment shows distorted pentagonal bipyramidal geometry where the equatorial sites are occupied by five oxygen atoms (O1, O2, O3^a, O4^a and O4^b) from three different 3,3-dmgluligands and two nitrogen atoms (N1 and N2^c) from two different bpe linkers occupy the axial positions (Figure 3a). However, the hexa-coordinated Cd2 shows distorted octahedral geometry with CdO_4N_2 coordination environment (Figure 3a). The equatorial positions of Cd2 are occupied by four oxygen atoms (O5, O6, O7^e and O8^f) from two different 3,3-dmgluligands and two nitrogen atoms (N3 and N4) from two different bpe linkers occupy the axial positions (Figure 3a). Selected bond lengths and bond angles for **1** are shown in the Table 2. In case of Cd1, each 3,3-dmgluligand connects the

adjacent three Cd(II) centers by bis-chelation and mono oxo-bridging fashion to create wavy type metal-carboxylate 2D (4,4) layer in the crystallographic *bc* plane, where both the metal and respective carboxylate behave as 3-connected nodes (Figures 3b and 3d). The linear bpe linkers connect the 2D metal-carboxylate sheet to create a bi-pillared 3D structure (Figure 4b) in such a manner that the distance between the centers of the adjacent C=C bonds of bpe are around 4.0 Å (Figure 4b). On the other hand, for Cd2, each 3,3-dmglu ligand connects adjacent three Cd(II) centers through bridging bidentate and chelating fashion to create almost flat 2D metal-carboxylate (4,4) layer in the crystallographic *bc* plane (Figures 3c and 3d).

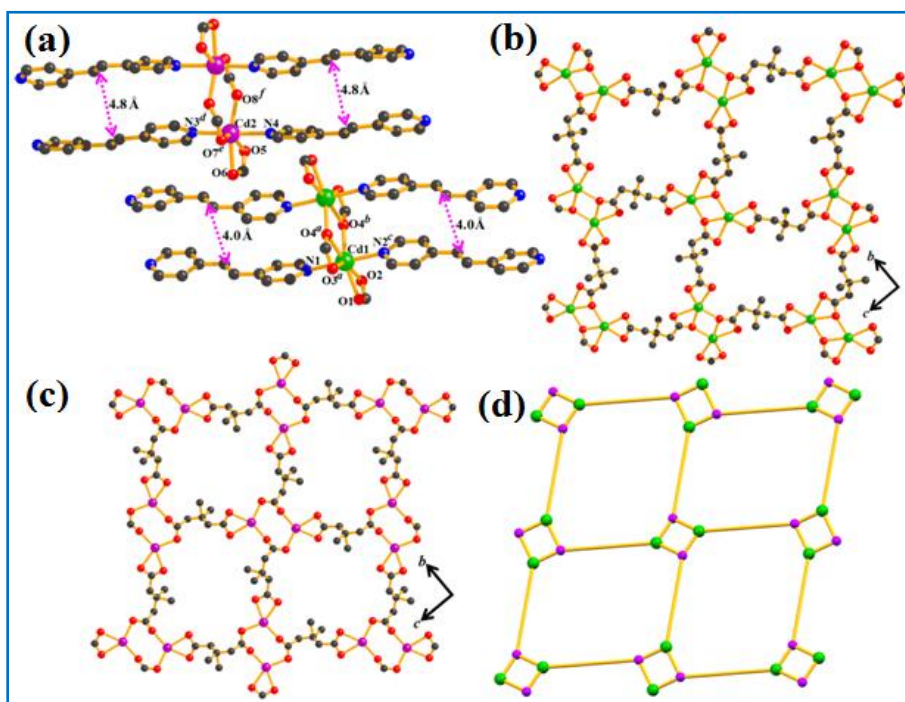


Figure 3. (a) A perspective view of the coordination environment of Cd1 and Cd2 in **1**. Cd1 (green), Cd2 (Pink), O (red), N (blue) and C (black). The separation of C=C in both the frameworks are depicted by magenta dotted lines. (b) View of wavy type 2D metal-dicarboxylate sheet with hepta-coordinated Cd1 in **1**. (c) View of almost flat 2D metal-dicarboxylate sheet with hexa-coordinated Cd2 in **1**. (d) Simplified topological representation of 2D metal-carboxylate (4,4) layer.

These 2D layers are also connected by linear bpe linkers to form bi-pillared 3D structure in such a manner that the distance between the centers of the adjacent C=C bonds of bpe are around 4.8 Å (Fig 4c). These two 3D bi-pillared arrangements for both Cd1 and Cd2 are interpenetrated to each other forming two fold interpenetrated 2(1+1) 3D structure (Fig 4a). The structure of **1** is

found to be microporous with total solvent accessible void of 127.0 \AA^3 which is 3.4 % of the total crystal volume (3742.6 \AA^3) (Table 1). The TOPOS^{52,53} analysis reveals that the structure of **1** can be represented as a (3,5) connected bi-nodal interpenetrating net with point symbol $\{4.6^2\}\{4.6^6.8^3\}$.

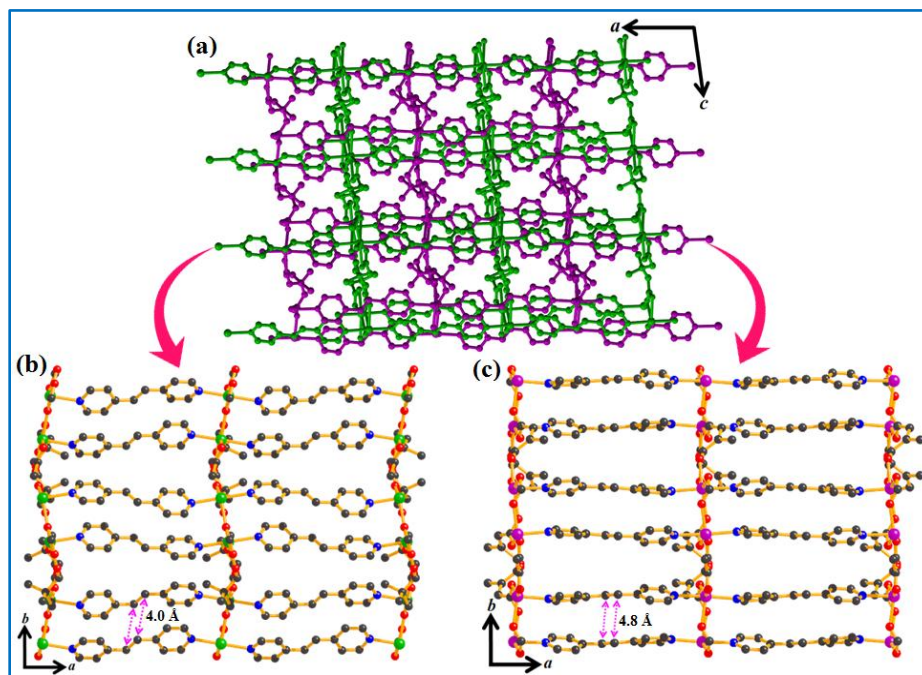


Figure 4. (a) Overall interpenetrated 3D structure of **1**. (b,c) Structural drawing of two 3D nets separately constructed by Cd1 and Cd2 that are part of the overall structure in **1**. The separation of C=C bonds in both the frameworks is depicted by magenta dotted lines.

3.1.2. Structure description of compound 2

Compound **2** crystallizes in the monoclinic $C2$ space group ($Z = 4$) and the structural analysis reveals the formation of a 2-fold interpenetrated 3D framework structure. The asymmetric unit of **2** also contains two crystallographically independent Cd(II) centers (Cd1 and Cd2), two molecules of 3,3-dmglu ligand and one molecule of rctt-tpcb linker (Figure 5a). The hepta-coordinated Cd1 displays distorted pentagonal bipyramidal geometry with CdO_5N_2 coordination environment where the five oxygen atoms (O1 , O2^d , O5 , O7^b and O8^b) of three different 3,3-dmgluligands form the equatorial plane and two nitrogen atoms (N1 and N2^c) of two different rctt-tpcb ligands occupy the axial positions (Figure 5a). Whereas, the hexa-coordinated Cd2 shows distorted octahedral geometry with CdO_4N_2 coordination environment (Figure 5a). Four oxygen atoms (O2^d , O3 , O4 and O6^d) from two different 3,3-dmgluligands comprise the equatorial positions and two nitrogen atoms (N3^d and N4^e) of two different rctt-tpcb ligands

Table 2. Selected bond lengths (Å) and bond angles (°) for compound **1**

Cd1–N2 ^c	2.365(4)	Cd1–O2	2.469(3)
Cd1–O4 ^b	2.329(3)	Cd2–O5	2.407(3)
Cd1–O3 ^a	2.559(3)	Cd2–O6	2.358(3)
Cd1–O4 ^a	2.347(3)	Cd2–N4	2.359(4)
Cd1–N1	2.355(4)	Cd2–N3 ^d	2.311(4)
Cd1–O1	2.287(3)	Cd2–O8 ^f	2.250(5)
Cd2–O7 ^e	2.301(3)	O2–Cd1–O4 ^a	164.22(10)
O2–Cd1–O3 ^a	143.19(10)	O3 ^a –Cd1–N1	92.71(12)
N1–Cd1–N2 ^c	177.72(12)	O4 ^b –Cd1–N2 ^c	89.45(10)
O4 ^b –Cd1–N1	90.27(10)	O4 ^a –Cd1–N2 ^c	93.69(11)
O4 ^a –Cd1–N1	88.38(11)	O4 ^b –Cd1–O4 ^a	72.46(10)
O3 ^a –Cd1–N2 ^c	89.31(12)	O1–Cd1–O4 ^b	145.60(10)
O3 ^a –Cd1–O4 ^b	124.63(10)	O1–Cd1–O4 ^a	141.38(10)
O3 ^a –Cd1–O4 ^a	52.41(10)	O1–Cd1–N1	95.60(13)
O1–Cd1–O3 ^a	88.99(11)	O2–Cd1–N1	88.27(13)
O1–Cd1–O2	54.35(11)	O2–Cd1–O4 ^b	92.14(10)
O1–Cd1–N2 ^c	83.38(13)	O5–Cd2–N4	84.99(11)
O2–Cd1–N2 ^c	89.48(13)	O5–Cd2–O8 ^f	101.2(2)
O5–Cd2–O6	54.85(14)	O6–Cd2–N4	89.92(13)
O5–Cd2–N3 ^d	91.43(11)	O6–Cd2–O8 ^f	155.73(19)
O5–Cd2–O7 ^e	145.67(14)	N3 ^d –Cd2–N4	174.64(12)
O6–Cd2–N3 ^d	91.26(13)	O7 ^e –Cd2–N4	86.77(13)
O6–Cd2–O7 ^e	91.94(11)	O7 ^e –Cd2–N3 ^d	98.41(13)
O8 ^f –Cd2–N4	83.46(13)	O7 ^e –Cd2–O8 ^f	110.88(19)
O8 ^f –Cd2–N3 ^d	93.36(13)		

Symmetry code: $a = 2-x, 1/2+y, 1/2-z$; $b = x, -1/2-y, -1/2+z$; $c = 1-x, -y, 1-z$; $d = 2-x, 1-y, 1-z$; $e = 1-x, 1/2+y, 1/2-z$; $f = x, 1/2-y, -1/2+z$.

occupy the axial positions (Figure 5a). Selected bond lengths and bond angles for **2** are shown in the Table 3. Both the Cd(II) centers are connected by three different bridging 3,3-dmglu ligands by means of chelation and oxo-bridging to form 2D metal-carboxylate (4,4) layer in crystallographic bc plane (Figures 5b and 5c). These sheets are further connected by rctt-tpcb linkers to form pillared 3D network structure (Figure 6a) with large void having two-fold interpenetration (Figures 6b and 6c). The structure of **2** is found to be microporous with total solvent accessible estimated void of 218.0 Å³ which is 5.9 % of the total crystal volume (3694.4

\AA^3). The structure can be described by TOPOS^{52,53} software, as a (3,4,5)-connected tri-nodal two fold interpenetrated net with Schläfli symbol $\{4.8^2\}2\{4^2.8^4\}\{4^6.8^4\}2$.

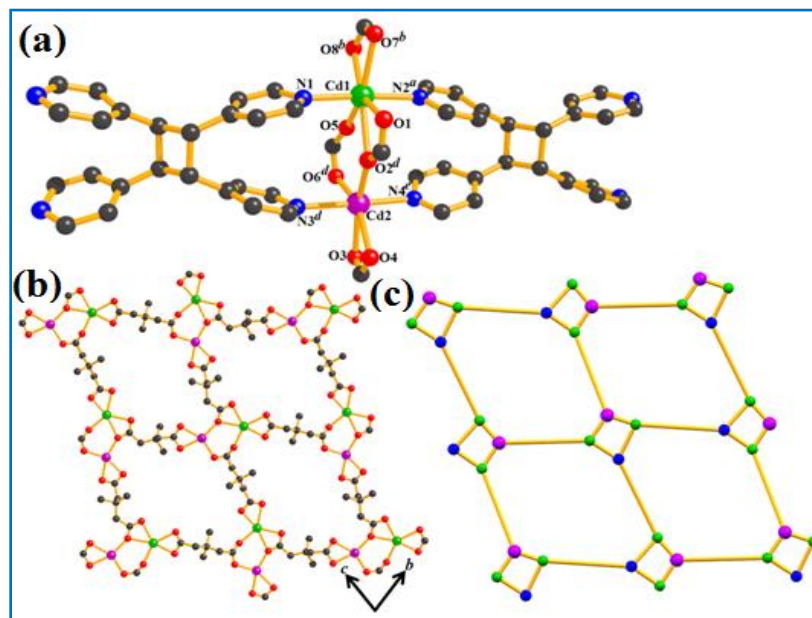


Figure 5. (a) A perspective view of the coordination environment of Cd1 and Cd2 in **2**. Cd1 (green), Cd2 (Pink), O (red), N (blue) and C (black). (b) View of wavy type 2D metal-dicarboxylate sheet in **2**. (c) Simplified topological representation of 2D metal-carboxylate (4,4) layer in **2**.

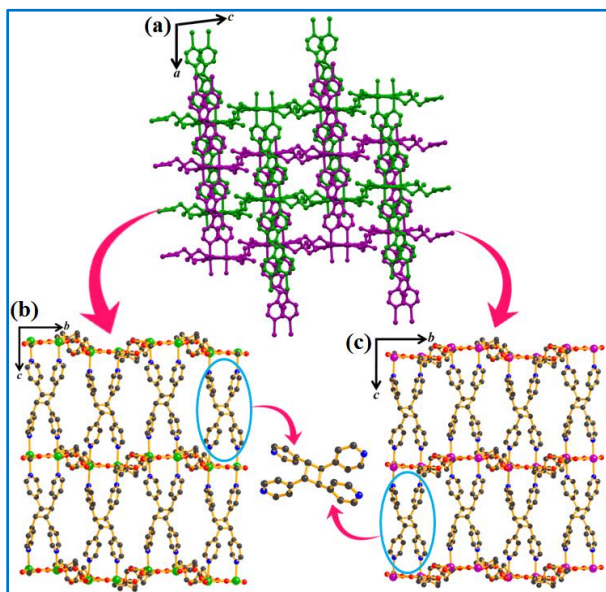


Figure 6. (a) Overall interpenetrated 3D structure of **2**; and (b,c) structural drawing of two 3D nets separately constructed by Cd1 and Cd2 that are involved in interpenetration to give the overall structure in **2**. Cd1 (green), Cd2 (Pink), O (red), N (blue) and C (black).

Table 3. Selected bond lengths (Å) and bond angles (°) for compound **2**

Cd1–O1	2.447(13)	Cd2–O3	2.336(15)
Cd1–O2	2.525(14)	Cd2–O4	2.369(15)
Cd1–O5	2.310(18)	Cd2–O2 ^d	2.267(13)
Cd1–N1	2.304(12)	Cd2–O6 ^d	2.256(15)
Cd1–N2 ^a	2.327(11)	Cd2–N3 ^d	2.457(13)
Cd1–O7 ^b	2.445(16)	Cd2–N4 ^e	2.353(11)
Cd1–O8 ^b	2.301(13)	O7 ^b –Cd1–N2 ^a	86.4(7)
O1–Cd1–O2	51.5(5)	O8 ^b –Cd1–N2 ^a	88.4(5)
O1–Cd1–O5	126.0(6)	O7 ^b –Cd1–O8 ^b	53.9(6)
O1–Cd1–N1	87.2(5)	O3–Cd2–O4	54.5(5)
O1–Cd1–N2 ^a	89.2(5)	O2 ^d –Cd2–O3	159.5(5)
O1–Cd1–O7 ^b	91.2(5)	O3–Cd2–O6 ^d	97.1(6)
O1–Cd1–O8 ^b	145.1(6)	O3–Cd2–N3 ^d	92.9(7)
O2–Cd1–O5	74.5(6)	O3–Cd2–N4 ^e	88.8(6)
O2–Cd1–N1	86.2(5)	O2 ^d –Cd2–O4	105.1(5)
O2–Cd1–N2 ^a	89.7(5)	O4–Cd2–O6 ^d	150.6(6)
O2–Cd1–O7 ^b	142.6(5)	O4–Cd2–N3 ^d	87.4(5)
O2–Cd1–O8 ^b	163.2(6)	O4–Cd2–N4 ^e	94.4(5)
O5–Cd1–N1	91.5(8)	O2 ^d –Cd2–O6 ^d	103.3(6)
O5–Cd1–N2 ^a	88.7 (7)	O2 ^d –Cd2–N3 ^d	86.6(7)
O5–Cd1–O7 ^b	142.4(6)	O2 ^d –Cd2–N4 ^e	92.2(7)
O5–Cd1–O8 ^b	88.7(7)	O6 ^d –Cd2–N3 ^d	86.7(6)
N1–Cd1–N2 ^a	175.7(5)	O6 ^d –Cd2–N4 ^e	92.2(6)
O7 ^b –Cd1–N1	96.0(7)	N3 ^d –Cd2–N4 ^e	178.1(7)
O8 ^b –Cd1–N1	96.0(5)	Cd1–O2–Cd2 ^c	124.1(6)

Symmetry code: $a = -1+x, 1+y, z$; $b = 3/2-x, 3/2+y, 2-z$; $c = 3/2-x, 1/2+y, 1-z$; $d = x, 1+y, z$; $e = -1+x, 1+y, z$.

3.2. Powder diffraction (PXRD) analysis

Phase purity of the bulk materials with the simulated patterns has been checked by powder X-ray diffraction (PXRD) analysis for **1** and **2** at room temperature. The experimental PXRD patterns of **1** and **2** are well matched with the simulated ones obtained from their corresponding single crystal structures (Figure 7), confirming the phase purity of the compounds **1** and **2**.

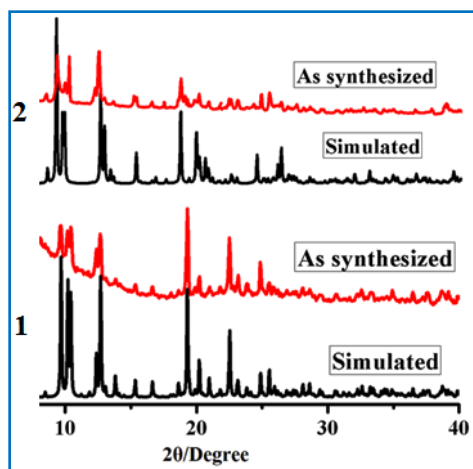


Figure 7. PXRD pattern of **1** and **2** simulated (black), as synthesized (red).

3.3. Gas sorption studies

Gas sorption (N_2 , CO_2) and solvent sorption (H_2O) studies has been carried out for the compounds **1** and **2**. For N_2 gas sorption, compound **1** shows moderate result and for others only surface sorption observed (Figure 8).

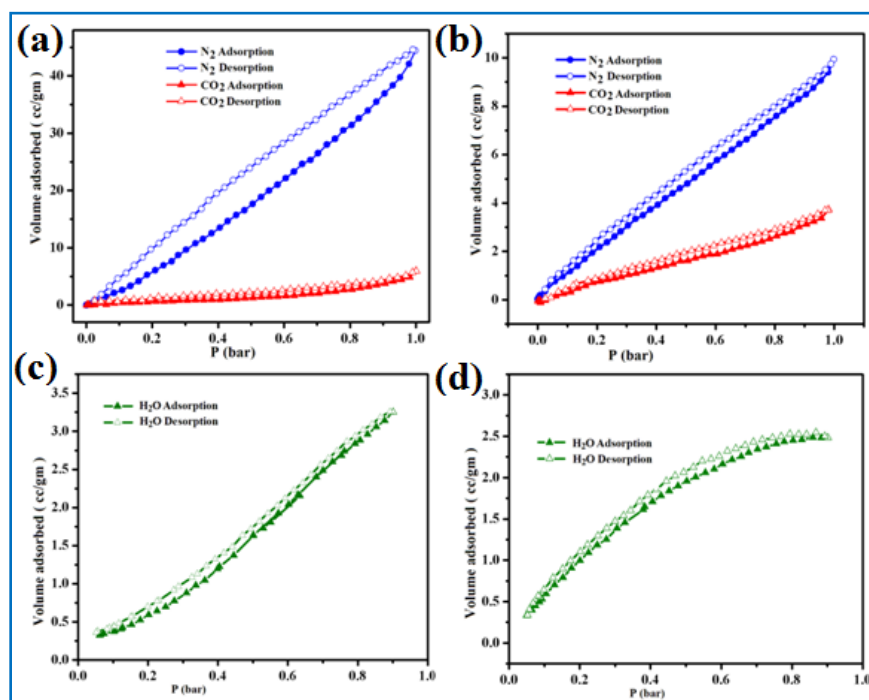


Figure 8. (a) Different sorption isotherms of **1**; N_2 at 77 K (blue circles), CO_2 at 195 K (red triangles). (b) Different sorption isotherms of **2**; N_2 at 77 K (blue circles), CO_2 at 195 K (red triangles). (c) H_2O sorption (green triangle) of **1** at 298 K; signifying adsorption (filled) and desorption (empty) curve. (d) H_2O sorption (green triangle) of **2** at 298 K; signifying adsorption (filled) and desorption (empty) curve.

3.4. Thermo gravimetric analysis (TGA)

Thermo gravimetric analysis for the compound **1** and **2** has been carried out. TGA curve of compound **1** and **2** shows, they are stable up to 290 °C and 300 °C respectively (Figure 9).

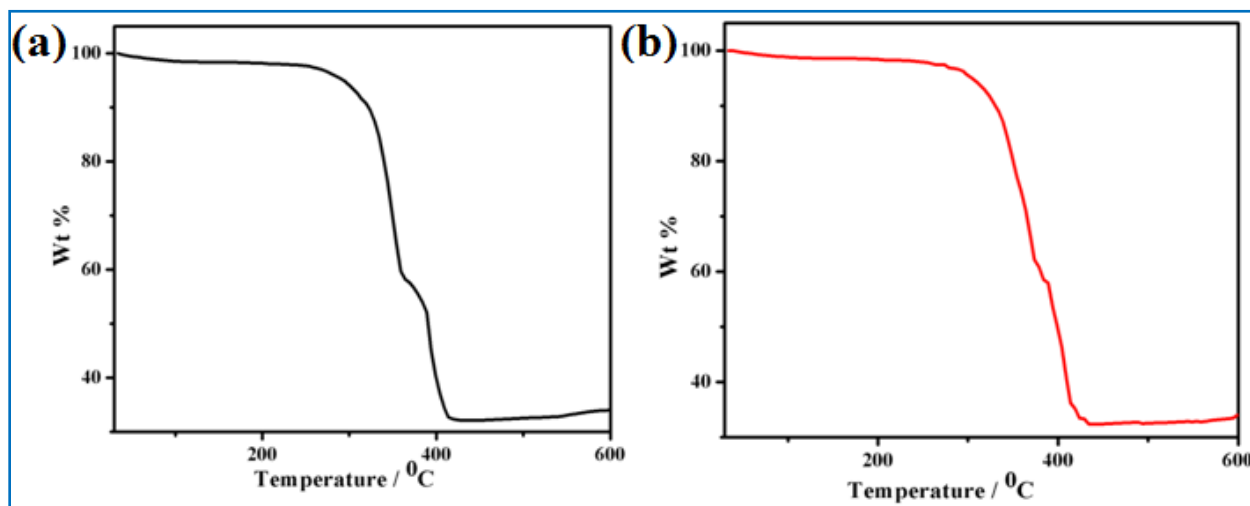


Figure 9. (a) TGA analysis of **1** at 30 °C – 600 °C, showing the stability of the MOF up to 290°C. (b) TGA analysis of **2** at 30 °C – 600 °C, showing the stability of the MOF up to 300°C.

3.5. Differential thermal analyses (DTA)

Differential thermal analyses (DTA) have been performed to understand the progress of the cycloaddition reaction. Here compound **1** upon irradiation with UV for 4 hours converted to compound **2** and **2** is also reverting back to **1** upon heating. Therefore, the formation of **2** with UV radiation can be monitored by the reverse thermal transition in the conversion temperature range, in DTA experiment, taking very slow heating rate of 2 degree/minute. In DTA, for the compound **2** (compound **1** on UV exposure for a duration of 4 hours, henceforth represented as **1** @4H UV) significant endothermic peak appear at the temperature range 110°C-210°C with ΔH value ~ 10.4 KJ/mole (Figure 10a). This clearly indicates the photo conversion of **1** into **2** that has been reverting back during the DTA study. The same experiment has done with the compound **1** after UV radiation for 1 hour (**1**@1H UV), 2 hours (**1**@2H UV) and 3 hours (**1**@3H UV) (Figures 10b, 10c & 10d). In none of the cases, endothermic curve has been obtained which indirectly proves that there is no conversion from **1** to **2** has been possible, when the UV irradiation has done below 4 hours. From this experiment it has been stipulated that the UV irradiation time (for the conversion of **1** to **2**) 4 hours and the heating temperature 250°C (for the conversion of **2** to **1**).

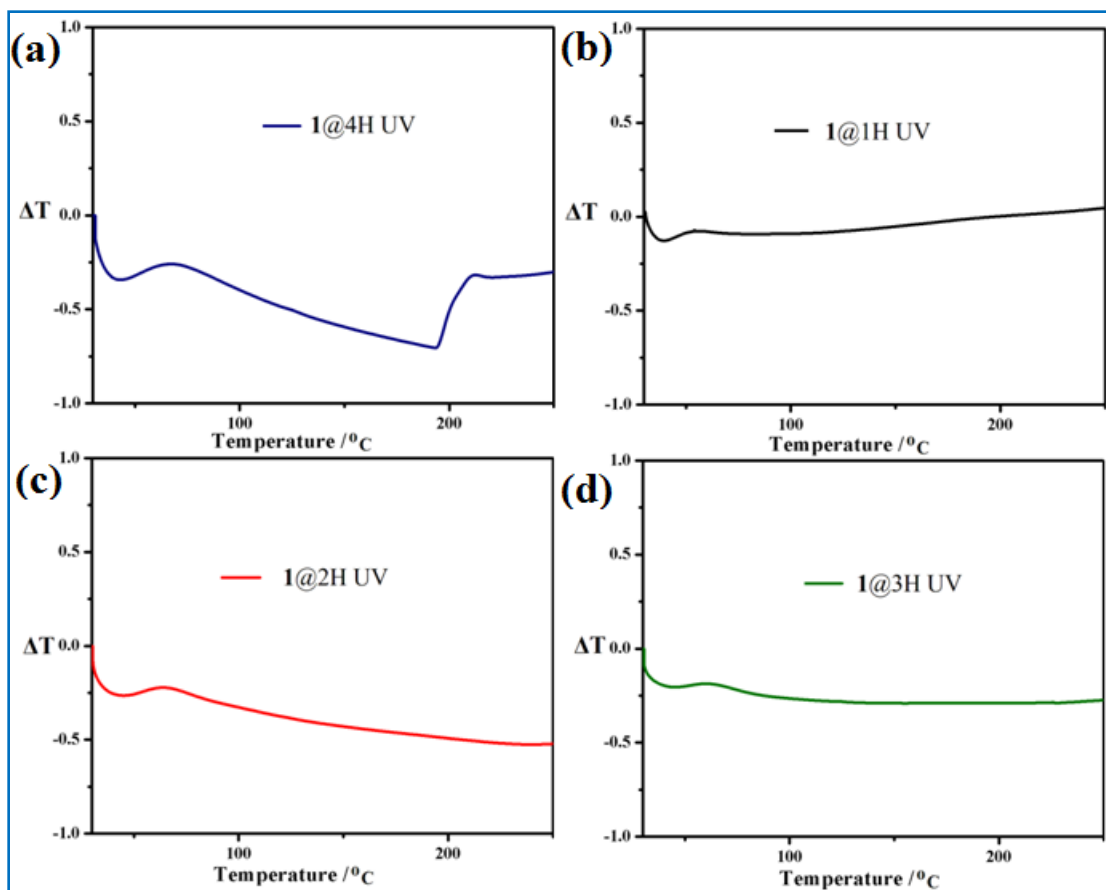


Figure 10. (a) DTA analysis of **1** @4H UV (**2**) at 30 °C – 250 °C. (b) DTA analysis of **1** @1H UV at 30 °C – 250 °C. (c) DTA analysis of **1** @2H UV at 30 °C – 250 °C. (d) DTA analysis of **1** @3H UV at 30 °C – 250 °C.

3.6. NMR study

To support the SCSC conversion, we have tried to carry out the ^1H -NMR spectroscopy of **1** and **2** has been attempted but the compound found insoluble in all common organic solvent and even in many strong acids. Only it is found soluble in strong HNO_3 and thus the ^1H -NMR spectra for **1** and **2** have been performed in DMSO-HNO_3 . For this, both the compounds have been taken in NMR tube and a drop of strong HNO_3 has been added along with DMSO . The mixture was sonicated for 10 min to dissolve the insoluble MOFs before recording the ^1H -NMR spectra. Here aqueous HNO_3 has gave an intense peak at δ 4.5-6, whereas the proton signal of the characteristic cyclized cyclobutane rings also come in the same region. As a result, the characteristic peak (of small amount of polymer dissolved in the acid) has been submerged and therefore no direct inference could be made from the ^1H -NMR regarding the transition. Although the ^1H -NMR

spectrum of compound **2** and **1** (Figure 11) has been done with few crystals, each characterized by single crystal X-ray diffraction before doing the H^1 -NMR in DMSO- HNO_3 . The conversion of **1** to **2** is evidenced here partially. Here in the H^1 -NMR spectrum of compound **2**, the characteristic peak for the proton of $CH=CH$ went off (which was present in the H^1 -NMR spectrum of compound **1**) but the CH proton of the cyclobutane ring is being fully masked in the area of the huge peak of aqueous HNO_3 and could not be analyzed.

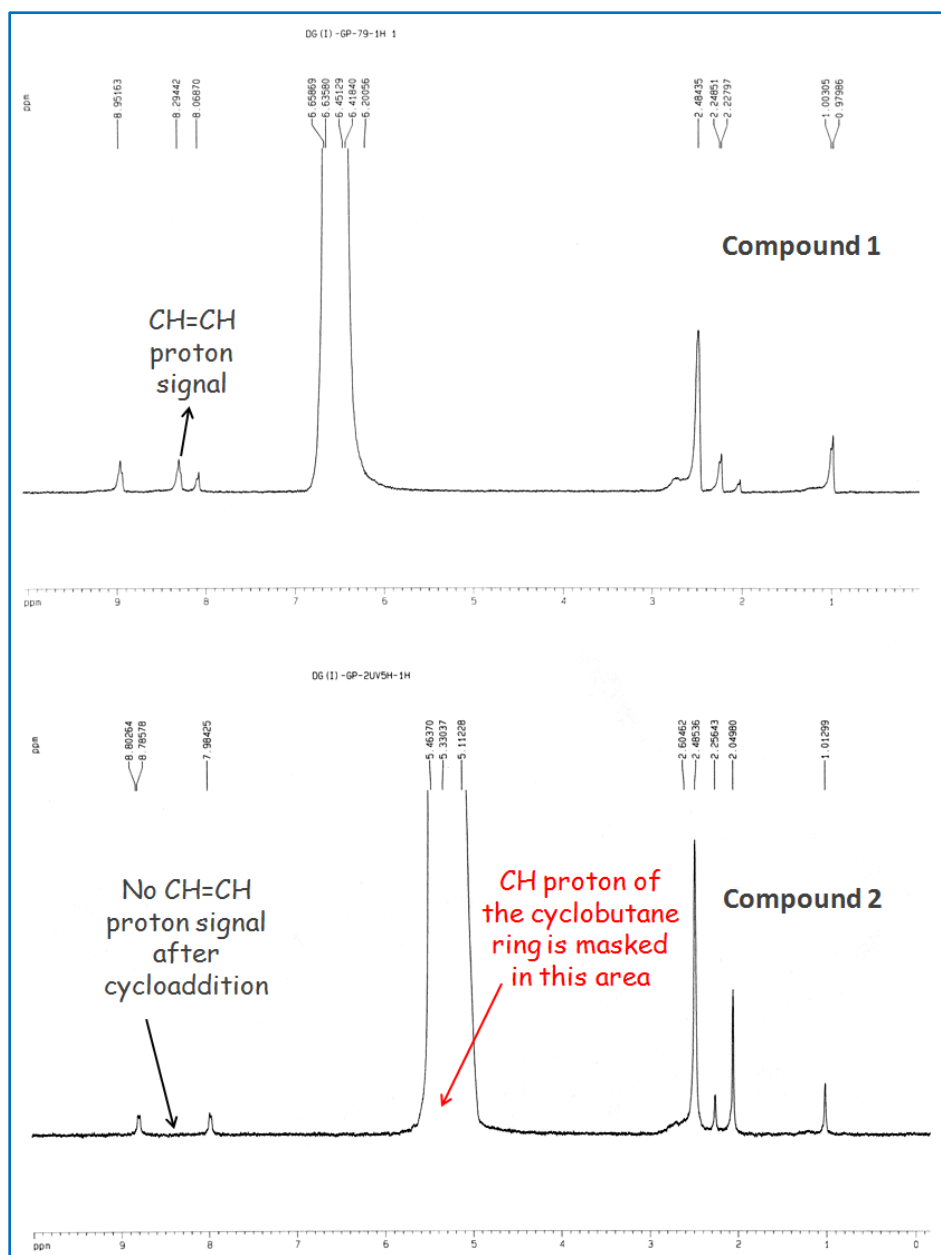


Figure 11. NMR spectra of **1** and **2**.

3.7. Reversible photochemical solid-state transformation

The adjacent C=C bond distances are different in two interpenetrated nets of compound **1**. These are 4.0 Å and 4.8 Å (Figure 3a), respectively for Cd1 and Cd2 containing 3D network. This unique structural feature facilitates the UV-irradiation-induced photodimerization of bpe. The adjacent C=C bonds only in the Cd1 unit satisfy the Schmidt's topochemical criteria for photochemical [2+2] cycloaddition reaction (parallel alignment and olefin separation less than 4.2 Å), whereas in Cd2 unit the distance is much higher. In spite of that when the single crystals of **1** have been subjected to UV irradiation (wavelength 350 nm) for 4 hrs, both the C=C bonds are cyclized with intranet [2+2] cycloaddition confirmed by single crystal X-ray analysis of the UV treated product **2**. It is interesting to note that the cycloaddition reaction here is associated with the change of space group from achiral *P*21/*c* to chiral *C*2.^{55,56} The structural analysis of **2** reveals the formation of a similar kind of two-fold interpenetrating 3D structure with the cyclized C-C bonds (Figures 6b & 6c). The basic arrangement of the structure in **2** is similar to that of **1** with a difference only in the pillaring of 2D sheets by the tpcb linkers.

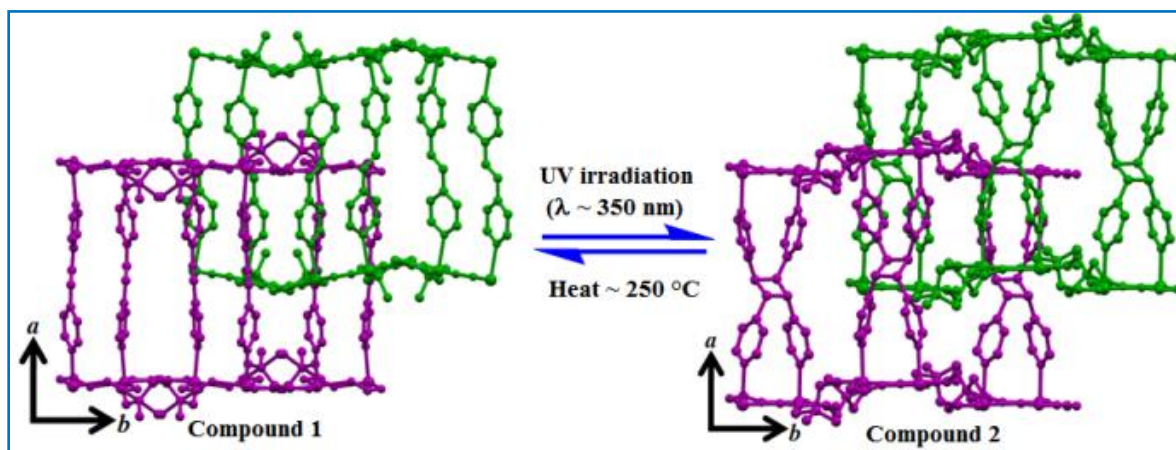


Figure 12. View of reversible [2 + 2] photocycloaddition between slip-stacked bpe ligand and its thermal cleavage in two-fold interpenetrated 3D networks of **1** and **2**.

The ^1H -NMR spectrum of **2** in DMSO- HNO_3 shows (Figure 11)) that the characteristic peak for the CH=CH proton of bpe went off, but the CH proton of the cyclobutane ring of tpcb has been masked in the area of the huge peak of aqueous HNO_3 . TGA of **1** and **2** indicate that they are stable up to 290 °C and 300 °C respectively (Figure 9). To study the reversibility of the photoinduced cycloaddition the single crystals of **2** have been heated at 250 °C. After 3 h, light white crystals of **1'** have been obtained. The single crystal X-ray analysis revealed that the

structure of **1'** is identical to that of the parent compound **1** with the achiral $P2_1/c$ space group (Table 1), confirming the complete reversible nature of photodimerization of the aforesaid MOF in solid state (Figure 12). Interestingly, the DTA study (Figure 10) indicates that no conversion from **1** to **2** is possible, when the UV irradiation has continued below 4 hours. The cyclization of both C=C bonds in **1** is possibly due to the enhanced void space around the coordination sphere generated by the probable reorganization of the interpenetrated forms, flexibility of the bpe ligands and also interpenetration induced molecular movement. In a two-fold interpenetrated structure once a net is subjected to cycloaddition the other net must reorganize itself to fit into the new structural environment. Hence, this structural stress is probably reduced when the second net also gets cyclized to maintain their overall structural pattern which is two-fold interpenetrated in present case. As discussed before, this is the first example in MOF where two different types of olefinic bonds have been cyclized together and therefore, it is an excellent case to investigate *Kaupp's* proposition of relating cycloaddition and long-range molecular movements taking place in the context of MOFs.

3.8. Mechano-structural property correlation by nanoindentation experiments

To understand the reasons for SCSC photochemical reaction, particularly between the molecules with 4.8 Å distance, and its reversible nature, the nanoindentation experiments has performed, which establish a mechano-structural property correlation between the two crystals. The nanoindentation experiments have been carried out on the crystals of parent compound **1** and photocyclized compound **2**. All the crystals have been indented on their major faces (001) which have been identified from face indexing using SCXRD (Figure 13). Typical load-displacement (P-h) curves and scanning probe microscopy (SPM) images of the indentation impressions of crystals of **1** and **2** are demonstrated in Figure 14. The nature of the accomplished P-h curves from nanoindentation of both the crystals is almost similar (Figure 14). They display considerable recovery of the indentation depths upon unloading. This suggests that these crystals display significant elastic deformation behavior. The elastic modulus, E, and hardness, H, values from the nanoindentation technique, obtained using the standard Oliver–Pharr (O–P) method⁵⁴ (summarized in Table 4) confirm that these crystals are soft. The aliphatic carboxylate chains of the MOF are extended in the direction of indentation on the (001) plane. Hence, the softness of this plane can be understood from the flexible nature of these aliphatic groups in crystal structures. The E and H values of photocyclized crystal **2** (7.07 GPa and 0.87 GPa; Table 4) have

been found to be marginally higher than that of parent crystal **1** (6.79 GPa and 0.79 GPa; Table 4), which signifies a higher resistance of the photocyclized crystal towards elastic and plastic deformations, respectively. Crystal structure greatly influences the ability of molecules to move in solid-state, thus mechanical deformation, in response to external stimuli.^{16,17,20-22,29,33-36} It is generally believed that easier the permanent molecular movement in the crystal packing, the lower the hardness. The slight stiffening and hardening observed in nanoindentation experiments on the cyclized product **2** compared to that of parent compound **1** could be primarily attributed to the enhancement of stiffness of the photocyclized framework due to cycloaddition of the C=C bonds of bpe ligand into rigid cyclobutane ring in **2**. This seems to restrict the mobility of molecules in crystal packing compared to **1**. The mechanical properties of the two crystals are

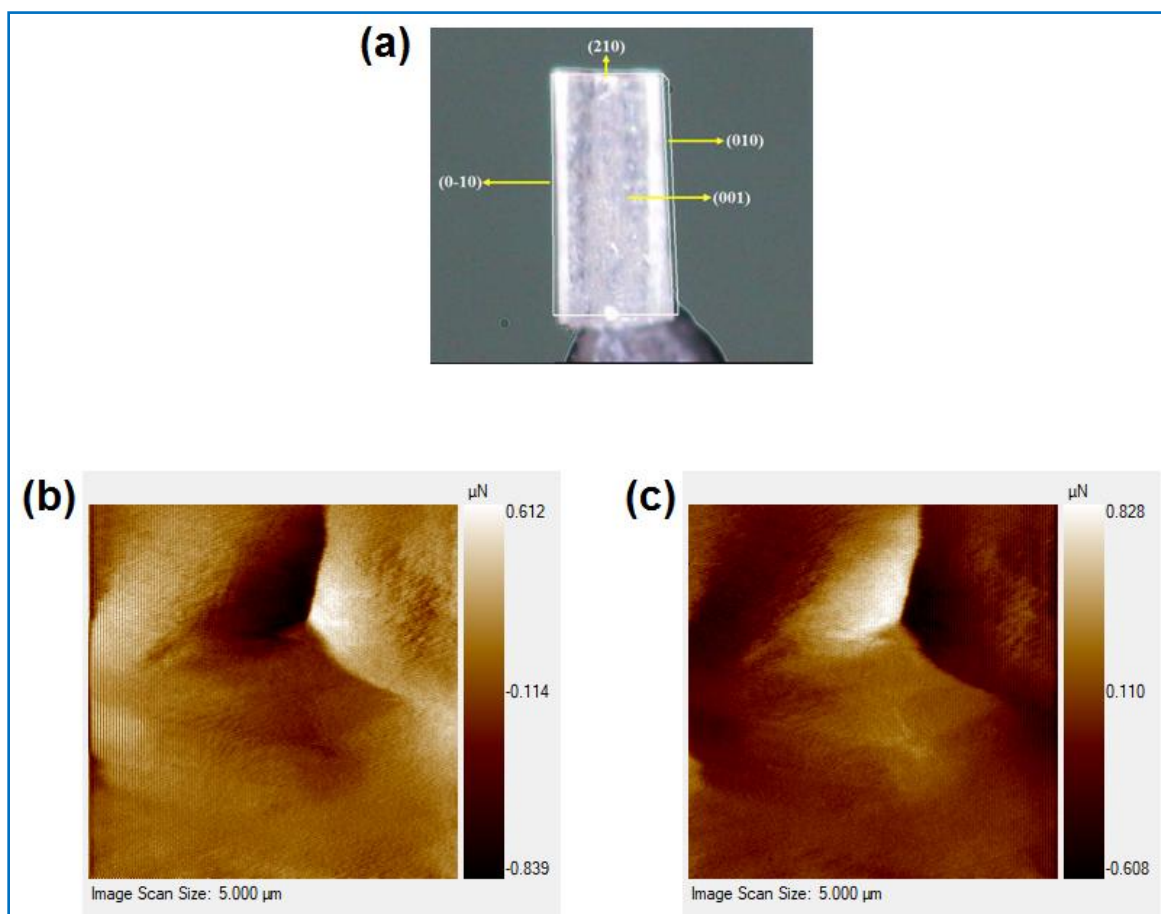


Figure 13. (a) Face indexed images of real crystal of compound **1**. The SPM images of the residual indent impressions of (b) compound **1**, and (c) compound **2** respectively.

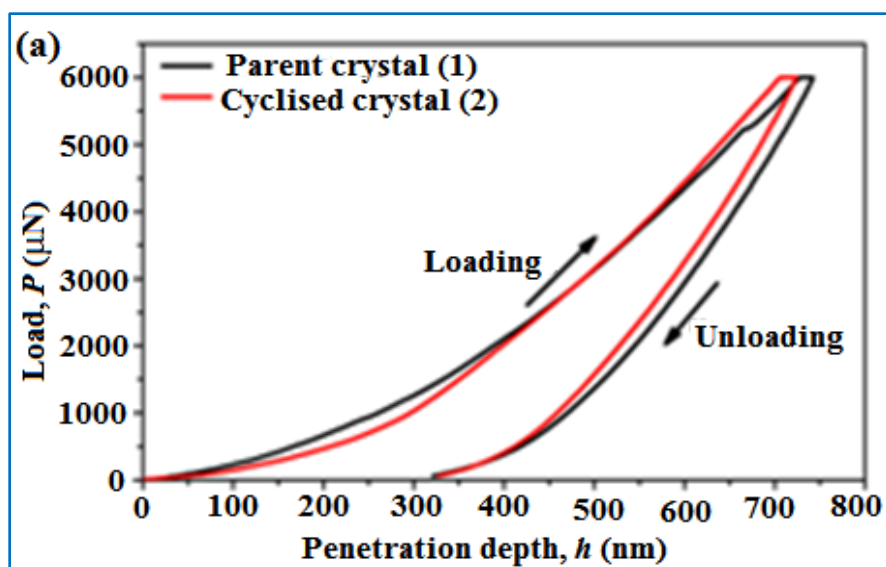


Figure 14. Representative P–h curves obtained from the molecular crystals of parent compound **1** (black line), and photocyclized compound **2** (red line).

Table 4. Crystal mechanical properties for compounds **1** and **2**

compound	indented plane	H (GPa) average	E_y (GPa) average
1	(001)	0.79	6.79
2	(001)	0.87	7.073

still not very different as both the parent and cyclized crystals display a similar two-fold interpenetrated 3D network structure and the cycloaddition reaction is intra-net. After cycloaddition, stiffness of the individual net is expected to increase slightly but not the stiffness of the whole network. As the overall E and H values of **1** and **2** are moderate compared to values of typical MOFs, these shall be considered as soft.²⁷ However, since the 3D network formation in **1** and **2** resists long range molecular movements, the changes primarily could be due to the flexible ligand and modular coordination center. In compound **1**, Cd1–Cd1 distance is 3.77 Å and Cd2–Cd2 distance is 4.35 Å, whereas after the cycloaddition the resultant compound **2** has Cd1–Cd2 distance of 4.23 Å. Thus, the comparison of the geometric parameters at the ligand and the coordination centers revealed that notable changes occur at these two locations. Hence, the local flexibility provided by these two regions seems sufficient for the molecules to move locally and come together to form the cycloaddition product during the chemical reaction.

On the other hand, the similarity in the mechanical behaviour of the two structures also suggests that the stiffness of the 3D network in **1** and **2** is comparable; hence equally facile reverse

movement of molecules is expected and that is the reason for the reversibility of the reaction in SCSC fashion. It is interesting to note that two polymorphs of 1,2,4,5-tetrabromobenzene with similar mechanical properties have been shown earlier to undergo SCSC phase transformation.³⁵ This correlation between “minimal change in mechanical properties” and occurrence of “SCSC transformation”³⁶ seems to be a general phenomenon across different types of materials.

4. Conclusion

In summary, this is an experimentally verified study of mechanical properties of hybrid framework materials undergo photochemical cyclization reaction to correlate local molecular movements in solid state, in a mechanistic point of view. The newly synthesized two-fold interpenetrated 3D MOF has been reversibly converted into a 3D interpenetrated MOF in SCSC manner by the cycloaddition of two distinct C=C bonds with shorter and longer separations, simultaneously. The soft mechanical behaviour in these two crystals indicates that the molecular movements and flexible coordination site in solid state is responsible for the reversible photochemical reactions in the molecular crystals of the said MOF. The SCSC process in the two forms seems to have correlation with the similarity of the crystal structures and mechanical behaviour of the two compounds. This reversible solid-state structural transformation of a MOF with their mechanical properties will certainly open up various new possibilities and outlooks in the development of new MOFs with unique functionalities, like the fabrication of mechanical switches.

References

- (1) R. Santra and K. Biradha, *Chem. Soc. Rev.*, 2013, **42**, 950–967.
- (2) G. K. Kole and J. J. Vittal, *Chem. Soc. Rev.* 2013, **42**, 1755–1775.
- (3) L. R. MacGillivray, G. S. Papaefstathiou, T. Friščić, T. D. Hamilton, D. K. Bucar, Q. Chu, D. B. Varshney and I. G. Georgiev, *Acc. Chem. Res.*, 2008, **41**, 280–291.
- (4) R. Medishetty, I. -H. Park, S. S. Lee and J. J. Vittal, *Chem. Commun.*, 2016, **52**, 3989–4001.
- (5) D. Takeuchi, *In Stereoregular Polymers, Encyclopedia of Polymer Science and Technology*; John Wiley & Sons, Inc.: New York, 2013.
- (6) Z. Wang, K. Randazzo, X. Hou, J. Simpson, J. Struppe, A. Ugrinov, B. Kastern, E. Wysocki and Q. R. Chu, *Macromolecules*, 2015, **48**, 2894–2900.

- (7) A. Chaudhary, A. Mohammad and S. M. Mobin, *Cryst. Growth Des.*, 2017, **17**, 2893–2910.
- (8) I. E. Claassens, V. I. Nikolayenko, D. A. Haynes and L. J. Barbour, *Angew. Chem., Int. Ed.*, 2018, **57**, 15563–15566.
- (9) I. -H. Park, J. Huiyeong, K. Kihwan, S. S. Lee, J. J. Vittal, *IUCrJ*, 2018, **5**, 182–189.
- (10) R. Medishetty, L. L. Koh, G. K. Kole and J. J. Vittal, *Angew. Chem., Int. Ed.*, 2011, **50**, 10949–10950.
- (11) R. Medishetty, R. Tandiana, L. L. Koh and J. J. Vittal, *Chem. – Eur. J.*, 2014, **20**, 1231–1236.
- (12) I. -H. Park, R. Medishetty, H. H. Lee, C. E. Mulijanto, H. S. Quah, S. S. Lee and J. J. Vittal, *Angew. Chem., Int. Ed.*, 2015, **54**, 7313–7317.
- (13) M. K. Mishra, A. Mukherjee, U. Ramamurty and G. R. Desiraju, *IUCrJ*, 2015, **2**, 653–660.
- (14) J. H. Lee, S. Park, S. Jeoung and H. R. Moon, *CrystEngComm*, 2017, **19**, 3719–3722.
- (15) A. Hazra, S. Bonakala, K. K. Bejagam, S. Balasubramanian and T. K. Maji, *Chem. – Eur. J.*, 2016, **22**, 7792–7799.
- (16) G. M. J. Schmidt, *Pure Appl. Chem.*, 1971, **27**, 647–678.
- (17) G. Wegner, *Pure Appl. Chem.*, 1977, **49**, 443–454.
- (18) M. H. Mir, L. L. Koh, G. K. Tan and J. J. Vittal, *Angew. Chem., Int. Ed.*, 2010, **49**, 390–393.
- (19) D. Liu, Z. -G. Ren, H. -X. Li, J. -P. Lang, N. -Y. Li and B. F. Abrahams, *Angew. Chem., Int. Ed.*, 2010, **49**, 4767–4770.
- (20) G. Kaupp, *Angew. Chem., Int. Ed. Engl.*, 1992a, **31**, 592–595.
- (21) G. Kaupp, *Angew. Chem., Int. Ed. Engl.*, 1992b, **31**, 595–598.
- (22) G. Kaupp and E. Zimmermann, *Angew. Chem., Int. Ed. Engl.*, 1981, **20**, 1018–1019.
- (23) Y. Sun, Z. Hu, D. Zhao and K. Zeng, *ACS Appl. Mater. Interfaces*, 2017, **9**, 32202–32210.
- (24) S. Bundschuh, O. Kraft, H. K. Arslan, H. Gliemann, P. G. Weidler and C. Wöll, *Appl. Phys. Lett.*, 2012, **101**, 101910–101914.
- (25) M. Kosa, J. -C. Tan, C. A. Merrill, M. Krack, A. K. Cheetham and M. Parrinello, *ChemPhysChem*, 2010, **11**, 2332–2336.

-
- (26) T. D. Bennett and A. K. Cheetham, *Acc. Chem. Res.*, 2014, **47**, 1555–1562.
- (27) J. C. Tan and A. K. Cheetham, *Chem. Soc. Rev.*, 2011, **40**, 1059–1080.
- (28) A. Gouldstone, N. Chollacoop, M. Dao, J. Li, A. M. Minor and Y. L. Shen, *Acta Mater.*, 2007, **55**, 4015–4039.
- (29) C. M. Reddy, G. R. Krishna and S. Ghosh, *CrystEngComm*, 2010, **12**, 2296–2314.
- (30) J. C. Tan, T. D. Bennett and A. K. Cheetham, *Proc. Natl. Acad. Sci. U. S. A.*, 2010, **107**, 9938–9943.
- (31) M. D. Jong, W. Chen, T. Angsten, A. Jain, R. Notestine, A. Gamst, M. Sluiter, C. K. Ande, S. Van Der Zwaag, J. J. Plata, C. Toher, S. Curtarolo, G. Ceder, K. A. Persson and M. Asta, *Sci. Data*, 2015, **2**, 150009.
- (32) A. Demessence, P. Horcajada, C. Serre, C. Boissière, D. Grosso, C. Sanchez and G. Férey, *Chem. Commun.*, 2009, 7149–7151.
- (33) M. S. R. N. Kiran, S. Varughese, C. M. Reddy, U. Ramamurty and G. R. Desiraju, *Cryst. Growth Des.*, 2010, **10**, 4650–4655.
- (34) G. R. Krishna, M. S. R. N. Kiran, C. L. Fraser, U. Ramamurty and C. M. Reddy, *Adv. Funct. Mater.*, 2013, **23**, 1422–1430.
- (35) S. C. Sahoo, S. B. Sinha, M. S. R. N. Kiran, U. Ramamurty, A. F. Dericioglu, C. M. Reddy and P. Naumov, *J. Am. Chem. Soc.*, 2013, **135**, 13843–13850.
- (36) R. Samanta, S. Ghosh, R. Devarapalli and C. M. Reddy, *Chem. Mater.*, 2018, **30**, 577–581.
- (37) L. R. MacGillivray, G. S. Papaefstathiou, T. Friščić, D. B. Varshney and T. D. Hamilton, *Top. Curr. Chem.*, 2005, **248**, 201–221.
- (38) L. R. MacGillivray, *CrystEngComm*, 2004, **6**, 77–78.
- (39) M. Nagarathinam, A. M. P. Peedikakkal and J. J. Vittal, *Chem. Commun.*, 2008, 5277–5288.
- (40) I. -H. Park, A. Chanthapally, Z. Zhang, S. S. Lee, M. J. Zaworotko and J. J. Vittal, *Angew. Chem.*, 2014, **126**, 414–419.
- (41) A. Chanthapally, G. K. Kole, K. Qian, G. K. Tan, S. Gao and J. J. Vittal, *Chem. Eur. J.*, 2012, **18**, 7869–7877.
- (42) G. K. Kole, T. Kojima, M. Kawano and J. J. Vittal, *Angew. Chem., Int. Ed.*, 2014, **53**, 2143–2146.
-

- (43) F. -L. Hu, H. -F. Wang, D. Guo, H. Zhang, J. -P. Lang and J. E. Beves, *Chem. Commun.*, 2016, **52**, 7990–7993.
- (44) Y. -J. Zhang, C. Chen, L. -X. Cai, B. Tan, X. -D. Yang, J. Zhang and M. Ji, *Dalton Trans.*, 2017, **46**, 7092–7097.
- (45) K. M. Hutchins, T. P. Rupasinghe, L. R. Ditzler, D. C. Swenson, J. R. G. Sander, J. Baltrusaitis, A. V. Tivanski and L. R. MacGillivray, *J. Am. Chem. Soc.*, 2014, **136**, 6778–6781.
- (46) SMART (V 5.628), SAINT (V 6.45a), XPREP, SHELXTL, Bruker AXS Inc., Madison, WI, 2004.
- (47) G. M. Sheldrick, *SADABS (Version 2.03)*, University of Göttingen, Germany, 2002.
- (48) G. M. Sheldrick, *Acta Cryst.*, 2015, **C71**, 3–8.
- (49) A. L. Spek, *Acta Crystallogr., Sect. D: Biol. Crystallogr.*, 2009, **65**, 148–155.
- (50) L. J. Farrugia, *J. Appl. Crystallogr.*, 1997, **30**, 565.
- (51) L. J. Farrugia, *J. Appl. Crystallogr.*, 1999, **32**, 837–838.
- (52) V. A. Blatov, A. P. Shevchenko and V. N. Serezhkin, *J. Appl. Crystallogr.*, 2000, **33**, 1193.
- (53) V. A. Blatov, L. Carlucci, G. Ciani and D. M. Proserpio, *CrystEngComm*, 2004, **6**, 377–395.
- (54) W. C. Oliver and M. Pharr, *J. Mater. Res.*, 1992, **7**, 1564–1583.
- (55) X. J. Li, Z. J. Yu, X. X. Li and X. F. Guo, *Chem. – Eur. J.*, 2015, **21**, 16593–16600.
- (56) F. -Y. Yi, J. Zhang, H. -X. Zhang and Z. -M. Sun, *Chem. Commun.*, 2012, **48**, 10419–10421.

List of Publications

1. Hydrogen Uptake by an Inclined Polycatenated Dynamic Metal–Organic Framework Based Material.

Dilip Kumar Maity, Arijit Halder, **Goutam Pahari**, Fazle Haque and Debajyoti Ghoshal

Inorganic Chemistry **2017**, **56** (2), 713-716

2. Five Diverse Multidimensional Polycarboxylate–Based Mixed–Ligand Coordination Polymers with Different N, N'–Donor Ligands: Synthesis, Characterization and Their Sorption Study.

Saheli Ghosh, **Goutam Pahari**, Dilip K. Maity, Arijit Halder, and Debajyoti Ghoshal

ChemistrySelect **2018**, **3** (31), 8980-899

***3.** A reversible photochemical solid-state transformation in an interpenetrated 3D metal–organic framework with mechanical softness.

Goutam Pahari, Biswajit Bhattacharya, C Malla Reddy and Debajyoti Ghoshal

Chemical Communications **2019**, **55** (83), 12515–12518

***4.** Mixed ligand coordination complexes by using multicomponent ligand: Syntheses, characterization and effect of non-covalent interactions on their framework structures.

Anamika Das, Arijit Halder, Biswajit Bhattacharya, **Goutam Pahari** and Debajyoti Ghoshal

Journal of Molecular Structure **2020**, **1201**, 127189

***5.** Structural Transformations in Metal Organic Frameworks for the Exploration of Their CO₂ Sorption Behavior at Ambient and High Pressure.

Goutam Pahari, Saheli Ghosh, Arijit Halder and Debajyoti Ghoshal

Crystal Growth & Design **2021**, **21**, 5, 2633–2642

***6.** Synthesis of two cationic Coordination polymers for the exploration of anion exchange properties.

Goutam Pahari, Saheli Ghosh, Arijit Halder and Debajyoti Ghoshal

Polyhedron **2022**, **211**, 115528

7. Multifunctional Porous Coordination Polymers Synthesized by the Variation of Chain Length and Flexibility of Dicarboxylates and Size of the Metal Ions.

Saheli Ghosh, Mrinmay Das, Susanta Dinda, **Goutam Pahari**, Partha Pratim Ray, and Debajyoti Ghoshal,

***Crystal Growth & Design* 2021, 21, 9, 4892–4903**

***8.** Designing of three mixed ligand MOFs in searching of length induced flexibility in ligand for the creation of interpenetration.

Saheli Ghosh, **Goutam Pahari**, Anupam Maiti, Susanta Dinda and Debajyoti Ghoshal

[Communicated]

*** These works are included in this thesis.**